NUREG/CR-4483
PNL-5727

Reactor Pressure Vessel Failure Probability Following Through-Wall Cracks Due to Pressurized Thermal Shock Events

Prepared by F. A. Simonen, M. R. Garnich, E. P. Simonen, S. H. Bian,
K. K. Nomura, W. E. Anderson, L. T. Pedersen

Pacific Northwest Laboratory
Operated by
Battelle Memorial Institute

Prepared for
U.S. Nuclear Regulatory Commission

NOTICE

This report was prepared as an account of work sponsored by an agency of the United States Government. Neither the United States Government nor any agency thereof, or any of their employees, makes any warranty, expressed or implied, or assumes any legal liability of responsibility for any third party's use, or the results of such use, of any information, apparatus, product or process disclosed in this report, or represents that its use by such third party would not infringe privately owned rights.

NOTICE

Availability of Reference Materials Cited in NRC Publications

Most documents cited in NRC publications will be available from one of the following sources:

1. The NRC Public Document Room, 1717 H Street, N.W. Washington, DC 20555
2. The Superintendent of Documents, U.S. Government Printing Office, Post Office Box 37082, Washington, DC 20013-7082
3. The National Technical Information Service, Springfield, VA 22161

Although the listing that follows represents the majority of documents cited in NRC publications, it is not intended to be exhaustive.

Referenced documents available for inspection and copying for a fee from the NRC Public Document Room include NRC correspondence and internal NRC memoranda; NRC Office of Inspection and Enforcement bulletins, circulars, information notices, inspection and investigation notices; Licensee Event Reports; vendor reports and correspondence; Commission papers; and applicant and licensee documents and correspondence.

The following documents in the NUREG series are available for purchase from the GPO Sales Program: formal NRC staff and contractor reports, NRC-sponsored conference proceedings, and NRC booklets and brochures. Also available are Regulatory Guides, NRC regulations in the *Code of Federal Regulations*, and *Nuclear Regulatory Commission Issuances*.

Documents available from the National Technical Information Service include NUREG series reports and technical reports prepared by other federal agencies and reports prepared by the Atomic Energy Commission, forerunner agency to the Nuclear Regulatory Commission.

Documents available from public and special technical libraries include all open literature items, such as books, journal and periodical articles, and transactions. *Federal Register* notices, federal and state legislation, and congressional reports can usually be obtained from these libraries.

Documents such as theses, dissertations, foreign reports and translations, and non-NRC conference proceedings are available for purchase from the organization sponsoring the publication cited.

Single copies of NRC draft reports are available free, to the extent of supply, upon written request to the Division of Technical Information and Document Control, U.S. Nuclear Regulatory Commission, Washington, DC 20555.

Copies of industry codes and standards used in a substantive manner in the NRC regulatory process are maintained at the NRC Library, 7920 Norfolk Avenue, Bethesda, Maryland, and are available there for reference use by the public. Codes and standards are usually copyrighted and may be purchased from the originating organization or, if they are American National Standards, from the American National Standards Institute, 1430 Broadway, New York, NY 10018.

NUREG/CR-4483
PNL-5727

Reactor Pressure Vessel Failure Probability Following Through-Wall Cracks Due to Pressurized Thermal Shock Events

Manuscript Completed: March 1986
Date Published: April 1986

Prepared by
F. A. Simonen, M. R. Garnich, E. P. Simonen, S. H. Bian,
K. K. Nomura, W. E. Anderson, L. T. Pedersen

Pacific Northwest Laboratory
Richland, WA 99352

Prepared for
Division of Safety Review and Oversight
Office of Nuclear Reactor Regulation
U.S. Nuclear Regulatory Commission
Washington, D.C. 20555
NRC FIN B2510

ABSTRACT

A fracture mechanics model was developed at the Pacific Northwest Laboratory (PNL) to predict the behavior of a reactor pressure vessel following a through-wall crack that occurs during a pressurized thermal shock (PTS) event. This study, which contributed to a U.S. Nuclear Regulatory Commission (NRC) program to study PTS risk, was coordinated with the Integrated Pressurized Thermal Shock (IPTS) Program at Oak Ridge National Laboratory (ORNL). The PNL fracture mechanics model uses the critical transients and probabilities of through-wall cracks from the IPTS Program. The PNL model predicts the arrest, reinitiation, and direction of crack growth for a postulated through-wall crack and thereby predicts the mode of vessel failure. A Monte-Carlo type of computer code was written to predict the probabilities of the alternative failure modes. This code treats the fracture mechanics properties of the various welds and plates of a vessel as random variables. Plant-specific calculations were performed for the Oconee-1, Calvert Cliffs-1, and H. B. Robinson-2 reactor pressure vessels for the conditions of postulated transients. The model predicted that 50% or more of the through-wall axial cracks will turn to follow a circumferential weld. The predicted failure mode is a complete circumferential fracture of the vessel, which results in a potential vertically directed missile consisting of the upper head assembly. Missile arrest calculations for the three nuclear plants predict that such vertical missiles, as well as all potential horizontally directed fragmentation type missiles, will be confined to the vessel enclosure cavity. The PNL failure mode model is recommended for use in future evaluations of other plants, to determine the failure modes that are most probable for postulated PTS events.

EXECUTIVE SUMMARY

The U.S. Nuclear Regulatory Commission (NRC) has supported several studies that have contributed toward the calculation of the risks from pressurized thermal shock (PTS) to reactor pressure vessels. One objective of the study reported here was to develop and apply a fracture mechanics model to predict the reactor pressure vessel failure modes that may occur following the development of a through-wall crack. This study was performed at Pacific Northwest Laboratory (PNL) and was closely coordinated with the Integrated Pressurized Thermal Shock (IPTS) program at Oak Ridge National Laboratory (ORNL). The objective of the IPTS program was to evaluate the significance of the transients that contribute to the probability of the through-wall cracks. The IPTS program results defined the starting conditions for the fracture mechanics model of the PNL study.

The failure mode evaluation consisted of two phases. In the first phase, the basics of the fracture mechanics model were developed and applied in preliminary calculations. In the second phase, the model was completed and refined and then was applied in calculations specific to the Oconee-1, Calvert Cliffs-1, and H. B. Robinson-2 nuclear power plants. These were the same reactors addressed in the ORNL/IPTS study. Data from the ORNL evaluation served as essential inputs to the failure mode evaluation at PNL. The results of the plant-specific calculations show that a workable methodology has been developed. This fracture mechanics model is available for use in future plant-specific calculations, for which the vessel and transient characteristics may result in predicted failure modes that differ from those predicted here for the limited sample of three plants.

FRACTURE MECHANICS MODEL

The fracture mechanics model has both deterministic and probabilistic aspects. In the probabilistic model, essential inputs to the deterministic model are described as distribution functions to simulate the variability and uncertainties in the input parameters. A Monte-Carlo computer code was written to perform the calculations of failure mode probabilities.

Detailed calculations were performed to support the assumptions for the initial length of the through-wall crack in the vessel wall. Detailed simulations were performed that addressed the growth of surface flaws in the directions of both depth and length. These calculations indicated that all through-wall cracks, in both axial and circumferential welds, will extend to the full length of the welds.

An important feature of the model is its ability to predict when an axial crack will turn and grow to follow an embrittled circumferential weld. Methods were developed to perform simplified calculations of crack-tip stress intensity factors for this turning behavior. Simplified methods were also developed to address the effects of elastic-plastic deformation, structural dynamics, and fluid-structural interactions on calculated stress intensity factors. The criteria for crack propagation were formulated to address crack arrest, crack initiation, ductile tearing resistance for upper shelf temperatures, and effects of neutron irradiation damage on fracture mechanics properties of the vessel materials.

The fracture mechanics model neglects thermal stresses for through-wall cracks. Detailed calculations show that the stress intensity factors due to such stresses are small relative to the corresponding contributions from internal pressure stresses. However, the model does account for the important through-wall variations in fracture toughness that result from the gradients in temperature and neutron fluence. A root-mean-square approach is used to calculate an average fracture toughness for the simplified computational model.

Detailed calculations were performed to support assumptions regarding the effects of the depressurization that occurs as a through-wall crack opens and grows in length. During the millisecond time frame of the crack opening event, the depressurization due to fluid structural interaction effects is significant. However, these effects are largely offset by the effects of structural dynamic response. Over the much longer time frame of PTS events, the effect of leakage through the through-wall cracks is significant. Calculations show that system depressurization occurs because the leakage rates exceed the capacity of high-pressure injection pumps to maintain pressure.

PLANT-SPECIFIC CALCULATIONS

The probabilistic fracture mechanics model was applied in plant-specific calculations for the Oconee-1, Calvert Cliffs-1, and H. B. Robinson-2 reactor vessels. As in the ORNL study, the hypothetical vessel HBR-HYPO was used in the H. B. Robinson-2 evaluation to permit an appropriate illustration of the methods of analysis. Data on pressures and temperatures for PTS transients were supplied by the ORNL/IPTS study. This study also provided data on the probabilities of through-wall cracks.

The fracture mechanics model predicted final crack lengths and opening areas. The major categories for the failure modes were 1) a complete circumferential fracture of the vessel; 2) a large opening in the vessel wall due to crack growth beyond the length of a single axial weld; and 3) a small opening in the vessel as a result of crack arrest at the ends on a single axial weld. The probabilities for each of these failure modes were calculated for each of the three specific vessels.

It was predicted that 50 to 90% of the vessel failures would be in the form of a complete circumferential fracture of the vessel. In the remainder of the cases, the axial cracks most often arrested at the ends of the axial weld, and no further crack growth occurred into the adjacent plate material, which had higher levels of fracture toughness. Clear differences were seen in the predicted failure modes for the three specific vessels. In general, the failure modes associated with crack arrest tended to occur most often when the lengths of the axial welds were relatively short and when the pressures for the transients were relatively low.

The possible generation and consequences of missiles during a vessel failure were addressed. Two types of missiles were considered: 1) vertical missiles that would result from the fracture of a circumferential weld and 2) horizontal missiles that would result from fragmentation of a vessel. In the plant-specific evaluations it was concluded that both types of missiles could be generated, but that all such missiles will be confined to the vessel enclosure cavity. Detailed calculations were performed for the motion of vertical missiles consisting of the upper head assembly. Fluid thrust forces and restraint forces from attached piping were simulated. The stiffness of the piping in combination with impact of the piping with adjacent concrete structures was found to arrest the upward motion of the missile. Missiles from vessel fragmentation were found to have insufficient velocities to penetrate the thick concrete structures of the reactor vessel cavity.

CONTENTS

FIGURES

TABLES

ACKNOWLEDGMENTS

This report contains an account of work sponsored by the Division of Safety Technology, Office of Nuclear Reactor Regulation of the U.S. Nuclear Regulatory Commission. This work was completed under the direction of Roy Woods, project technical monitor, Generic Issues Branch of the Division of Safety Technology.

Other NRC staff providing encouragement and support include M. Vagins, J. Strosnider, C. E. Johnson, R. E. Johnson, and P. N. Randall. From Oak Ridge National Laboratory, J. G. Merkle, R. D. Cheverton, D. G. Ball, J. D. White and D. L. Selby provided valuable input and advice. Information for the H. B. Robinson-2 evaluation was provided by J. H. Phillips of Carolina Power and Light. Finally, many useful suggestions and insights into the difficult fracture mechanics issues were provided by Dr. G. R. Irwin at the University of Maryland.

REACTOR PRESSURE VESSEL FAILURE PROBABILITY
FOLLOWING THROUGH-WALL CRACKS DUE TO
PRESSURIZED THERMAL SHOCK EVENTS

1.0 INTRODUCTION

In recent years the issue of pressurized thermal shock (PTS) has been investigated in great detail by the U.S. Nuclear Regulatory Commission (NRC), the electric utility industry, and the nuclear steam supply system contractors. The concern in PTS has been the brittle fracture of welds in reactor pressure vessels under conditions of both rapid cooling and high system pressures.

This report describes a contribution by Pacific Northwest Laboratory (PNL) to NRC's effort to resolve the PTS safety issue (A-49). This PNL study was coordinated closely with NRC's Integrated Pressurized Thermal Shock (IPTS) Program (White 1983) at Oak Ridge National Laboratory (ORNL).

The study described here was part of ongoing technical support to the NRC staff by PNL on the PTS issue. This effort began with a technical review of PTS issues and recommended regulatory positions (Pedersen et al. 1982a). In a subsequent study (Pedersen et al. 1982b) PNL provided a technical critique of the NRC near-term screening criteria (Dircks 1982).

In SECY-82-465 (Dircks 1982), the significance of vessel failure relative to safety goals for nuclear power plants was addressed. It was conservatively assumed that all through-wall cracks will lead to core melt. However, it was recognized that this approach could give unrealistic estimates of risks. The objective of the PNL study was to develop a methodology that can be used to predict the modes of vessel failure that will result after a crack has penetrated the wall of a vessel.

The first step was to develop a methodology suitable for predicting vessel failure modes. This analysis method was then applied to the three vessels evaluated in the IPTS project at ORNL. The through-wall crack probabilities and thermal transients of the IPTS study were used as inputs to the failure mode evaluations. The failure modes of interest range from "catastrophic" vessel rupture to a crack in a single weld that gives only a small opening in the vessel wall.

In the failure mode evaluations, PNL was requested by NRC to address the following types of questions:

- Will a crack in an axial weld extend into the plate material of the next shell course?
- Will the axial crack turn and follow the circumferential weld joining the adjacent shell courses?
- Does a through-wall crack in a circumferential weld necessarily lead to a complete circumferential fracture of the vessel?

- Given a complete circumferential fracture, what is the effect of the fluid thrust forces and attached piping on the motion of the vessel fragments?
- What are the sizes, velocities, and hazards of other potential fragments of the vessel?

This report describes the fracture mechanics model and results of the application of the model to the Oconee-1, Calvert Cliffs-1, and H. B. Robinson-2 vessels. Appendixes to this report describe details of the fracture mechanics model along with a number of analyses that were performed to support simplifying assumptions made in the failure mode predictions. Fluid mechanics calculations needed to predict the motion of missiles generated by vessel fracture also are described in an appendix.

2.0 BACKGROUND

The pressure vessel of a nuclear reactor is subjected to pressurized thermal shock when an extended cooling transient to the inner vessel wall is accompanied by system pressurization. Under these conditions, thermal and pressurization stresses in the inner part of the vessel wall are additive. Moreover, these stresses are in tension and tend to open any cracks that may be located at or near the inner vessel surface. Although PTS type cooling transients have occurred at operating pressurized water reactors, the toughness of the materials of these relatively new vessels was sufficient to preclude concerns with brittle fracture.

The failure of a vessel in a PTS scenario requires the simultaneous occurrence of three factors (Cheverton, Iskander, and Whitman 1983):

- tensile thermal stresses from the rapid cooling (e.g., 200°F per hr) of the inside surface of the vessel with prevailing pressures at a significant fraction of the normal operating pressure (e.g., 1000 psi or greater)

- a significant loss of fracture toughness near the inner wall due to irradiation damage - This loss of toughness is a result of an upward shift in the ductile-brittle transition temperature of the ferritic steel of the vessel wall (e.g., RT_{NDT} in excess of 200°F). The current concern for embrittlement is greatest for welds in the beltline region of vessels, particularly for welds with high copper contents (e.g., 0.35 wt% copper).

- the existence of a crack-like flaw in the highly stressed and embrittled region of the vessel wall.

To address concerns with PTS, NRC has promulgated a rule that 1) establishes a screening criterion for the reference temperature for nil-ductility transition (RT_{NDT}), 2) requires licensees to submit plans for the reduction of neutron flux to avoid exceeding the screening criterion, and 3) requires plants that will exceed the screening criterion to submit plant-specific safety analyses to determine the need for modifications to continue safe operation after the screening limit has been exceeded.

The NRC has also continued research to provide technical bases for the proposed screening criterion. Another objective of these research studies has been to provide guidance to licensees for plant-specific analyses. The IPTS program at ORNL has developed and demonstrated a methodology for predicting the probability that a PTS transient will result in growth of a crack through the wall of a reactor pressure vessel. The main concern has been with fracture of welds in the beltline region of a vessel. In the case of axial welds, the ORNL study has predicted a final crack length that is the full length of the axial weld. However, the ORNL fracture mechanics model does not address growth of cracks beyond the ends of the axial welds.

In its study, PNL developed a fracture mechanics model to predict the growth of through-wall cracks in reactor pressure vessels under PTS conditions. The model is applied in demonstration calculations to the three vessels evaluated in the ORNL/IPTS project (i.e., Oconee-1, Calvert Cliffs-1, and H. B. Robinson-2/HBR-HYPO). This report documents the PNL study. The report is intended to provide guidance to the preparation of plant-specific evaluations of the vessel failure modes that will occur after through-wall cracks result during PTS events.

3.0 DETERMINISTIC FRACTURE MECHANICS MODEL

This section describes the deterministic fracture mechanics model that was developed to predict the growth of through-wall cracks in reactor pressure vessels. Particular aspects of this model are discussed in greater detail in appendixes to this report. The model begins by assuming a through-wall crack of prescribed length and location in the vessel, and then predicts the subsequent growth and/or arrest of this crack. In specific applications of the model, the required information on the initial through-wall cracks was provided by the results of the fracture mechanics calculations performed at Oak Ridge National Laboratory. The deterministic model described in this section formed the core of the probabilistic model that was developed to predict vessel failure modes. This probabilistic model is described in Section 4.0 of this report.

Figure 3.1 shows a typical reactor pressure vessel. A fabricated vessel consists of a collection of rolled plates and rings that are welded together into a complete vessel. The PNL fracture mechanics model simulates the growth of a crack from its initial location in a weld. The path of crack growth along the welds and through the base metal is predicted. Appendix A presents a set of exploratory calculations that illustrates and explains the various features of the deterministic fracture mechanics model.

3.1 HEAT TRANSFER ANALYSIS

The failure mode analyses make use of temperature data from evaluations of pressurized thermal shock events. This input data was obtained from the ORNL/IPTS study and was in the form of temperatures at the inner surface of the vessel.

The fracture mechanics model required distributions of temperatures through the thickness of the wall of the vessel. These temperatures were calculated using the transient heat conduction routine of the computer code VISA (Stevens et al. 1983). It should be noted that these temperatures were used only for predicting the temperature-dependent fracture toughness at different locations within the wall of the vessel. In this regard, thermal stresses were neglected.

3.2 STRESS ANALYSIS

The fracture mechanics model was based on simplified calculation of stress in the wall of the vessel. As described below and in Appendix B, thermal stresses were neglected in the analyses of through-wall cracks. Pressure stresses were assumed to be distributed uniformly through the wall of the vessel. This uniform distribution was consistent with the use of published solutions that gave stress intensity factors for cracks in cylindrical shells.

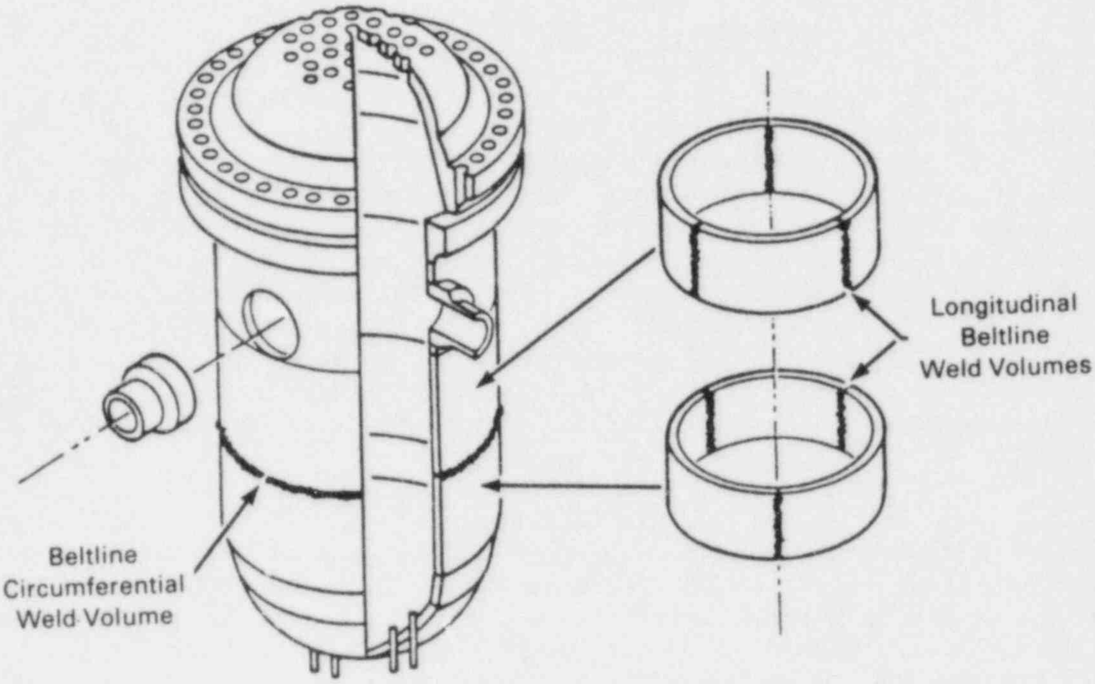

a. Rolled and Welded Beltline Shell

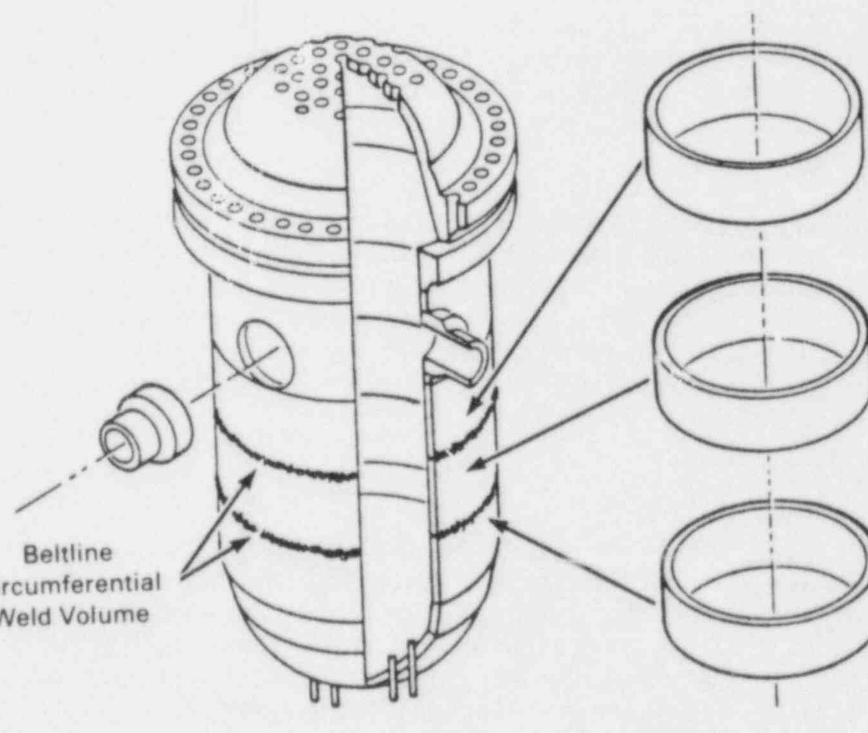

b. Welded-Ring-Forging Beltline Shell

FIGURE 3.1. Fabrication Configurations of PWR Beltline Shells

3.3 AXIAL CRACK ANALYSIS

The model assumes that all through-wall cracks have a straight crack front that is normal to the vessel wall. This idealized shape is consistent with the geometries used in published solutions for crack-tip stress intensity factors. The predicted lengths of the axial cracks from the ORNL/IPTS study were usually the full length of the axial weld. Appendix C discusses the bases for assumptions concerning the initial crack length. Solutions are applied for finite length surface flaws as given in Appendix D. In some cases, axial welds extend beyond that region of the vessel that is most embrittled by the neutron fluence from the active core. For these welds the initial length of the axial crack was terminated approximately two wall thicknesses beyond the limits of the active core.

3.4 ARREST AND INITIATION PREDICTIONS

In the analysis, the initial axial crack was taken to be a propagating crack that must be arrested, rather than a stationary crack for which growth may initiate. This assumption was consistent with the objective of the model, which was to evaluate the growth of cracks beginning at the time when a surface flaw becomes unstable and propagates through the wall of the vessel. Appendix E presents details of the criteria for crack arrest and for the reinitiation of a crack after it has arrested.

The method used to predict crack arrest is, in many respects, similar to the method used by ORNL to interpret the observations from wide plate tests of crack arrest (Bass, Pugh, and Walker 1985). The crack must first arrest in a manner consistent with measured values of crack arrest toughness. In applying this criterion, inertial effects were considered as a factor that would prevent the full development of the crack driving force that would exist under static conditions of loading. In the PNL vessel calculations, the bulging factor for axial cracks was neglected for arrest predictions, in order to approximate inertial effects. However, in the arrest evaluation it was also required that the arrested crack not continue to grow under static conditions by ductile tearing. In this static crack growth analysis, the bulging factor was utilized. This predicted an increase in crack driving force, once static load conditions were achieved.

3.5 CIRCUMFERENTIAL CRACK ANALYSIS

The calculations of Appendix C show that cracks in circumferential welds are expected to extend around the entire circumference of the vessel before they become through-wall cracks. It was therefore assumed that a through-wall crack in a circumferential weld always implies a complete circumferential fracture of the vessel. As such, no further fracture mechanics analyses were required.

The main focus of the model for circumferential fracture was the turning of cracks in axial welds to follow a circumferential weld. Appendix F presents the methods used for this part of the predictive model. It was determined that the crack driving force for circumferential growth was about one-half that for continued growth in the axial direction.

The failure mode analyses assumed that axial cracks will always turn to follow a circumferential weld, provided that the calculated stress intensity factor for such growth exceeds the fracture toughness of the material of the circumferential weld. Detailed analysis of the extent of the full circumferential growth was not possible. Hence, it was conservatively assumed that the turning of an axial crack will always result in a complete circumferential fracture of the vessel.

3.6 THROUGH-WALL THERMAL GRADIENT

Detailed calculations of stress intensity factors are shown in Appendix B for axial cracks subjected to pressurized thermal shock types of thermal stresses. The results indicate that such thermal stresses can be neglected for through-wall cracks. Their contribution to crack growth is small relative to the contribution of pressure stresses. Such stresses also tend to offset the contribution of bulging effects induced by pressure loading.

The variation in fracture toughness through the wall of the vessel was treated by calculating a root mean square average of the toughness distribution through the wall of the vessel. In this case the thermal gradient effect was included along with the toughness variation due to the through-wall variations in the neutron fluence.

3.7 STRESS INTENSITY FACTOR SOLUTIONS

The fracture mechanics model required predictions of stress intensity factors and crack opening areas for axial cracks. Appendix G provides details on the procedures used for these calculations. Published linear elastic fracture mechanics solutions for axial cracks in cylindrical shells provided the starting point for the calculations. However, it was necessary to correct these elastic equations for the effects of plasticity.

Finite element solutions were performed for axial cracks in reactor vessels to derive factors that could correct for the effects of plastic deformation. It was then determined that an existing strip yield approach for the analysis of cracks in cylinders could be modified to describe the trends of the vessel solutions. The plastic solutions were further generalized by using the estimation scheme of Kumar, German, and Shih (1981) to extend the solutions to higher levels of stress.

3.8 IRRADIATION DAMAGE

An important feature of the fracture mechanics model was the prediction of the effects of neutron fluence on fracture toughness and other material properties. The shift in RT_{NDT} (reference temperature for nil-ductility transition) is predicted using the same equations as used in the ORNL/IPTS evaluation

(Cheverton and Ball 1984). The mean shift is calculated using a correlation proposed by Randall (of the NRC staff) as follows:

$$\Delta RT_{NDT} = [-10 + 470\ Cu + 350\ Cu\ Ni]\ (f \times 10^{-19})^{0.27},\ °F \qquad (3.1)$$

or

$$= 283\ (f \times 10^{-19})^{0.194}\ -48,\ °F,$$

whichever is smaller,

where Cu = wt% of copper
Ni = wt% of nickel
f = fluence, neutrons/cm^2.

The mean value of shift plus two standard deviations is calculated as

$$\Delta RT_{NDT}\ (2\sigma) = [38 + 470\ Cu + 350\ Cu\ Ni]\ (f \times 10^{-19})^{0.27},\ °F \qquad (3.2)$$

or

$$= 283\ (f \times 10^{-19})^{0.194},\ °F,$$

whichever is smaller.

Predictive equations were also required to estimate the effect of fluence on the upper shelf Charpy energy (CVN) and the material flow stress. For ΔUSE (change in upper shelf energy), equations from Combustion Engineering (1982) were selected:

$$\Delta USE\ (\%) = (24.97 + 79.65\ Cu - 43.29\ Si)\ f^{0.15},\ \text{for welds} \qquad (3.3)$$

$$= (-1.19 + 102.49\ Cu)\ f^{0.27},\ \text{for plates}$$

where Cu = wt% of copper
Si = wt% of silicon
f = fluence, 10^{19} neutrons/cm^2.

The increase in flow stress ($\Delta\sigma_0$, MPa) was taken to be the same as the increase in yield strength as predicted by Odette and Lombrozo (1983):

$$\Delta\sigma_0 = 1.25\ \Delta RT_{NDT} \qquad (3.4)$$

$$\Delta RT_{NDT} = \text{Shift in } RT_{NDT},\ °C.$$

New correlations are currently being developed by the nuclear industry as more surveillance data becomes available. It is recommended that the above equations be updated as improved equations become available.

3.9 UPPER SHELF ANALYSIS

The methods of elastic-plastic fracture mechanics were used in the PNL model to predict the growth and arrest of cracks. In many cases cracks propagated from embrittled welds into the tougher material of adjacent plates whose fracture resistance was governed by upper shelf behavior.

The use of elastic-plastic fracture mechanics has been accepted by NRC in the resolution of the A-11 safety issue of low upper shelf weld materials (Johnson 1982). Ongoing work on other NRC research programs (Pugh 1985) continues to expand the understanding of the arrest of cracks that extend into material on the upper shelf. The approach taken in the PNL study is believed to be conservative. However, the model should be reviewed and revised before future calculations are performed. Appendix E provides additional discussion of the approach used to treat fracture behavior on the upper shelf. Limitations of the available methods are also addressed.

The calculations presented in this report are based on a preliminary correlation of the J-resistance curve with values of CVN energy (Johnson 1982). Recent work by Hiser (1985) has provided updated correlations, which were not available at the time that the PNL calculations were performed. The Hiser correlations (1985) predicted allowable values of $K_J = \sqrt{EJ}$ that were about 200 ksi $\sqrt{in.}$ for irradiated welds with CVN = 50 ft-lb. This was essentially the value of upper shelf toughnesses used by ORNL in linear elastic fracture mechanics evaluations. In contrast, for a good quality vessel plate material with CVN = 140 ft-lb, the method of Johnson (1982) predicted a value of allowable K_J of about 700 ksi $\sqrt{in.}$

The J_{50} approach (Johnson 1982) was first considered for use in crack stability predictions. This approach was judged to be overly conservative. Consequently, the allowable value of applied J was taken to be the value of J corresponding to Δa = 2.0 in. of crack growth. There is some limited data from large specimens (Shih and Andrews 1981) to support the CVN correlation of Johnson (1982) to crack growths of 2.0 in. In the simplified analysis it was assumed that axial cracks were stable for J-applied less than this value for 2.0 in. of crack growth. The cracks were taken to be unstable if this critical value was exceeded. The arrest values of allowable J-applied were conservatively assumed to be equal to the values for crack initiation.

3.10 DYNAMIC EFFECTS

Dynamic effects were addressed in the development of the fracture mechanics model. Appendix H presents details of finite element calculations that simulated the sudden opening of an axial crack in a reactor pressure vessel. These calculations included the effects of fluid structural interactions that occur as a crack opens.

The detailed finite element calculations supported the many important simplifying approximations made in the final version of the fracture mechanics model. All effects of dynamic response and fluid-structural interactions were neglected in the simplified fracture mechanics model. Only static solutions were used to predict crack opening behavior, but the key assumption was that the full fluid pressure present prior to crack opening can be used as the loading for the static calculations. This assumption was consistent with results of other investigators for the dynamic opening of cracks in reactor coolant piping (Ayres 1975).

It appears that the expected dynamic effects associated with the sudden opening of the crack in a vessel are offset by depressurization of the fluid in the region near the crack. Thus, the net effect of structural dynamics and fluid-structural interaction is relatively small. The ability to use static solutions greatly eased the computational requirements for the fracture mechanics analysis. This was particularly helpful when the method was implemented into the probabilistic computer code for evaluation of vessel failure modes.

3.11 LEAK RATE AND DEPRESSURIZATION EFFECTS

A method was developed to predict the rates of leakage through an open axial crack in a reactor pressure vessel. The leak rate model is described in Appendix I. This model also includes a scheme to estimate the system depressurization that can occur as a result of coolant loss through the leaking crack.

The selected leak rate model was based on the flow of subcooled water through a crack. Existing equations for saturated flow through stress corrosion cracks (Mayfield et al. 1980) were considered as an alternative, but these equations were found to be inappropriate for the conditions of pressurized thermal shock.

In the depressurization calculation, the leakage is balanced against the makeup of water provided by the injection pumps. An equilibrium pressure is calculated. This pressure is used to calculate stresses in the vessel for evaluations of crack propagation.

In example calculations, it was determined that the leak rates were too slow to affect crack propagation over the millisecond time periods associated with dynamic crack opening events. However, leak rates had a large effect on depressurization over longer time periods on the scale of the duration of the overcooling transient. Depressurization over such time is important in consideration of through-wall cracks that might arrest early in the transient, but then reinitiate later when the vessel wall had cooled further into the temperature range of brittle fracture.

The depressurization model has been applied in plant-specific evaluations of vessel fracture. It appears that the leakage through an axial crack will result in a bleed-down in pressure to a final level of about 200 psi within about 5 minutes. It is unlikely that the growth of arrested cracks will reinitiate for such low levels of pressure. It has been concluded that depressurization effects are important. Furthermore, in future analyses it is probably justified to omit detailed consideration of leak rates. It can be assumed that arrested through-wall cracks will not grow further, because the system pressure will be lost soon after the crack arrests.

4.0 PROBABILISTIC FRACTURE MECHANICS MODEL

This section describes the probabilistic fracture mechanics model that was developed to predict probabilities of occurrence for the different failure modes relevant to reactor pressure vessels subjected to conditions of pressurized thermal shock. Specific aspects of the analytical model are discussed in greater detail in appendices to this report.

A flow chart for the probabilistic analysis is shown in Figure 4.1. The actual calculations were performed as Monte-Carlo simulations by a computer program that was written as part of this research project. Each of the large number of simulations is an application of the deterministic fracture mechanics model that was described in the previous section. The inputs to each simulation are obtained by sampling from distribution functions that describe the variability and/or uncertainty in the parameters. In the PNL model the uncertainties are associated primarily with the prediction of fracture toughness.

The discussion below reviews important features of the flow chart. A basis for understanding the probabilistic model is provided through a discussion of the input and output parameters for the computer code. Plant-specific analyses are presented in subsequent sections of this report, and these example calculations provide additional background on features of the probabilistic model.

4.1 INPUTS TO PROBABILISTIC MODEL

The computer program for the probabilistic calculations requires a combination of both deterministic and probabilistic inputs. Except as noted, the probabilistic inputs are specified as mean values and standard deviations of normal distributions that describe the parameters. In some cases the input data also specifies how the tails of the distributions are to be truncated.

The major inputs to the analysis are listed below. Those parameters that are treated as deterministic variables are indicated as such.

Vessel Dimensions - The inside diameter and wall thickness are specified as deterministic parameters.

Material Properties - Elastic constants and heat conduction properties are deterministic inputs.

Pressures and Temperatures - The pressures and temperatures at the inner surface of the vessel are specified as a function of time during the transient. Each computer run is for only one transient, and the pressures and temperatures are deterministic variables. However, there are conditional probabilities associated with each transient, and these probabilities enter into the calculations of integrated probabilities for the failure modes.

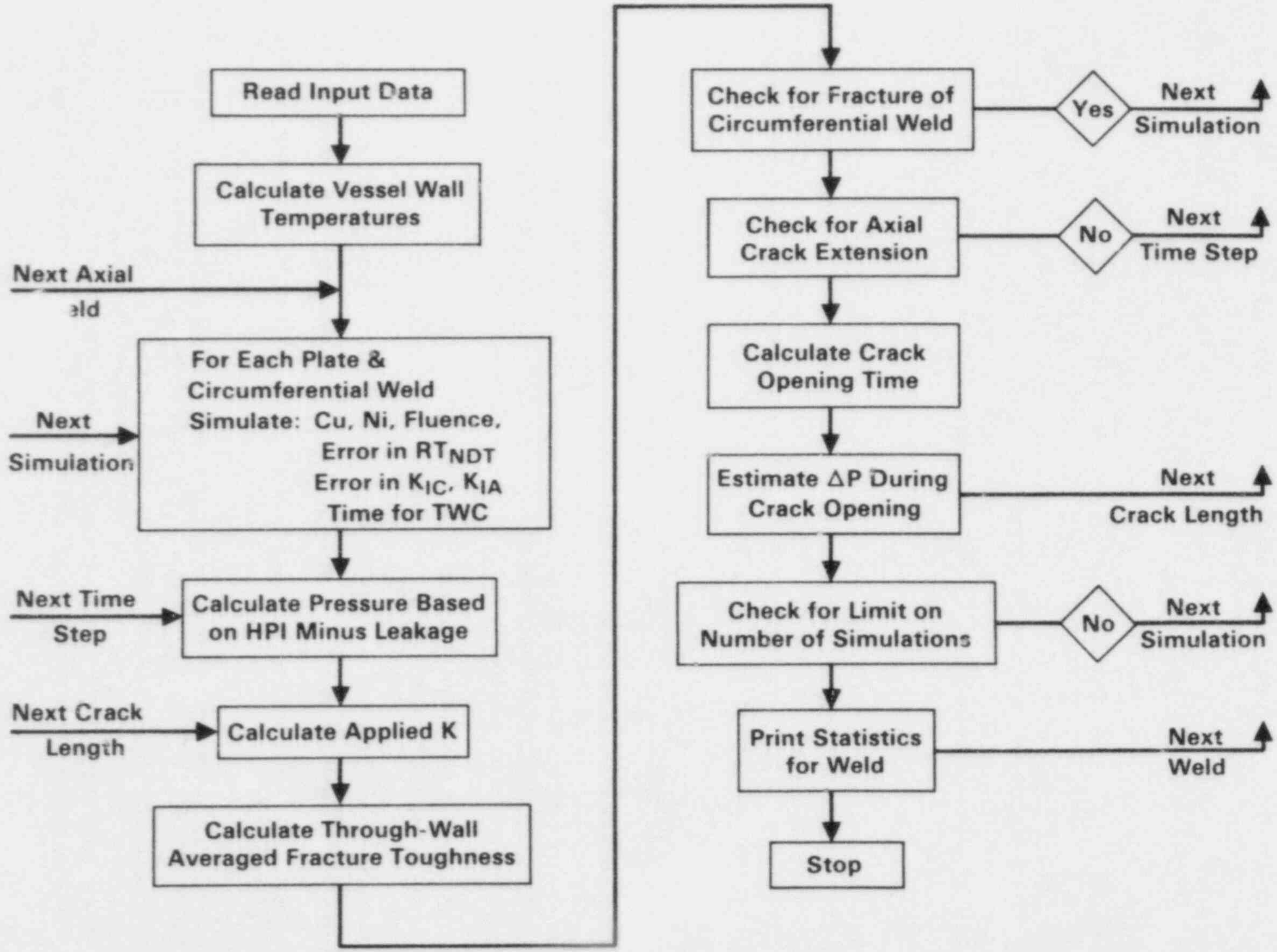

FIGURE 4.1. Flow Chart for Probabilistic Analysis of Vessel Failure Modes

Pressure-Volume Characteristics - A deterministic constant specifies the decrease in system pressure for a unit loss of coolant from the system. In the model, the fluid loss is through leaking axial cracks. The pressure and volume characteristics of the injection pumps are described by a user-supplied subroutine to the computer program.

Time of Crack Occurrence - This probabilistic input is specified as a histogram. Results from previous calculations of the probability of a through-wall crack for the given weld and transient are used. The histogram describes the fraction of the time that the through-wall crack was predicted to occur during each particular time interval.

Initial Crack Lengths - The initial lengths of the cracks in the axial welds must be prescribed deterministically by the coordinate locations of the ends of the through-wall cracks. Each computer run can address any number of axial welds with initial cracks. However, a separate Monte-Carlo analysis is performed for each weld.

Crack Growth Trajectories - This set of deterministic parameters specifies the arrangement of welds and plates for the assembled pressure vessel. A series of coordinates that define "nodes" on an axial line is specified, and the axial line is aligned with the axial weld under consideration. A fluence is specified at each node. The particular material present at the node is prescribed as a label. This material may be either weld metal or base metal. If the node is at the elevation of a circumferential weld, then the designation for this weld is specified so that the potential for crack extension along this weld can be evaluated.

Material Variables - A set of material variables is prescribed for use in probabilistic estimates of fracture toughness. This input is in the form of a table with a complete set of parameters for each material designation. Each material will typically correspond to a given plate or weld in the vessel. Mean values and standard deviations of the material constants are specified as required by the fracture mechanics model. The following parameters are included in the list of inputs, where M indicates mean value, SD indicates standard deviation, T indicates truncation for the normal distribution, and D indicates that the parameter is a deterministic variable:

Initiation toughness	SD, T
Arrest toughness	SD, T
Shift in RT_{NDT}	T
Copper content	M, SD
Nickel content	M, SD
Initial RT_{NDT}	M, SD
Silicon content	D
Unirradiated flow stress	D
Initial upper shelf Charpy impact energy	D
Fluence	SD

4.2 OUTPUTS OF PROBABILISTIC MODEL

The computer program provides tables of output, with each table corresponding to a given weld and transient. A line of output is provided for each simulation. The output gives a set of parameters that describe the outcome of the crack growth prediction. A typical analysis would be for 200 simulations. The following output data is generated:

- locations of cracked circumferential welds
- time at which the through-wall axial crack first appeared
- time at which the crack achieves its maximum size
- final locations of the ends of the crack
- final crack opening area.

4.3 SIMULATION PROCEDURE

The simulation procedure is summarized in the flow chart of Figure 4.1. Most of the logic deals with the simulation of fracture toughness. The approach taken in the PNL model closely follows the ORNL/IPTS study (Cheverton and Ball 1984; White 1984) in order to be consistent with the approach used to calculate the probabilities of through-wall cracks.

Each simulation shown in Figure 4.1 begins by establishing the characteristics of a hypothetical vessel that is consistent with the inputs for the variability of the materials in the vessel. The calculations are purely deterministic once this hypothetical vessel is established. An essential assumption in the probabilistic model is that there is no correlation between the random variations in properties of the various welds and plates of a given vessel. This assumption is believed to be reasonable because the different classes of materials of a given vessel (e.g., plates, axial welds, and circumferential welds) are fabricated at different facilities and by different procedures.

There may be correlations between the random variations in the properties of, for example, all the circumferential welds of the vessel. These correlations could have some effect on the predictions of failure modes. However, there was a lack of data to estimate such correlations in properties, and the development of a suitable stochastic model was beyond the scope of this study.

Each material in the simulated vessel is permitted to assume random variations in fracture resistance. Thus, it is possible for a crack to encounter sudden increases or decreases in toughness as it grows into a different plate or weld. In this way, a crack that may arrest in one simulated (or hypothetical) vessel may, in another vessel, continue to grow and result in a catastrophic mode of failure.

A key feature of the simulation should be noted. The copper, nickel, fluence, and random variations in toughness parameters are simulated only once for all the materials that make up a vessel. The subsequent calculations of the through-wall average of fracture toughness are a simple deterministic evaluation. The toughnesses at different locations in a weld or plate do have systematic variations. These variations are a direct result of differences in the spatial variations in fluence and metal temperature. In particular, the attenuation in fluence as a function of distance from the inner surface is considered. In a similar manner, the through-wall gradient in temperature and its effect on local fracture toughness is included in the calculations.

It is assumed that the occurrence of a through-wall crack does not affect the temperature of the coolant adjacent to the vessel wall. However, the pressure may decrease due to leakage through the open crack. The procedure for estimating the pressure loss was described in Section 3.0.

The other steps in the simulation model as presented in Figure 4.1 are deterministic calculations, and have been described in Section 3.0 of this report. The number of simulations to be performed is specified as an input to the computer code. The computational requirements for the Monte-Carlo analysis have proven to be quite modest. In actual calculations, a total of 200 simulations has been sufficient to establish that 50% or more of the axial through-wall cracks will result in the fracture of a circumferential weld.

4.4 COMBINING OF FAILURE PROBABILITIES

The output data from the probabilistic computer code must be compiled and interpreted as the first step in calculating probabilities for the different failure modes of concern. The procedure used in these calculations is outlined here. The procedure is further illustrated by the plant-specific calculations described in subsequent sections.

The output of the computer code is a table of final crack sizes and crack opening areas. These results are first scanned to identify trends, so that a convenient and meaningful set of failure mode categories can be defined. Having defined these categories, the results of each simulation in the output table are manually assigned to their appropriate category. Totals for each category are then calculated, and fractions of the total for each category are then determined. These fractions are calculated for each transient and for each weld addressed in the evaluation, in order to establish the $Q_{mwt}(f)$ factors as defined below.

The calculations of the probabilities for the failure modes were performed using the following equations:

$$P_m = \sum_{t=1}^{T} H_t(f) \sum_{w=1}^{W} G_{tw}(f) \cdot Q_{mwt}(f), \quad m = 1,2 \ldots M \qquad (4.1)$$

where $P_m(f)$ = probability of failure mode m given that a through-wall crack occurs at the fluence level f

$G_{tw}(f)$ = contribution of weld w to the probability of a through-wall crack for the transient t at the fluence level f

$H_t(f)$ = contribution of transient t to the probability of a through-wall crack at the fluence level f

$Q_{mwt}(f)$ = contribution of weld w to failure mode m for transient t at the fluence level f

M = total number of failure modes

W = total number of welds

T = total number of transients.

The factors G and H are provided by the output of the fracture mechanics analysis that predicts the probabilities of through-wall cracks. For this study, the ORNL/IPTS calculations provided this needed information. The factor Q is obtained from the failure mode model as outlined above. It should be noted that, by definition, the following must be satisfied:

$$\sum_{m=1}^{M} P_m(f) = 1.0$$

$$\sum_{w=1}^{W} G_{tw}(f) = 1.0$$

$$\sum_{t=1}^{M} H_t(f) = 1.0$$

$$\sum_{m=1}^{M} Q_{mwt}(f) = 1.0 \ .$$

In neglecting the welds and transients that gave relatively small contributions to through-wall cracks, some of the above factors no longer gave the required summation of unity. Adjustments were made by scaling all factors upward, thereby including the contributions of the neglected welds and transients by augmenting the contributions of those that were considered.

The factors P_m give the probabilities for the failure modes in terms of relative or fractional contributions. To obtain the absolute values of the probabilities, the factors P_m must be multiplied by the probabilities for through-wall cracks as calculated in the ORNL/IPTS study.

5.0 MISSILE CONSIDERATIONS

This section summarizes evaluations of the characteristics and consequences of missiles that may be generated by the failure of a reactor pressure vessel under conditions of pressurized thermal shock. Two classes of missiles were considered. The first was that of vertical missiles that would result from the fracture of a circumferential weld. The second class encompassed horizontal missiles that would result from the fragmentation of a vessel. Details of the missile evaluations are given in Appendixes J and K. In these evaluations it was recognized that detailed predictions of missile effects (particularly for fragmentation phenomena) are beyond the state of the art of fracture mechanics modeling. Therefore, a range of missiles has been postulated, with the sizes and shapes of these missiles taken to be consistent with empirical data. Calculations were then performed to estimate the velocities of these missiles and to predict if such missiles could cause penetration and escape from the vessel cavity.

5.1 VERTICAL MISSILES

The evaluations of vertical missiles are documented in Appendix K of this report. In the calculations it was assumed that a circumferential weld suddenly fractured. The upper head of the vessel then became a large fragment or missile. Figure 5.1 shows how this missile was modeled for a bottom supported vessel such as at the Oconee-1 nuclear power plant. Additional calculations in Appendix L estimate the dynamic pressure loading on the reactor core structure following a severe vessel rupture.

Figure 5.2 shows typical results of the predicted vertical acceleration and the subsequent arrest of this upper head missile. In this worst-case calculation, a volume of steam was postulated within the upper portion of the vessel to give a condition of maximum fluid thrust. Nevertheless, the results displayed in Figure 5.2 show that the restraint forces from the attached primary coolant piping are capable of arresting the missile after less than 1 ft of vertical motion. The restraint forces were due, in part, to the bending stiffness of the piping. However, the main restraint occurred after about 6 in. of relatively free motion when the piping impacted the penetrations in the adjacent concrete structure.

All calculations were performed for the vessel and system parameters of the Oconee-1 reactor. For the Calvert Cliffs-1 and H. B. Robinson-2 reactors, the main difference, from the standpoint of vertical missiles, is the support of these vessels from the top at the locations of inlet nozzles for the primary coolant piping. The bottoms of these vessels were unsupported, which allowed the bottom of the vessel to become a missile that is accelerated in the opposite direction of the upper head assembly. Calculations were performed for the Oconee-1 vessel with a hypothetical top support arrangement, as an approximation for the missile evaluations in the Calvert Cliffs-1 and H. B. Robinson-2 studies.

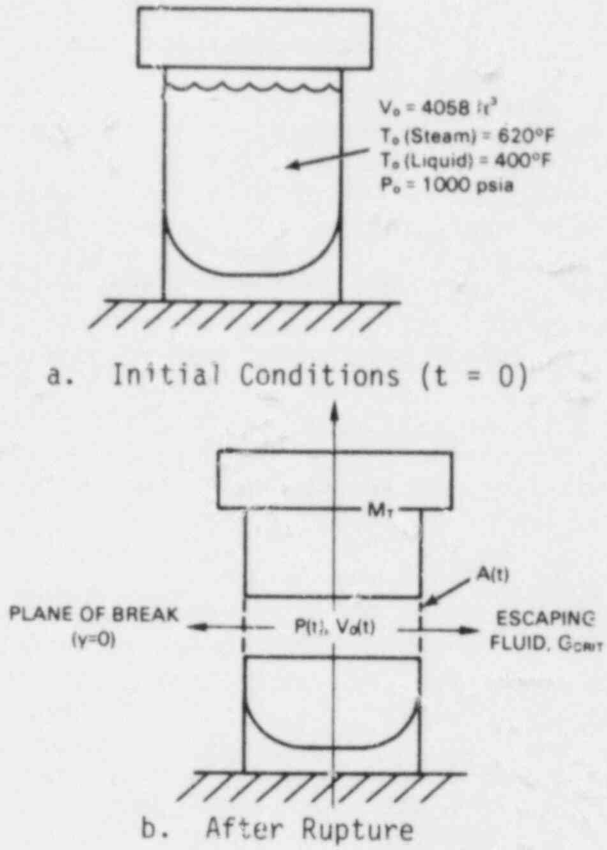

FIGURE 5.1. Model of Ruptured Vessel

Calculations were performed for both the bottom and top support conditions. Alternative assumptions were made regarding the core support and fuel assemblies. In one case these components were attached to the upper head assembly and became part of the vertical missile. In the other case, separation was assumed to occur. The final outcome of the calculations was found to be insensitive to modeling assumptions. In all cases the motion of the upper head missile was arrested after about a foot of vertical motion.

The predicted deformation of the large-diameter coolant piping was about 6 in. on diameter. Although there is some possibility of cracking the piping at the impact points, complete pipe severance is believed to be unlikely. Furthermore, such local cracking of the piping would be of little significance to core cooling in the light of the associated full circumferential rupture of the vessel.

The model of the vertical missiles also predicted a velocity for the impact with the stationary lower half of the vessel. This impact occurs due to the downward motion that will occur subsequent to the arrest of the upper head missile. For the top support conditions, the impact will involve coolant piping striking the penetrations in the concrete structure. All such impacts may

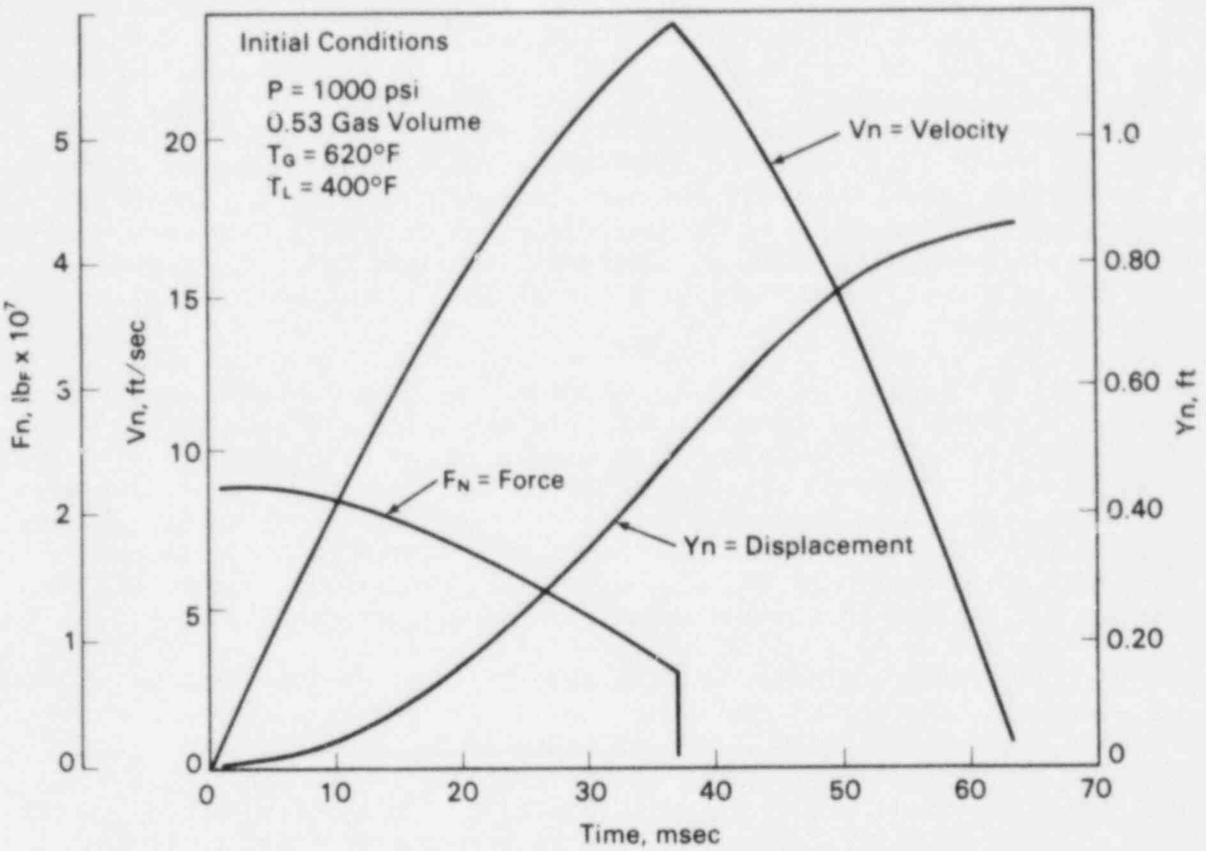

FIGURE 5.2. Force, Velocity, and Displacement Characteristics

have consequences related to fuel damage and the geometric configuration of the core. Consideration of these consequences was beyond the scope of the PNL study.

5.2 HORIZONTAL MISSILES

Appendix J describes evaluations for fragmentation types of missiles that may be accelerated horizontally during a vessel fracture event. The objective was to determine the possibility of such missiles being formed, the probable sizes of these missiles, the velocities of these missiles, and the ability of the missiles to penetrate the concrete surrounding the reactor vessel.

A set of documents was collected to obtain data from both service failures and burst tests of vessels. The approach was to generalize from the trends seen in these data, and to apply the trends to conditions of a reactor vessel subject to conditions of pressurized thermal shock. Once the sizes of missiles had been estimated, it was then possible to make predictions of their velocities and penetration characteristics.

The literature showed examples of vessel fractures that both did and did not result in the formation of fragments. In general, fragmentation occurs when the vessel is "brittle" and the pressurizing medium is "energetic" in nature. Gas pressure would be energetic, whereas liquid or hydraulic pressure would not be energetic. Fragmentation sometimes occurs when the elastic stored energy in the vessel wall is large compared to the dynamic toughness of the vessel materials. The evaluation was qualitative in nature, and indicated that the vessel embrittlement and fluid conditions of interest to pressurized thermal shock are somewhat short of observed conditions for fragmentation. However, for purposes of a conservative evaluation, a spectrum of possible missiles was assumed.

Photographs of fragmented vessels were studied. Aside from small inconsequential shards, the smallest and potentially highest velocity fragments appeared to have a characteristic dimension of about $\sqrt{Rt}$, where R is the vessel radius and t is the wall thickness. For a reactor vessel, this would be a fragment that is about 24 in. x 24 in. x 8.5 in. thick with a weight of about 1380 lb. This fragment may also be a worst case, because it is about as large a fragment that could rotate to an "edge-on" impact orientation within the confined space between the vessel and the surrounding concrete shield.

Figure 5.3 shows a mass-velocity relationship that was derived from an energy balance approach. The entire energy stored as compression of the subcooled water within the vessel (at 2000 psi) was assumed to be transferred into kinetic energy of single missiles of the indicated weights. In Figure 5.3, the velocities for small missiles (less than about 200 lb) are bounded by the free jet velocity of water through an opening in the vessel wall. It has also been observed that the predicted velocities for large missiles are consistent

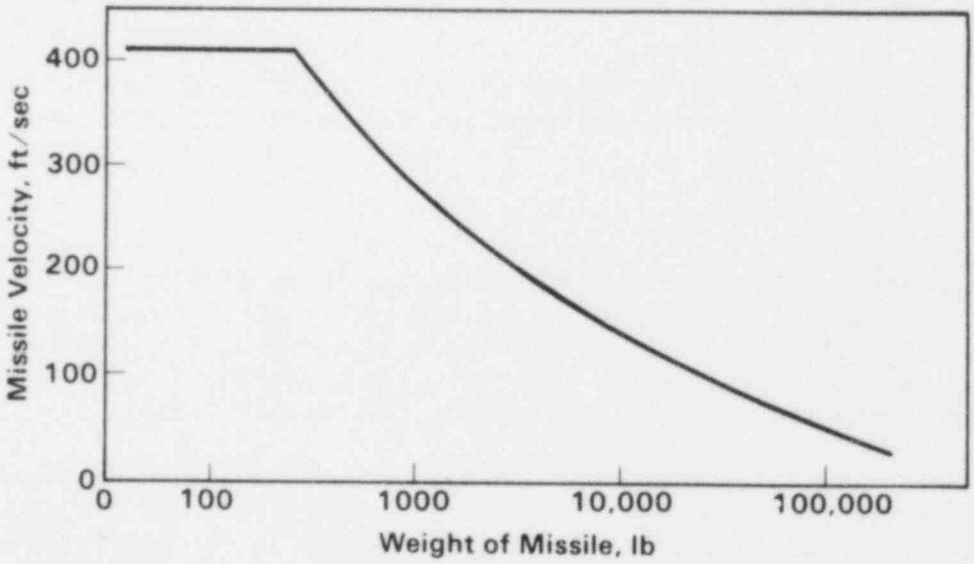

FIGURE 5.3. Velocity of Horizontal Fragments When Accelerated by 2000-psi Subcooled Water

with the detailed calculations of vertical velocities from the upper head missile study.

Figure 5.4 shows the calculated penetration depths for the worst-case horizontal missile of 1380 lb as a function of the impact velocity. The penetration depths were predicted using empirical equations that describe the results of tests performed for purposes of military ballistics. A worst-case "edge-on" orientation was assumed for these calculations of penetration depth. Other calculations have predicted that the penetration depth is relatively insensitive to the missile weight. In appears that the greater weight of the larger missiles is offset by the lower velocities attained by these missiles. The estimated impact velocity for the 1380-lb missile is about 200 ft/sec. For this velocity, the 1380-lb fragment has a predicted penetration of less than 1 ft of concrete, whereas the actual concrete thickness is on the order of 4 to 5 ft.

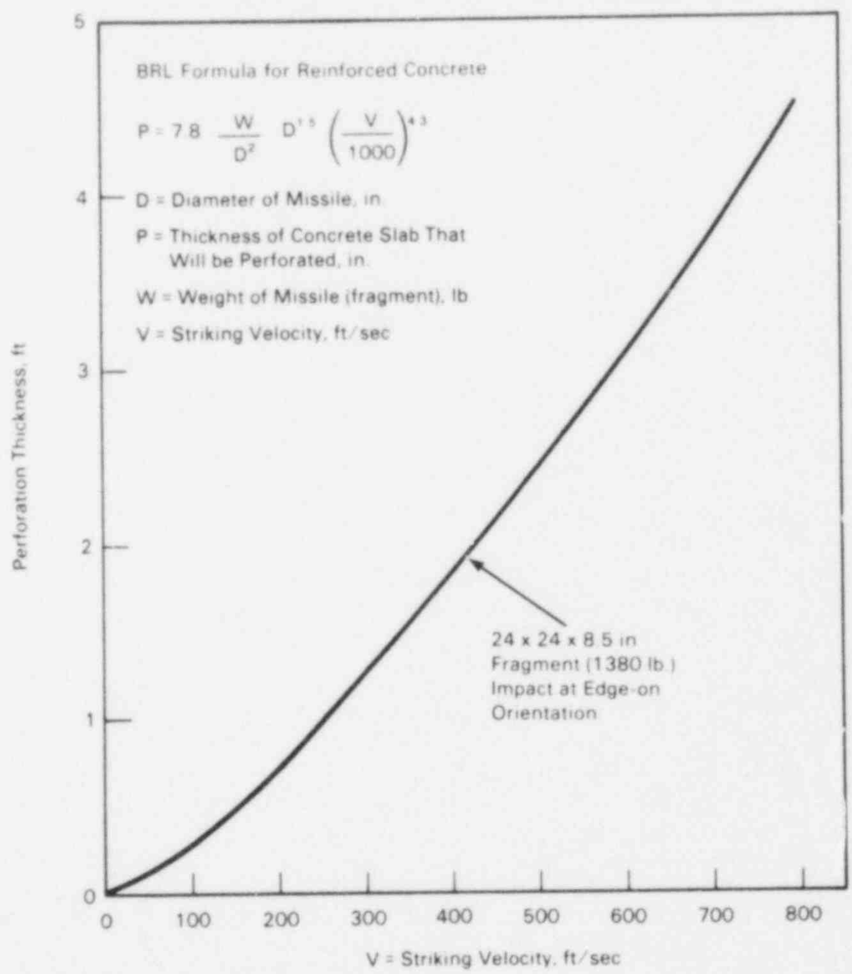

FIGURE 5.4. Penetration Potential of Representative Vessel Fragment in Horizontal Direction

In has been concluded that horizontal missiles as created by fragmentation during fracture of a vessel do not constitute a threat to reactor containment or containment cooling equipment. It is not certain if any such fragments will even be created. Furthermore, the potential velocities would be far short of the velocities needed to penetrate the thick concrete shields that are adjacent to the vessel.

6.0 OCONEE-1 EVALUATION

This section describes an application of the fracture mechanics model to predict vessel failure modes for the Oconee-1 nuclear power plant. The calculations were based on simulated pressure and temperature transients from the ORNL/IPTS research program as reported in Burns et al. (1984). As in the ORNL study, Oconee-1 was the first plant evaluated by PNL. The methods as described here for the Oconee-1 vessel were used with only minor changes in the subsequent evaluations for the Calvert Cliffs-1 and H. B. Robinson-2 vessels.

6.1 VESSEL CHARACTERISTICS

The first step in the evaluation was to assemble information on the fabrication details and materials used in the construction of the Oconee-1 reactor vessel. This information was obtained from the ORNL/IPTS study whenever possible, to maintain consistency between the two fracture mechanics models. However, a number of additional material parameters, such as upper shelf toughness and properties of noncritical beltline materials, entered into the PNL evaluation of vessel failure modes.

The first source of additional information was the ORNL research staff. The search was then directed to Parker (1982). Other information was obtained from a reactor vessel database assembled by the Electric Power Research Institute (McConnell et al. 1982).

Figure 6.1 is a cross-sectional view of the Oconee-1 vessel. The drawing indicates the various plates and welds that make up the assembled vessel. Not indicated is the ring structure that supports the vessel at its bottom. The location of the active fuel of the reactor core can also be seen in Figure 6.1. Those plates and welds adjacent to the core will experience the greatest damage due to neutron irradiation.

Figure 6.2 shows an unwrapped view of the irradiated beltline region of the vessel. Dimensions of the plates and welds are shown. Also indicated are the labels or designations used to identify the different plates and welds. Figure 6.2a provides the designations used by Duke Power and ORNL, while Figure 6.2b provides a cross reference of designations that correspond to the standardized scheme used in the PNL vessel failure mode analyses.

Table 6.1 lists the material characterization data provided by the ORNL/IPTS study. The complete set of material data used in the failure mode evaluation is given by Table 6.2. Also listed are the standard deviations for the material characteristics that were estimated for inputs to the probabilistic evaluations of the vessel failure modes. These standard deviations were assigned values that were consistent with the values used in ORNL calculations for the probabilities of through-wall cracks.

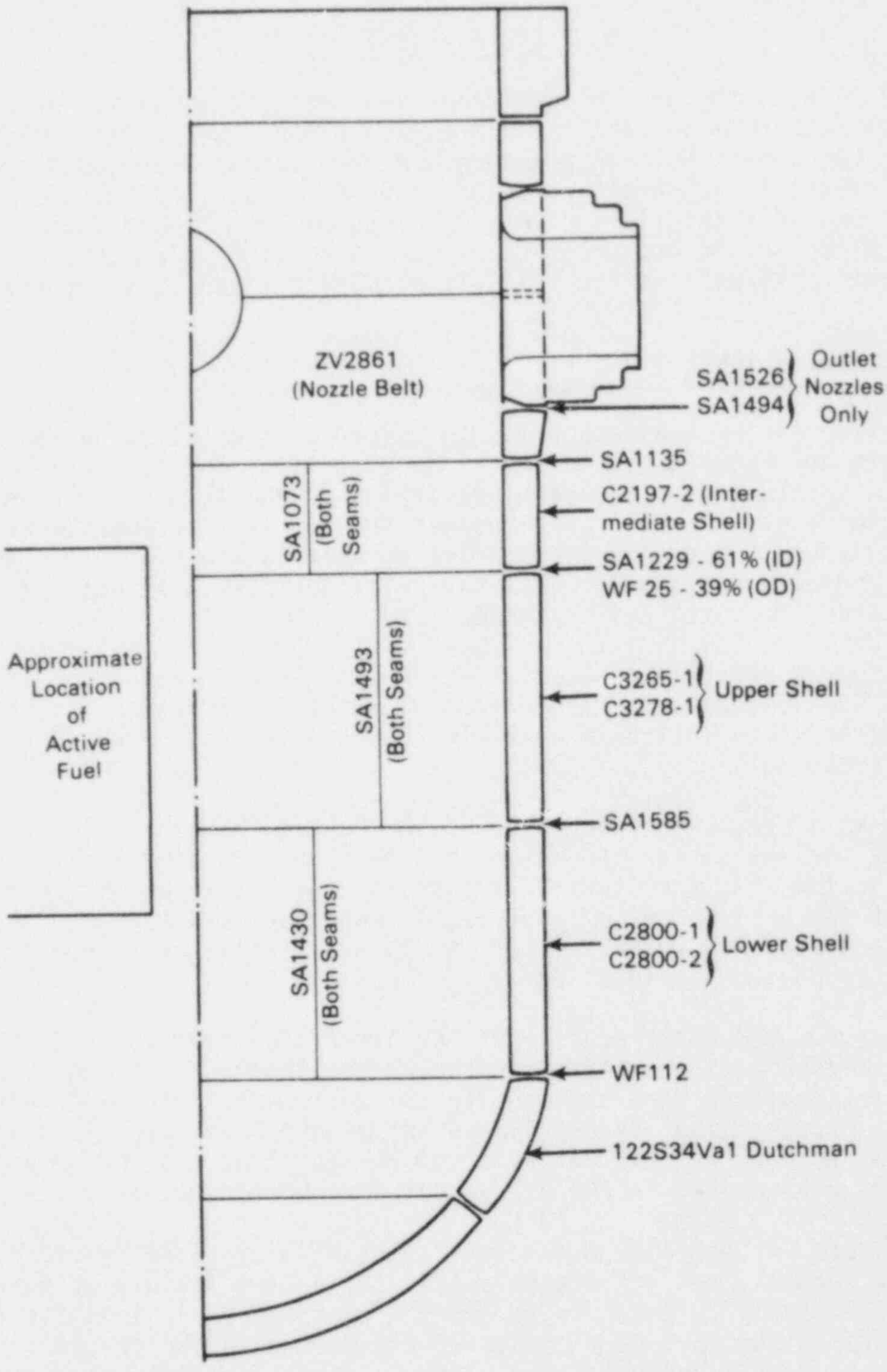

FIGURE 6.1. Location and Identification of Materials Used in Fabrication of Oconee Unit 1 Reactor Pressure Vessel

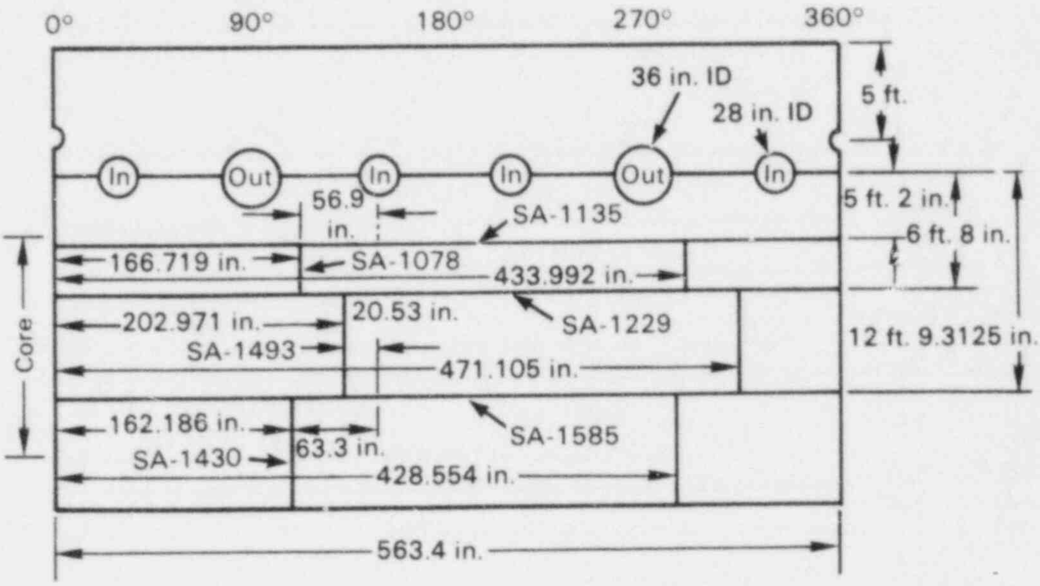

a. Dimensions

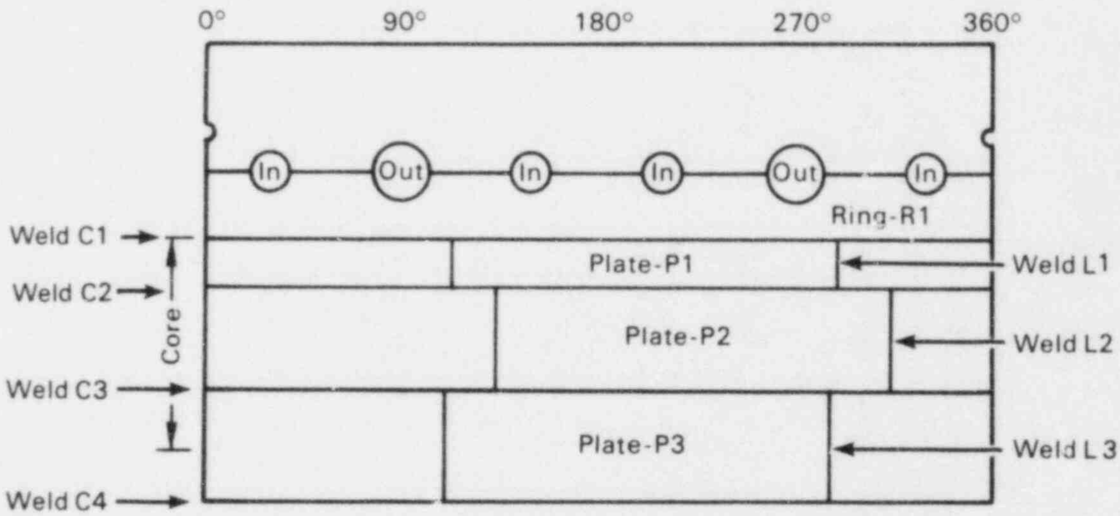

b. Weld and Plate Designations

FIGURE 6.2. Inner Surface of Oconee-1 Reactor Vessel Showing Weld Locations

TABLE 6.1. Material Properties Used by ORNL in Oconee-1 Vessel LEFM Analysis

Material Identification			Chemistry		Neutron Fluence, Inside Surface, n/cm^2, at 32 EFPY[a]	Initial RT_{NDT}, °C
Designation	Weld or Heat Number	Description	Cu, wt%	Ni, wt%		
R1	AHR-54	SA508,CL2 (upper ring)	0.16	NA	1.97E18	+16
C1	SA1135	Circumferential weld (upper shell course to upper ring)	0.25	0.54	1.97E18	- 7
P1	C2197	SA302B (plates of upper shell course)	0.15	NA	9.35E18	+ 4
L1	SA1073	Longitudinal weld (upper shell course)	0.31	0.64	7.38E18	- 7
C2	SA1229	Circumferential weld (middle to upper shell course)	0.26	0.61	9.35E18	- 7
L2	SA1493	Longitudinal weld (middle shell course)	0.29	0.55	8.9E18	- 7
P2	C3278-1	SA302B (plates of middle shell course)	0.12	NA	1.23E19	+ 4
C3	SA1585	Circumferential weld, (middle to lower shell course)	0.21	0.59	1.23E19	+ 4
P3	C2800-1	SA302B (plates of lower shell course)	0.11	NA	1.23E19	+ 4
L3	SA1430	Longitudinal weld (lower shell course)	0.29	0.55	1.09E19	-7

(a) EFPY = Effective Full Power Years

TABLE 6.2. Material Properties Used by PNL in Oconee-1 Vessel Failure Mode Analysis

Material Number	Material Designation	Copper, wt% Mean	Copper, wt% σ	Nickel, wt% Mean	Nickel, wt% σ	Initial RT_{NDT}, °F Mean	Initial RT_{NDT}, °F σ	σ of K_{IC}, Fraction of Mean	Silicon, wt%
1	L1	0.31	0.03	0.64	0.00	20.0	16.0	0.15	0.600
2	L2	0.29	0.03	0.55	0.00	20.0	16.0	0.15	0.600
3	L3	0.29	0.03	0.55	0.00	20.0	16.0	0.15	0.600
4	C1	0.25	0.03	0.54	0.00	20.0	16.0	0.15	0.600
5	C2	0.26	0.03	0.61	0.00	20.0	16.0	0.15	0.600
6	C3	0.21	0.03	0.59	0.00	20.0	16.0	0.15	0.600
7	C4	0.31	0.03	0.59	0.00	20.0	16.0	0.15	0.600
8	R1	0.16	0.03	0.60	0.00	60.0	10.0	0.15	0.600
9	P1	0.15	0.03	0.60	0.00	40.0	10.0	0.15	0.600
10	P2	0.12	0.03	0.60	0.00	40.0	10.0	0.15	0.600
11	P3	0.11	0.03	0.60	0.00	40.0	10.0	0.15	0.600

Material Number	Material Designation	σ of K_{IA}, Fraction of Mean	σ of ΔRT_{NDT} °F	Unirradiated Flow Stress, ksi	Unirradiated Charpy Energy, ft-lb	σ of Fluence, Fraction of Mean
1	L1	0.15	24.0	76.0	70.0	0.30
2	L2	0.15	24.0	76.0	70.0	0.30
3	L3	0.15	24.0	76.0	70.0	0.30
4	C1	0.15	24.0	76.0	70.0	0.30
5	C2	0.15	24.0	76.0	70.0	0.30
6	C3	0.15	24.0	76.0	70.0	0.30
7	C4	0.15	24.0	76.0	70.0	0.30
8	R1	0.15	12.0	76.0	120.0	0.30
9	P1	0.15	12.0	76.0	120.0	0.30
10	P2	0.15	12.0	76.0	120.0	0.30
11	P3	0.15	12.0	76.0	120.0	0.30

Data on unirradiated tensile strengths and upper shelf Charpy impact energies were particularly difficult to establish. These properties were important to the predictions of fracture behavior on the upper shelf. The data in McConnell et al. (1982) suggested values of Charpy energy of 70 ft-lb for the welds and 120 ft-lb for the plate materials. Although more precise and specific data for the welds and plates of the Oconee-1 vessel may be available, the search for such data was beyond the scope of these demonstration calculations.

6.2 CRITICAL TRANSIENTS

In the ORNL/IPTS project (Burns et al. 1984) there were extensive evaluations of potential transients that could produce conditions of pressurized thermal shock to the Oconee-1 reactor pressure vessel. Table 6.3 lists the three transients that gave the greatest contribution to the probability of a through-wall crack. Burns et al. (1984) provide information on the sequences of events that correspond to the listed transients. Each of the three transients had relatively high probabilities both of occurring and of producing a through-wall crack, given that the transient did occur.

The fractional contributions of the transients to the probability of through-wall cracks are listed in Table 6.3. Transient 44 [designated as TBV(6A) or LANL10] was clearly the dominant contributor in the ORNL analysis. The values of the fractional contributions as listed in Table 6.3 have been increased to ensure that the total of the contributions is equal to 1.0. As such, the contributions of less important transients were included indirectly as increases in the contributions from the three that were selected for detailed evaluation.

TABLE 6.3. Critical Transients Used in Oconee-1 Vessel Failure Mode Analysis

Transient		Fractional Contribution to Probability of Through-Wall Crack	
Number	Designation	$f = 0.545 \times 10^{19}$	$f = 1.417 \times 10^{19}$
44	TBV(6A) or LANL10	0.77	0.53
26	MSLB1	0.14	0.29
4	TBVG4	0.09	0.18

Figures 6.3 and 6.4 are plots from Burns et al. (1984) of pressure and temperature versus time for transients 44 and 26. These two transients differ in certain important characteristics. Transient 44 is more severe in the sense that the pressure rapidly recovers to a high level and remains high while the downcomer temperature simultaneously continues to decrease throughout the transient. In contrast, the temperature for transient 26 achieves a minimum early in the transient but then increases continuously during the later part of the transient. Of perhaps greater significance is the fact that the pressure is relatively low at the critical time in the transient when the minimum temperature occurs. As will be seen, this association of low pressure with the minimum temperature enhances the probability that through-wall cracks will arrest and not result in catastrophic failure of the vessel.

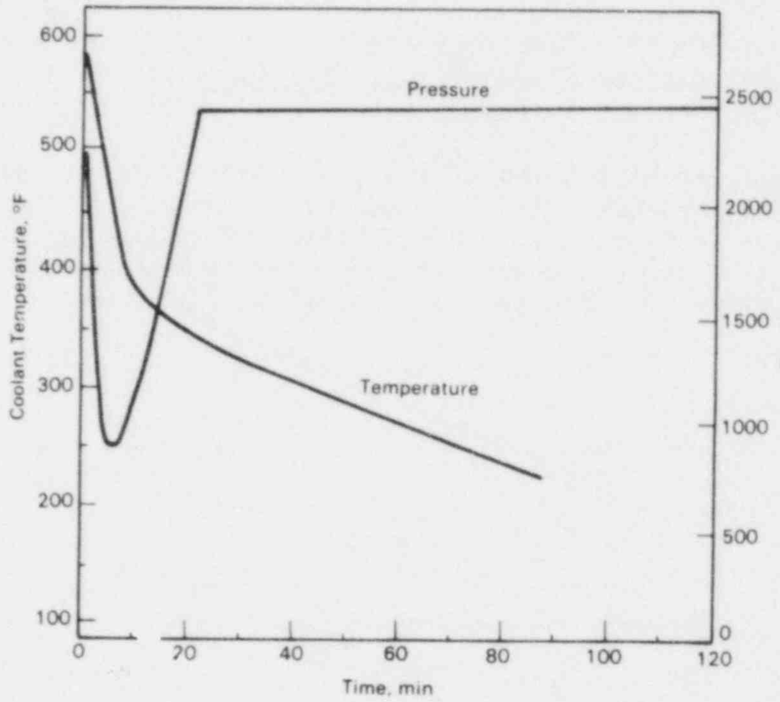

FIGURE 6.3. Pressure and Temperature for Oconee-1 Transient 44/TBV(6A)

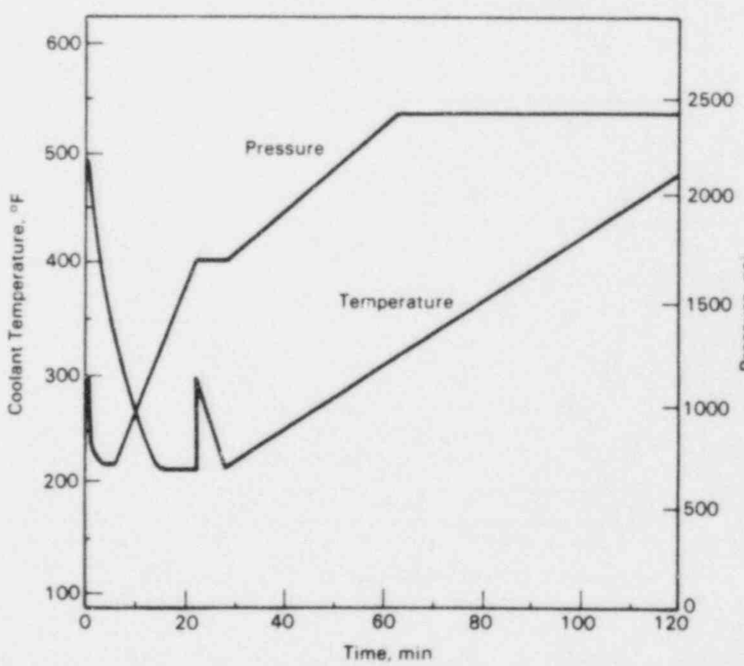

FIGURE 6.4. Pressure and Temperature for Oconee-1 Transient 26/MSLB1

Other data from the ORNL/IPTS analyses are shown in Figures 6.5 through 6.7. The failure probabilities of Figure 6.5 clearly increase as the RT_{NDT} values of the vessel welds increase in response to higher levels of fluence.

Figures 6.6 and 6.7 are histograms of the times during the transients at which through-wall cracks were predicted to occur by the ORNL/IPTS analyses. These histograms were used as inputs in the evaluation of vessel failure modes. A separate distribution (or histogram) was used for each transient and for each level of fluence. However, the same histogram was used for all the welds of

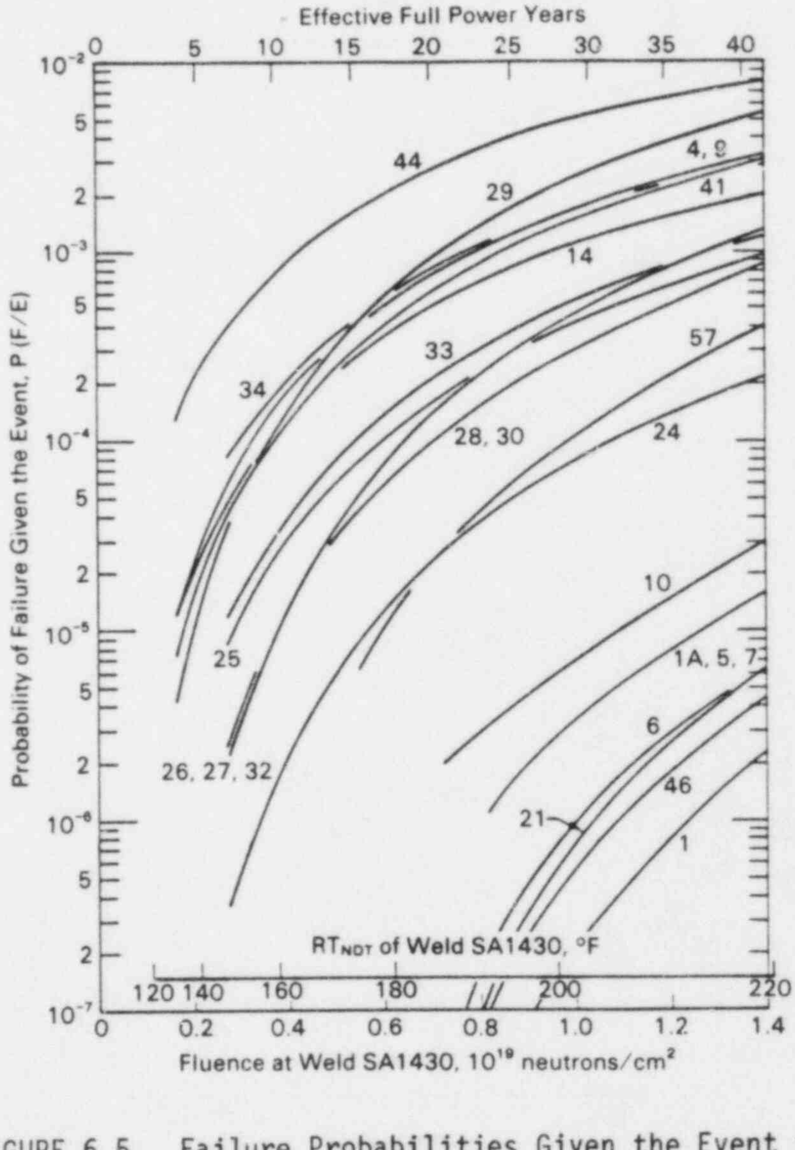

FIGURE 6.5. Failure Probabilities Given the Event for Oconee-1 Postulated Over Cooling Accidents

Source: Burns et al. (1984, p. 5.34)

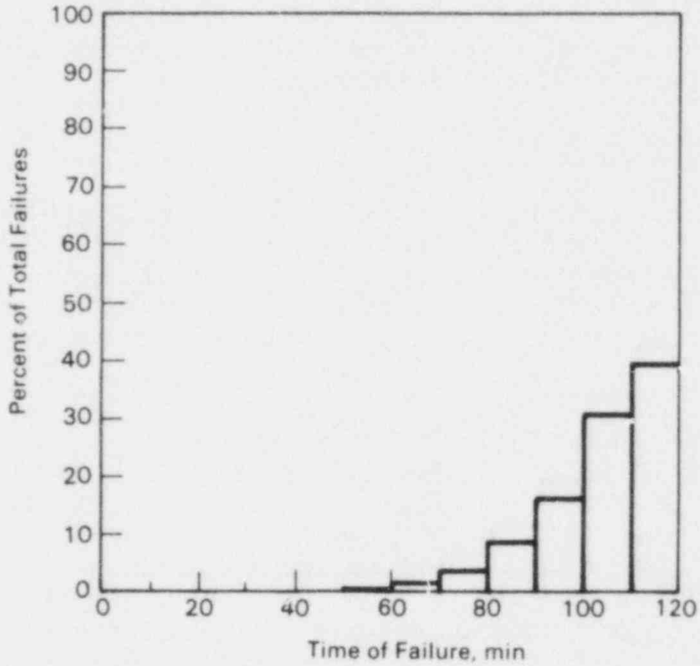

FIGURE 6.6. Percentage of Failures Versus Time of Failure for Transient 44/TBV(6A) at 32 Effective Full Power Years

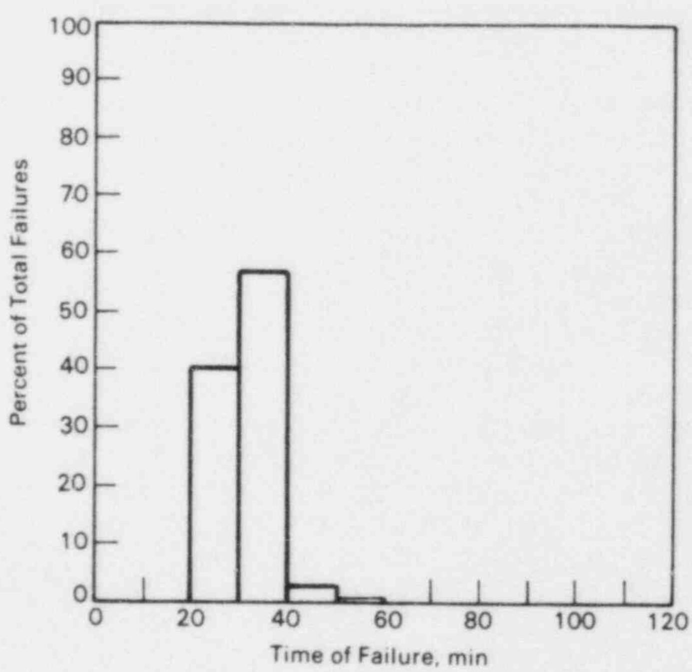

FIGURE 6.7. Percentage of Failures Versus Time of Failure for Transient 26/MSLB1 at 32 Effective Full Power Years

the vessel beltline region, because the ORNL computer output did not provide separate data for each weld in the vessel.

6.3 FRACTURE MECHANICS MODEL

Details of the fracture mechanics model used to predict the failure modes for the Oconee vessel have been described in previous sections of this report. Further details are provided in appendixes to this report. A computer program was used for the calculations. Inputs to this program described the configuration of the vessel, the material properties, and the transient loading conditions.

The computer program was modified to describe certain hydraulic characteristics of the Oconee-1 reactor system. In particular, the characteristics of the high and low head injection pumps were simulated. In addition, the rate of depressurization of the primary coolant system was related to the volume of coolant lost from the system by leakage through an open crack in the wall of the reactor vessel. The method used to estimate system leak rates is discussed in Appendix I. It was conservatively assumed that all of the injection pumps operate at full capacity during all of the transients. This resulted in a maximum capability to maintain system pressure in the presence of a leaking crack in the vessel.

In the Oconee-1 reactor model, three high-pressure pumps were capable of delivering a total of 1500 gpm at a pressure of 1500 psi. In the simplified model, the capacity (gpm) was taken to be independent of the system pressure. The low-pressure injection pumps at Oconee-1 supply pressure at a nominal pressure of 200 psi. This pressure is sufficiently low that through-wall cracks will not propagate at the stress levels produced by this pressure. Therefore, the effects of low-pressure injection were neglected in the fracture mechanics analyses.

For the short durations of time associated with the sudden opening of a crack in a pressure vessel, the injection pumps cannot replace the coolant lost as flow through the opening crack. In this case, the fracture mechanics model estimated the decrease in system pressure by calculating the volume of coolant lost as flow through the opening crack. The volume of water in the Oconee vessel was taken as 8,000 ft^3. Estimates of the volume of water in the remainder of the primary coolant loop resulted in a total coolant volume of 12,000 ft^3. The drop in system pressure due to a unit loss of coolant volume was estimated on the basis of the compressibility of water and the elastic compliance of coolant boundary (the reactor vessel, coolant piping, and steam generator tubing). Specifically, the calculations were based on a pressure decrease of 21 psi for the loss of each cubic foot of coolant water from the system.

An assumption in the calculations was that the appearance of a through-wall crack does not affect the coolant temperatures adjacent to the inner wall of the vessel. However, as discussed above, the pressure can decrease over an extended period of time as coolant flows out through the open crack. In the fracture mechanics model, the pressure was allowed to drop to a level consistent with a balance between the leak rate and the capacity of the injection pumps. However, the pressure was not permitted to decrease below the saturation pressure corresponding to the prescribed temperature of the coolant in the downcomer.

It should be noted that predictions of the failure mode evaluation for Oconee-1 were found to be significantly affected by the inclusion of depressurization in the model. For Oconee-1 it was predicted that the flow through the open cracks was sufficient to reduce pressures to insignificant levels within a few minutes after the cracking had occurred. On the other hand, during the millisecond time frame of the crack opening event, the flow through the opening cracks was insufficient to depressurize the system to a significant extent.

6.4 MISSILE CONCERNS

Missile concerns are addressed in Appendixes J and K on a generic basis using the Oconee-1 vessel as typical for a pressurized water reactor. The analyses predict that all missiles will be contained within the vessel cavity. Vertical (upper head) missiles will be arrested by the restraint provided by the attached primary coolant piping. Horizontal missiles formed by fragmentation are predicted to be arrested readily by impact with the concrete adjacent to the reactor vessel (estimated to be about 5 ft thick).

6.5 OCONEE-1 SIMULATION RESULTS

Table 6.4 gives results of probabilistic simulations that predicted the failure modes for the Oconee-1 vessel. Data are given for the three critical transients, but only for the fluence level of 1.417×10^{19} n/cm^2. Additional fluence levels were addressed in the calculations, but the trends of the failure mode predictions were found to be relatively insensitive to the level of fluence.

The continuous spectrum of failure modes has been sorted in Table 6.4 into six categories. The ORNL/IPTS study predicted that only axial welds have a significant probability of cracking; therefore, all cracks in the PNL analysis began in this mode. Although the ORNL/IPTS study predicted relatively low probabilities for through-wall cracks in the circumferential welds, the PNL failure mode evaluations predict that many of the axial cracks will change direction and will then continue to propagate by following an embrittled circumferential weld.

The results are presented in Table 6.4 as two main categories: 1) those fractures that extend only in the axial direction, and 2) those axial fractures that turn to extend along a circumferential weld and then lead to a complete circumferential fracture of the vessel. It should be emphasized that the

TABLE 6.4. Results of Failure Mode Analyses for Individual Welds and Transients (for Fluence of 1.417×10^{19} n/cm^2 at Weld SA1430)

Axial Weld	Contribution of Weld to ϕ(TWC), Fraction of Total	Vessel Failure Mode, Fraction of Total: Circumferential Failures, Weld Location[(a)] C1	C2	C3	Axial Failures Opening Area, in.^{2} 0 to 10	10 to 100	100 to 1000
Transient 44/TBV(6A)/LANL10							
L1	0.13	0.050	0.080	0.055	0.815	0.0	0.0
L2	0.38	0.0	0.625	0.375	0.0	0.0	0.0
L3	0.49	0.0	0.130	0.355	0.175	0.0	0.340
Transient 26/MSLB1							
L1	0.15	0.0	0.0	0.0	1.000	0.0	0.0
L2	0.31	0.055	0.170	0.120	0.645	0.0	0.10
L3	0.54	0.0	0.0	0.005	0.995	0.0	0.0
Transient 4/TBVG4							
L1	0.13	0.010	0.010	0.025	0.945	0.0	0.0
L2	0.35	0.005	0.625	0.370	0.0	0.0	0.0
L3	0.52	0.0	0.120	0.205	0.270	0.0	0.405

(a) Weld locations are as follows:

- C1 is at 64 in.
- C2 is at 46 in.
- C3 is at 26 in.

fracture mechanics methodology can predict only that circumferential crack growth will begin to occur. Details of the subsequent growth along the circumferential weld were not addressed because such predictions were beyond the capabilities of available fracture mechanics methods. Nevertheless, there is much evidence that axial cracks do turn and follow circumferential welds and that complete circumferential fractures of vessels can result. This study assumed simply that a complete circumferential fracture always occurs whenever an axial crack turns and follows a circumferential weld.

Table 6.4 lists results for each of three axial welds (L1, L2 and L3). Also listed are the relative contributions of each of these welds to the probability of through-wall cracks. These contributions were part of the output from the ORNL/IPTS calculations. The relative contributions from each of the welds are seen to be about the same for each of the three transients shown in Table

6.4. The data in Table 6.4 show that the ORNL/IPTS calculations predict that the lower axial weld (L3) has the greatest probability of having a through-wall crack. A combination of chemistry and fluence factors gives this weld a higher failure probability than the other axial welds.

The circumferential failures listed in Table 6.4 are identified also by weld numbers. A failure of weld C3 is of particular concern because it is at a lower elevation in the vessel. The failure of a lower weld is significant because core cooling will be affected most by a leak near the bottom of the active core. It is predicted that about half of the circumferential failures will occur in weld C3.

The purely axial weld failures are described by their opening areas (as calculated for an internal pressure of zero). These areas are separated in Table 6.4 into categories covering a decade each. It is significant that the calculated areas are either very small (0 to 10 $in.^2$) or relatively large (100 to 1000 $in.^2$). This is an indication of the behavior of those cracks that do not arrest at the ends of the initially cracked axial weld. Once such cracks grow into adjacent plate material, the growth readily extends over the entire length of the vessel.

Figure 6.8 summarizes the results of the failure mode evaluations for the Oconee-1 vessel. These results include the contributions from all the welds in the vessel for all three critical transients. Each of the individual failure mode calculations was summed after being weighted by the fractional contribution of the transient (from Table 6.3) and the fractional contribution of the weld (from Table 6.4). Figure 6.8 shows that the probabilities for all the failure modes increase with increasing fluence. However, the probabilities of each failure mode relative to the total failure probability is relatively insensitive to the level of fluence.

The results of the failure mode calculations for the Oconee-1 vessel can be summarized as follows:

1. About 50% of the through-wall axial cracks extend and turn to follow a circumferential weld.

2. For most of the other cases, the axial cracks arrest at a final length corresponding to the length of the axial weld. These cracks do not extend axially into the adjacent plate material, nor do they turn to follow the circumferential welds at the ends of the arrested cracks.

3. Cracks tend to arrest for short axial welds (weld L1) and low-pressure transients (transient 26).

4. Missiles that may result from fracture of the Oconee-1 vessel will be confined to the vessel cavity.

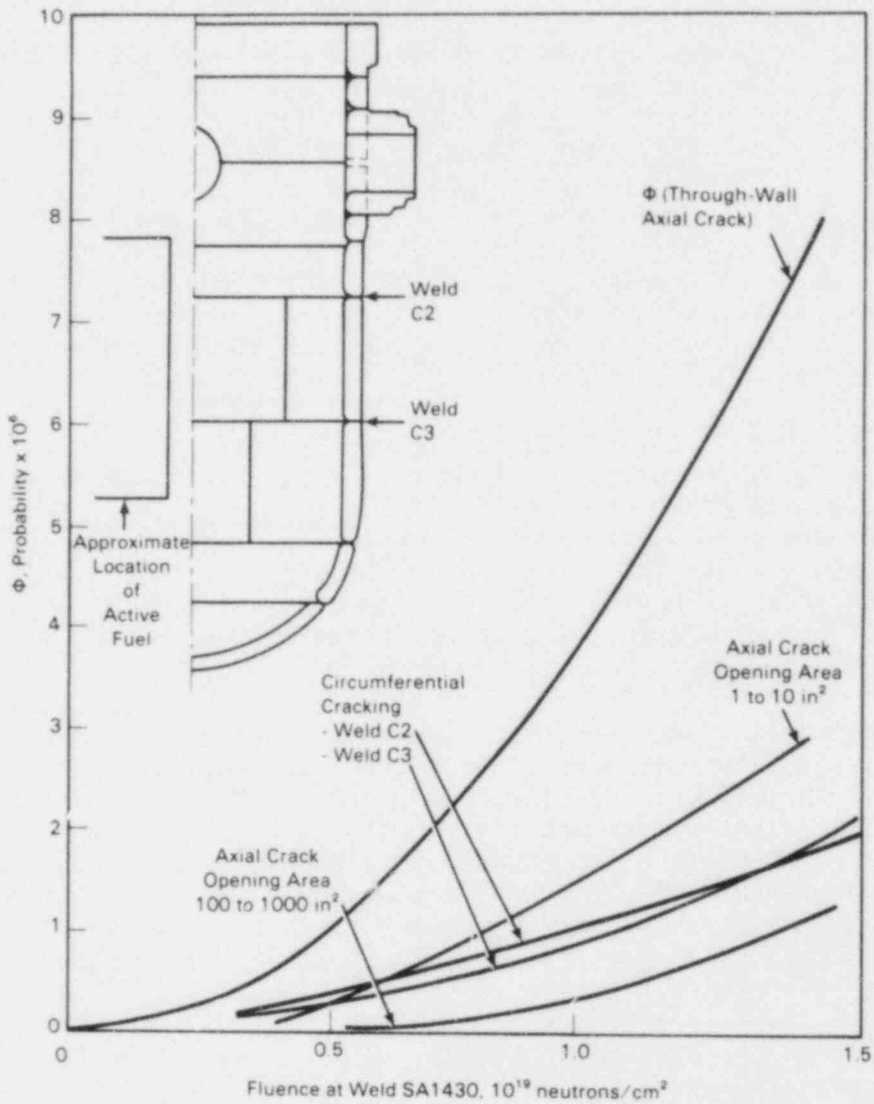

FIGURE 6.8. Oconee-1 Failure Mode Prediction

6.6 SENSITIVITY STUDIES

A set of sensitivity calculations was performed for the Oconee-1 vessel to evaluate the importance of specific uncertainties in both the model and the input parameters to the model. These calculations were performed for transient 44 and a fluence of 1.417×10^{19} n/cm^2 (32 effective full power years). The variables considered were

- duration of the transient
- maximum pressure during the transient
- upper shelf fracture toughness.

Results of the sensitivity calculations are given in Table 6.5.

TABLE 6.5. Sensitivity Study Results for Oconee-1 Vessel

Max. Pressure, psi	Transient Duration, min.	Toughness Enhanced by β-Factor	Percent Circumferential Failures
Effect of Transient Duration			
2460	120	No	97%
2460	60	No	90%
Effect of Maximum Pressure			
2460	120	No	97%
1200	120	No	3%
Effect of Including Irwin β-Factor			
2460	120	No	97%
2460	120	Yes	90%

The first item in Table 6.5 is the duration of the transient. This was identified in the ORNL/IPTS study as an important uncertainty that is a consequence of assumptions about operator action (or inaction). The ORNL study assumed that all transients had a duration of 2 hr. The IPTS sensitivity calculations clearly showed that the probability of a through-wall crack was quite sensitive to the duration of the transient. However, the results displayed in Table 6.5 show that the predictions of failure modes are relatively insensitive to the transient duration. The fraction of circumferential failures is only slightly reduced (from 97% to 90%) when the transient duration was reduced from 2 hr to 1 hr.

The second item of Table 6.5 is that of the maximum pressure. Transient 26 assumed that the pressure rapidly reaches the relief valve setting of 2460 psi. The sensitivity study considered the effect of limiting this pressure to 1200 psi. Such a pressure would be consistent with an operator action to maintain the pressure at a level sufficient to only maintain subcooling. The prediction of Table 6.5 for the lower pressure shows that the undesired failure mode of circumferential fracture will be greatly reduced in frequency. A larger fraction of the through-wall axial cracks will arrest at the ends of the axial welds. This benefit is in addition to the expected reduction in the probability of the through-wall axial crack.

The final item of Table 6.5 is that of the assumption regarding the fracture resistance of the vessel material for temperatures that define the upper shelf fracture domain. This concern was addressed by performing calculations that include the Irwin beta-factor as described in Appendix E. The fracture resistance of very tough materials (as used in many reactor pressure vessels) is the subject of continuing research. In the context of these failure mode evaluations, the plate materials of those parts of the vessel with little radiation embrittlement may exhibit a very high resistance to fracture.

The beta-factor is a means of estimating the increased fracture resistance of components with insufficient thickness to exhibit plane strain conditions within the strain field at the tip of crack. At the suggestion of Dr. Irwin of the University of Maryland, the beta-factor was applied in exploratory calculations for vessels. For the very high toughness levels of of some vessel steels, the beta-factor predicted an enhanced fracture resistance, even for a thickness of 8 in. Table 6.5 shows the effect of applying the beta-factor in the failure mode evaluations. The number of circumferential failures is reduced only slightly. Apparently, the circumferential welds in the Oconee-1 vessel are sufficiently embrittled that they exhibit plane strain toughness behavior, both with and without the beta-factor correction.

7.0 CALVERT CLIFFS-1 EVALUATION

This section describes predictions of vessel failure modes for the Calvert Cliffs-1 nuclear power plant. These calculations were based on simulated pressure and temperature transients from the ORNL/IPTS study (Selby et al. 1984). The Calvert Cliffs evaluation was the second in the series of plant-specific studies. Because the methodology was essentially the same as that for the Oconee-1 study, the discussion will focus on specific results of the Calvert Cliffs-1 predictions and will highlight only those aspects of the fracture mechanics model that apply specifically to the Calvert Cliffs vessel.

7.1 VESSEL CHARACTERISTICS

Information on the construction and materials for the Calvert Cliffs-1 vessel was assembled from various sources. The primary source was the ORNL/IPTS study (Selby et al. 1984), which was used extensively to ensure that the PNL failure mode analysis would be consistent with the previous fracture mechanics evaluations at ORNL.

Additional information on weld and plate characteristics was obtained from Lundvall (1982). However, the available sources of data for the Calvert Cliffs-1 vessel were incomplete and did not provide needed data on yield strength, ultimate strength, and upper shelf Charpy impact energy. These data were essential inputs to the elastic-plastic fracture mechanics calculations. Therefore, generic data were used in order to complete the calculations in a timely manner. For this purpose, data from Mager, Anderson, and Yanichko (1983) for the Maine Yankee vessel were selected because the characteristics of this vessel were well documented. The Maine Yankee vessel was fabricated by Combustion Engineering during the same time frame as was the Calvert Cliffs-1 vessel, and the data from the Maine Yankee vessel were believed to be generally relevant to the Calvert Cliffs-1 vessel. In any case, possible differences between the two vessels should not detract from the illustrative purposes of the failure mode calculations.

Figure 7.1 shows a view of the Calvert Cliffs-1 vessel with the various plates and welds of the vessel indicated. The location of the active core is shown in Figure 7.1 to indicate the region of irradiation damage. Figure 7.2 shows an "unwrapped" view of the vessel. Dimensions are shown along with labels to identify each plate and weld in the beltline region of the vessel.

Table 7.1 lists the material characterization data available from the ORNL/IPTS study. These data were combined with information from other sources. Table 7.2 lists the complete set of material characterization data used in the PNL failure mode predictions. Data on unirradiated upper shelf Charpy impact energies were of particular importance to the calculations. The Maine Yankee data suggested values of 105 ft-lb for the welds and 160 ft-lb for the plate materials of a typical Combustion Engineering vessel.

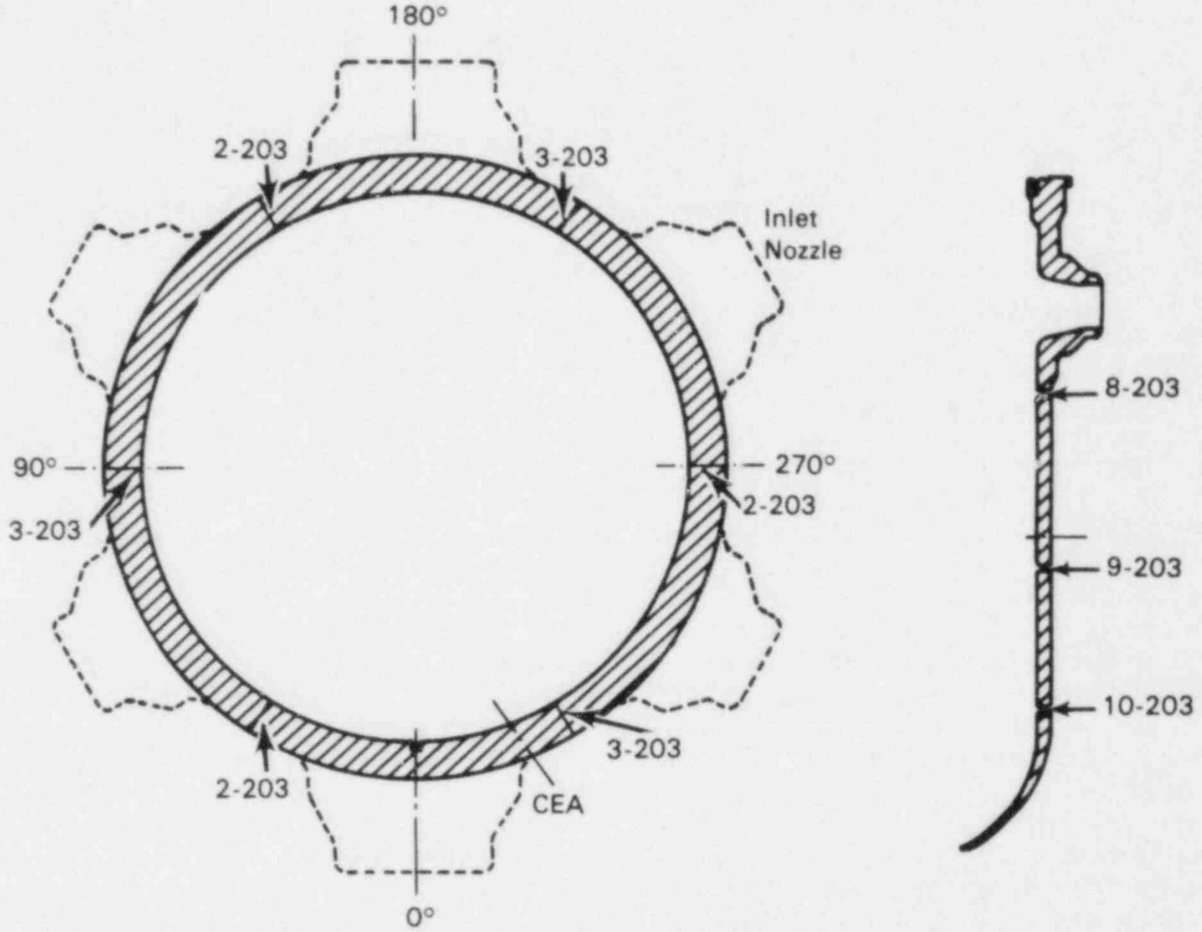

FIGURE 7.1. Location and Identification of Materials Used in Fabrication of Calvert Cliffs-1 Reactor Pressure Vessel

7.2 CRITICAL TRANSIENTS

Table 7.3 lists the three most critical transients from Selby et al. (1984) that gave the greatest contribution to the predicted probability of through-wall cracks for the Calvert Cliffs-1 vessel. Fractional contributions of each of these transients to through-wall cracks are indicated. These fractions were increased slightly from those given in Selby et al. (1984) to account for the contributions of the less critical transients that were not included in the failure mode evaluation. Thus, the fractional contributions for the three most critical transients have been adjusted in Table 7.3 so that their total contributions add up to unity.

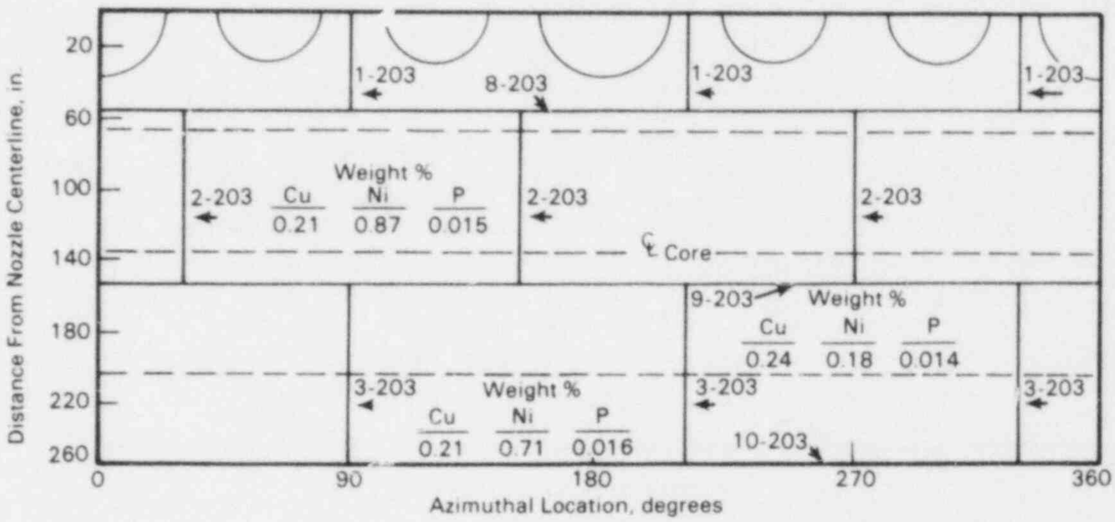

a. CE/ORNL Weld Designations and Chemistries

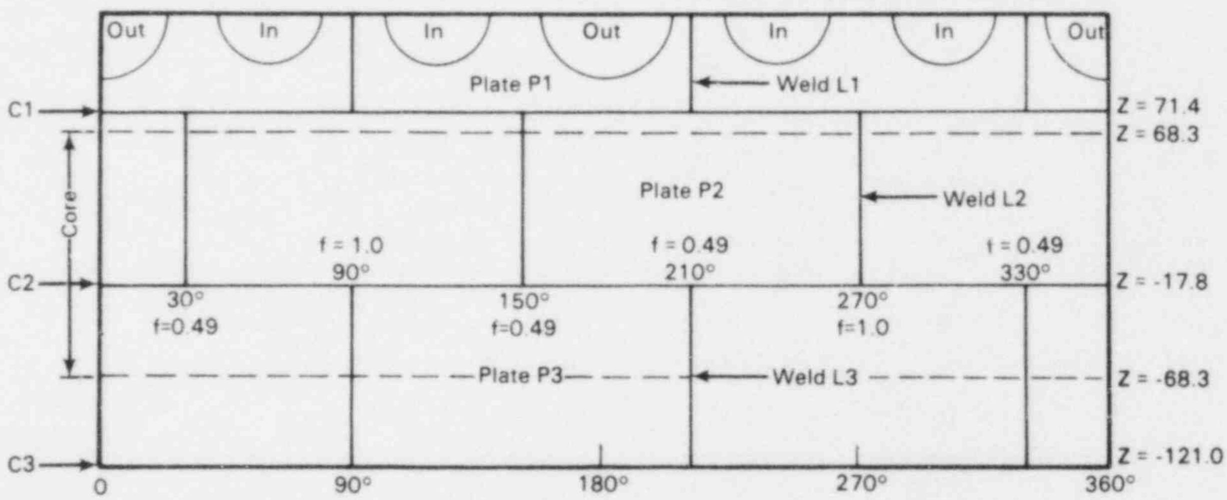

b. Weld and Plate Designations Used in PNL Evaluation

FIGURE 7.2. Inner Surface of Calvert Cliffs-1 Reactor Vessel

TABLE 7.1. Material Properties Used by ORNL in Calvert Cliffs-1 Reactor Vessel Analysis

Material Identification		Chemistry Cu, wt%	Chemistry Ni, wt%	Neutron Fluence at Inner Surface, at 32 EFPY[a] (10^{19} n/cm^2)	Initial RT_{NDT}, °C
Plates	D-7205-1	0.12	0.57	0.33	-12
	D-7205-2	0.12	0.50	0.33	-12
	D-7205-3	0.12	0.54	0.33	-12
	D-7206-1	0.11	0.55	6.06	-7
	D-7206-2	0.12	0.64	6.06	-34
	D-7206-3	0.12	0.64	6.06	-12
	D-7207-1	0.13	0.54	6.06	-12
	D-7207-2	0.11	0.56	6.06	-12
	D-7207-3	0.11	0.53	6.06	-7
Axial Welds	1-203A	0.21	0.85	0.33	-49
	1-203B,C	0.21	0.85	0.17	-49
	2-203A	0.21	0.87	6.06	-49
	2-203B,C	0.21	0.87	3.03	-49
	3-203A	0.20	0.71	6.06	-49
	3-203B,C	0.20	0.71	3.03	-49
Circumferential Welds	8-203	0.35	0.74	0.33	-51
	9-203	0.24	0.18	6.06	-62

(a) EFPY = effective full power years

TABLE 7.2. Material Properties Used in PNL Failure Mode Analysis of Calvert Cliffs-1 Vessel

Material Number	Material Designation	Copper, wt% Mean	Copper, wt% σ	Nickel, wt% Mean	Nickel, wt% σ	Initial RT_{NDT}, °F Mean	Initial RT_{NDT}, °F σ	σ of K_{IC}, Fraction of Mean	Silicon, wt%
1	L1 (1-203)	0.21	0.025	0.85	0	-56	24	0.15	0.22
2	L2 (2-203)	0.21	0.025	0.87	0	-56	24	0.15	0.22
3	L3 (3-203)	0.20	0.025	0.71	0	-56	24	0.15	0.22
4	C1 (8-203)	0.35	0.025	0.74	0	-60	24	0.15	0.22
5	C2 (9-203)	0.24	0.025	0.18	0	-80	24	0.15	0.22
6	C3	--	--	--	-	--	--	--	--
7	P1 (D-7205-1)	0.12	0.025	0.50	0	10	16	0.15	0.22
8	P2 (D-7206-2)	0.12	0.025	0.64	0	-30	16	0.15	0.22
9	P3 (D-7206-1)	0.11	0.025	0.56	0	10	16	0.15	0.22

Material Number	Material Designation	σ of K_{IA}, Fraction of Mean	σ of ΔRT_{NDT} °F	Unirradiated Flow Stress, ksi	Unirradiated Charpy Energy, ft-lb	σ of Fluence, Fraction of Mean
1	L1 (1-203)	0.10	24.0	75.0	105.0	0.3
2	L2 (2-203)	0.00	24.0	75.0	105.0	0.3
3	L3 (3-203)	0.00	24.0	75.0	105.0	0.3
4	C1 (8-203)	0.00	24.0	75.0	105.0	0.3
5	C2 (9-203)	0.00	24.0	75.0	105.0	0.3
6	C3	--	--	--	--	--
7	P1 (D-7205-1)	0.10	12.0	70.0	160.0	0.3
8	P2 (D-7206-2)	0.10	12.0	70.0	160.0	0.3
9	P3 (D-7206-1)	0.10	12.0	70.0	160.0	0.3

TABLE 7.3. Critical Transients Used in Failure Mode Analysis of Calvert Cliffs-1 Vessel

Transient	Fractional Contribution to Probability of Through-Wall Crack: 9.2 EFPY, $f = 1.52 \times 10^{19}$	Fractional Contribution to Probability of Through-Wall Crack: 32 EFPY, $f = 6.06 \times 10^{19}$
8.1	0.00	0.02
8.2	0.14	0.59
8.3	0.86	0.39

Transients 8.2 and 8.3 were clearly the dominant contributors to through-wall cracks in the ORNL analyses. Transient 8.1 also was included in the failure mode evaluations because its contribution, although smaller, was nevertheless significant.

The reader is directed to Selby et al. (1984) for a discussion of the sequence of events that result in the critical transients of Table 7.3. Figures 7.3 and 7.4 are plots of the time histories of pressure and temperature for transients 8.2 and 8.3. Transient 8.2 differs from transient 8.3 in one important aspect. The pressure in transient 8.2 increases to a high level during the later period of the transient, at a time when the temperatures are at their minimum values. This trend suggests that transient 8.2 has the greater potential to result in a more severe type of failure mode (i.e., nonarrested axial crack).

Other data from the ORNL/IPTS analyses are given in Figures 7.5 through 7.7. The increase in through-wall crack probability due to neutron exposure with years of operation is indicated in Figure 7.5. The data of Figures 7.6 and 7.7 were essential inputs to the failure mode predictions. These histograms show the times during the transients at which the ORNL/IPTS analyses predicted the occurrence of through-wall cracks. A separate histogram was used for each transient and for each level of fluence. However, the histograms were assumed to be independent of the particular weld that experienced through-wall cracking during the transient.

7.3 FRACTURE MECHANICS MODEL

The fracture mechanics model used to predict failure modes for the Calvert Cliffs-1 vessel was essentially the same as the model used for the Oconee-1 vessel. The primary revision to the analysis was the selection of inputs to the computer program to describe the configuration and materials of the Calvert Cliffs-1 vessel.

Minor changes were made in the computer program to describe the characteristics of the injection pumps for the Calvert Cliffs-1 reactor. It was conservatively assumed that all the high-pressure pumps were operating during the transients of interest. The total capacity of the high-pressure pumps was prescribed as 1500 gpm at a pressure of 1500 psi. The low- pressure pumps were neglected in the analyses because the pressure capacities were insufficient to stress the vessel to the levels required to maintain crack propagation.

PNL noted that the inclusion of injection pumps actually nad little or no impact on the predicted failure modes. The results indicated that the pumps had insufficient capacity to maintain pressure in the vessel in the presence of a through-wall crack.

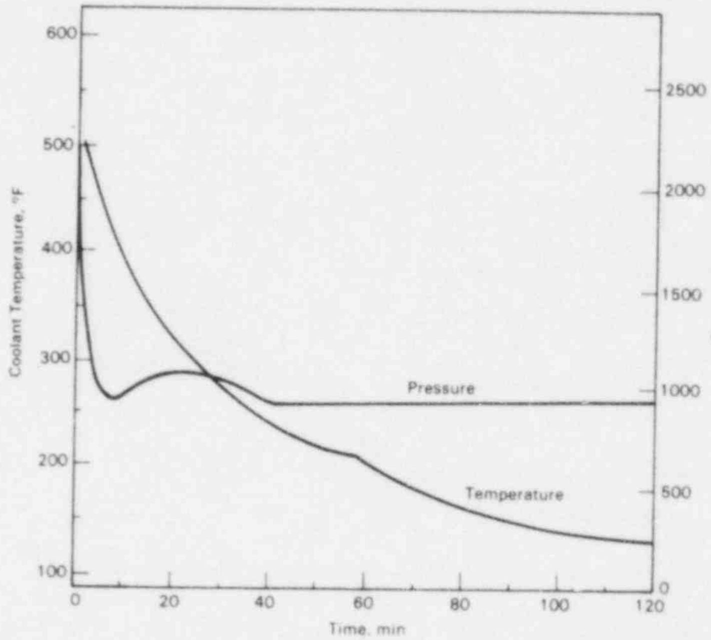

FIGURE 7.3. Pressure and Temperature for Calvert Cliffs-1 Transient 8.2

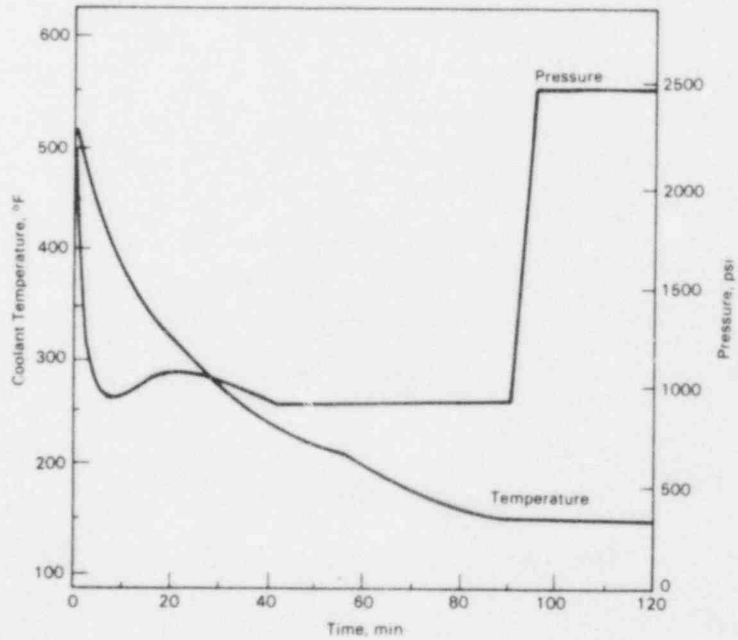

FIGURE 7.4. Pressure and Temperature for Calvert Cliffs-1 Transient 8.3

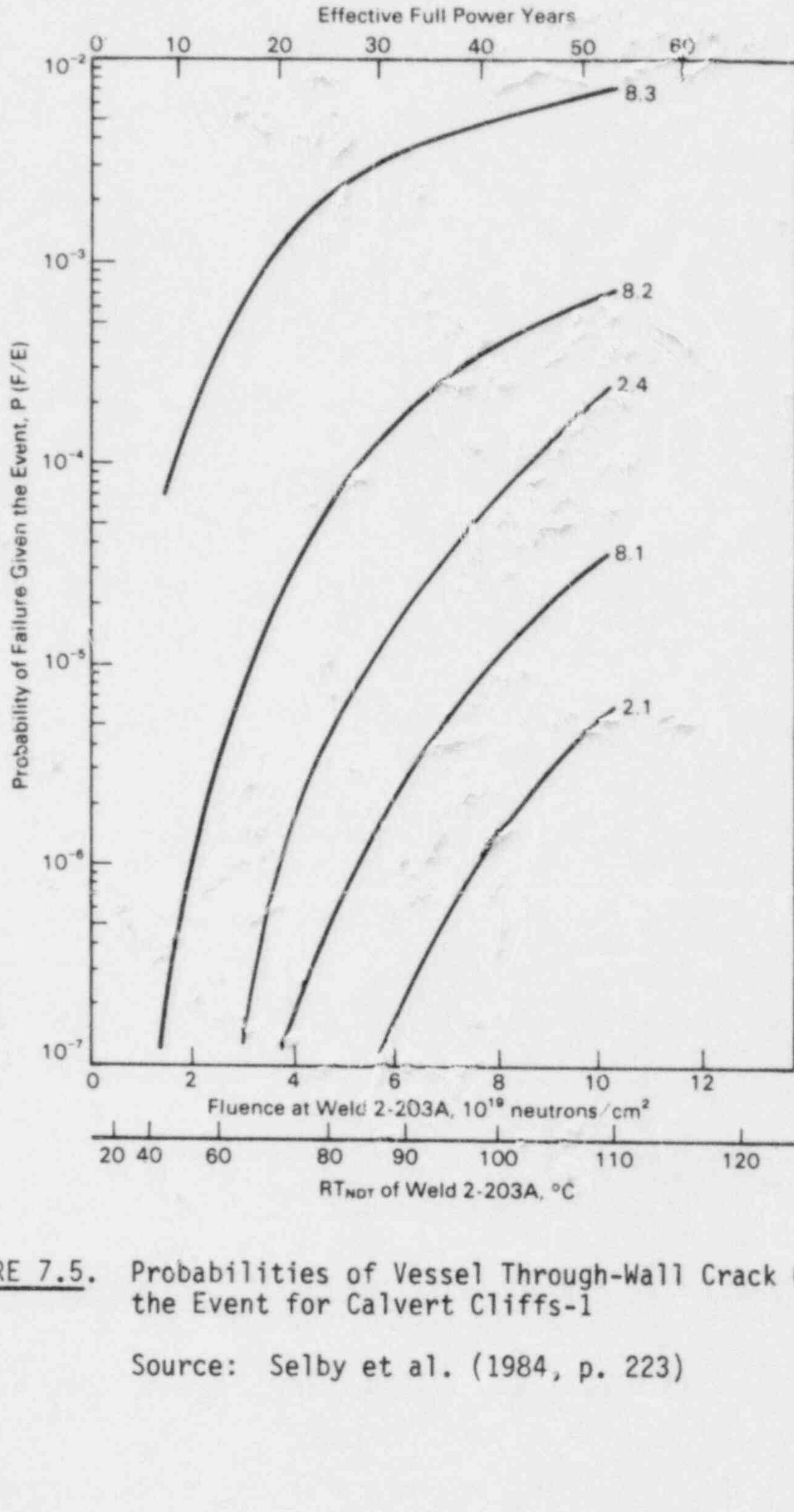

FIGURE 7.5. Probabilities of Vessel Through-Wall Crack Given the Event for Calvert Cliffs-1

Source: Selby et al. (1984, p. 223)

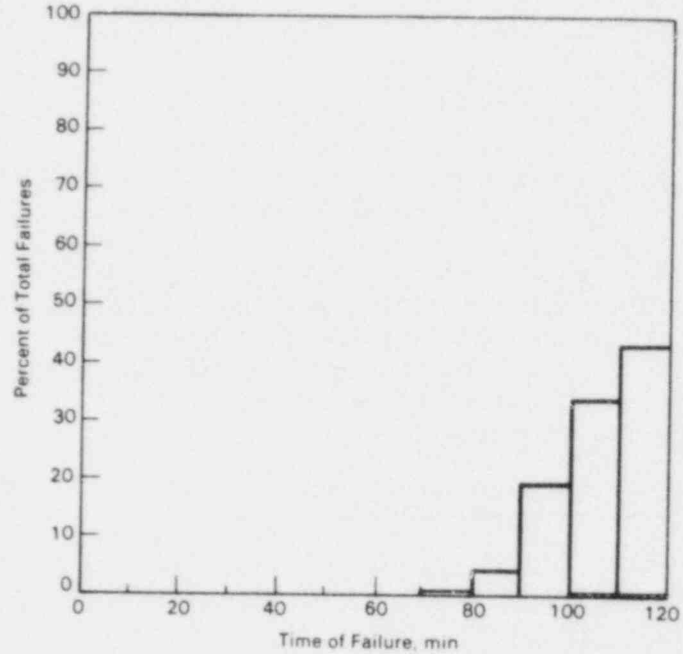

FIGURE 7.6. Percentage of Failures Versus Time of Failure for Calvert Cliffs-1 Transient 8.2

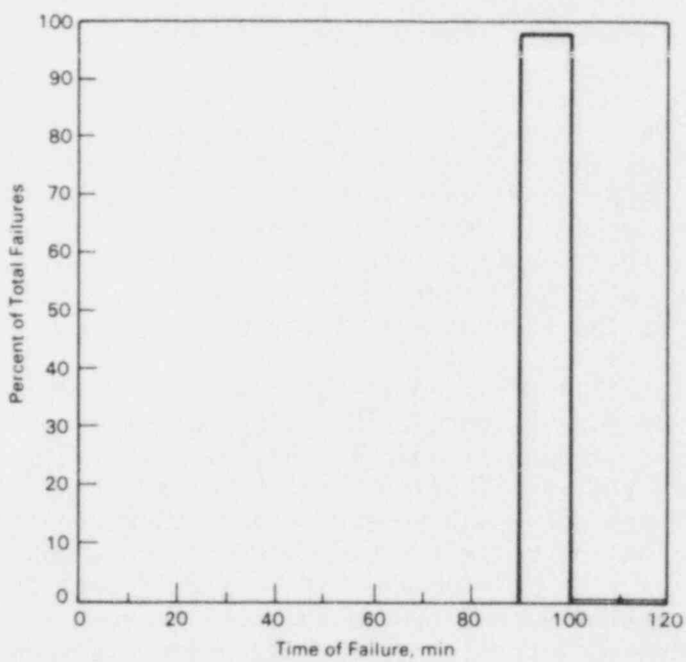

FIGURE 7.7. Percentage of Failures Versus Time of Failure for Calvert Cliffs-1 Transient 8.3

7.4 MISSILE CONCERNS

Missile concerns are addressed in Appendixes J and K on a generic basis using the Oconee-1 vessel as typical for a pressurized water reactor. The Calvert Cliffs-1 vessel is supported at the inlet locations of the reactor coolant piping; the evaluations documented in Appendix K for a top supported vessel apply to the concerns for upper head missiles.

The conclusions of the generic evaluations for missiles are that such missiles will be confined to the vessel cavity. Vertical (upper head) missiles will be arrested by the restraint provided by the attached primary coolant piping. Horizontal missiles are likely to be produced, but these missiles will be arrested readily by impact with the concrete adjacent to the reactor vessel (estimated to be about 5 ft thick).

7.5 CALVERT CLIFFS-1 SIMULATION RESULTS

Table 7.4 gives the output of the probabilistic simulations to predict the failure modes for the Calvert Cliffs-1 reactor vessel. Only data for a fluence of 6.06×10^{19} are given. The trends for predicted failure modes appear to be relatively insensitive to fluence level.

The continuous spectrum of failure modes has been sorted in Table 7.4 into six categories. The ORNL/IPTS analyses predicted that only axial welds give a significant contribution to the probability of a through-wall crack because the contribution of circumferential welds was estimated to be relatively small. However, the PNL failure mode model predicts that many of the through-wall axial cracks will change direction and follow a path along a circumferential weld.

Table 7.4 lists two main categories of failure modes: 1) those fractures that extend only in the axial direction, and 2) those axial fractures that turn to extend along a circumferential weld and then lead to a complete circumferential fracture of the vessel. Table 7.4 lists results for each of three critical transients that result in the initial through-wall axial cracks. Also listed are the calculated contributions from the ORNL/IPTS study of each of the axial welds to the through-wall crack probability.

The circumferential failures listed in Table 7.4 are described by the identification number for the particular weld that is predicted to fracture. A failure of any circumferential weld in the Calvert Cliffs vessel will result in the lower part of the vessel being accelerated to the bottom of the vessel cavity. As such, there will be a severe loss of core cooling capability. The purely axial fractures are described by their opening areas and are separated into decade ranges of size categories. It is significant that the opening areas are either relatively small (0 to 10 in.^{2}) or much larger (100 to 1000 in.^{2}). The model predicts that, once a crack extends beyond the ends of an axial weld, it will readily extend much farther to a length of essentially the entire length of the vessel.

TABLE 7.4. Results of Calvert Cliffs-1 Failure Mode Analysis for Individual Welds and Transients at 32 EFPY (Peak Fluence of 6.06×10^{19} n/cm^2)

Axial Weld	Contribution of Weld to ϕ(TWC), Fraction of Total	Vessel Failure Mode, Fraction of Total: Circumferential Failures, Weld Location[a] C1	C2	C3	Axial Failures, Opening Area, in.^{2} 0 to 10	10 to 100	>100
Transient 8.1							
L2A	0.833	0.195	0.005	0.000	0.780	0.005	0.015
L2B,C	0.051	0.040	0.000	0.000	0.960	0.000	0.000
L3	0.116	0.010	0.000	0.000	0.990	0.000	0.000
Transient 8.2							
L2A	0.730	0.565	0.020	0.000	0.160	0.005	0.255
L2B,C	0.080	0.295	0.005	0.000	0.375	0.000	0.325
L3	0.190	0.095	0.005	0.000	0.780	0.015	0.105
Transient 8.3							
L2A	0.476	0.830	0.170	0.000	0.000	0.000	0.000
L2B,C	0.258	0.775	0.225	0.000	0.000	0.000	0.000
L3	0.266	0.775	0.225	0.000	0.000	0.000	0.000

(a) Weld locations are as follows:

- C1 is at 71.4 in.
- C2 is at -17.8 in.
- C3 is at -121 in.

Figure 7.8 summarizes the results of the failure mode evaluations for the Calvert Cliffs-1 vessel. These results include the contributions from failures initiating in all the welds of the vessel and the contributions from all three of the most critical transients. Figure 7.8 shows that the probabilities for all the failure modes increase with fluence. However, the relative contributions for the different modes remain about the same for all levels of fluence.

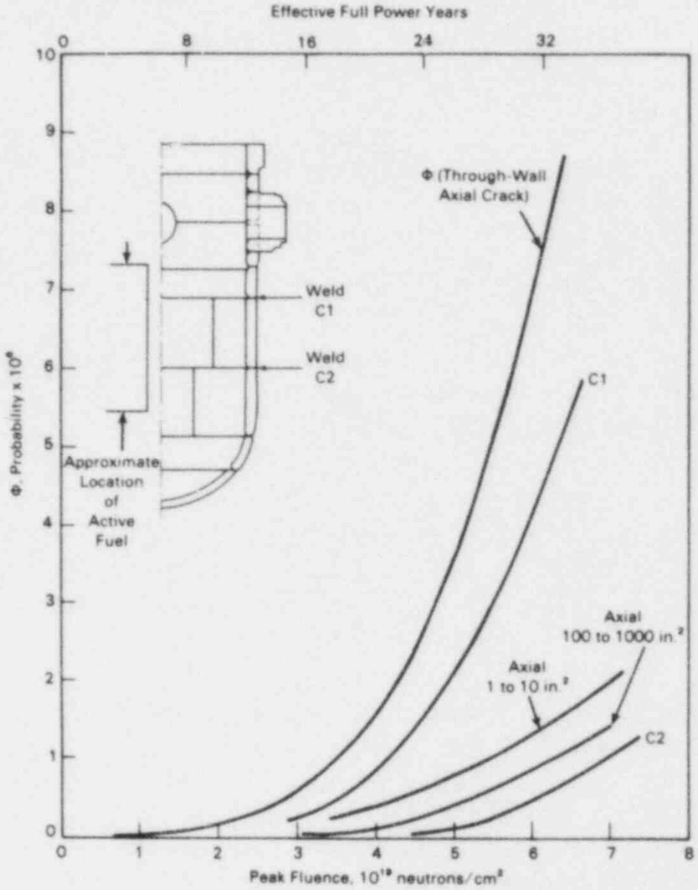

FIGURE 7.8. Calvert Cliffs-1 Failure Mode Prediction

The results of the failure mode evaluations for the Calvert Cliffs-1 vessel can be summarized as follows:

1. About 70% of the through-wall axial cracks turn to follow a circumferential weld.

2. About 15% of the through-wall axial cracks arrest at a final length corresponding to the length of the axial weld. Another 15% of the through-wall axial cracks continue to extend as axial cracks into the adjacent plate material.

3. Cracks in the Calvert-Cliffs-1 vessel tend to arrest at the ends of the axial welds for those transients with lower pressures.

4. Missiles that may result from fracture of the Calvert Cliffs-1 vessel will be confined to the reactor vessel cavity.

8.0 H. B. ROBINSON-2 EVALUATION

This section describes predictions of vessel failure modes for the H. B. Robinson-2 nuclear power plant using the properties of a hypothetical vessel (identified as HBR-HYPO). These calculations were based on simulated pressure and temperature transients from the ORNL/IPTS study (Selby et al. 1985). This evaluation was the last in the series of three plant-specific studies. Because the methodology was essentially the same as that for the Oconee-1 and Calvert Cliffs-1 studies, the discussion will focus on specific results of the H. B. Robinson-2 predictions. Only those aspects of the fracture mechanics model that apply specifically to the H. B. Robinson-2 evaluation will be highlighted.

8.1 VESSEL CHARACTERISTICS

Information on the construction and materials for the H. B. Robinson-2 vessel was assembled from various sources. The primary source was the ORNL/IPTS study (Selby et al. 1985), which was used extensively to ensure that the PNL failure mode analysis would be consistent with the previous fracture mechanics evaluations at ORNL.

The ORNL/IPTS study and the PNL failure mode evaluation are focused on the HBR-HYPO vessel. The reason for using a hypothetical vessel was that early calculations at ORNL for the actual H. B. Robinson vessel predicted very low failure probabilities. This was due to the relatively low level of irradiation-induced embrittlement that was estimated for the actual vessel. It was nevertheless desired to perform calculations that would permit an appropriate illustration of the methods of analysis. Therefore, the actual weld characteristics (initial fracture toughness and concentrations of copper and nickel) were modified by ORNL to create a hypothetical vessel that would have a higher probability of a through-wall crack for the predicted transients of the H. B. Robinson-2 reactor.

Figure 8.1 shows a view of the H. B. Robinson-2 vessel with the various plates and welds of the vessel indicated. The location of the active core is shown in Figure 8.1 to indicate the region of irradiation damage. Figure 8.2 shows an "unwrapped" view of the vessel. Dimensions are shown along with labels to identify each plate and weld in the beltline region of the vessel.

Table 8.1 lists the input parameters for the vessel materials that were used in the failure mode evaluation. Except for silicon content, flow stress, and upper shelf Charpy impact energy, all the values listed are the same as those used by ORNL in their calculations for the HBR-HYPO vessel. Values for the additional parameters were selected from the information given for the H. B. Robinson-2 vessel in the EPRI database (McConnell et al. 1982).

The failure mode evaluations were performed for only a single fluence level corresponding to 32 effective full power years of operation. Data from the ORNL/IPTS study were insufficient to perform calculations for other levels of fluence.

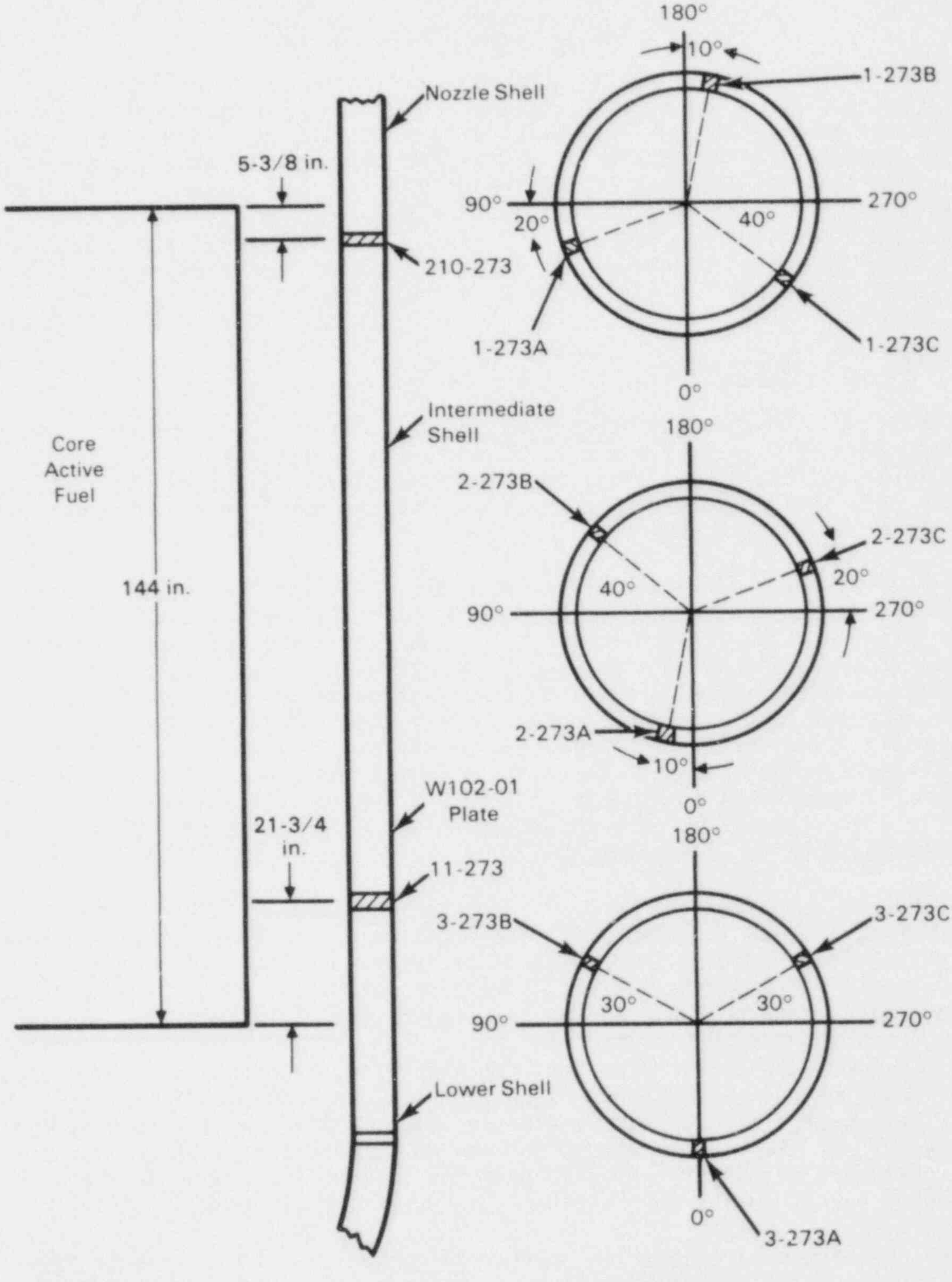

FIGURE 8.1. Location and Identification of Materials Used in Fabrication of H. B. Robinson-2 Reactor Pressure Vessel

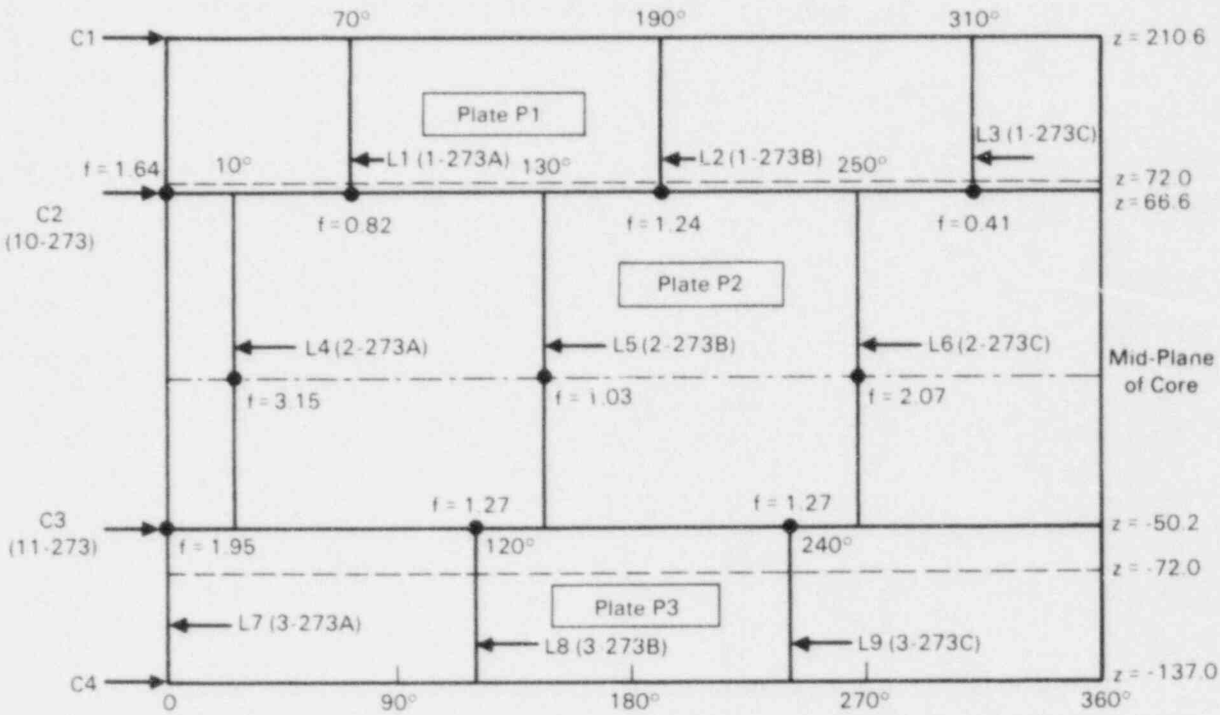

FIGURE 8.2. Inner Surface of H. B. Robinson-2 Reactor Pressure Vessel

The calculations performed in the ORNL study and in the PNL evaluations both were based on fluence patterns that reflect recent changes in the fuel assemblies at the H. B. Robinson-2 nuclear power plant. These changes include part-length shielded assemblies that have been installed by the Carolina Power & Light Company (CP&L). For the failure mode evaluation it was necessary to construct a fluence map for the entire inner surface of the vessel. Information for the fluence map was obtained from Selby et al. (1985) and from 1983 data supplied by J. H. Phillips of CP&L.

Fluence values at critical locations of the vessel are indicated on Figure 8.2. These values were estimated from the available information. Some estimation was required because the available information gave only fluence variations along selected axial and circumferential coordinate lines.

8.2 CRITICAL TRANSIENTS

Table 8.2 lists the six most dominant sequences and pressure-temperature transients from Selby et al. (1985). These were identified as giving the greatest contributions to the predicted probability of through-wall cracks for the HBR-HYPO vessel. Table 8.2 also gives the relative contributions of each sequence to the occurrence of through-wall cracking.

TABLE 8.1. Material Properties Used in Failure Mode Analysis of the HBR-HYPO Vessel

Material Number Designation	Copper, wt% Mean	Copper, wt% σ	Nickel, wt% Mean	Nickel, wt% σ	Initial RT_{NDT}, °F Mean	Initial RT_{NDT}, °F σ	σ of K_{IC}, Fraction of Mean	Silicon, wt%
L1 (1-273A)	--	--	--	--	--	--	--	--
L2 (1-273B)	--	--	--	--	--	--	--	--
L3 (1-273C)	--	--	--	--	--	--	--	--
L4 (2-273A)	0.22	0.025	0.80	0	0	24	0.15	0.22
L5 (2-273B)	0.22	0.025	0.80	0	0	24	0.15	0.22
L6 (2-273C)	0.22	0.025	0.80	0	0	24	0.15	0.22
L7 (3-273A)	--	--	--	--	--	--	--	--
L8 (3-273B)	--	--	--	--	--	--	--	--
L9 (3-273C)	--	--	--	--	--	--	--	--
C1	0.22	0.025	0.80	0	0	24	0.15	0.22
C2 (10-273)	0.22	0.025	0.80	0	0	24	0.15	0.22
C3 (11-273)	0.22	0.025	0.80	0	0	24	0.15	0.22
C4	0.22	0.025	0.80	0	0	24	0.15	0.22
P1	0.12	0.025	0.80	0	0	16	0.15	0.22
P2	0.12	0.025	0.80	0	0	16	0.15	0.22
P3	0.12	0.025	0.80	0	0	16	0.15	0.22

Material Number Designation	σ of K_{IA}, Fraction of Mean	σ of ΔRT_{NDT}, °F	Unirradiated Flow Stress, ksi	Unirradiated Charpy Energy, ft-lb	σ of Fluence, Fraction of Mean
L1 (1-273A)	--	--	--	--	--
L2 (1-273B)	--	--	--	--	--
L3 (1-273C)	--	--	--	--	--
L4 (2-273A)	0.15	24	70	120	0.3
L5 (2-273B)	0.15	24	70	120	0.3
L6 (2-273C)	0.15	24	70	120	0.3
L7 (3-273A)	--	--	--	--	--
L8 (3-273B)	--	--	--	--	--
L9 (3-273C)	--	--	--	--	--
C1	0.15	24	70	120	0.3
C2 (10-273)	0.15	24	70	120	0.3
C3 (11-273)	0.15	24	70	120	0.3
C4	0.15	24	70	120	0.3
P1	0.15	12	65	100	0.3
P2	0.15	12	65	100	0.3
P3	0.15	12	65	100	0.3

TABLE 8.2. The Six Most Dominant Risk Sequences and Through-Wall Crack Frequencies for HBR-HYPO Vessel and HBR-2 Vessel

		Through-Wall Crack Frequency (yr^{-1})		
Sequence	Transient	HBR-HYPO Reactor Vessel at 32 EFPY	HBR-2 Reactor Vessel at 32 EFPY	Fractional Contribution of Transient to TWC for HBR-HYPO
9.41	9.41	4E-9	<5E-12	0.430
9.33	9.33	3E-9	<2E-13	0.323
9.19B	9.19B	7E-10	4E-12	0.075
9.94	9.19B	7E-10	4E-12	0.075
9.43	9.43	5E-10	<5E-14	0.054
9.20B	9.20B	4E-10	2E-12	0.043

The ORNL/IPTS study predictions for the H. B. Robinson-2 reactor differed markedly from the predictions for the Oconee-1 and Calvert Cliffs-1 reactors. The risk of vessel fracture was not limited to only a few transients. Rather, a large number of transients together contributed to the overall risk. The six sequences listed in Table 8.2 contribute to about 75% of the calculated probability of through-wall cracks. The remaining contribution of about 25% came from a large number of other sequences or transients. In the PNL failure mode evaluation it was assumed that these other transients could be taken into account by adjusting the probabilities in Table 8.2 upward. The adjusted probabilities then accounted for 100% of the through-wall crack probability.

The other excluded transients were reviewed to determine if any might result in types of failure modes different from those predicted for the six transients that were included in the evaluation. None of these excluded transients was found to have the particular feature of a relatively low pressure for the critical time period when through-wall cracking was predicted by the ORNL/IPTS study. Therefore, it was not expected that through-wall cracks would tend to arrest at the ends of the affected axial welds for any of the excluded transients. Consequently, including these transients should not change the trends for the failure modes as predicted on the basis of the limited selection of six transients.

Figure 8.3 shows the histories of pressure and temperature for the six sequences listed in Table 8.2. It should be noted that one pressure-temperature transient applies for two sequences (sequences 9.19B and 9.94). It should also be noted that the temperature curves have been adjusted to give metal temperatures at the vessel inner surface rather than fluid temperatures. The reader is directed to Selby et al. (1985) for a discussion of the sequence of events that result in the critical transients of Table 8.2.

Other data from the ORNL/IPTS calculations were also of interest to the failure mode evaluations for the HBR-HYPO vessel. These data (not listed in

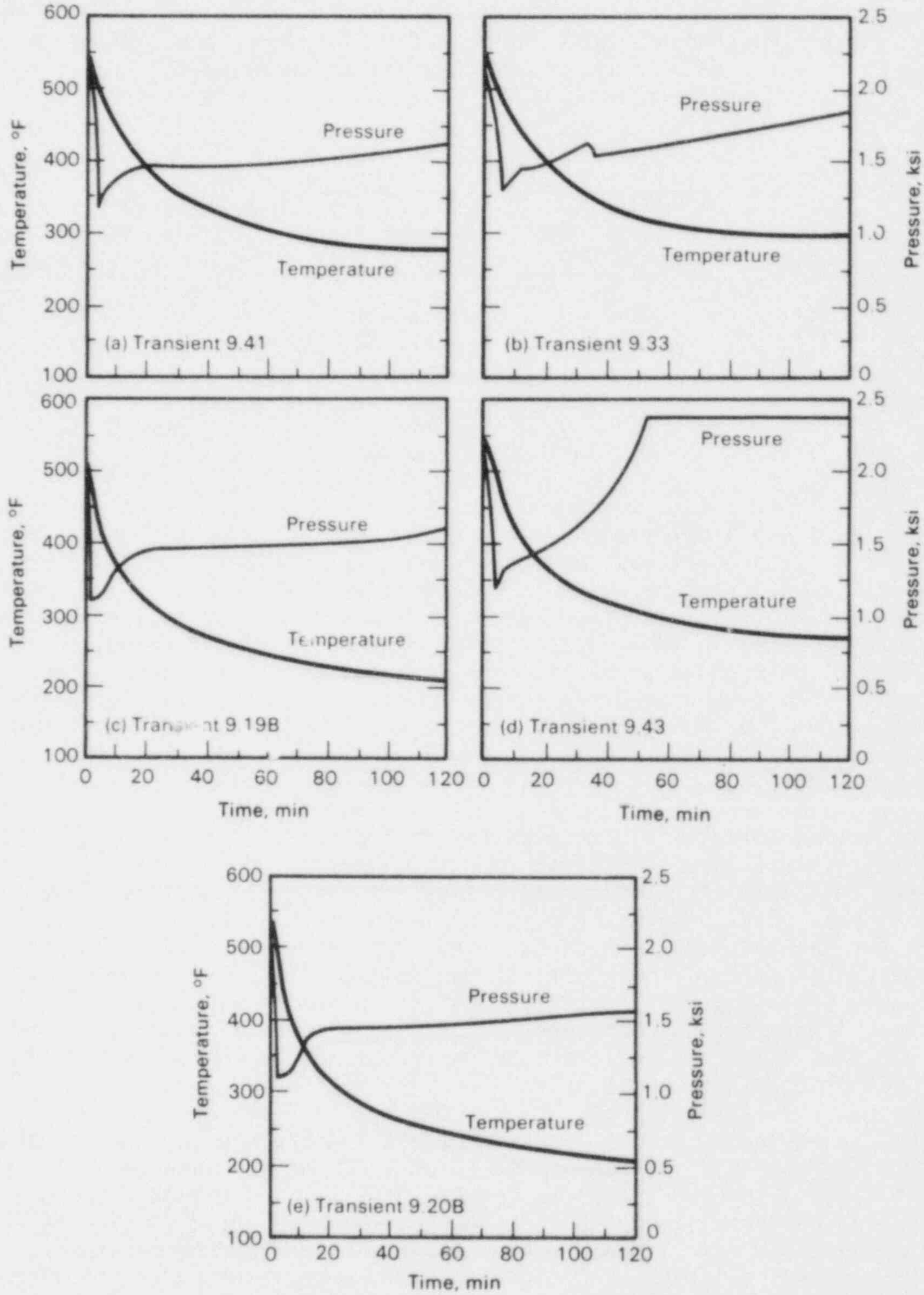

FIGURE 8.3. Pressure and Temperature Transients of Simulated PTS Events for H. B. Robinson-2 Reactor

this report) included 1) the distribution of times during the 120-minute transients corresponding to the occurrence of through-wall cracks, and 2) the relative contributions to through-wall cracking from the two axial welds that were addressed in the ORNL/IPTS study.

8.3 FRACTURE MECHANICS MODEL

The fracture mechanics model used to predict failure modes for the H. B. Robinson-2 vessel was essentially the same as the model used for the Oconee-1 and Calvert Cliffs-1 vessels. The primary revision to the analysis was the selection of inputs to the computer program to describe the configuration and materials of the HBR-HYPO vessel.

PNL noted that the inclusion of injection pumps had little or no impact on the predicted failure modes for the Oconee-1 and Calvert Cliffs-1 vessels. The results indicated that the pumps had insufficient capacity to maintain pressure in the vessel in the presence of a through-wall crack. Therefore, the calculations for the HBR-HYPO vessel neglected any ability of the injection pumps to maintain sufficient pressure to propagate a through-wall crack following the initial fracture event.

The ORNL/IPTS study concluded that most of the contribution to the probability of through-wall cracks came from two axial welds in the middle (beltline) shell course. The contribution from the third axial weld in the middle shell course was relatively small, due to lower levels of fluence at this weld. The contributions from the circumferential welds and plate material were also not significant, due to lower stress levels and/or lower values of RT_{NDT}.

Contributions from axial welds in the upper and lower shell courses were relatively small in the ORNL/IPTS analyses. These welds have only a small volume of their material within the highly irradiated beltline region of the vessel. However, the inclusion of these welds could have had some impact on the trends of the failure mode predictions. It is more likely that through-wall axial cracks in these welds would arrest without causing a large opening in the vessel. Thus, the exclusion of these welds from the failure mode analyses introduces some conservatism into the evaluations.

8.4 MISSILE CONCERNS

Missile concerns are addressed in Appendixes J and K on a generic basis using the Oconee-1 vessel as typical for a pressurized water reactor. The H. B. Robinson-2 vessel is supported at the inlet locations of the reactor coolant piping; the evaluations in Appendix K for a top supported vessel apply to the concerns for upper head missiles.

The conclusions of the generic evaluations for missiles are that such missiles will be confined to the vessel cavity. Vertical (upper head) missiles will be arrested by the restraint provided by the attached primary coolant piping. Horizontal missiles are likely to be produced, but these missiles will be arrested readily by impact with the concrete adjacent to the reactor vessel (estimated to be about 5 ft thick).

8.5 H. B. ROBINSON-2 SIMULATION RESULTS

Table 8.3 gives the output of the probabilistic simulations of the failure modes for the HBR-HYPO vessel. Only data for the fluence at 32 effective full power years are given in this table, because this was the only fluence level addressed for the HBR-HYPO vessel.

The continuous spectrum of failure modes has been sorted in Table 8.3 into three categories. Table 8.3 lists two main categories of failure modes: 1) those fractures that extend only in the axial direction, and 2) those axial fractures that turn to extend along a circumferential weld and then lead to a complete circumferential fracture of the vessel. The purely axial mode of fracture is further divided into two subcategories: small opening area and large opening area.

TABLE 8.3. Results of H. B. Robinson-2 Vessel Failure Mode Analysis of HBR-HYPO for Individual Welds and Transients at 32 EFPY

Axial Weld	Contribution of Weld to ϕ(TWC), Fraction of Total	Circumferential Failures	Axial Failures: Opening Area, >1000 in.^{2}	Axial Failures: Opening Area, 0 to 1000 in.^{2}
Sequence 9.41				
2-273A	0.930	0.895	0.105	0.000
2-273C	0.070	0.975	0.025	0.000
Sequence 9.33				
2-273A	0.980	1.000	0.000	0.000
2-273C	0.020	1.000	0.000	0.000
Sequence 9.19B				
2-273A	0.820	0.975	0.025	0.000
2-273C	0.180	0.980	0.020	0.000
Sequence 9.94				
2-273A	0.820	0.975	0.025	0.000
2-273C	0.180	0.980	0.020	0.000
Sequence 9.43				
2-273A	0.890	1.000	0.000	0.000
2-273C	0.110	1.000	0.000	0.000
Sequence 9.20B				
2-273A	0.810	0.985	0.015	0.000
2-273C	0.190	0.970	0.030	0.000

From Table 8.3 it is clear that most of the fractures of axial welds lead to a predicted circumferential fracture of the vessel. Less than 10% of the fractures for any of the six transients continue to grow as purely axial cracks. Even this small fraction of purely axial cracks grows to sufficient length that a very large opening in the vessel wall results. None of the simulations predicted an arrest of an axial crack at a length that would result in only a small opening in the vessel wall.

The calculations for the Oconee-1 and Calvert Cliffs-1 vessels predicted that only about 50% of the through-wall cracks in axial welds resulted in a circumferential vessel failure. The larger fraction of such failures for the HBR-HYPO vessel is because 1) all the transients have relatively high pressures during the critical part of the transient, 2) the lengths of the axial welds for the HBR-HYPO vessel are greater than the lengths for the other two vessels, and 3) the upper shelf toughness for the circumferential welds is relatively low for the HBR-HYPO vessel. Most of the predicted circumferential weld failures were in the form of ductile tearing of the weld metal at upper shelf temperature conditions.

Table 8.4 gives the summary of the failure mode simulations for the HBR-HYPO vessel. In this table, the results of Table 8.3 have been combined. Each result was properly weighted in accordance with the relative contribution of each weld and each transient. The prediction is that about 95% of the through-wall cracks in the vessel will grow to become full circumferential fractures of the vessel. The remaining 5% of the through-wall cracks are predicted to grow in only the axial direction. However, this growth will result in a large axial slit in the vessel, and the opening area will be greater than 1000 $in.^2$.

TABLE 8.4. Results of H. B. Robinson-1 Failure Mode Predictions (HBR-HYPO at 32 EFPY)

Vessel Failure Mode, Fraction of Total		
Circumferential Failures	Axial Failure Opening Area, >1000 $in.^2$	Axial Failure Opening Area, 0 to 1000 $in.^2$
0.950	0.050	0.000

The results of the failure mode evaluations for the HBR-HYPO vessel can be summarized as follows:

1. About 95% of the through-wall axial cracks turn to follow a circumferential weld.

2. Another 5% of the through-wall axial cracks continue to extend as axial cracks into the adjacent plate material.

at the zero level of fluence. Nevertheless, the fraction of small axial fractures (crack arrest at the ends of the axial weld) remains zero, even at fluences that approach zero. This indicates that the upper shelf fracture toughness is insufficient to arrest axial crack growth for the pressures and weld lengths of concern to the HBR-HYPO vessel.

A second set of calculations addressed the effect of internal pressure. The pressure for transient 9.41 is about 1500 psi during the critical parts of the transient. Table 8.5 shows a clear change in the failure mode as the pressure is decreased from 1500 psi to 500 psi. At 1000 psi the fraction of circumferential fractures is quite small (about 1.5%). Most of the cracks are predicted to arrest at the ends of the axial welds. As the pressure is reduced further to 500 psi, it is predicted that 100% of the cracks will arrest at the ends of the axial welds. The corresponding opening areas in the vessel wall are relatively small.

The final set of calculations addressed the effect of upper shelf toughness. The variable of concern was the initial unirradiated level of the Charpy impact energy. As given in Table 8.1, the impact energy was 120 ft-lb for the welds and 100 ft-lb for the plate materials. In comparison with the values for the Oconee-1 and Calvert Cliffs-1 vessels, it appears that HBR-HYPO plate material has relatively low impact properties. On the other hand, the impact properties of the HBR-HYPO welds are perhaps somewhat better than average. In the sensitivity study for upper shelf toughness, it was assumed that the plate and weld material had the same values of Charpy energy. This value was varied from 100 ft-lb to an extreme value of 200 ft-lb. The results predict a significant fraction of circumferential failures (about 20%), even for an extreme impact energy of 200 ft-lb. This suggests that the relatively large fraction of predicted circumferential fractures for the HBR-HYPO vessel is due to the adverse combination of long axial welds and high pressures during the critical transients. Table 8.5 also shows the effect of increasing the impact energy of the plate material to a quite realistic level of 150 ft-lb. The number of arrests of cracks at the ends of axial welds is predicted to increase. Some 30% of the axial cracks were predicted to arrest, compared to 0% for the HBR-HYPO vessel with an impact energy of 100 ft-lb.

3. Missiles that may result from fracture of the HBR-HYPO vessel will be confined to the reactor vessel cavity.

8.6 SENSITIVITY STUDIES

The results presented in Tables 8.3 and 8.4 show a relatively large fraction of predicted circumferential weld failures. In addition, the calculations did not predict any arrests of cracks at the ends of the axial welds. To gain insight into the reasons for these trends, a set of sensitivity calculations was performed. The baseline case for this study was as follows:

- fluence = 32 EFPY
- transient = transient number 9.41
- material properties = HBR-HYPO (Table 8.1)
- weld = axial weld number 2-273A.

Results of the sensitivity study are summarized in Table 8.5.

The first set of results indicates the effect of fluence. The level of fluence was varied from 1.6 EFPY to 50 EFPY. Results given in Table 8.5 indicate the predicted effects on failure modes. For low levels of fluence, the circumferential mode of failure becomes less probable and approaches 50%

TABLE 8.5. Results of H. B. Robinson-2 Sensitivity Calculations[(a)]

	Fractions of Failure Modes		
Effect of Fluence	Circumferential Fracture	Large Axial Fracture	Small Axial Fracture
f = 1.6 EFPY	0.550	0.450	0.000
f = 8 EFPY	0.625	0.375	0.000
f = 16 EFPY	0.760	0.240	0.000
f = 32 EFPY	0.895	0.105	0.000
f = 50 EFPY	0.960	0.040	0.000
Effect of Pressure			
p = 500 psi	0.000	0.000	1.000
p = 1000 psi	0.015	0.225	0.760
p = 1500 psi	0.895	0.105	0.000
Effect of Upper Shelf Toughness			
CVN = 100 ft-lb	0.995	0.005	0.000
CVN = 125 ft-lb	0.830	0.135	0.035
CVN = 150 ft-lb	0.465	0.205	0.330
CVN = 200 ft-lb	0.195	0.055	0.750

(a) Baseline = transient 9.41, 32 EFPY, HBR-HYPO vessel, Weld 2-273-A at the zero level of fluence. Nevertheless, the fraction of small axial fractures (crack arrest at the ends of the axial weld) remains zero, even at fluences that approach zero. This indicates that the upper shelf fracture toughness is insufficient to arrest axial crack growth for the pressures and weld lengths of concern to the HBR-HYPO vessel.

A second set of calculations addressed the effect of internal pressure. The pressure for transient 9.41 is about 1500 psi during the critical parts of the transient. Table 8.5 shows a clear change in the failure mode as the pressure is decreased from 1500 psi to 500 psi. At 1000 psi the fraction of circumferential fractures is quite small (about 1.5%). Most of the cracks are predicted to arrest at the ends of the axial welds. As the pressure is reduced further to 500 psi, it is predicted that 100% of the cracks will arrest at the ends of the axial welds. The corresponding opening areas in the vessel wall are relatively small.

The final set of calculations addressed the effect of upper shelf toughness. The variable of concern was the initial unirradiated level of the Charpy impact energy. As given in Table 8.1, the impact energy was 120 ft-lb for the welds and 100 ft-lb for the plate materials. In comparison with the values for the Oconee-1 and Calvert Cliffs-1 vessels, it appears that HBR-HYPO plate material has relatively low impact properties. On the other hand, the impact properties of the HBR-HYPO welds are perhaps somewhat better than average. In the sensitivity study for upper shelf toughness, it was assumed that the plate and weld material had the same values of Charpy energy. This value was varied from 100 ft-lb to an extreme value of 200 ft-lb. The results predict a significant fraction of circumferential failures (about 20%), even for an extreme impact energy of 200 ft-lb. This suggests that the relatively large fraction of predicted circumferential fractures for the HBR-HYPO vessel is due to the adverse combination of long axial welds and high pressures during the critical transients. Table 8.5 also shows the effect of increasing the impact energy of the plate material to a quite realistic level of 150 ft-lb. The number of arrests of cracks at the ends of axial welds is predicted to increase. Some 30% of the axial cracks were predicted to arrest, compared to 0% for the HBR-HYPO vessel with an impact energy of 100 ft-lb.

REFERENCES

Ayres, D. J. 1975. "Elastic-Plastic Dynamic Analysis of Opening Area of an Axial Crack in a Pipe Under Pressure." Paper L-716, presented to the 3rd International Conference on Structural Mechanics in Reactor Technology, September 1975, London.

Bass, B. R., C. E. Pugh, and J. K. Walker. 1985. "Elastodynamic Fracture Analyses of Large Crack-Arrest Experiments." In Transactions of the Thirteenth Water Reactor Safety Research Information Meeting, NUREG/CP-0071, U.S. Nuclear Regulatory Commission, Washington, D.C.

Burns, T. J., R. D. Cheverton, G. F. Flanagen, J. D. White, D. G. Ball, L. B. Lamonica, and R. Olsen. 1984. Pressurized Thermal Shock Evaluation of the Oconee-1 Nuclear Power Plant. NUREG/CR-3770, U.S. Nuclear Regulatory Commission, Washington, D.C.

Cheverton, R. D., and D. G. Ball. 1984. OCA-P - A Deterministic and Probabilistic Fracture-Mechanics Code for Application to Pressure Vessels. NUREG/CR-3618, U.S. Nuclear Regulatory Commission, Washington, D.C.

Cheverton, R. D., S. K. Iskander, and G. D. Whitman. 1983. "The Integrity of PWR Pressure Vessels During Overcooling Accidents." In Proceedings of the International Meeting on Thermal Nuclear Reactor Safety, NUREG/CP-0027 Vol. 1, pp. 421-430. U.S. Nuclear Regulatory Commission, Washington, D.C.

Combustion Engineering, Inc. 1982. Evaluation of Irradiation Response of Reactor Pressure Vessel Materials. EPRI NP-2720, Electric Power Research Institute, Palo Alto, California.

Dircks, J. W. 1982. "Enclosure A: NRC Staff Evaluation of Pressurized Thermal Shock, November 1982." SECY-82-465, Division of Nuclear Reactor Regulation, U.S. Nuclear Regulatory Commission, Washington, D.C.

Hiser, A. 1985. Estimation of Reactor Vessel Upper Shelf Fracture Toughness Properties. MEA-2068, Materials Engineering Associates, Lanham, Maryland.

Johnson, R. 1982. Resolution of the Task A-11 Reactor Materials Toughness Safety Issue. NUREG-0744, U.S. Nuclear Regulatory Commission, Washington, D.C.

Kumar, J., M. D. German, and C. F. Shih. 1981. An Engineering Approach for Elastic-Plastic Analysis. EPRI NP-1931, Electric Power Research Institute, Palo Alto, California.

Lundvall, A. E. 1982. 150 Day Response to NRC Request on Pressurized Thermal Shock to Reactor Pressure Vessels. Baltimore Gas and Electric, Calvert Cliffs Nuclear Power Plant Unit 1, Baltimore, Maryland.

Mager, T. R., S. L. Anderson, and S. E. Yanichko. 1983. The Westinghouse Electric Corporation Reactor Vessel Radiation Surveillance Program. ASTM STP-784, American Society of Testing and Materials, Philadelphia, Pennsylvania.

Mayfield, M. E., T. P. Forte, E. C. Rodabaugh, B. N. Leis, and R. J. Eiber. 1980. Cold Leg Integrity Evaluation. NUREG/CR-1319, U.S. Nuclear Regulatory Commission, Washington, D.C.

McConnell, P., W. L. Server, W. Oldfield, and F. M. Oldfield. 1982. Irradiated Nuclear Pressure Vessel Steel Data Base. EPRI NP-2428, Electric Power Research Institute, Palo Alto, California.

Odette, G.R., and P. Lombrozo. 1983. "A Physically Statistically Based Correlation for Transition Temperature Shifts in Pressure Vessel Surveillance Weld." Transactions of the American Nuclear Society. 44: 224-225.

Parker, W. O. 1982. 150 Day Response to NRC Request on Pressurized Thermal Shock to Reactor Pressure Vessels. DPC-RS-1001, Duke Power Company, Oconee Nuclear Power Station Unit 1, Charlotte, North Carolina.

Pedersen, L. T., W. J. Apley, S. H. Bian, L. J. Defferding, M. H. Morgenstern, P. J. Pelto, E. P. Simonen, F. A. Simonen, D. L. Stevens, and T. T. Taylor. 1982a. PNL Technical Review of Pressurized Thermal Shock Issues. NUREG/CR-2837, U.S. Nuclear Regulatory Commission, Washington, D.C.

Pedersen, L. T., W. J. Apley, S. H. Bian, P. J. Pelto, E. P. Simonen, F. A. Simonen, D. L. Stevens, and T. T. Taylor. 1982b. PNL Technical Review of Pressurized Thermal Shock Issues - Supplement 1: Technical Critique of the NRC Near-Term Screening Criteria. NUREG/CR-2837 Supp. 1, U.S. Nuclear Regulatory Commission, Washington, D.C.

Pugh, C. E. 1985. "HSST Crack Arrest Studies Overviews." In Transactions of the Thirteenth Water Reactor Safety Research Information Meeting, NUREG/CP-0071, U.S. Nuclear Regulatory Commission, Washington, D.C.

Selby, D. L. 1984. Pressurized Thermal Shock Evaluation of the Calvert Cliffs-1 Nuclear Power Plant. NUREG/CR-4022, U.S. Nuclear Regulatory Commission, Washington, D.C.

Selby, D. L. 1985. Pressurized Thermal Shock Evaluation of the H. B. Robinson Unit 2 Nuclear Power Plant. NUREG/CR-4183, U.S. Nuclear Regulatory Commission, Washington, D.C.

Shih, C. F., and W. R. Andrews. 1981. Methodology for Plastic Fracture. EPRI NP-1735, Electric Power Research Institute, Palo Alto, California.

Stevens, D. L., F. A. Simonen, J. Strosnider, Jr., R. W. Klecker, D. W. Engel, and K. I. Johnson. 1983. VISA - A Computer Code for Predicting the Probability of Reactor Pressure Vessel Failure. NUREG/CR-3384, U.S. Nuclear Regulatory Commission, Washington, D.C.

White, J. D. 1983. "Integration of PTS Studies to Calculate Through-Wall Crack Probabilities." In Transactions of the Eleventh Water Reactor Safety Research Information Meeting, NUREG-CP-0047, U.S. Nuclear Regulatory Commission, Washington, D.C.

White, J. D. 1985. "Results of PTS Probalistic Analysis Based on Oconee, Calvert Cliffs and H. B. Robinson." In Proceedings of the Twelfth Water Reactor Safety Information Meeting, NUREG-CP-0058, U.S. Nuclear Regulatory Commission, Washington, D.C.

APPENDIX A

EXPLORATORY CALCULATIONS

APPENDIX A

EXPLORATORY CALCULATIONS

This appendix describes a series of example calculations that were performed to demonstrate and apply the deterministic fracture mechanics model for the growth of the through-wall cracks in reactor pressure vessels. This deterministic model was the basis of the probabilistic simulations used in the evaluations of plant-specific failure modes for vessels. The objective of this appendix is to provide insight into the features of the model that are not apparent from the discussions of the probabilistic results. Details of prediction methods for crack-tip stress intensity factors and fracture toughness are presented elsewhere in this report; only results of such predictions are provided in this appendix.

PRESSURIZED THERMAL SHOCK SCENARIO

The calculations used the following inputs:

Vessel Characteristics - The vessel parameters were selected to describe a hypothetical vessel consisting of plates, axial welds, and circumferential welds. The different materials showed a range of radiation-induced embrittlement. Through-wall cracks were postulated in specific beltline axial welds. Values of RT_{NDT} were calculated for all welds and plates in the vessel for an assumed maximum end of life fluence of 2.0×10^{19} n/m^2.

PTS Transient - The pressures and temperatures for the postulated transient shown in Figure A.1 were used in the calculations.

TRANSITION TO THROUGH-WALL CRACK

Typical scenarios of crack propagation prior to the occurrence of a through-wall crack are described in Appendix C. In one example, a postulated 1.0-in.-deep crack with a 6:1 aspect ratio initiates and arrests at 40 minutes into the transient, but does not become a through-wall crack. The crack then

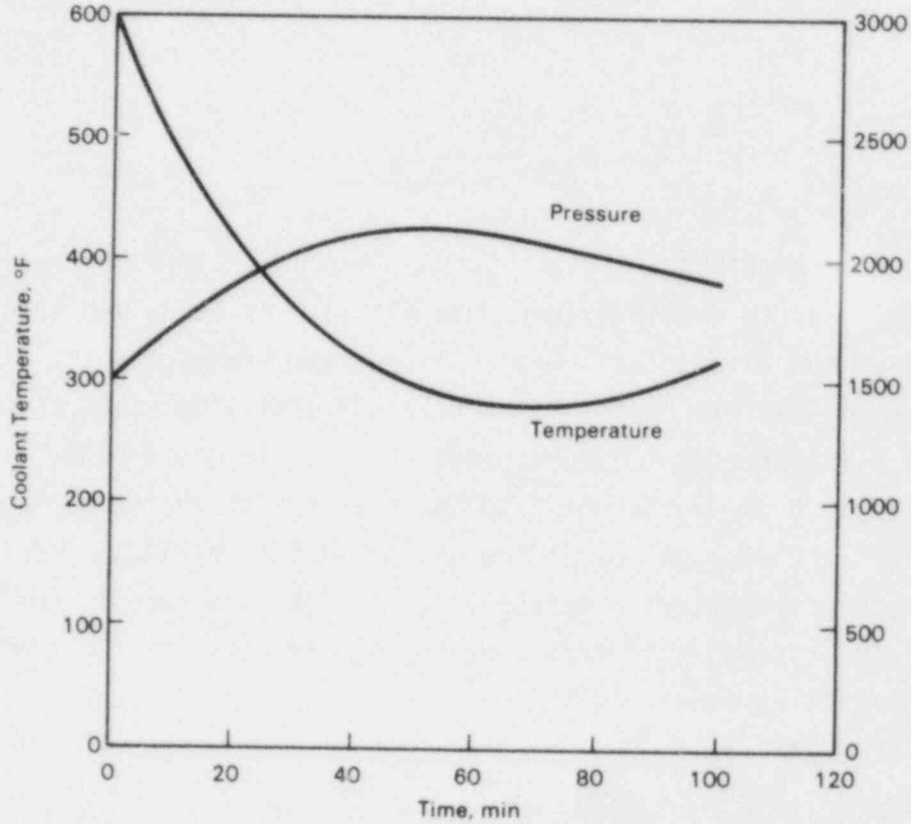

FIGURE A.1. Pressure and Temperature for Postulated Transient

reinitiates at 70 minutes and grows through the wall. The analyses in this appendix consider the growth of the through-wall crack at 70 minutes into the transient of Figure A.1.

At 70 minutes into the transient, the 6.0-in.-deep part-through flaw was assumed to become a through-wall crack of total length of 72 in. (i.e., the length of an axial weld). The pressure at 70 minutes is 2,060 psi. The method used to calculate the stress intensity factors is described in Appendix D. Table A.1 gives results for the part-through and through-wall cracks at 70 minutes.

The estimated fracture toughness values are for a copper content of 0.35%, a fluence of 2.0 x 10^{19} n/m^2, and an initial RT_{NDT} of 40°F. The upper shelf toughnesses (K_{Ic} and K_{Ia}) were estimated on the basis of Charpy

TABLE A.1. Comparison of Through-Wall and Part-Through Stress Intensity Factor - Total Crack Length = 72 in.

Crack Size	Applied K, ksi $\sqrt{in.}$	K_{Ic}, ksi $\sqrt{in.}$	K_{Ia}, ksi $\sqrt{in.}$
Part-Through Crack - 6.0 in. deep x 72 in. long			
At point of maximum depth	208	189	81
At inside surface location	151	38	31
Through-Wall Crack - 72 in. long			
Average values (averaged through the thickness of the vessel wall)	398	134	69

energies. The initial energies were first reduced to account for irradiation damage, and then correlations of J-resistance curves to Charpy energies were applied.

Table A.1 indicates that the surface value of applied K for the part-through flaw is 151 ksi $\sqrt{in.}$, which exceeds K_{Ic} = 38 ksi $\sqrt{in.}$ for the weld. No further lengthwise crack is predicted because the crack has already extended to the ends of the axial weld.

Table A.1 indicates that the applied value of K at the end of the crack more than doubles, once the crack grows through the wall. The applied K of 398 ksi $\sqrt{in.}$ greatly exceeds the through-thickness average initiation toughness of 134 ksi $\sqrt{in.}$ for the weld metal. Unstable crack growth would be predicted for the toughness levels calculated for the longitudinal weld, because the applied K for the through-wall crack exceeds even the assumed upper shelf toughness of the weld metal.

MAPS OF WELD CHARACTERISTICS

Figures A.2 through A.4 show the estimated values of chemistries and fluences, RT_{NDT} values (before and after irradiation), and upper shelf fracture toughness. Both welds and plate characteristics are indicated for an end of life fluence of 2.0×10^{19} n/m^2.

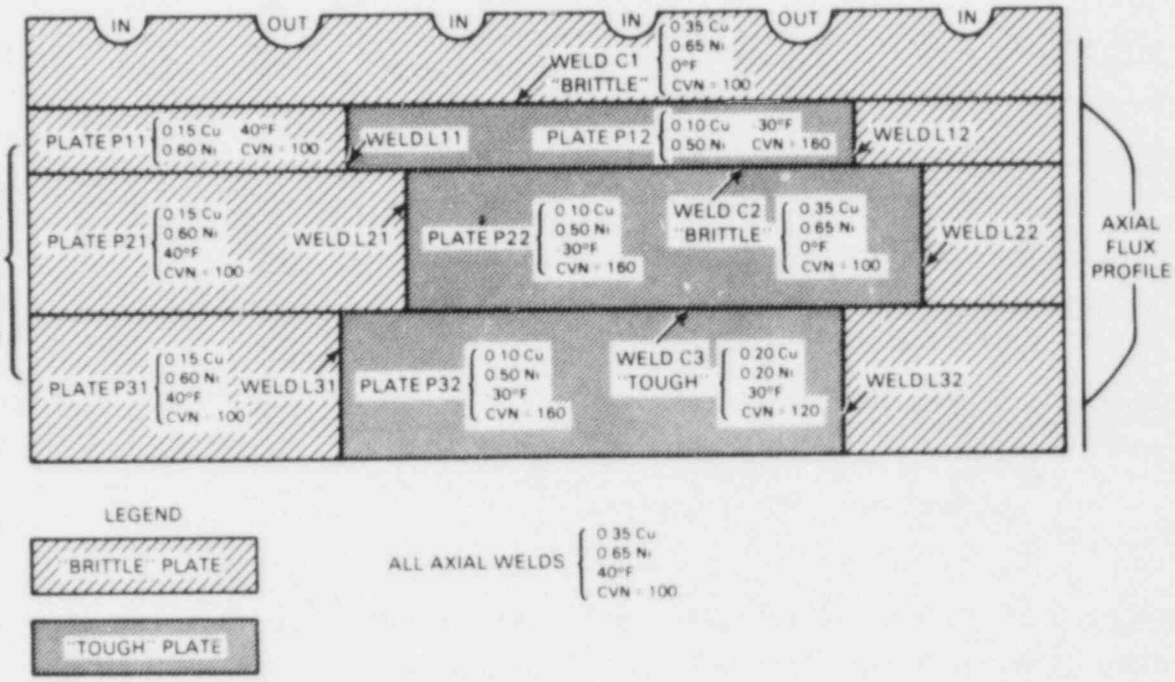

FIGURE A.2. Chemistry/Fluence Maps

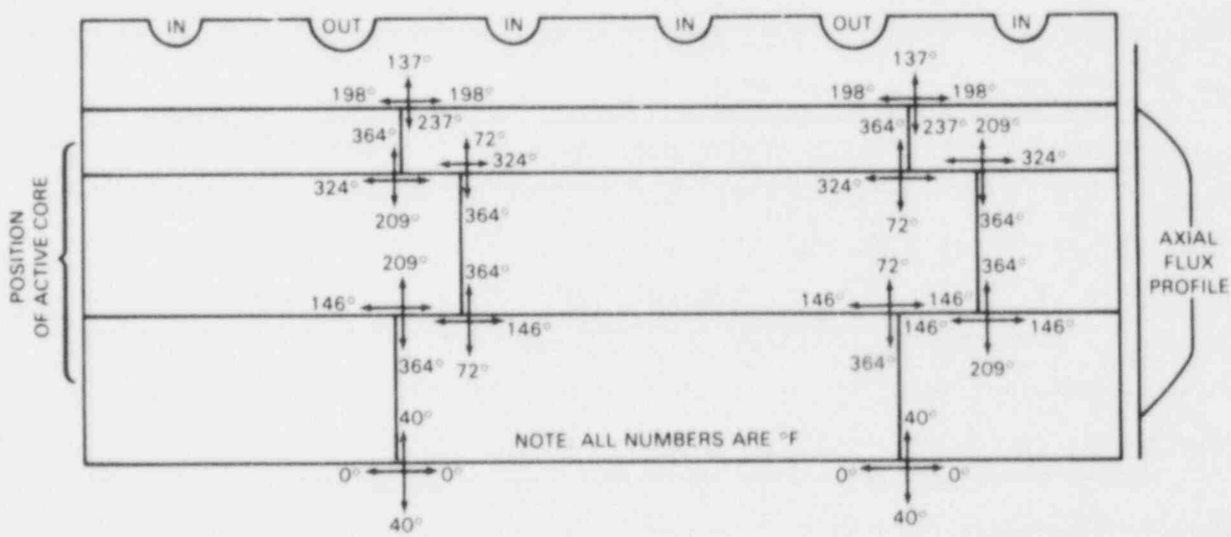

FIGURE A.3. RT_{NDT} for End-of-Life Fluence for Material at the Inner Surface of the Vessel

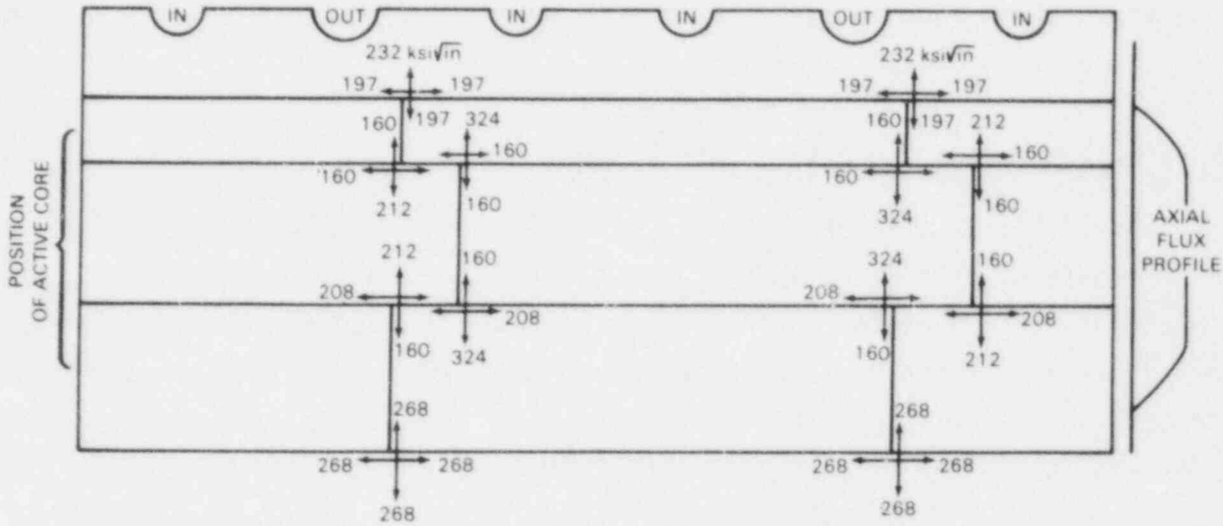

FIGURE A.4. Upper Shelf Toughness Map at End-of-Life Fluence for Material at the Inner Surface of Vessel

The axial fluence distribution is shown by the profile in the margin of Figure A.2. The circumferential fluence distribution was taken to be uniform.

As indicated in Figure A.2, the copper, nickel, and initial RT_{NDT} values for the plates were assigned such that plates P12, P22, and P32 were relatively "tough" compared to plates P11, P21, and P31. The embrittlement characteristics were selected to bound the data cited in this report for plate materials. In a similar manner, circumferential weld C3 was assigned material parameters to be characteristic of low embrittlement, whereas welds C1 and C2 were assigned parameters characteristic of high embrittlement. All axial welds were assigned the same material parameters so to be characteristic of relatively high embrittlement.

The critical locations for the prediction of crack propagation are the intersections of longitudinal and circumferential welds. At each of these locations, Figures A.3 and A.4 show arrows and associated property values that govern crack growth in the directions indicated by the arrows. Each point has a value for a longitudinal weld and two identical values for each of the two directions of crack propagation for the circumferential weld. The fourth direction corresponds to continued growth of the longitudinal crack into plate material above or below the axial weld.

FRACTURE EVALUATION FOR AXIAL CRACK IN WELD L21

The stability of a through-wall crack in an axial weld of the middle shell course of the vessel is considered. The initial crack length is 72 in., or the full length of the weld. A crack in weld L21 is positioned to extend into relatively tough plate material at both its upper and lower ends. It encounters a relatively brittle circumferential weld at its upper end, and a relatively tough circumferential weld at its lower end.

Axial Growth Into Plates P12 and P32

The governing stress intensity factors and thickness averaged toughnesses are:

- $K_{applied}$ (with bulging factor) = 409 ksi $\sqrt{in}$.
- $K_{applied}$ (without bulging factor) = 221 ksi $\sqrt{in}$.
- K_{Ic} = 339 ksi $\sqrt{in}$.
- K_{Ia} = 339 ksi $\sqrt{in}$.

Note that the thickness averaged toughness can and does exceed the upper shelf toughness at the inner surface of the vessel as indicated in Figure A.4. The crack is predicted to extend into the plate material whose toughness is on the upper shelf. Clearly the applied K without bulging factor is much less than the governing through-thickness mean value of arrest toughness (for plate material with RT_{NDT} = 72°F). It is predicted that rapidly propagating brittle fractures in weld L21 will arrest in the plate material. When the bulging factor and full initial pressure is considered, the applied K values exceed the estimated value of K_{Ic}. Therefore, reinitiation of crack growth is predicted.

Circumferential Growth Along Weld C2

The circumferential weld at the upper end of axial weld L21 has RT_{NDT} = 324°F at the vessel inner surface. The parameters for crack growth along this circumferential weld are:

- $K_{applied}$ (without bulging factor) = 110 ksi $\sqrt{in.}$
- K_{Ic} = 153 ksi $\sqrt{in.}$
- K_{Ia} = 105 ksi $\sqrt{in.}$

The model predicts that a running axial crack will change direction and will propagate along the circumferential weld, because $K_{applied}$ (110 ksi $\sqrt{in.}$) is greater than K_{Ia} (105 ksi $\sqrt{in.}$). However, the conditions for such growth are marginal.

Circumferential Growth Along Weld C3

For this weld with RT_{NDT} = 146°F at the inner surface, the parameters for crack growth are:

- $K_{applied}$ (without bulging factor) = 110 ksi $\sqrt{in.}$
- K_{Ic} = 226 ksi $\sqrt{in.}$
- K_{Ia} = 221 ksi $\sqrt{in.}$

It is predicted that the running axial crack will not change direction and will not propagate along the lower circumferential weld C3.

FRACTURE EVALUATION FOR AXIAL CRACK IN WELD L22

The stability of through-wall cracks in the other axial weld of the middle shell course of the vessel is considered. The initial crack length is 72 in., or the full length of the weld. A crack in weld L22 extends into relatively brittle plate material at both its upper and lower ends. It encounters a relatively brittle circumferential weld at its upper end, and a relatively tough circumferential weld at its lower end.

Axial Growth Into Plates P11 and P31

The governing stress intensity factors and the thickness averaged toughnesses are:

- $K_{applied}$ (with bulging factor) = 409 ksi $\sqrt{in.}$
- $K_{applied}$ (without bulging factor) = 221 ksi $\sqrt{in.}$
- K_{Ic} = 210 ksi $\sqrt{in.}$
- K_{Ia} = 187 ksi $\sqrt{in.}$

Clearly, the $K_{applied}$ value without bulging factor greatly exceeds the through-thickness mean value of arrest toughness (for the plate material with inner surface RT_{NDT} = 209°F). Continuation of crack growth into the adjacent plates is predicted.

<u>Circumferential Growth Along Welds C2 and C3</u>

The analysis of crack growth for weld L22 is the same as for weld L12. Although the conditions for growth are marginal, it is nevertheless predicted that the axial crack will change direction and propagate along circumferential weld C2. However, for the lower circumferential weld C3, it is predicted that the crack will not change direction and will not propagate down the weld.

<u>FRACTURE EVALUATION FOR AXIAL CRACKS IN WELDS L11 and L12</u>

The stability of a through-wall crack in the axial weld of upper shell course of the vessel is considered. The initial length of the crack is 18 in. or the full length of the weld in the relatively short shell course. Only calculations for weld L11 were performed. These results are conservative for weld L12 because a crack in weld L11 encounters lower toughness material than a corresponding crack in weld L12. At its upper end, the crack grows into only mildly irradiated material. At its lower end, the crack grows into the highly irradiated and embrittled material of plate P21 and circumferential weld C2.

<u>Axial Growth Into Plate P21</u>

The governing stress intensity factors and toughnesses for downward growth into the plate material with RT_{NDT} = 173°F are:

- $K_{applied}$ (with bulging factor) = 120 ksi $\sqrt{in.}$
- $K_{applied}$ (without bulging factor) = 109 ksi $\sqrt{in.}$
- K_{Ic} = 210 ksi $\sqrt{in.}$
- K_{Ia} = 187 ksi $\sqrt{in.}$

It is predicted that downward crack growth into the plate material of the middle shell course will arrest.

Circumferential Growth Along Weld C2

The circumferential weld at the lower end of weld L11 is highly irradiated and has a relatively high value of RT_{NDT} = 324°F. Parameters for growth along this circumferential weld are:

- $K_{applied}$ (without bulging factor) = 54 ksi $\sqrt{in.}$
- K_{Ic} = 153 ksi $\sqrt{in.}$
- K_{Ia} = 105 ksi $\sqrt{in.}$

No propagation of the axial crack along circumferential weld C2 is predicted. Circumferential crack growth will be arrested, because the arrest toughness of 105 ksi $\sqrt{in.}$ is greater than $K_{applied}$ of 54 ksi $\sqrt{in.}$

Axial Growth Into Nozzle Ring

The governing stress intensity factors and toughnesses for upward growth into the ring material with RT_{NDT} = 137°F are:

- $K_{applied}$ (with bulging factor) = 120 ksi $\sqrt{in.}$
- $K_{applied}$ (without bulging factor) = 109 ksi $\sqrt{in.}$
- K_{Ic} = 232 ksi $\sqrt{in.}$
- K_{Ia} = 323 ksi $\sqrt{in.}$

No upward crack growth into the ring is predicted, because $K_{applied}$ (109 ksi $\sqrt{in.}$) is less than K_{Ia} (232 ksi $\sqrt{in.}$). The crack will arrest as it grows into the ring material, which has little fluence expcsure.

Circumferential Growth Along Weld C1

The circumferential weld at the upper end of weld L11 has a relatively low value of RT_{NDT} = 198°F. Parameters for growth along this circumferential weld are:

- $K_{applied}$ (without bulging factor) = 54 ksi $\sqrt{in.}$
- K_{Ic} = 197 ksi $\sqrt{in.}$
- K_{Ia} = 197 ksi $\sqrt{in.}$

No growth along circumferential weld C1 is predicted.

FRACTURE EVALUATION FOR AXIAL CRACK IN WELD L31

The stability of a through-wall crack in the axial weld of the lower shell course is considered. The initial length of this axial crack is 50 in., which is less than the 72-in. length of the axial weld. Based on analyses in Appendix C, it was assumed that this through-wall crack extends two vessel wall thicknesses below the lower position of the high fluence region of the active core.

Axial Growth Into Plate P21

The governing stress intensity factors and toughness for upward growth into the plate of the middle shell course are:

- $K_{applied}$ (with bulging factor) = 273 ksi $\sqrt{in.}$
- $K_{applied}$ (without bulging factor) = 182 ksi $\sqrt{in.}$
- K_{Ic} = 210 ksi $\sqrt{in.}$
- K_{Ia} = 180 ksi $\sqrt{in.}$

The analysis predicts that the crack will grow upward into the plate of the middle shell course, because $K_{applied}$ is slightly greater than the estimated arrest toughness. However, a less conservative analysis for the effects of depressurization and of ductile crack extension might well predict arrest and subsequent stability of the crack.

Circumferential Growth Along Weld C3

The circumferential weld C3 at the upper end of axial weld L31 has an RT_{NDT} value of 146°F. Parameters for crack growth along this weld are:

- $K_{applied}$ (without bulging factor) = 91 ksi $\sqrt{in.}$
- K_{Ic} = 226 ksi $\sqrt{in.}$
- K_{Ia} = 221 ksi $\sqrt{in.}$

It is predicted that the axial crack will not turn and will not grow along circumferential weld C3.

Axial Growth Further Into Plate P31

The crack in weld L31 is initially assumed to extend less than the full length of the axial weld. For further extension downward along this weld, the governing parameters are:

- $K_{applied}$ (with bulging factor) = 273 ksi $\sqrt{in}$.
- $K_{applied}$ (without bulging factor) = 182 ksi $\sqrt{in}$.
- K_{Ic} = 275 ksi $\sqrt{in}$.
- K_{Ia} = 275 ksi $\sqrt{in}$.

Unirradiated values of upper shelf toughness are assumed for the very low fluence levels that are present at the lower end of the crack. No downward crack growth is predicted.

FRACTURE EVALUATIONS FOR AXIAL CRACK IN WELD L32

The analysis for weld L32 differs from the analysis for weld L31 in only one respect. Upward growth for weld L32 encounters relatively tough plate P22 rather than the lower toughness plate P21. For weld L32, it is predicted that the upward growth is arrested in plate P22.

REQUIRED RT_{NDT} DIFFERENCE TO ARREST CRACK

The above results suggest that axial cracks will not extend beyond the ends of a longitudinal weld if:

1. The longitudinal weld is sufficiently short.
2. RT_{NDT} of the adjacent plate and circumferential weld is much lower than RT_{NDT} of the longitudinal weld.

Calculations have been performed to estimate the required difference in RT_{NDT} for arrest of the growth of axial cracks of various lengths. These estimates are based on the parameters of the above exploratory calculations. The characteristics of the cracked axial weld are:

- time at which through-wall crack appears = 70 min
- inside vessel metal temperature at 70 min = 292°F
- copper content = 0.35%
- nickel content = 0.65%
- initial RT_{NDT} = 40°F
- fluence = 2.0×10^{19} n/m^2
- RT_{NDT} at inside surface = 364°F.

Toughness values for less severely embrittled plate and circumferential welds were calculated by assuming lower copper contents and/or lower values of initial RT_{NDT}. The important variable was the difference between the inside surface value of RT_{NDT} for the axial weld and that for the adjacent plate or weld material at the ends of the axial weld.

Figures A.5 and A.6 show the results of the crack arrest study. In Figure A.5, the value of K_{Ia} is shown as a function of RT_{NDT} of the plate (or circumferential weld) material. These toughness values were calculated as averages of the local toughness through the thickness of the vessel wall and are plotted in Figure A.5 as a function of RT_{NDT} at the inside surface of the vessel. Also shown are calculated $K_{applied}$ values for a range of lengths of through-wall axial cracks.

Figure A.6 shows the increment in RT_{NDT} that can prevent axial crack propagation into a circumferential weld. Also shown is the corresponding increment in RT_{NDT} to prevent further axial extension into adjacent plate material. These results assume that the internal pressure is relatively high (2000 psi) at the time that the through-wall crack occurs. For a 72-in.-long axial weld, a RT_{NDT} difference of about 70°F is required to prevent further axial extension.

Figure A.6 can be used in plant-specific analyses for preliminary evaluations of vessel failure modes. These curves can be used along with maps of RT_{NDT} to identify those axial welds for which crack arrest is likely. Detailed analyses can then focus on welds for which the arrest/propagate situation is in question.

INTERPRETATION OF RESULTS

Figure A.7 depicts the predicted crack growth scenarios. As indicated, cracks in longitudinal welds L21 and L22 will turn and grow into the circumferential weld C2. Furthermore, cracks in welds L21 and L22 will extend in the axial direction by growing into adjacent plate material. Axial cracks in the upper shell course will arrest at the ends of welds L11 and L12. No circumferential growth is predicted for cracks in the lower shell course

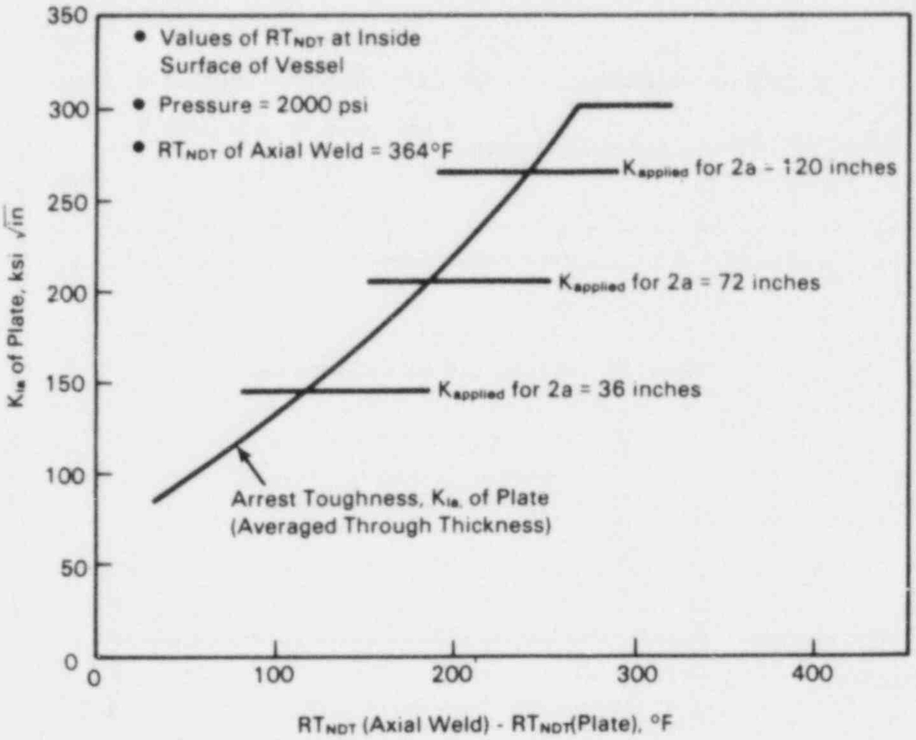

FIGURE A.5. Toughness Plot Used in Evaluation of Conditions for Arrest of Through-Wall Axial Cracks

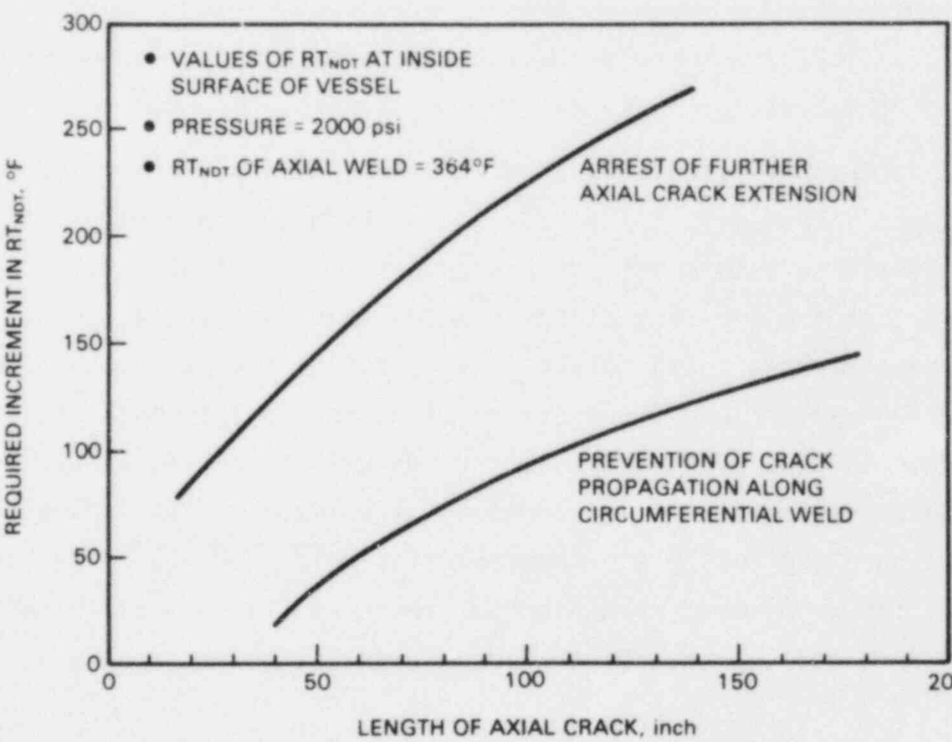

FIGURE A.6. Conditions for Arrest of Extension of Axial Through-Wall Cracks

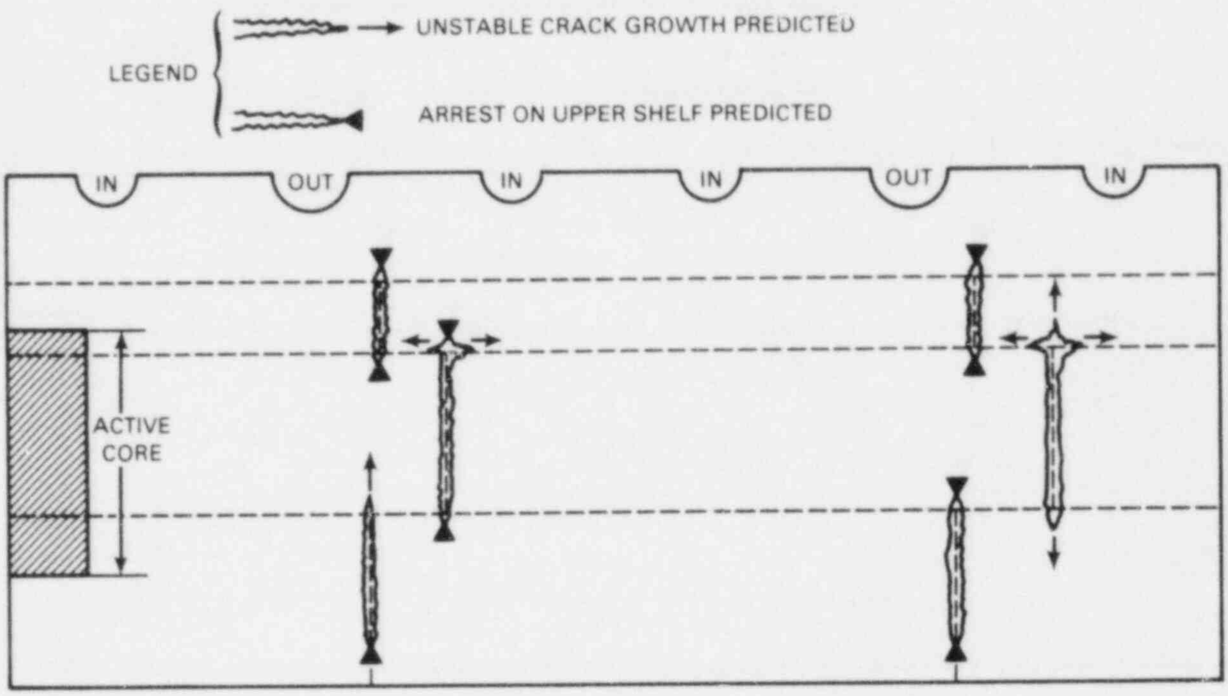

FIGURE A.7. Predicted Crack Growth Scenarios

(welds L31 and L32). However, upward axial growth is predicted into the plate material of the next shell course for one of these two welds.

The exploratory calculations for the hypothetical vessel and postulated transient are intended to illustrate the methodology, and results should not be extrapolated to assessments of plant-specific PTS risks. It should be emphasized that the severity of the cooling transient and amount of vessel embrittlement were selected to attain a condition that was capable of producing a through-wall crack. However, it is of interest to note that the illustrative calculations predicted that through-wall axial cracks can propagate beyond the ends of beltline axial welds. The results also indicate that axial cracks can turn and follow a circumferential weld. On the other hand, cracks in half of the welds were predicted to arrest at the ends of the welds, with no growth into adjacent plates or circumferential welds.

Probabilistic calculations, as described in the body of this report for a wider range of vessels and PTS transients, may predict more crack arrest events for the following reasons:

- In many transients, the pressure may be lower than 2000 psi at the time that the through-wall crack appears. The lower pressures will significantly reduce the $K_{applied}$ levels for the through-wall cracks.
- The probabilistic model will consider random variations in copper content, fluence, and fracture toughness. These variations are in addition to differences between the various welds and plates of a given vessel as treated in the current deterministic calculations. In this regard, a probabilistic analysis will usually predict through-wall cracks in the most embrittled of the welds with lower bound properties. Such a crack will most likely encounter material in adjacent plates and welds that will have RT_{NDT} and toughness levels that are more typical of the mean values of material property distributions. In contrast, the deterministic calculations as described in the appendix have assumed lower bound (or worst-case behavior) for all welds and plates in the vessel.

APPENDIX B

THERMAL STRESS FOR THROUGH-WALL CRACKS

APPENDIX B

THERMAL STRESS FOR THROUGH-WALL CRACKS

The fracture mechanics model for failure mode evaluations neglects thermal stresses relative to pressure stresses in the calculation of stress intensity factors for through-wall cracks. In this appendix, calculations for both pressure and thermal stress contributions to applied K are presented. The objective is to provide a basis for neglecting thermal stresses in the fracture mechanics evaluations of through-wall cracks.

EQUATIONS FOR STRESS INTENSITY FACTORS

Published solutions are available for through-wall axial cracks in cylindrical shells. In Rooke and Cartwright (1976), equations are presented in the following format:

Pressure Stress

$$\text{Inside surface, } K_I = (G_m - G_b)\, \sigma_m \sqrt{\pi a} \qquad \text{(B.1)}$$
$$\text{Outside surface, } K_I = (G_m + B_b)\, \sigma_m \sqrt{\pi a}$$

Thermal Stress

$$\text{Inside surface, } K_I = (G_m - G_b)\, \sigma_m \sqrt{\pi a}\, \left(\frac{1 + \nu}{3 + \nu}\right) \qquad \text{(B.2)}$$
$$\text{Outside surface, } K_I = (G_m + B_b)\, \sigma_m \sqrt{\pi a}\, \left(\frac{1 + \nu}{3 + \nu}\right)$$

where σ_m = membrane stress at the crack site in the uncracked vessel due to internal pressure

σ_b = thermal (bending) stress at the crack site in the uncracked vessel due to through-wall thermal gradients

ν = Poisson's ratio (0.3)

$2a$ = crack length

G_m and G_b = factors given in Rooke and Cartwright (1976) as a function of $a/\sqrt{Rt}$

R = mean radius of vessel (90 in.)

t = wall thickness (9 in.)

The thermal stress solution assumes that the stresses can be approximated by a linear variation of stress through the wall of the vessel. For times late into PTS transients, when through-wall cracking is most likely to occur, the linear variation is a reasonable approximation. However, for early times in the transient, the linear approximation is relatively inaccurate.

NUMERICAL EXAMPLE

The occurrence of a through-wall crack in a PTS event will often be associated with relatively high levels of pressure. Thermal stresses will have decreased somewhat from the high levels that occur earlier in the transient. Accordingly, the following conditions were selected for evaluation:

- pressure = 2000 psi
- thermal stress = 10 to 25 ksi
- typical length of through-wall crack = 80 in.

Tables B.1 and B.2 give values of stress intensity factors for the pressure and the thermal stresses. Values were calculated for the inner and outer surface locations. These results are plotted in Figures B.1 and B.2. Results for thermal stress levels ranging from 10 ksi to 25 ksi show the sensitivity of the predictions to the level of thermal stress. The 25-ksi

TABLE B.1. Stress Intensity Factors for Pressure Stress σ_m = 20,000 psi

Crack Length 2a, in.	$a/\sqrt{Rt}$	G_m	G_b	K_I Inside Surface, ksi $\sqrt{in.}$	K_I Outside Surface, ksi $\sqrt{in.}$
20	0.34	1.10	0.15	106	140
40	0.69	1.25	0.25	158	236
80	1.37	1.87	0.40	330	508
120	2.06	2.45	0.30	590	756
160	2.74	3.04	0.12	930	1008

TABLE B.2. Stress Intensity Factors for Pressure Stress σ_b = 10 ksi (Inner Surface)

Crack Length 2a, in.	$a/\sqrt{Rt}$	G_m	G_b	K_I Inside Surface, ksi $\sqrt{in.}$	K_I Outside Surface, ksi $\sqrt{in.}$
20	0.34	0.02	0.98	21	-22
40	0.69	0.04	0.96	29	-31
80	1.37	0.06	0.90	37	-42
120	2.06	0.08	0.84	41	-50
160	2.74	0.10	0.79	43	-55

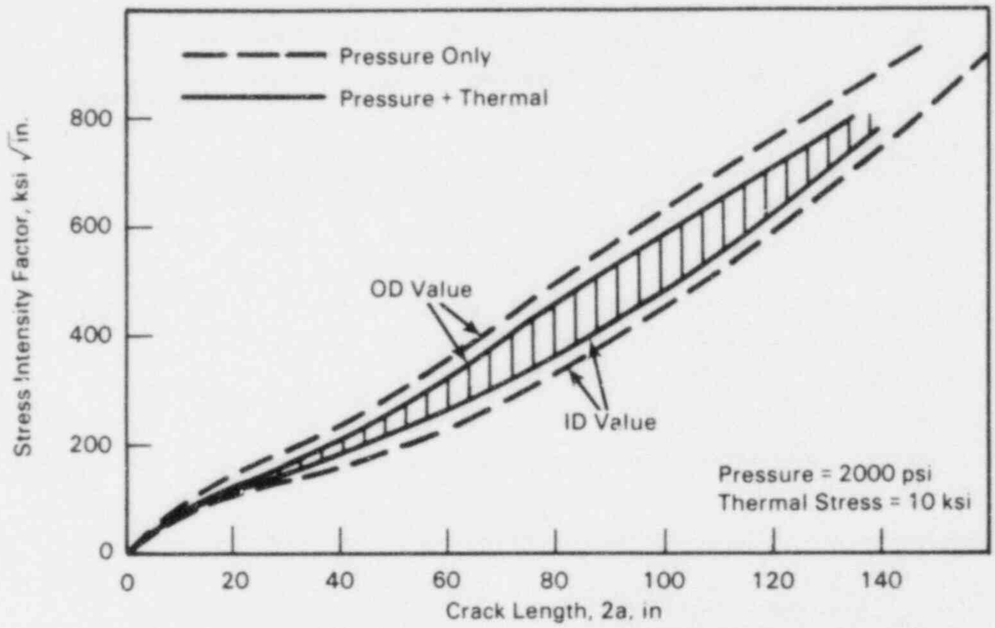

FIGURE B.1. Effect of Low Level (10-ksi) Thermal Stress on Calculated Stress Intensity Factors for Through-Wall Cracks

value is representative of the levels of stress that occur early in a PTS transient, whereas 10 ksi is representative of stress levels rather late in the transient.

The results show that the pressure loading produces a bending action. This action (bulging effect) gives a through-wall variation in the stress intensity factor that exceeds the corresponding through-wall variation due to the thermal stress. In fact, the addition of thermal stresses tends to give a

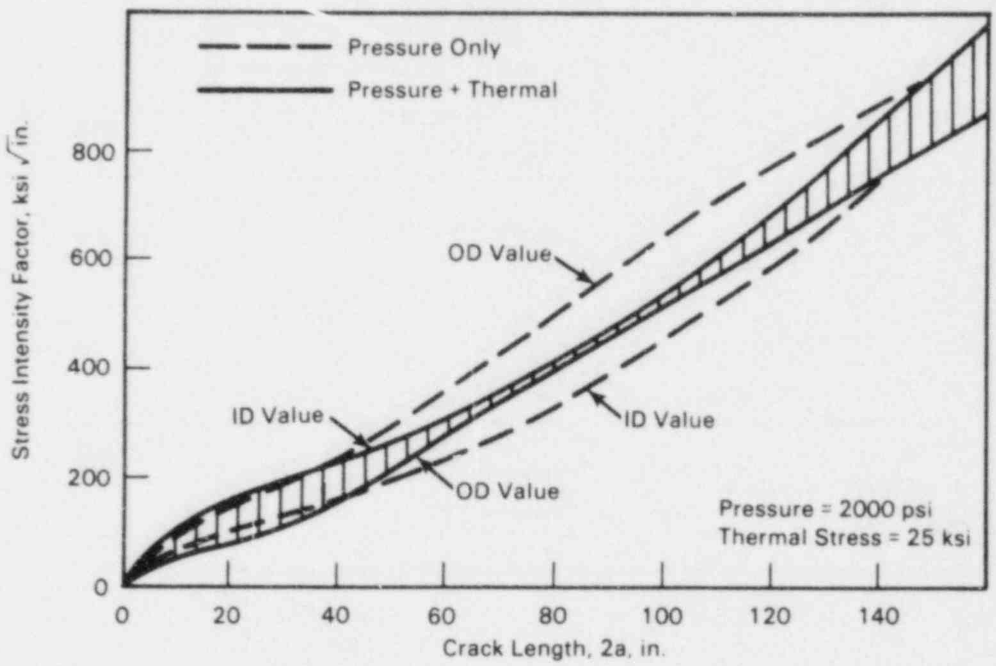

FIGURE B.2. Effect of High Level (25-ksi) Thermal Stress on Calculated Stress Intensity Factors for Through-Wall Cracks

more uniform value of stress intensity factor through thickness of the vessel wall.

RELATIONSHIP TO CRACK GROWTH CRITERIA

The fracture mechanics model of this report is based on calculations of stress intensity factors that neglect thermal stress and consider only pressure effects. In addition, this model uses a stress intensity factor for pressure stresses that is an average of the inside and outside surface values. The results of Figure B.1 indicate that this use of an average value is a particularly reasonable approach when the effects of thermal stresses are neglected. For a typical situation (as indicated by Figure B.1) the net thermal plus pressure value of stress intensity factor will be somewhat greater at the outer surface. In considering crack propagation criteria, this greater value of applied K at the outer surface will, in part, be offset by the fact that the materials fracture toughness is greater at the outside surface than at the inside surface (due to the lower fluences and higher temperatures at the outside surface of the vessel).

REFERENCE

Rooke, D. P., and D. J. Cartwright. 1976. Compendium of Stress Intensity Factors. Her Majesty's Stationary Office, London, United Kingdom.

APPENDIX C

GROWTH OF PART-THROUGH CRACKS

APPENDIX C

GROWTH OF PART-THROUGH CRACKS

The main objective of the failure mode analyses was to evaluate the stability and growth of through-wall cracks in reactor pressure vessels for the conditions of PTS events. This appendix describes other analyses of part-through cracks that predict the length of the crack at the time that it grows through the wall. The predictions supplement calculations performed at ORNL as part of the IPTS project for NRC (White 1984).

The ORNL fracture mechanics model predicts the growth of a surface flaw and stops once the crack has grown through the wall of the vessel. In the ORNL model, the length of an axial crack is assumed to be 2 m, which corresponds to the total length of an axial weld in a shell course of a typical PWR vessel. For circumferential welds, the assumed length of the through-wall crack in the ORNL model is the full circumference of the vessel.

This appendix describes analyses that predict the lengthwise growth of inside surface flaws for which the final crack length is not assumed a priori. The results provide a check on the ORNL assumption on crack length. In the current analyses, factors such as gradients in both neutron fluence and metal temperatures are considered. These gradients result in variations in fracture toughness that have the potential to arrest the lengthwise growth of surface flaws before they extend the full length of a weld.

CRACK GROWTH MODEL

The crack growth model was based on an extension of the VISA computer code (Stevens et al. 1983). The main additions to the code were a solution procedure for semi-elliptic surface flaws, provision to describe axial and circumferential fluence and temperature gradients, and a two-degree-of-freedom model (depth and length) for crack growth. The features of the deterministic fracture mechanics model are outlined as follows.

Heat Transfer - The VISA thermal analysis is used in its original form.

Stress Analysis - The VISA calculations of pressure and thermal stresses are used in their original form.

Cladding Effects - All effects of cladding on both applied stress intensity factor ($K_{applied}$) and fracture toughness are ignored in the crack propagation model.

Stress Intensity Factors - Stress intensity factors are calculated at the point of maximum flaw depth and at the ends of the elliptical flaw (where the flaw intersects the inside surface of the vessel). Correction factors are applied to the stress intensity factors calculated by VISA for two-dimensional long flaws. These correction factors are described in Appendix D. The factor for uniform membrane stress is applied to the pressure contribution to $K_{applied}$. For the $K_{applied}$ contribution due to thermal stress, the correction factor for linear bending stresses is applied. The factors as described in Appendix D were developed for axial surface flaws, but not for circumferential surface flaws. For the current calculations, the correction factors for axial flaws were also applied for circumferential cracks as a conservative approximation.

Shift in RT_{NDT} - The Randall-Guthrie 1982 equations (Dircks 1982) for irradiation induced shift in RT_{NDT} are applied with two standard deviations used to predict an upper bound on shift.

Fluence Gradients - Axial and circumferential gradients of surface levels of fluence are provided by the user as input. These gradients can be based on fluence maps for specific vessels. Through-wall attenuation of fluence is based on an exponential attenuation with a constant of 0.25 in.$^{-1}$.

Initial Crack Size - The depth and length of the initial surface crack is specified as a user input to the calculation. In these exploratory calculations, the initial crack depth was 1.0 in. and the crack length was 6.0 in. The initial location of the surface crack along the length of the weld is also user specified.

Temperature Gradients - User input specifies axial and circumferential variations of metal temperature at the inside surface of the vessel. These temperature variations are used only for calculations of fracture toughness. Thermal stresses are based on the solution for the nominal or unperturbed through-wall temperature gradients. In calculations of fracture toughness, temperatures at each location within the wall are increased or decreased by the specified perturbation in temperature at the inside surface.

Crack Growth Criteria - Stress intensity factors are calculated at the point of maximum crack depth and at the ends of the crack. These values are then compared with the local fracture toughness at each of the three locations. For the ends of the crack, the toughness is calculated at the inside surface of the vessel.

If the applied stress intensity factor is less than the initiation toughness (K_{Ic}), then no crack growth is predicted. If crack extension is predicted at more than one of the three locations, then only the location with the greatest ratio of $K_{applied}$ to K_{Ia} (arrest toughness) is allowed to extend. The extension at this location is continued until the extension criterion dictates that one of the other locations governs. The crack is extended in small increments in depth or length. At each step in the growth process, new values of $K_{applied}$ and crack-tip fracture toughness are calculated at each of the three locations.

The direction of continued crack growth or crack arrest is predicted for each small increment of crack growth. If arrest is predicted for both ends of the crack and at the point of maximum depth, then the simulation proceeds to the next time step in PTS transient.

The user may impose limits on the extent of lengthwise crack growth, and the crack growth is forced to stop at these positions regardless of the level of $K_{applied}$ compared to the material toughness. Such locations of imposed crack arrest can correspond to the ends of an axial weld.

Criteria for Through-Wall Crack - A through-wall crack is predicted if one of two alternate criteria are met. The first criterion is that the value of $K_{applied}$ exceeds the arrest toughness for a crack depth that is essentially the thickness of the vessel wall. The second criterion is based on plastic instability of the remaining ligament. Plastic instability is based on equations developed by Merkle for surface flaws of finite length (Johnson 1982).

Stability of Through-Wall Crack - The stability and growth of the predicted through-wall cracks are evaluated. The approach is essentially that for the probabilistic model for through-wall crack growth. Thermal stresses are neglected and fracture toughness values are averaged through the wall thicknesses. A strip yield model as described in Appendix G for axial cracks is used to calculate $K_{applied}$ values for internal pressure loadings.

AXIAL FLAW EXAMPLE CALCULATIONS

Two example calculations are reported here. In the first example, the initial flaw is in an axial weld within the beltline of a vessel with the fluence along this weld being essentially uniform. The second example considers a weld that extends below the position of the active core of the reactor, so that a significant decrease in fluence occurs over the lower portion of the weld.

Vessel and Transient Specifications

The following parameters describe the situation assumed for the axial weld calculations:

- vessel dimensions = 85 in. inner radius x 8.5 in. wall
- Rancho Seco transient (Figure C.1)
- no warm prestress
- copper content = 0.35%
- nickel content = 0.65%
- initial RT_{NDT} = 40°F
- upper shelf K_{Ic} and K_{Ia} = 300 ksi $\sqrt{in.}$
- peak surface fluence = 2.0×10^{19} n/m^2
- length of axial weld = 72 in.

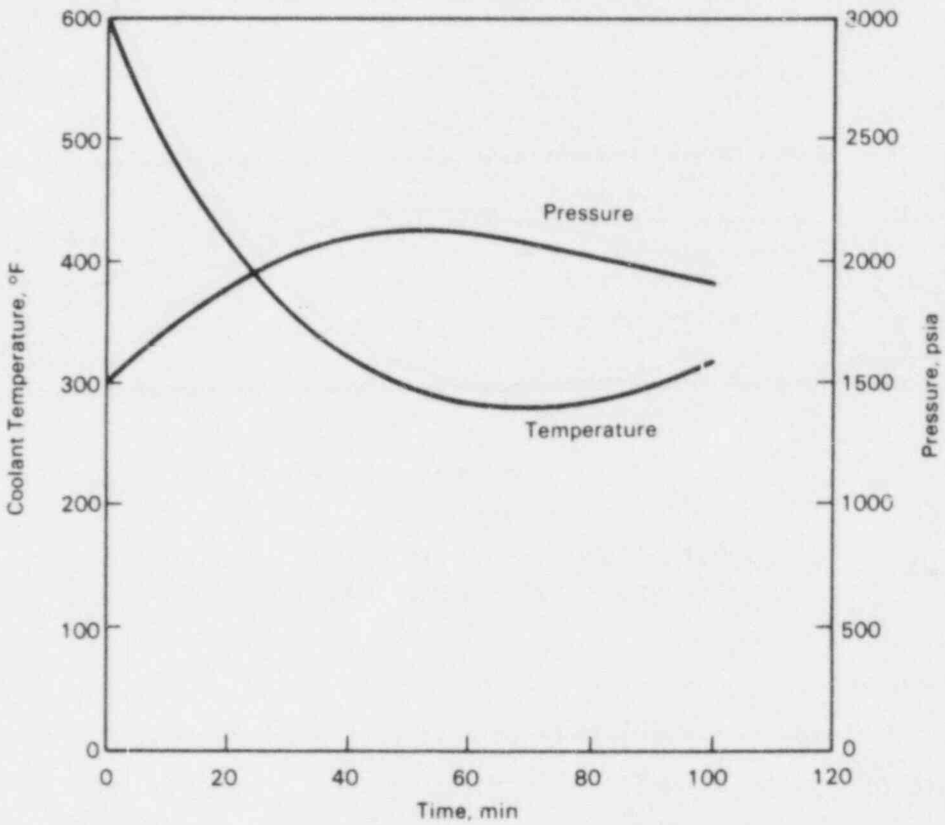

FIGURE C.1. Temperature and Pressure Transients for Rancho Seco Accident (1978)

The combination of the postulated transient and vessel characteristics was selected only to illustrate the analysis method. The results are not intended to apply to any specific operating reactor and vessel.

Axial Weld with Uniform Fluence

Figure C.2 shows the predicted growth of a semi-elliptical surface flaw in an axial weld for the situation of no axial variation in fluence and temperature. Crack growth initiates in the depthwise direction at 40 minutes into the transient. Dashed lines in Figure C.2 show successive positions of the crack front during propagation and prior to arrest. The crack also extends rapidly in length as it extends in depth. The final arrested crack at 40 minutes extends the full length of the axial weld and has a depth of about 70% of the wall thickness.

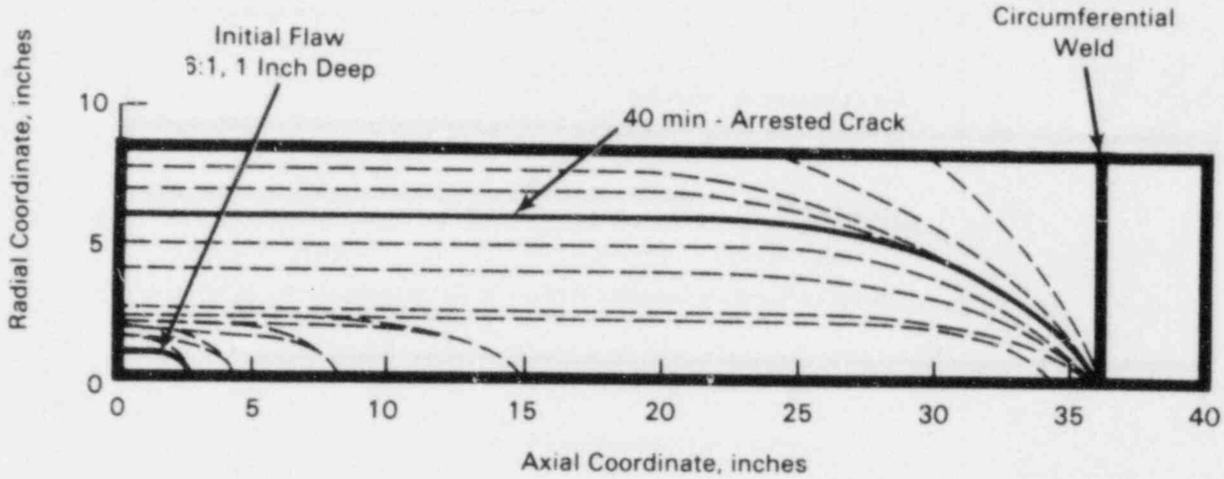

FIGURE C.2. Calculated Growth of Axial Crack for Conditions of Zero Axial Fluence Gradient

At 70 minutes, the crack growth initiates again. Then the crack grows completely through the vessel wall with a length of 72 in., which is equal to full length of the axial weld. The stress intensity factor was calculated for this through-wall crack. Dynamic effects and depressurization associated with formation of the through-wall crack were neglected. The applied value of K was 398 ksi $\sqrt{in.}$, which is greater than the assumed value of upper shelf fracture toughness (300 ksi $\sqrt{in.}$). Thus, crack extension beyond the ends of the axial weld, while probable, was not addressed in these calculations.

The predicted lengthwise crack growth behavior, as shown in Figure C.1, supports the assumptions used by ORNL in their fracture mechanics calculations for the IPTS project (White 1984). The ORNL model is, however, based on experimental observations and engineering judgment rather than detailed computations of crack growth as described here.

Axial Weld with Fluence Gradient

Figure C.3 shows the axial fluence gradient estimated for the Calvert Cliffs-1 reactor (Baltimore Gas and Electric 1982). This fluence gradient was used to calculate the crack growth scenario shown in Figure C.3. In this example, based on the Calvert Cliffs vessel design, the axial weld was 120 in.

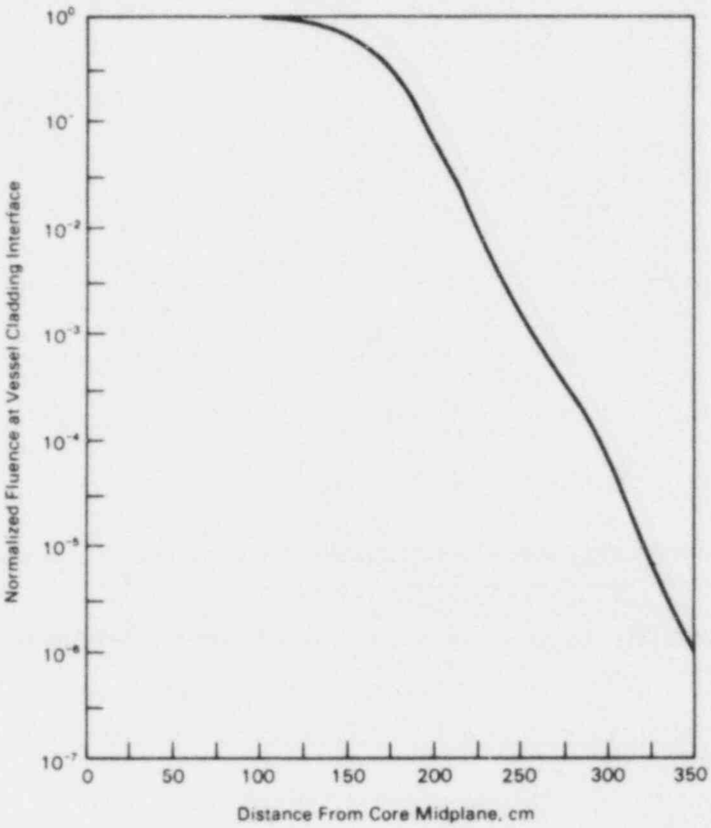

FIGURE C.3. Axial Fluence Variation

long and extended well below the lower position of the active core. Thus, an axial crack can grow out of the high fluence region of the vessel before it encounters the lower end of the axial weld.

As shown in Figure C.4, the crack growth initiates and then arrests at 40 minutes into the transient as it did for the previous case, which did not include an axial fluence gradient. However, the arrested length is less than the full length of the weld, and the depth is about 60% of the wall thickness as opposed to about 70% for the previous case. Crack growth initiates again at 70 minutes. After some lengthwise growth, the resulting length of the through-wall crack is about 70 in. The crack extends about two vessel wall thicknesses below the lower position of the active core. The total crack length is much less than the full length of the axial weld. The calculated applied K for the through-wall crack was 379 ksi $\sqrt{in.}$, and further extension

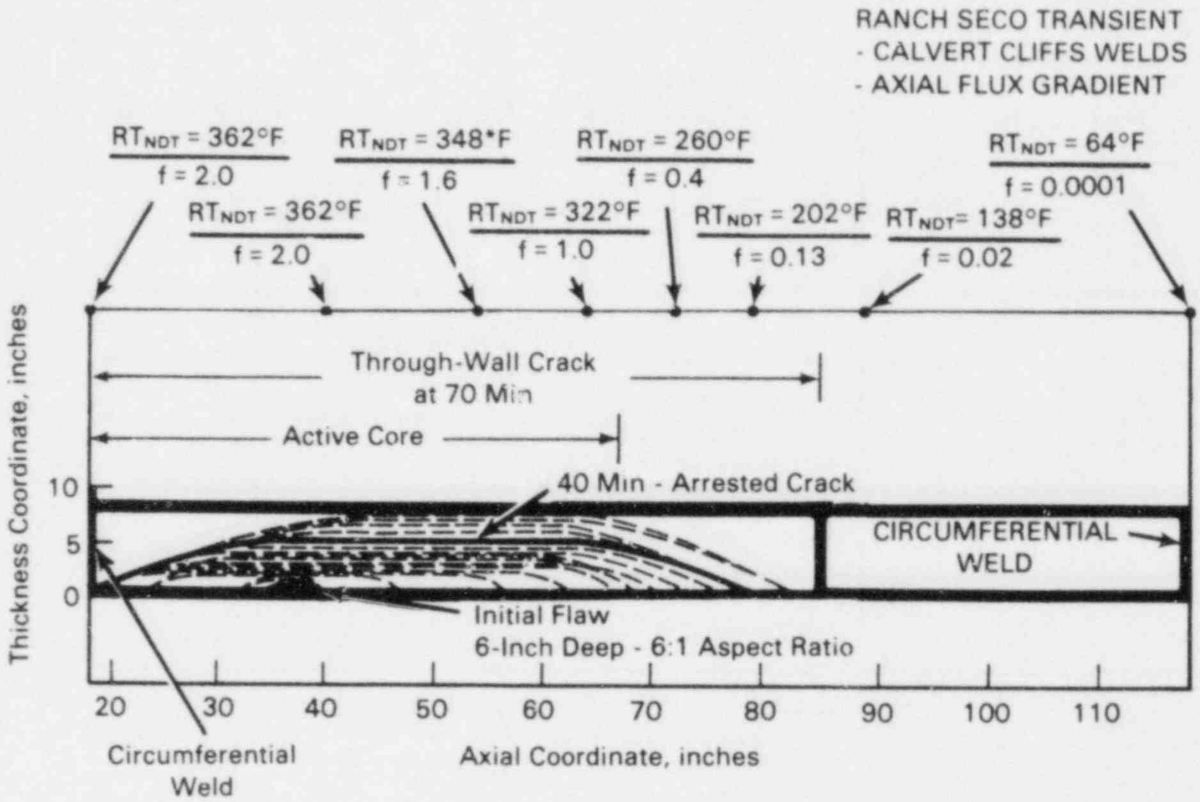

FIGURE C.4. Calculated Growth of Axial Crack for Condition of Axial Fluence Gradient

of the crack would be predicted because the assumed upper shelf level of fracture toughness is exceeded.

Other Analysis of Axial Cracks

A number of other analyses of crack growth were performed, and the results were similar to those shown by Figures C.2 and C.4. The axial gradient calculation was performed for lower peak fluences of 0.25×10^{19}, 0.5×10^{19}, and 1.0×10^{19} rather than 2.0×10^{19} n/m^2. For the 0.25×10^{19} and 0.5×10^{19} fluence values, no initiation of crack growth was predicted. For the 1.0×10^{19} fluence value, crack growth did not initiate until 70 minutes into the transient, but the crack then grew to become a through-wall crack with a length of 68 in.

The calculation of Figure C.3 was also performed with warm prestress assumed to be effective, and no initiation of crack growth was predicted.

CIRCUMFERENTIAL FLAW EXAMPLE CALCULATIONS

In these predictions of circumferential flaw growth, the impact of circumferential variations in both fluence and metal temperatures was evaluated. The objective was to establish the level of such variations that would be required to arrest the lengthwise growth of a surface flaw before it extended around the full 360 degrees of a circumferential weld.

Vessel and Transient Specification

The following parameters describe the situation assumed for the circumferential weld calculations:

- vessel dimensions = 85 in. inner radius x 8.5 in. wall
- Rancho Seco transient (Figure C.1)
- no warm prestress
- copper content = 0.35%
- nickel content = 0.65%
- initial RT_{NDT} = 65°F
- upper shelf K_{Ic} and K_{Ia} = 300 ksi $\sqrt{in.}$
- peak surface fluence = 2.0×10^{19} n/m^2.

The value of initial RT_{NDT} was increased to 65°F from the 40°F value of the axial weld calculations in order to achieve initiation of crack growth for the lower stresses of the circumferential weld.

The aximuthal fluence variation of Figure C.5 was used in all calculations. The variation was based on data for the Calvert Cliffs reactor (Baltimore Gas and Electric 1982). Fluence values decrease to about 50% of peak values over an angle of about 20 degrees. In all the calculations, the initial flaw was assumed to be located at the point of peak fluence in order to address conditions most likely to result in the arrest of lengthwise crack growth.

Also shown by Figure C.5 are three assumed conditions of circumferential temperature variations. To enhance the opportunity for lengthwise crack

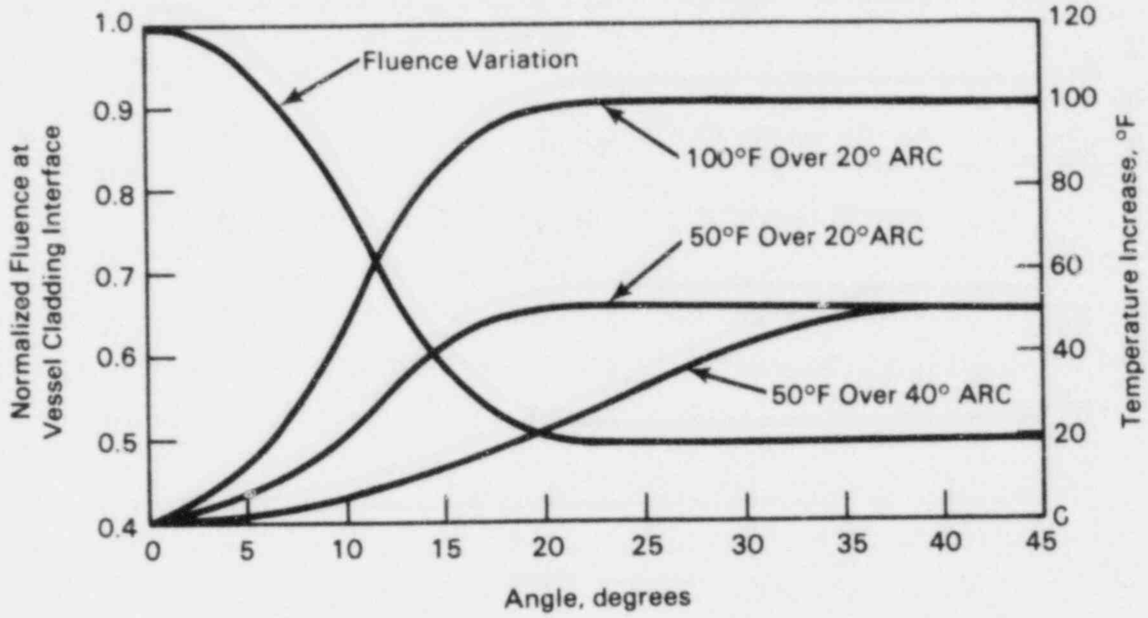

FIGURE C.5. Aximuthal Fluence and Temperature Variations

arrest, the location of minimum inner wall temperature was taken to coincide with the location of the flaw. The temperature was assumed to increase at circumferential positions away from the initial flaw location. The resulting increase in fracture toughness contributed to the possible arrest of lengthwise crack growth.

Predictions of possible circumferential temperature gradients during PTS events were not available for the calculations. However, the curve in Figure C.5 labeled "50°F over a 40-degree arc" is believed to be as great a temperature variation as can be expected. Sources of this temperature variation could be a lack of complete mixing in the downcomer or asymmetric flows in different loops of the primary system. The other cases labeled "50°F over a 20-degree arc" and "100°F over a 20-degree arc" are believed to be unrealistic, but were used as bounding conditions for purposes of the sensitivity calculations.

Circumferential Weld with Fluence and Temperature Gradients

Figures C.6 through C.10 show the results of calculations to study the sensitivity of crack growth to circumferential gradients in fluence and

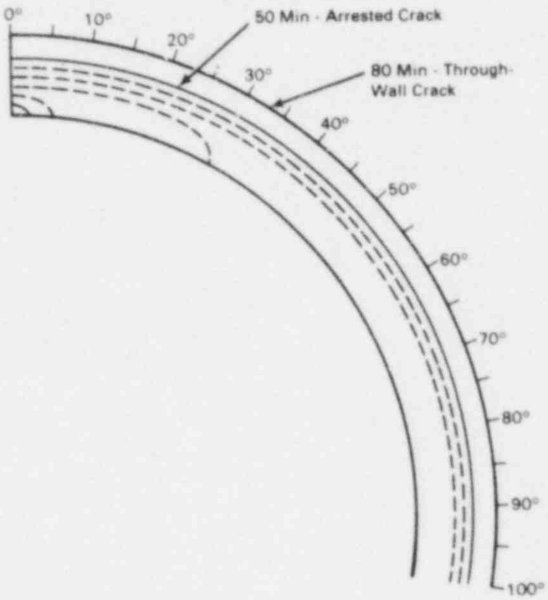

FIGURE C.6. Calculated Growth of Circumferential Crack - No Circumferential Gradients in Fluence or Temperature

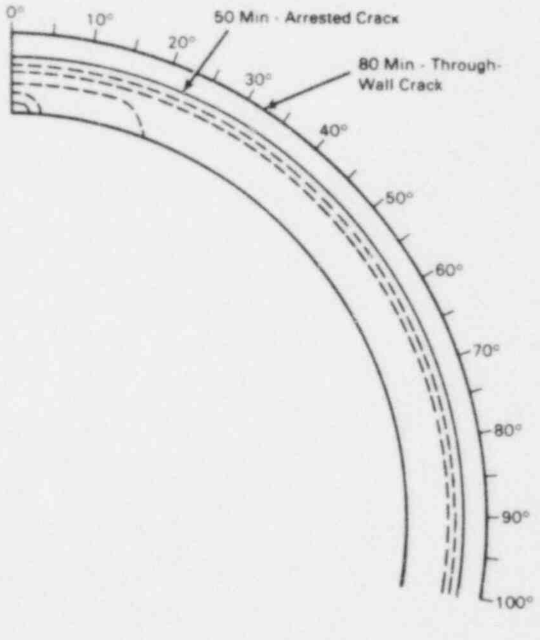

FIGURE C.7. Calculated Growth of Circumferential Crack - Circumferential Gradient in Fluence But Not Temperature

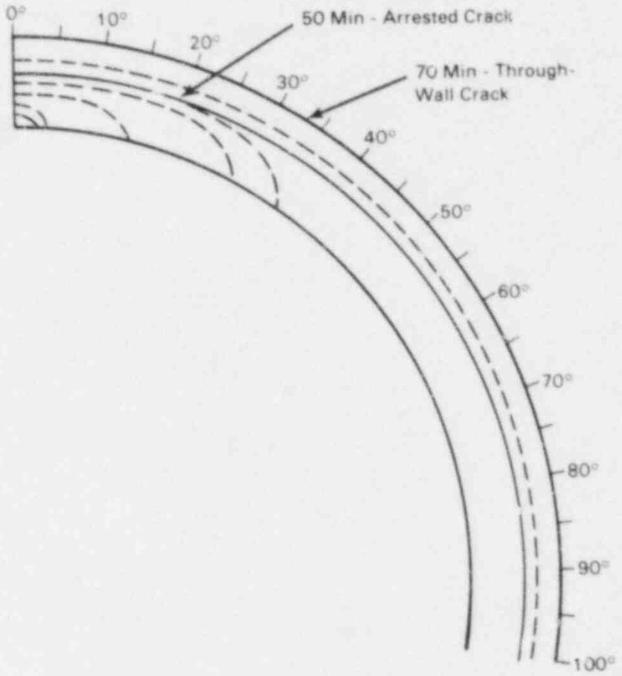

FIGURE C.8. Calculated Growth of Circumferential Crack - Circumferential Gradient in Fluence and Temperature (50°F over 40° Arc)

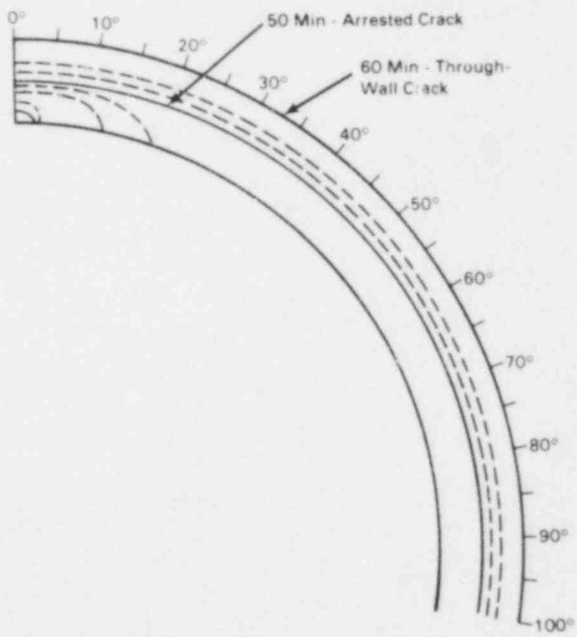

FIGURE C.9. Calculated Growth of Circumferential Crack - Circumferential Gradient in Fluence and Temperature (50°F over 20° Arc)

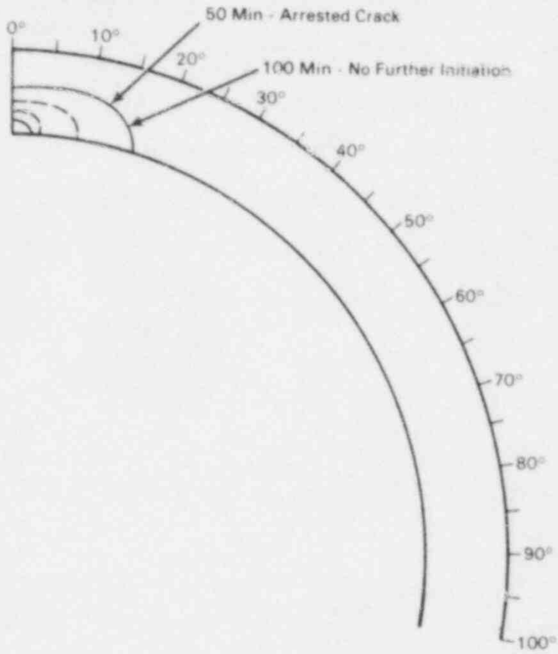

FIGURE C.10. Calculated Growth of Circumferential Crack - Circumferential Gradient in Fluence and Temperature (100°F over 20° Arc)

temperature. The results show that circumferential cracks will grow in length around the entire circumference of the weld, even in the presence of bounding estimates of fluence and temperature gradients. Although the gradients did affect the sequence and pattern of growth, none of the calculations predicted a through-wall crack before the crack had extended lengthwise around the entire weld.

Figure C.6 shows the predicted crack growth when neither fluence nor temperature gradients are present. The initiation of the crack growth occurs at 50 seconds into the transient and arrests with a 360-degree circumferential crack at a depth of 70% of the wall. The growth initiates again at 80 minutes and the crack then grows through the wall. The dashed lines show that the growth at 50 minutes into the transient proceeds simultaneously in both the depthwise and lengthwise directions. However, the circumferential growth eventually becomes uncontrolled and leads to a 360-degree circumferential crack.

The case of Figure C.10 shows that an extreme circumferential thermal gradient can give a prediction of arrest with a resulting crack length that is much less than the full circumference of the vessel. However, the crack also arrests in this depthwise growth, and no through-wall crack is predicted. Therefore, these sensitivity calculations have failed to identify a scenario that can give a through-wall circumferential crack that is less than the full circumference of the vessel in length.

REFERENCES

Baltimore Gas and Electric. 1982. "Calvert Cliffs Nuclear Power Plant Unit 1, Licensee 150-Day Response to NRC," dated January 28, 1982. Baltimore, Maryland.

Dircks, J. W. 1982. "Enclosure A: NRC Staff Evaluation of Pressurized Thermal Shock, November 1982." SECY-82-465, Division of Nuclear Reactor Regulation, U.S. Nuclear Regulatory Commission, Washington, D.C.

Johnson, R. 1982. Resolution of the Task A-11 Reactor Materials Toughness Safety Issue. NUREG-0744, U.S. Nuclear Regulatory Commission, Washington, D.C.

Stevens, D. L., F. A. Simonen, J. Strosnider, Jr., R. W. Klecker, D. W. Engel, and K. I. Johnson. 1983. VISA - A Computer Code for Predicting the Probability of Reactor Pressure Vessel Failure. NUREG/CR-3385, U.S. Nuclear Regulatory Commission, Washington, D.C.

White, J. D. 1984. "Results of PTS Probabilistic Analysis Based on Oconee, Calvert Cliffs and H. B. Robinson." In Proceedings of the Twelfth Water Reactor Safety Research Information Meeting, NUREG/CP-0057, U.S. Nuclear Regulatory Commission, Washington, D.C.

APPENDIX D

SOLUTIONS FOR FINITE LENGTH AXIAL FLAWS

APPENDIX D

SOLUTIONS FOR FINITE LENGTH AXIAL FLAWS

This appendix describes how the computer code VISA (Stevens et al. 1983) has been modified to calculate crack-tip stress intensity factors for semi-elliptical axial surface flaws of finite length. These modified solutions are used in Appendix C to predict the lengthwise growth of both axial and circumferential surface flaws under PTS conditions. The objective of these detailed calculations was to better establish the initial lengths of the through-wall cracks that are of concern to the vessel failure mode evaluations of this report.

The computer code VISA utilizes an influence function approach to calculate stress intensity factors for "long" flaws at the ID surface of the vessel. Both the actual cylindrical geometry of the vessel and the nonlinear variation of stress through the vessel wall are treated. However, flaws of finite length (e.g., semi-elliptical surface flaws) are not treated. For these cases, a method has been developed to modify solutions for the long flaws to account for finite length effects. This method uses an approach similar to that given in Appendix A of Section XI of the ASME Code (ASME 1983).

A compilation of solutions by Yukawa (1982) provided the basis for correction factors corresponding to situations of a uniform stress and a linear gradient of stress through the vessel wall. Figures D.1 through D.4 show the correction factors. In the calculations of Appendix C, the factor for uniform membrane stress was applied to the pressure-induced stress intensity factor from VISA. The linear gradient factor was applied to the stress intensity factor corresponding to thermal stresses. Results for this approximate method are compared in Figures D.5 through D.8 to more exact results that were based on influence functions for the 6:1 flaw. The agreement is within 10 percent, which is adequate for the purpose of the calculations of Appendix C.

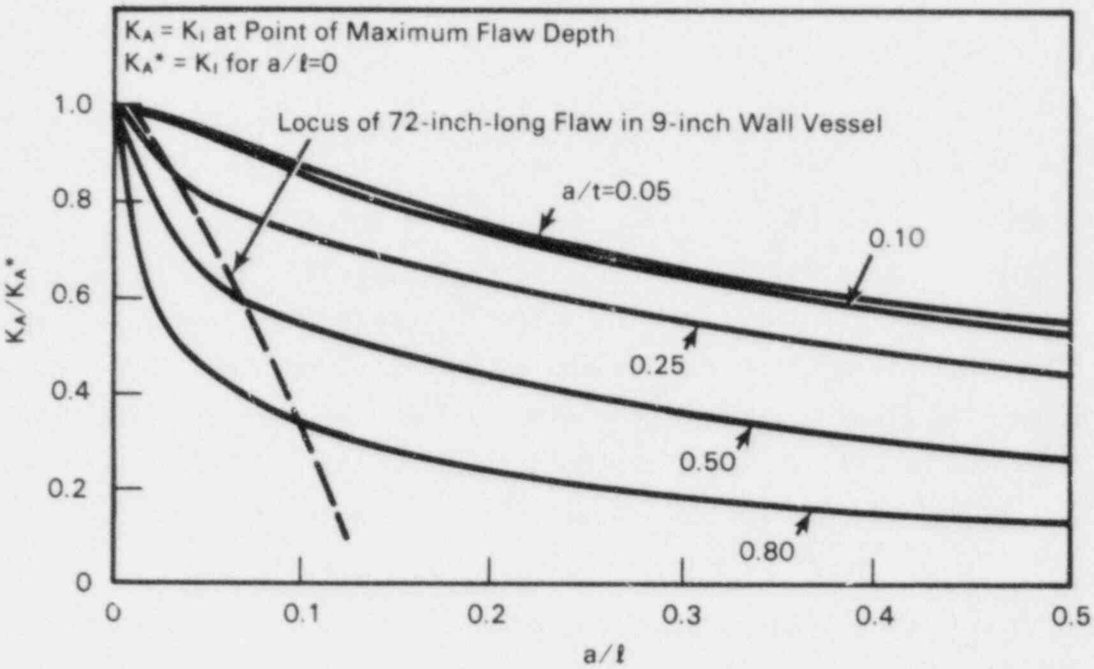

FIGURE D.1. Factor for K_A for Uniform Membrane Stress

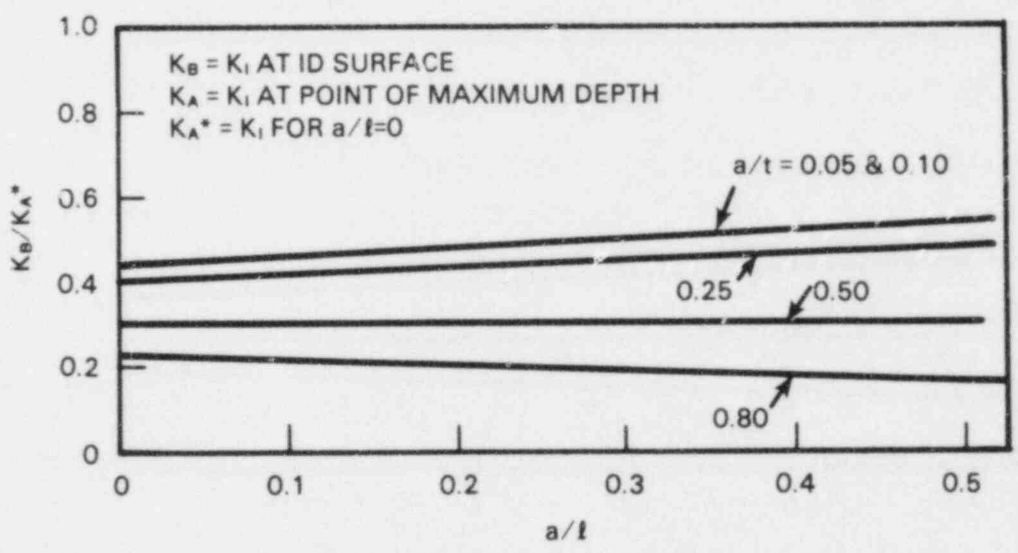

FIGURE D.2. Factor for K_B for Uniform Membrane Stress

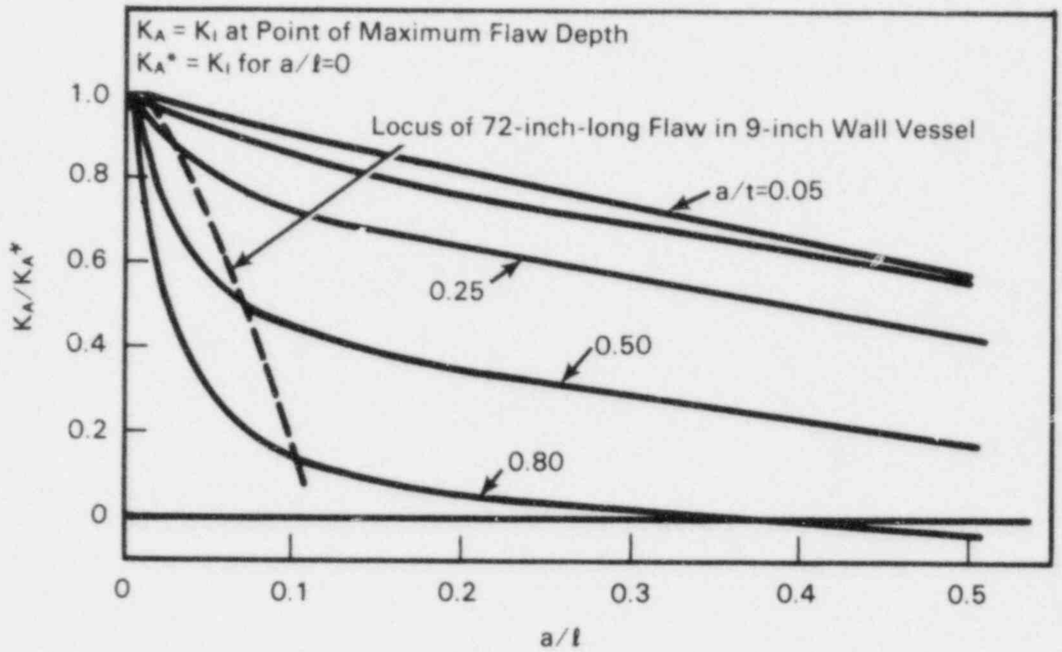

FIGURE D.3. Factor for K_A for Linear Bending Stress

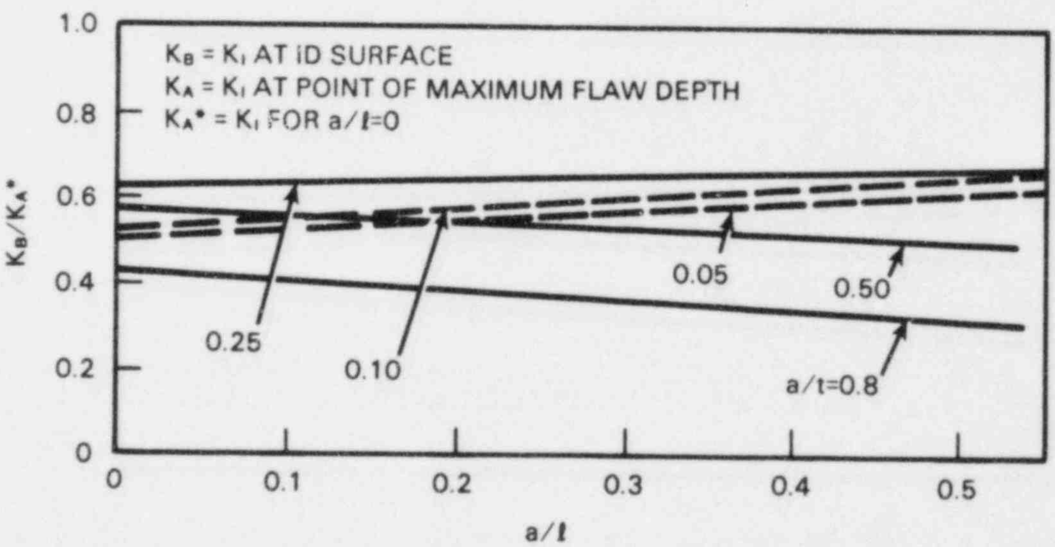

FIGURE D.4. Factor for K_B for Linear Bending Stress

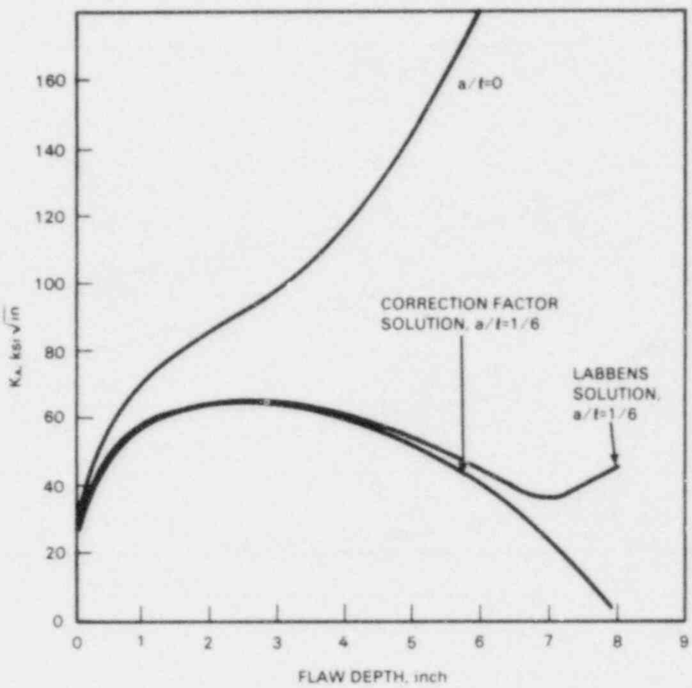

FIGURE D.5. Thermal Component of K_A at Time = 38.4 of Rancho Seco Transient

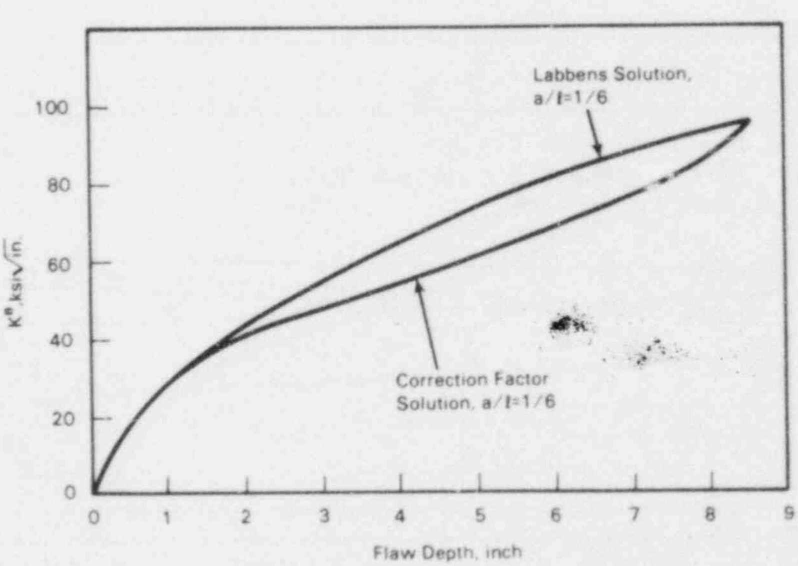

FIGURE D.6. Thermal Component of K_A at Time = 38.4 of Rancho Seco Transient

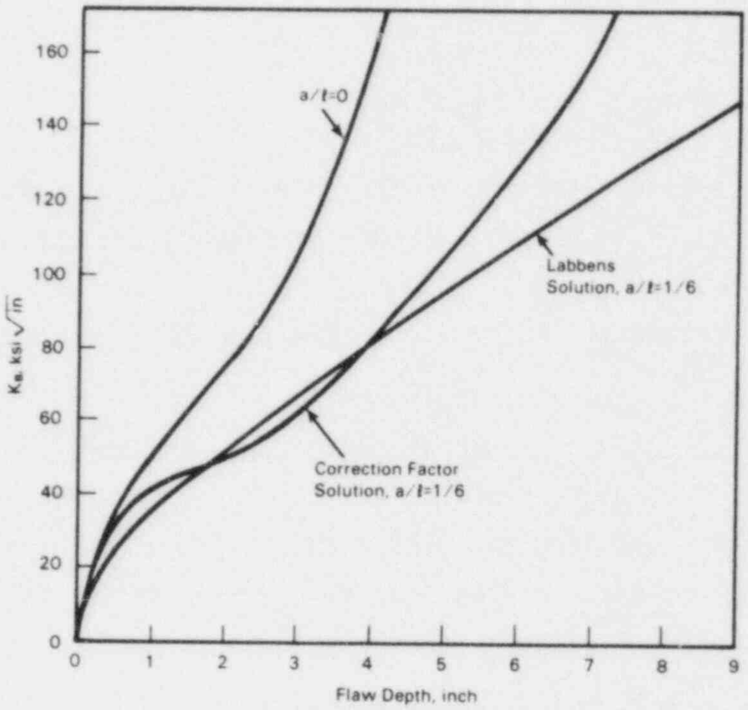

FIGURE D.7. Thermal Component of K_A at Time = 38.4 of Rancho Seco Transient

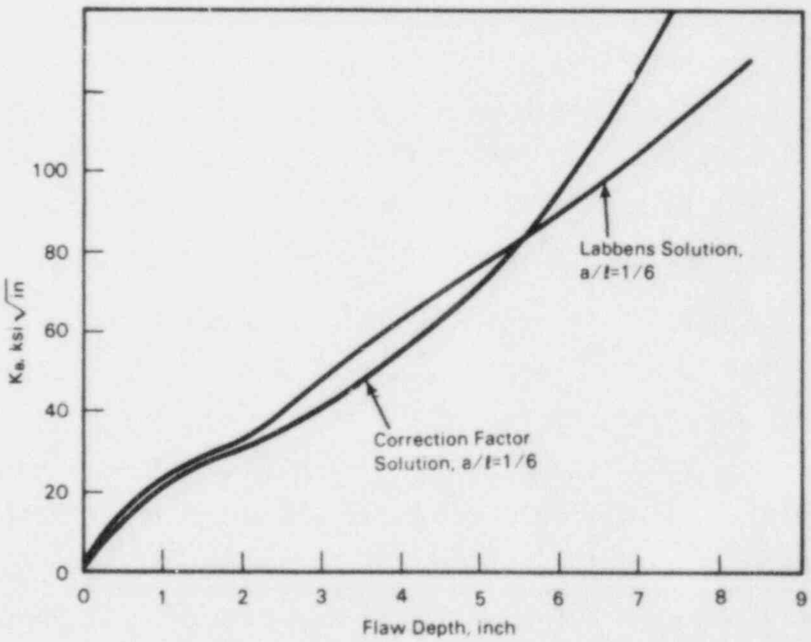

FIGURE D.8. Thermal Component of K_A at Time = 38.4 of Rancho Seco Transient

In Figures D.1 through D.4, the following definitions apply:

- a = flaw depth
- ℓ = flaw length
- t = wall thickness of vessel
- K_A = stress intensity factor at the point of maximum flaw depth
- K_B = stress intensity factor at ends of flaw (i.e., inside surface location)
- K_A^* = stress intensity factor for a flaw of depth = a, but of infinite length.

In Figures D.1 and D.2, a dashed curve shows the locus of points that corresponds to a 72-in.-long crack in a 9-in.-thick vessel wall. This represents a crack whose length is the total length of an axial weld. Thus, the region below this curve corresponds to cracks outside the range of interest to the current vessel integrity analyses.

The very deep cracks show a substantial reduction in K_A values as the cracks become shorter ($a/\ell \rightarrow 0.5$). In contrast, the factors for K_B are insensitive to flaw length, as seen in Figures D.2 and D.4.

The curves of Figures D.1 through D.4 were constructed by fitting data points from published numerical solutions for specific flaw geometries. The sources of these solutions were Newman and Raju (1980, 1981); Heliot, Labbens, and Pellisier-Tanon (1980); Labbens, Pellisier-Tannon, and Heliot (1976, p. 368); and McGowan and Raymund (1979, p. 365). The fitted curves were then programmed for bivariant interpolation relative to a/t and a/ℓ.

As seen in Figures D.5 through D.8, the agreement between the correction factor approach and the more exact calculation for the $a/\ell = 1/6$ geometry is quite good. This comparison is for an analysis of the Rancho Seco transient (Cheverton, Iskander, and Whitman 1982) for a time about 40 minutes into the transient. This time is particularly critical because crack initiation is most likely to occur at about 40 minutes. The accuracy of the correction factor solutions at earlier times is not nearly as good. At these times, the stress variation through the wall of the vessel is poorly approximated by a linear fit. However, errors in calculated stress intensity factors are not critical at these early times because the initiation of crack growth is unlikely.

REFERENCES

American Society of Mechanical Engineers. 1983. Rules for Inservice Inspection of Nuclear Power Plant Components. Section XI of ASME Boiler and Pressure Vessel Code. New York, New York.

Cheverton, R. D., S. K. Iskander, and G. D. Whitman. 1982. "The Integrity of PWR Pressure Vessels During Overcooling Accidents." In Proceedings of the International Meeting on Thermal Reactor Safety, pp. 421-430, NUREG/CP-0027, Vol. 1, U.S. Nuclear Regulatory Commission, Washington, D.C.

Heliot, J., R. Labbens, and A. Pellisier-Tanon. 1980. "Application of Boundary Integral Equation Method to Three-Dimensional Crack Problems." ASME Paper 80-C2/PVP-119, American Society of Mechanical Engineers, New York, New York.

Labbens, R., A. Pellisier-Tanon, and J. Heliot. 1976. Practical Method for Calculating Stress Intensity Factors Through Weight Functions. ASTM STP 590, American Society for Testing and Materials, Philadelphia, Pennsylvania.

McGowan, J. J., and M. Raymund. 1979. Stress Intensity Factor Solutions for Internal Longitudinal Semi-Elliptical Surface Flaws in a Cylinder Under Arbitrary Loadings. ASTM STP 677, American Society for Testing and Materials, Philadelphia, Pennsylvania.

Newman, J. C., Jr., and I. S. Raju. 1981. "An Empirical Stress Intensity Factor Equation for the Surface Crack." Eng. Fracture Mechanics. 15:185.

Newman, J. C., Jr., and I. S. Raju. 1980. "Stress Intensity Factors for Internal Surface Cracks in Cylindrical Pressure Vessels." Journal of Pressure Vessel Technology. 102:342.

Stevens, D. L., F. A. Simonen, J. Strosnider, R. W. Klecker, D. W. Engel, and K. I. Johnson. 1983. VISA - A Computer Code for Predicting the Probability of Reactor Vessel Failure. NUREG/CR-3384, U.S. Nuclear Regulatory Commission, Washington, D.C.

Yukawa, S. 1982. "Summary of Surface Flaw K Solutions." Prepared for Working Group on Flaw Evaluation, ASME Boiler and Pressure Vessel Code - Section XI, San Diego, California.

APPENDIX E

CRACK GROWTH MODEL

APPENDIX E

CRACK GROWTH MODEL

This appendix presents the methods and criteria that were used to predict the initiation and arrest of through-wall cracks in pressure vessels. Topics include predictions of arrest at and near the upper shelf temperature range and the prediction of J-resistance curves on the basis of Charpy V-notch (CVN) data. Predictions of fluence attenuation through the wall of the vessel are described. The method for calculating an average fracture toughness through the thickness of the vessel wall is documented. Equations for calculating fracture toughness as a function of temperature in the transition temperature range are given. This appendix also covers the scheme for simulating the variability in fracture toughness. A final topic is the use of the Irwin beta factor to predict the effect of specimen thickness on fracture resistance.

INITIATION AND ARREST CRITERIA

Initiation and arrest predictions for this report are made by calculating values of stress intensity factors using the methods of Appendices D and G, and then comparing these values with the fracture toughness values as calculated by the methods described in this appendix. However, it should be noted that there are some differences in the procedure for the part-through crack analyses of Appendix C in comparison to the procedure described here for through-wall cracks.

It must be emphasized that the level of understanding of dynamic crack propagation and arrest behavior continues to advance as additional research results in the field of fracture mechanics become available. Therefore, the assumptions made in this report, while reasonable and appropriate for the current study, should be reviewed and revised in the future on the basis of new information that becomes available.

For part-through flaws, the flaw growth calculations were essentially identical to the procedures used in the VISA code and the OCA-P code (Stevens et al. 1983; Cheverton and Ball 1984). There was no consideration of structural dynamics effects in the fracture mechanics calculations. The predictions of initiation and arrest were based entirely on linear elastic fracture mechanics. In the linear elastic analysis, an upper shelf fracture toughness was used in the manner of Stevens et al. (1983) and Cheverton and Ball (1984). This toughness was 200 ksi $\sqrt{in.}$ for irradiated material of the beltline region of the vessel, and 300 ksi $\sqrt{in.}$ for material outside this region of high fluence.

For through-wall cracks, the flaw growth calculations were modified to account for dynamic effects and upper shelf fracture behavior, with both effects being treated in an approximate manner. The first assumption was that all through-wall cracks must be treated initially as propagating cracks that must be arrested. For these predictions of arrest, the governing stress intensity factors were less than the values given by static solutions. The bulging factors for axial cracks were neglected in these crack arrest calculations, in recognition of the inability of a vessel to fully respond structurally to a rapidly changing crack length. No specific analytical justification was developed to support this assumption. However, a similar approach has been used to interpret the results of recent wide plate tests for crack arrest (Bass, Pugh, and Walker 1985). In these tests, certain deformation modes of the static solutions appear to have been suppressed during the short time spans of dynamic crack propagation and arrest events.

Once crack arrest is predicted by the fracture mechanics model, a second evaluation is made to ensure that the crack remains stable under conditions of static loading. The resistance of the material to crack initiation and/or ductile tearing is addressed. In this static analysis, the calculated crack driving force is at an increased level because the bulging factor is now applied. On the other hand, the material's fracture resistance may also increase if the initiation toughness is greater than the arrest toughness (as in the ductile brittle transition temperature range). If crack arrest has occurred on the upper shelf, the initiation and arrest toughnesses in the present model have the same values. In this case, the arrested crack will be predicted to continue its growth in a ductile tearing mode until it encounters material of sufficient upper shelf toughness (e.g., material with low irradiation embrittlement) to ensure a stable crack length.

Once crack stability is predicted, the fracture evaluation continues by considering possible reinitiation of growth at later times in the transient. The cracks can grow again, if the pressure increases or if the material becomes more brittle as the temperatures decrease.

Recent tests of crack arrest with wide plate specimens (Bass, Pugh, and Walker 1985) provide additional insight into crack arrest behavior. These tests have exhibited the phenomenon of the arrest of a rapidly growing crack, followed by additional growth of the crack by slow ductile tearing. In this respect, the test results support the assumptions of the current fracture mechanics model. However, these tests indicate that the estimates of fracture arrest toughness are conservative in the current model. The crack arrest behavior in the tests appears to be governed by an extrapolation of the rapidly rising portion of measured arrest toughness curve. This extrapolation appears to be valid beyond the transition temperature range, for temperatures that are well above range of existing laboratory test data. There appears to be no bound on arrest toughness imposed by upper shelf behavior, as is observed for static initiation toughness. In this regard, the current analysis imposes an upper shelf on arrest fracture toughness with the assumption being that the arrest toughness never exceeds the initiation toughness. Thus, the current model should give conservative predictions for crack arrest.

FLUENCE SIMULATION

Input data to the model prescribes the mean, or best estimate, of the neutron fluence at all relevant locations of the inner surface of the vessel. The uncertainty or variation of the fluence from this mean value is then calculated by sampling from a normal distribution. The standard deviation of this distribution is a user input to the calculation. Sampling is performed only once for each weld or plate of the vessel during simulation of a given vessel in the Monte Carlo analysis. This value of fluence, relative to the mean level, is then applied to all locations along the length and depth of each weld or plate.

The attenuation of fluence through the wall of the vessel is calculated from an equation that is based on the displacements per atom (DPA) model of irradiation damage. Specifically, this equation has the form

$$f = f_o \cdot e^{-ax} \tag{E.1}$$

where x = depth below the inner surface, in.

f_o = fluence at the inner surface, n/cm^2

f = fluence at depth x, n/cm^2

a = attenuation constant, $in.^{-1}$

For the DPA model, a value of 0.24 has been used for the attenuation constant.

AVERAGE TOUGHNESS

The fracture mechanics model calculates an average value of stress intensity factor for through-wall cracks, and does not calculate any variation of this factor through the thickness of the vessel wall. Accordingly, an averaged value of fracture toughness is used in the predictions of crack initiation and arrest.

A root-mean-square average of fracture toughness is calculated as follows:

$$R_{Ic} = \left(\frac{1}{t} \int_o^t K_{Ic}{}^2 \, dx\right)^{\frac{1}{2}} \tag{E.2}$$

$$R_{Ia} = \left(\frac{1}{t} \int_o^t K_{Ia}{}^2 \, dx\right)^{\frac{1}{2}} \tag{E.3}$$

This approach was adopted following discussions with Dr. G. Irwin at the University of Maryland. The use of the root-mean-square averaging procedure is consistent with the use of a mean energy release rate in calculating an average value of stress intensity factor in the treatment of the through-the-wall variations in crack driving force.

TOUGHNESS VERSUS TEMPERATURE

Fracture toughness in the transition temperature range was calculated with the same equations as given by ORNL in the user document for the OCA-P computer code (Cheverton and Ball 1984). These equations predict toughness as a function of the parameter $T\text{-}RT_{NDT}$, where T is the metal temperature and RT_{NDT} is the temperature for nil ductility transition.

For the deterministic fracture mechanics evaluation of part-through cracks, the lower bound curves of the ASME Section XI Code are used:

$$K_{Ic} = 33.2 + 2.806 \exp\left[0.02\left(T\text{-}RT_{NDT} + 100.0\right)\right], \text{ ksi } \sqrt{\text{in.}} \qquad \text{(E.4)}$$

$$K_{Ia} = 26.8 + 1.223 \exp\left[0.0145\left(T\text{-}RT_{NDT} + 160.0\right)\right], \text{ ksi } \sqrt{\text{in.}} \qquad \text{(E.5)}$$

As in the ORNL/IPTS study, the probabilistic fracture mechanics evaluations were based on the following mean curves for fracture toughness:

$$\bar{K}_{Ic} = 1.43 \times \text{Equation (E.4)}$$

$$\bar{K}_{Ia} = 1.25 \times \text{Equation (E.5)}$$

When the above curves for fracture toughness exceeded the assumed upper bound for the initiation and arrest toughness, the upper shelf values of toughness were used instead of the values given by the equations. The methods used to estimate fracture toughness on the upper shelf are described below.

UPPER SHELF TOUGHNESS

In the deterministic fracture mechanics calculations, the values of upper shelf fracture toughness were specified as an input to the analysis. A typical value for irradiated weld metal of high copper content was 200 ksi $\sqrt{in}$.

In the probabilistic analyses, the upper shelf toughness was calculated from an estimate of the J-resistance curve for the weld or plate material in question. The first step in the calculation was to estimate the upper shelf level of Charpy impact energy (CVN). The impact energies prior to irradiation were obtained from data for the welds and plates of the specific vessel being analyzed. The decrease in impact energy due to neutron fluence was then calculated from Equations (3.3) and (3.4) given in the body of this report.

The J-resistance curve was estimated from the irradiated impact energy by using equations given by Merkle and Johnson (1983). These equations provide a power law representation as follows:

$$J = 1000\ C \left(\frac{\Delta a}{1.0}\right)^{M} \tag{E.6}$$

$$C = -0.114 \left(\frac{CVN}{100}\right) + 5.382 \left(\frac{CVN}{100}\right)^{2} \tag{E.7}$$

$$x = C + 1.5 \left(\frac{\sigma_o}{100}\right)$$

$$M = \frac{0.473\ x^{3}}{14.42 + x^{3}} \tag{E.8}$$

where CVN = Charpy impact energy, ft-lb

J = J-integral, in.-lb/in.^{2}

Δa = increase in crack length, in.

σ_o = flow stress, psi.

The correlation of the J-resistance curve with CVN values is a necessary approximation in the current study. The J-resistance curves were not available for the materials that are used in the specific vessels of interest, whereas CVN data were usually available. For future calculations, better correlations for predicting J-resistance curves are expected to be developed as results of ongoing research programs are completed (Hiser 1985).

Figure E.1 shows a correlation of predicted and measured J-resistance curves for a relatively high toughness specimen of unirradiated A533-B steel. The predicted curve is conservative because it gives J-values that are lower than the measured curve. These predicted J-values are only about 60% of the measured values. However, the pressure needed to cause crack growth will be more accurately predicted. When pressures are well below limit load, the applied values of J are proportional to the pressure squared. Thus, the 40% error in the J-resistance curve will imply only a 20% error in the allowable pressure. Furthermore, when the pressure approaches the limit load, the errors in predictions of allowable pressure can be shown to be significantly less than 20%.

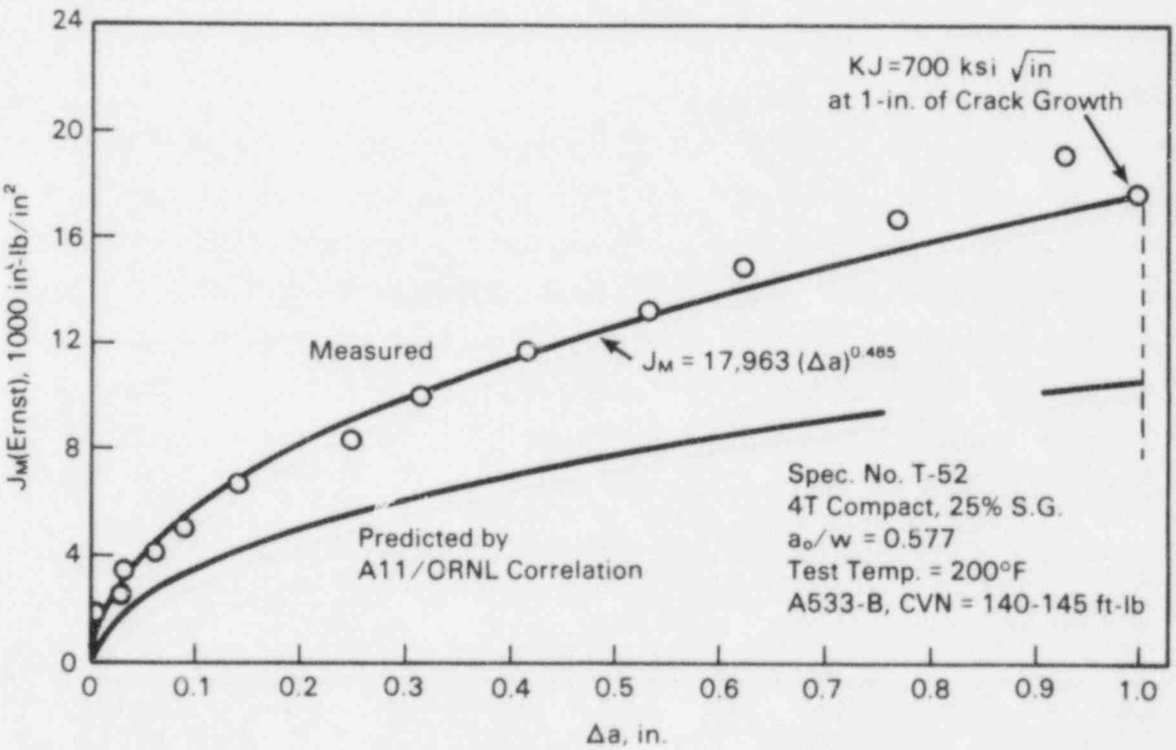

FIGURE E.1. Correlation of Predicted and Measured J-Resistance Curves for High Upper Shelf Plate Material

Source: Shih et al. (1981)

The fracture evaluations did not involve any detailed calculations of stable crack growth or any detailed predictions of instability loads. Rather, a critical value of J was estimated by assuming that crack growth greater than 2.0 in. was unacceptable. For low toughness materials there appears to be little increase in the J-resistance curve once the crack growth is greater than a fraction of an inch. On the other hand, there are some data for high toughness vessel steels for crack growths out to about an inch (see, for example, Figure E.1). Extrapolation of these curves out to 2 in. of crack growth was judged to be reasonable. For the relatively long through-wall cracks (e.g., 72 in.) of interest in this study, a 2.0-in. increase in crack length has little effect on the calculated values of the applied J-integral. Accordingly, the applied values of J were calculated only for the initial crack length and then compared to the allowable values that corresponded to 2.0 in. of crack growth. The values of initiation and arrest toughness were assumed to be identical at upper shelf temperatures.

BETA FACTOR CORRECTION

The fracture mechanics model has the option available to account for finite thickness effects by use of the Irwin beta factor. This factor has often been used to adjust fracture toughness values obtained from small specimens (Merkle 1984). In this application, the method provides an estimate of plane strain fracture toughness from specimens that are too thin to satisfy validity requirements. In the current analyses, the beta factor is used to estimate the enhancement in fracture resistance for situations where plane strain conditions are not achieved at the crack tip.

The equations for the beta factor correction are

$$K_c^2 = K_{Ic}^2 \,(1.0 + 1.4\,\beta_{Ic}^2) \tag{E.9}$$

$$\beta_{Ic} = \frac{1}{t}\,(K_{Ic}/\sigma_o)^2 \tag{E.10}$$

where t is the wall thickness and σ_0 is the material flow stress. The upward adjustment in calculating the toughness K_c is not allowed to exceed a factor of 3.0.

In the current fracture mechanics model, it has been assumed that the beta factor concept can be extended beyond the transition range of temperature and can be applied to ductile tearing on the upper shelf. The linear elastic parameters of K_{Ic} and K_c are replaced by the K_J representation of ductile tearing resistance.

A set of calculations was performed to estimate the potential effects of finite thickness on fracture resistance for reactor pressure vessels. A wall thickness of 9.0 in. was used for these calculations, which were intended to apply to a very tough vessel steel (e.g., Figure E.1) with a maximum J value of about 15,000 in.-lb/in.^{2}. The results are given in Table E.1. Substantial increases in fracture resistance were calculated, even for the wall thickness of 9.0 in.

The beta factor correction was used only in sensitivity calculations, and its use did not significantly change the trends of the failure mode predictions. None of the actual plant specific failure mode evaluations incorporated the beta factor approach. Corrections for finite thickness effects in the context of ductile tearing fracture were believed to be beyond

TABLE E.1. Evaluation of Potential Effects of Finite Thickness for Reactor Vessel ($t = 9$ in., $\sigma_0 = 60$ ksi)

Maximum Value of J, in.-lb/in.^{2}	$K_J = \sqrt{JE}$, ksi $\sqrt{in.}$	Corrected Toughness, K_c, for Finite Thickness Vessel, ksi $\sqrt{in.}$
600	130	153
2,000	237	540
5,000	374	1,122
10,000	529	1,590
15,000	648	1,944

the range of established experimental validation. Also, the available J-resistance curves for high toughness vessel steels often may already reflect some effects of finite thickness, because specimen thicknesses do not often approach 9.0 in. Nevertheless, it should be recognized that side grooved specimens (as in Figure E.1) may understate the fracture resistance in certain cases.

In conclusion, it is not recommended that the beta factor correction be used in predictions of vessel failure modes. However, thickness corrections may be appropriate in future calculations, if additional data and validation tests become available for the materials and thicknesses of interest.

SIMULATION OF TOUGHNESS

The failure mode evaluations involved calculations of toughness for each simulated position of the crack tip in the vessel. The sequence and procedure for these calculations are presented here.

For each simulated vessel, the random values of the parameters that govern fracture toughness are calculated only once for each weld and plate that makes up the simulated vessel. Samples are taken from the distributions that describe copper content, nickel content, fluence, the variations from the mean initiation and arrest toughness, initial RT_{NDT}, and shift in RT_{NDT}. The copper distribution is truncated at values of 0.08 and 0.40 wt%. The nickel content is truncated only if a value less than zero is predicted. Similarly, the fluence distribution is truncated so that only positive fluences can be predicted.

Once the governing parameters have been simulated for a weld, the remaining calculations are deterministic. The mean values of initiation and arrest toughness are calculated at each of 33 positions through the wall of the vessel. These mean values are calculated from the mean curves of toughness versus temperature using the temperature and the calculated value of RT_{NDT} that applies to the particular location in the vessel wall being addresssed. The predicted toughness is truncated at the upper shelf values. The 33 values of toughness are then averaged by the root-mean-square approach.

Following averaging, the resulting toughnesses are then increased or decreased in accordance with the previous simulation for the relative toughness of the particular weld in comparison to a mean toughness correlation. Finally, this adjusted toughness may be further adjusted for finite thickness effects using the beta factor approach.

REFERENCES

Bass, B. R., C. E. Pugh, and J. K. Walker. 1985. "Elastodynamic Fracture Analysis of Large Crack-Arrest Experiments." In Transactions of the Thirteenth Water Reactor Safety Research Information Meeting, NUREG/CP-0071, U.S. Nuclear Regulatory Commission, Washington D.C.

Cheverton, R. D., and D. G. Ball. 1984. OCA-P, A Deterministic and Probabilistic Fracture Mechanics Code for Application to Pressure Vessels. NUREG/CR-3618, U.S. Nuclear Regulatory Commission, Washington, D.C.

Hiser, A. 1985. Estimation of Reactor Vessel Upper Shelf Fracture Toughness Properties. MEA-2068, Materials Engineering Associates, Lanham, Maryland.

Merkle, J. G. 1984. Evaluations of the Irwin β_{Ic} Adjustment for Small Specimen Fracture Toughness Data. CONF-8310143-57, National Technical Information Service, Springfield, Virginia.

Merkle, J. G., and R. E. Johnson. 1983. Example Calculations Illustrating Methods for Analyzing Ductile Flaw Stability in Nuclear Pressure Vessels. NUREG-0939, U.S. Nuclear Regulatory Commission, Washington D.C.

Shih, C. F., W. R. Andrews, H. G. deLorenzi, M. D. German, R. A. Van Stone, and D. F. Mowbray. 1981. Methodology for Plastic Fracture. NP-1735, Electric Power Research Institute, Palo Alto, California.

Stevens, D. L., F. A. Simonen, J. Strosnider, R. W. Klecker, D. W. Engel, and K. I. Johnson. 1983. VISA - A Computer Code for Predicting the Probability of Reactor Pressure Vessel Failure. NUREG/CR-3384, U.S. Nuclear Regulatory Commission, Washington, D.C.

APPENDIX F

<u>TURNING OF AXIAL CRACKS</u>

APPENDIX F

TURNING OF AXIAL CRACKS

This appendix describes calculations of elastic stress intensity factors for through-wall axial cracks in reactor vessels. The solutions were developed to predict whether an existing axial crack will continue to extend axially or will turn and extend circumferentially (as, for example, along an embrittled circumferential weld). Finite element models for cracked cylinders and flat plates were used for numerical calculations of elastic stress intensity factors. In the case of flat plates, a published analytical solution (Hussain, Pu, and Underwood 1974) was used to evaluate the accuracy of the numerical solution.

FINITE ELEMENT MODELS

Two finite element models were developed to provide crack opening displacements and nodal forces for numerical calculations of applied stress intensity factors. Figure F.1 illustrates the two-dimensional model that was loaded to simulate the state of stress in a cylindrical pressure vessel. The bold lines along element boundaries of the model indicate the locations of the pre-existing axial crack, as well as the postulated circumferential crack extensions.

A model of a cylindrical vessel is shown in Figure F.2. This same model was also used in Appendices G and H to calculate crack opening behavior. An expanded view of the mesh refinement at the crack tip in Figure F.3 shows the paths of longitudinal and circumferential crack extensions.

To simulate the cracks in both models, displacement constraints on nodes along the crack plane were released for the energy release rate calculations, as indicated in Figures F.1 and F.3. The energy release rates were evaluated by calculating crack closure work for each increment of crack growth. The usual relationship between energy release rate and crack-tip stress intensity factor was then utilized.

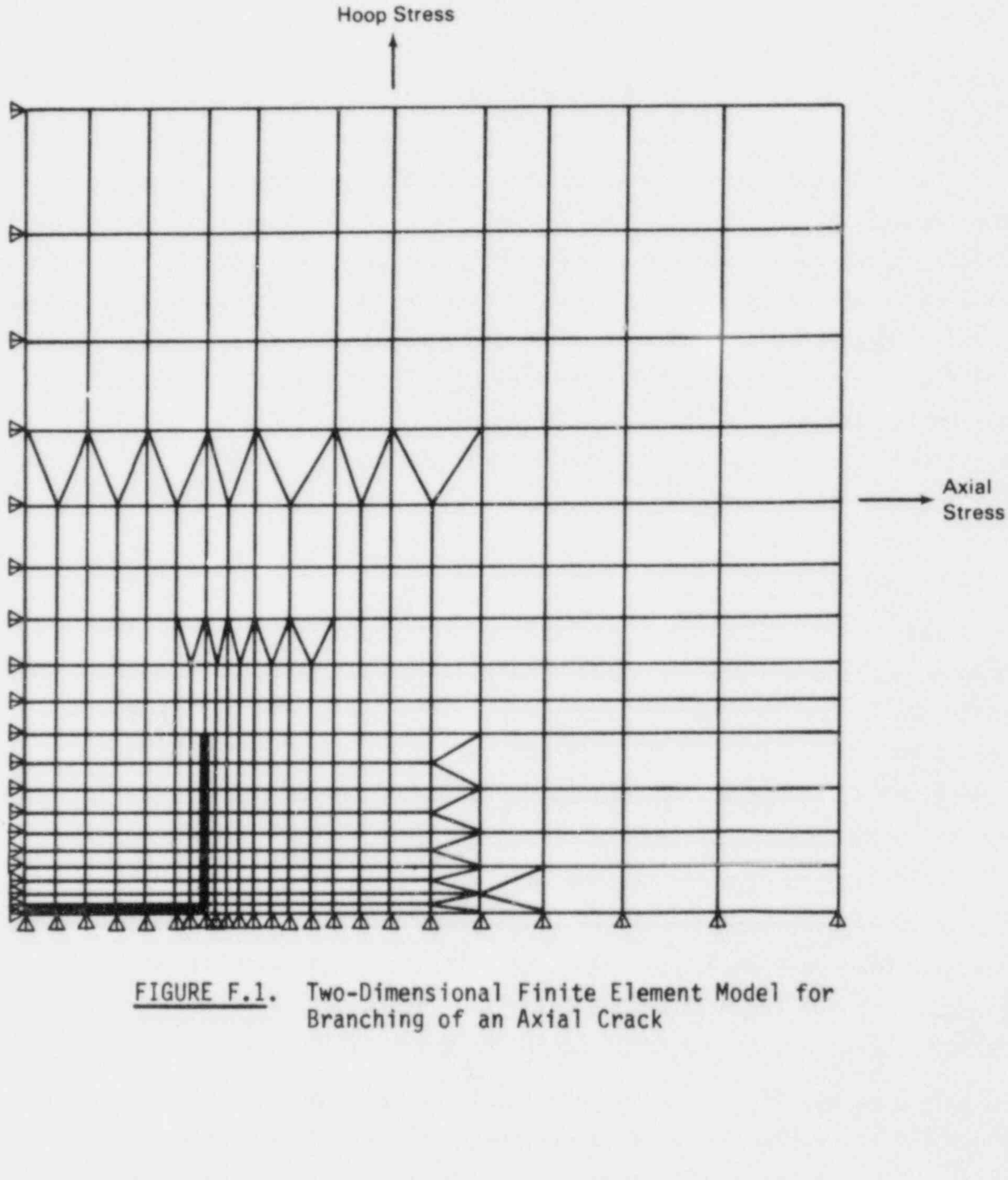

FIGURE F.1. Two-Dimensional Finite Element Model for Branching of an Axial Crack

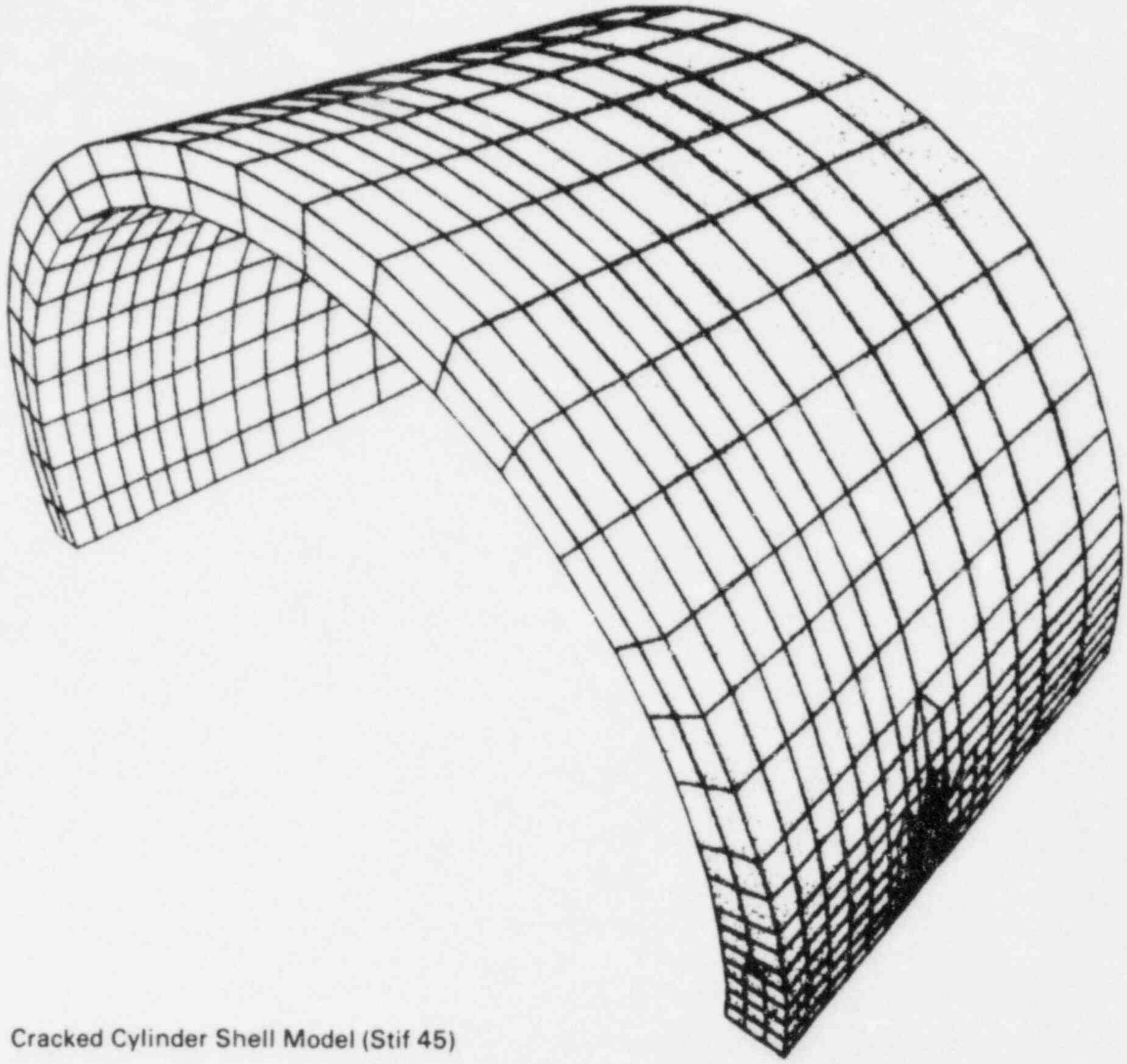

FIGURE F.2. Three-Dimensional Finite Element Model for Branching of an Axial Crack

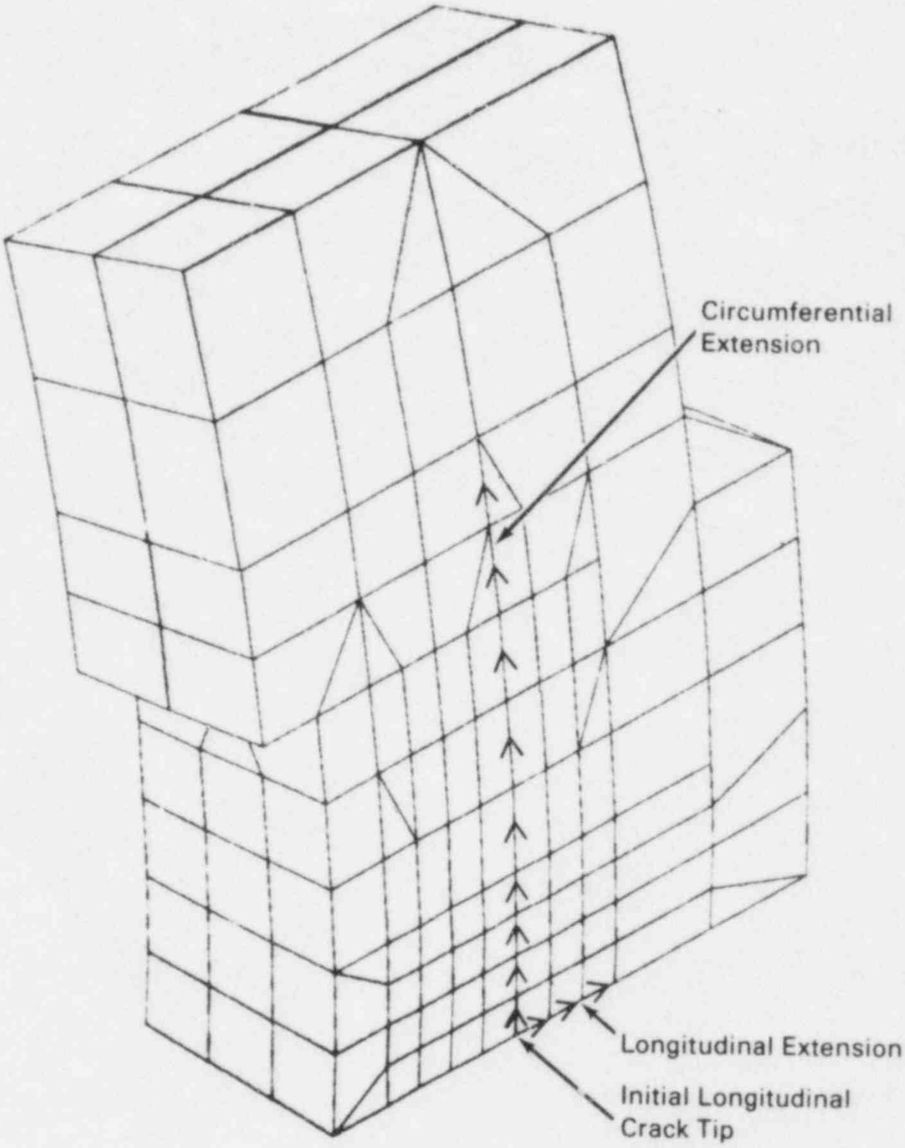

FIGURE F.3. Mesh Refinement Near Crack Tip and Crack Extension Paths

NUMERICAL RESULTS

Figures F.4 and F.5 are the plotted results for stress intensity factors from the two- and three-dimensional models, respectively. Numerical results are given for both continued axial crack extension and for crack extension at a direction 90 degrees to the original crack plane. The finite element models were symmetric about the plane of the original crack. As such, the simulated circumferential crack extensions represent crack bifurcation or two equal extensions at angles of ±90 degrees from the original crack.

For continued crack extension in the axial direction, it was possible to compare the current numerical results with other published stress intensity factor solutions (Hussain, Pu, and Underwood 1974). Figures F.4 and F.5 indicate an acceptable level of accuracy for the numerical solutions.

Figure F.4 shows results for the flat plate model loaded only by stress parallel to the initial crack (axial loading) compared with results for loading only by a stress perpendicular to the initial crack (hoop stress loading). It is seen that the circumferential crack extension is governed by the stress component normal to the original axial crack. It also appears that the stress intensity factor for a very small crack extension begins with a finite value. In particular, the stress intensity factor does not begin with a value of zero, which would correspond to the small dimension of the crack extension itself, as measured normal to the direction of the original crack.

The results from the flat plate and cylinder show good agreement with each other. It appears that the applied stress intensity factor for circumferential growth is about half that for continued axial growth.

CLOSED FORM SOLUTION

The above solutions were based on numerically calculated strain energy release rates for cracks in a cylindrical pressure vessel. A closed form solution for the flat plate geometry has been published in the literature (Hussain, Pu, and Underwood 1974). This was used as a benchmark for the

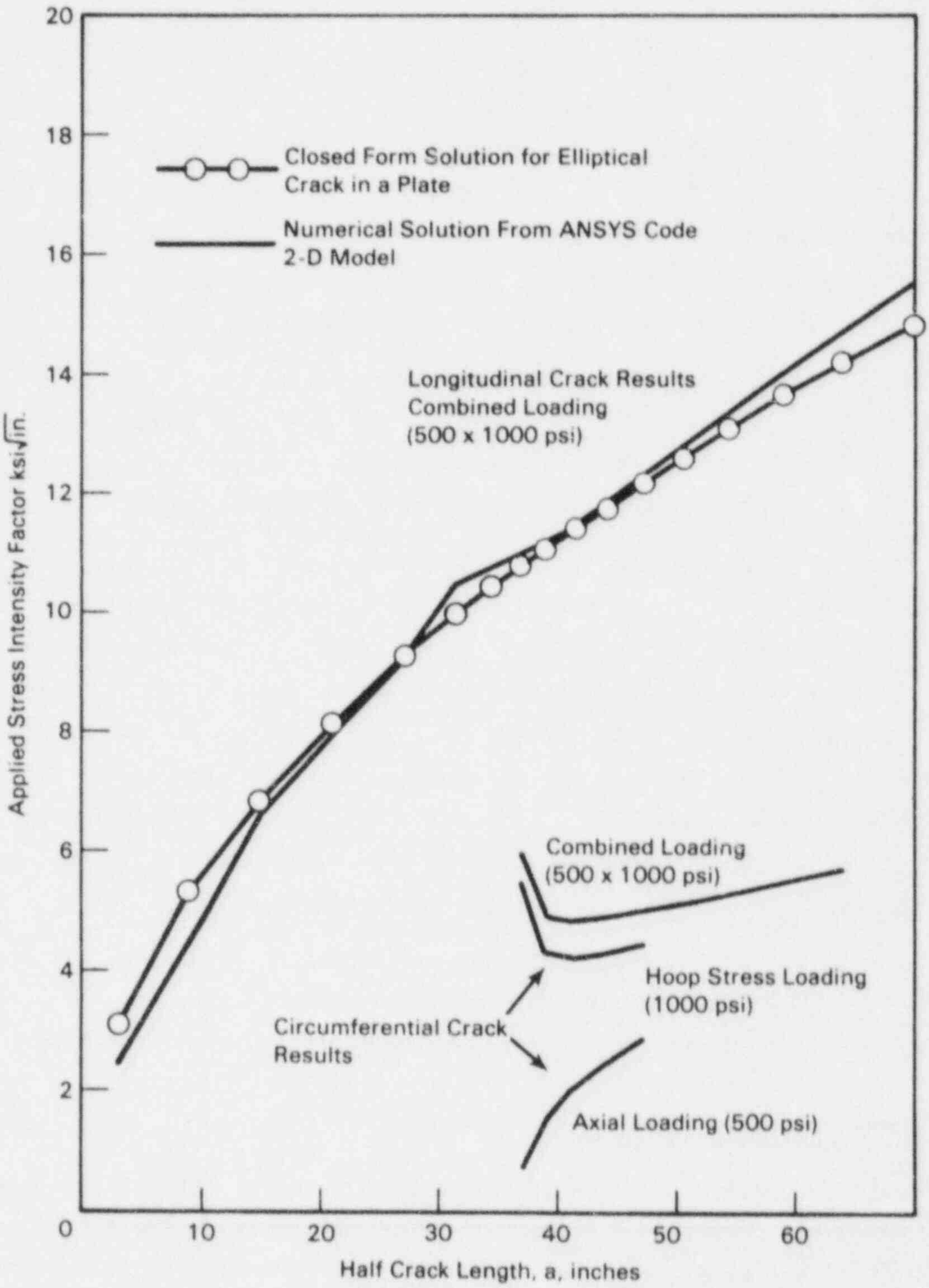

FIGURE F.4. Comparison of Stress Intensities for Axial and Circumferential Crack Extensions from the Flat Plate Model

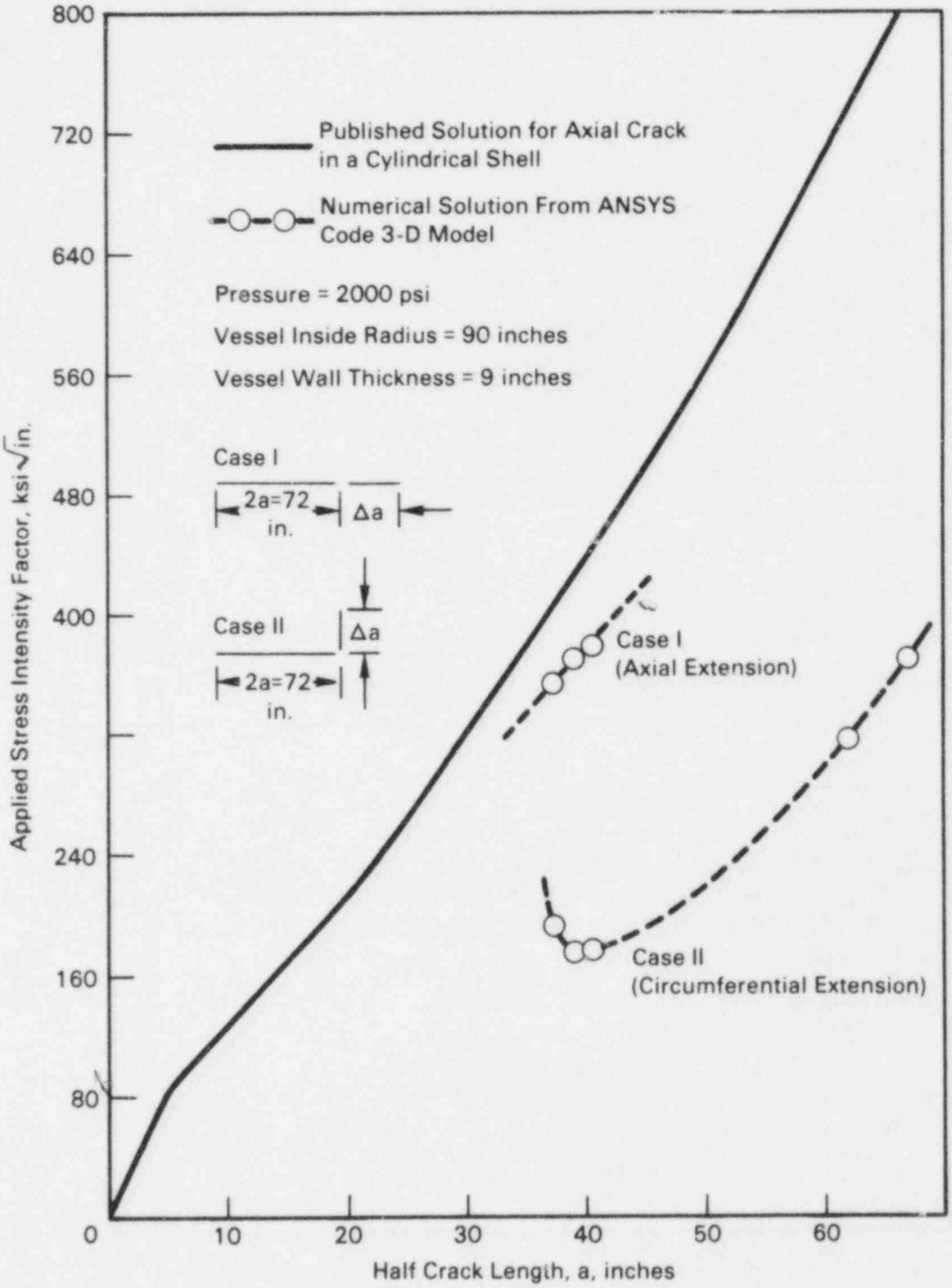

FIGURE F.5. Comparison of Stress Intensities for Axial and Circumferential Crack Extensions numerical solutions. The closed form solution of Hussain, Pu, and Underwood (1974) gives the following energy release rate:

$$G(\gamma) = \frac{4}{E}\left(\frac{1}{3 + \cos^2 \gamma}\right)^2 \left(\frac{1 - \gamma/\pi}{1 + \gamma/\pi}\right)^{\gamma/\pi} \Big[(1 + 3 \cos^2 \gamma)\, K_I^{\,2}$$

$$+ (8 \sin \gamma \cos \gamma)\, K_I K_{II} + (9 - 5 \cos^2 \gamma)\, K_{II}^{\,2}\Big] \qquad \text{(F.1)}$$

where K_I = mode I stress intensity factor

K_{II} = mode II stress intensity factor

γ = angle between crack extension and main branch of crack.

When a crack turns from an axial weld in a vessel to follow a circumferential weld, the parameter γ is $\pi/2$, and $K_{II} = 0$. This gives

$$G(\gamma) = \frac{1}{E}\,(0.506\ K_I)^{2} \qquad \text{(F.2)}$$

Thus, the stress intensity factor for growth along a circumferential crack is 0.506 times that for continued growth along an axial weld. This factor of about ½ is consistent with the numerical results shown in Figures F.4 and F.5.

REFERENCE

Hussain, M. A., S. L. Pu, and J. Underwood. 1974. "Strain Energy Release Rate for a Crack Under Combined Mode I and Mode II." In Fracture Analysis, pp. 2-28, ASTM STP 560, American Society for Testing and Materials, Philadelphia, Pennsylvania.

APPENDIX G

PLASTIC FRACTURE SOLUTIONS

APPENDIX G

PLASTIC FRACTURE SOLUTIONS

This appendix describes procedures used in the failure mode analyses to calculate stress intensity factors for through-wall axial cracks in reactor pressure vessels. For very long cracks and for high stresses it was necessary to account for plasticity effects by use of a plasticity correction factor. This factor was used also in calculations of crack opening areas and vessel volume changes.

The plastic solutions address only pressure-induced stresses in the vessel wall. No thermal stress contribution was considered for through-wall cracks, because the results of Appendix B show that thermal stresses make only a second-order contribution to the growth of through-wall cracks.

ELASTIC SOLUTIONS

For completeness, elastic solutions are described, because these published solutions were used in conjunction with the plastic correction factors. The elastic solution for stress intensity factor was taken from Rooke and Cartwright (1976) as follows:

$$K_I = (G_m \pm G_b)\, \sigma_m \sqrt{\pi a} \qquad (G.1)$$

where σ_m = membrane stress at the crack site in the uncracked shell

G_m and G_b = functions of λ [given in graphical form in Rooke and Cartwright (1976)]

$\lambda = a/\sqrt{Rt}$

$2a$ = crack length

R = mean radius of vessel

t = wall thickness of vessel.

In keeping with the use of an average of the fracture toughness through the wall of the vessel, the G_b term was neglected in calculating a stress intensity factor for the midwall location of the vessel.

A closed form elastic solution from Tada and Paris[a] was used to calculate the crack opening as follows:

$$\text{AREA} = \frac{\sigma}{E} (2\pi Rt)\, G(\lambda) \qquad (G.2)$$

where $G(\lambda) = \lambda^2 + 0.625\,\lambda^4 \qquad \lambda < 1$

$G(\lambda) = 0.14 + 0.36\,\lambda^2 + 0.72\,\lambda^3 + 0.405\,\lambda^4 \qquad \lambda > 1$

$\lambda = a/\sqrt{Rt}$

σ = nominal membrane stress (hoop stress)

E = elastic modulus

R = nominal radius

t = shell thickness

a = crack half length.

The use of an elastic plastic beam model also was explored as a method to predict crack opening areas (Irwin et al. 1967). This simple model, based also on information provided by J. Merkle of Oak Ridge National Laboratory, assumed a unit width strip along the crack face. The beam deflection represented the radial and tangential deflections along the crack. The beam length was equal to the length of the axial crack. Details of the method are not given here because it was found to underpredict the opening areas for longer axial cracks (i.e., 144-in.-long crack in a vessel of 90-in. radius and 9-in. wall thickness). Nevertheless, the beam model was found to give relatively accurate predictions for cracks of shorter length.

STRIP YIELD MODEL

The strip yield model for stress intensity factors in axially cracked cylinders was tried as an approximation to the plastic deformation behavior.

(a) "Estimation of Stress Intensity Factors and the Crack Opening Area of a Circumferential and Longitudinal Through-Crack in a Pipe," presented by H. Tada and P. C. Paris to the Section XI Task Group on Pipe Flaw Evaluation, San Diego, California, May 1982.

This model is based on a Dugdale plastic zone correction (Mayfield et al. 1980) and is given as follows:

$$K_I = \left[\frac{8}{\pi^2 (\sigma/\sigma_0)^2} \ln \sec\left(\frac{\pi}{2}\frac{M_T\sigma}{\sigma_0}\right)\right]^{1/2} \sigma_m \sqrt{\pi a}$$

where σ_0 = flow stress

M_T = bulging factor.

The bulging factor M_T can be taken to be the same as the G_m factor of Rooke and Cartwright (1976).

ESTIMATION SCHEME FOR J-INTEGRAL

In this method the estimation scheme for the J-integral as given in Kumar, German, and Shih (1981) was applied. As for the strip yield model, the calculations were based on an application and modification of flat plate solutions. However, this method treated the strain hardening of the material and was based on elastic plastic solutions of Kumar, German, and Shih (1981) that do not have the restrictive assumption of the Dugdale plastic zone shape.

The published estimation scheme did not include the case of an axial crack in a cylinder. Following the approach of the strip yield model, the flat plate solutions were applied with the membrane stress σ_m multiplied by the cylindrical bulging factor M_T. Details of the equations and calculations are not included here; the reader is directed to Kumar, German, and Shih (1981).

FINITE ELEMENT SOLUTIONS FOR J-INTEGRAL

The ANSYS computer program (DeSalvo and Swanson 1983) was applied to calculate stresses and displacements for elastic plastic behavior using the models of axially cracked vessels as described in Appendix F. Lacking a numerical procedure in ANSYS for calculating values of the J-integral, estimates were made by using the magnitude of the crack-tip crack opening displacements. In the elastic range, the value of stress intensity factor is proportional to the crack opening displacement, and the value of the J-integral is proportional to the crack opening displacement squared. On this basis the ratio between the elastic and plastic stress intensity factors was inferred from the relative values of calculated displacements from the plastic finite element solutions relative to the displacements from the elastic solutions.

COMPARISON OF SOLUTIONS

Numerical results were generated for typical vessel dimensions and material properties. The vessel inner radius was 90 in. and the wall thickness was 9 in. Figure G.1 shows the stress-strain curve, which was taken from Whitman and Bryan (1982) for use in the calculations. The J estimation scheme uses a Ramberg-Osgood fit of the stress-strain curve. The constants used for the calculation and a comparison of the fit to the actual

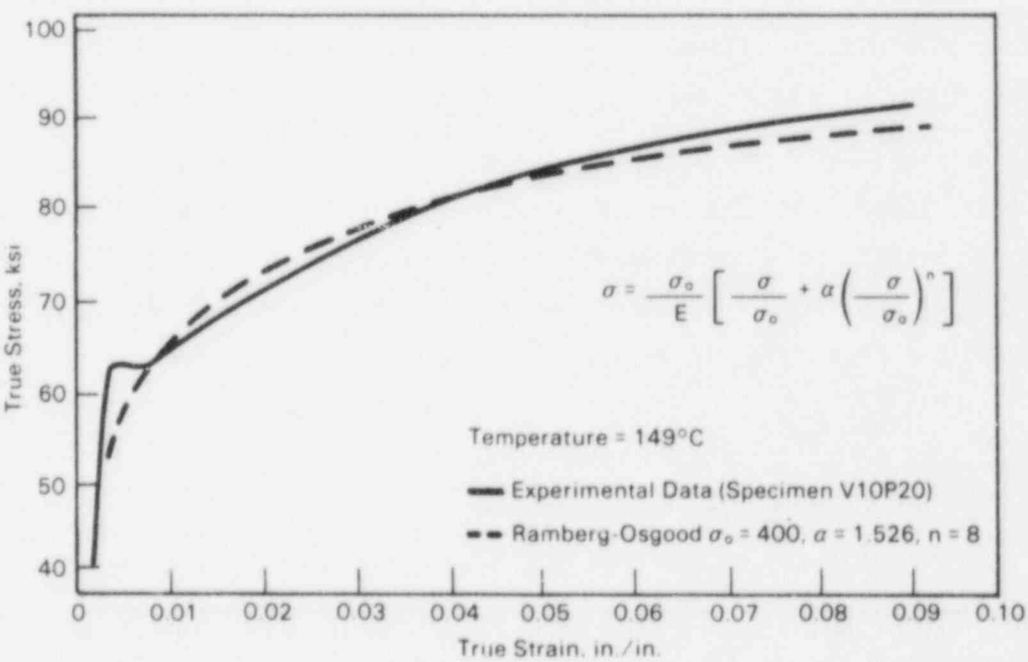

FIGURE G.1. Uniaxial True Stress-Strain Curve of Tensile Specimen V100P20 Tested at 149°C stress-strain curve can be seen in Figure G.1. For the finite element solution, a multi-linear fit of the stress strain curve was used as input to the computer code.

Figure G.2 shows the ratio of the elastic and plastic solutions. The elastic stress intensity factor is designated as $K_{elastic}$. The parameter K_J can be termed a "plastic stress intensity factor" that was calculated from the J-integral using the equation

$$K_J = \sqrt{EJ} \tag{G.4}$$

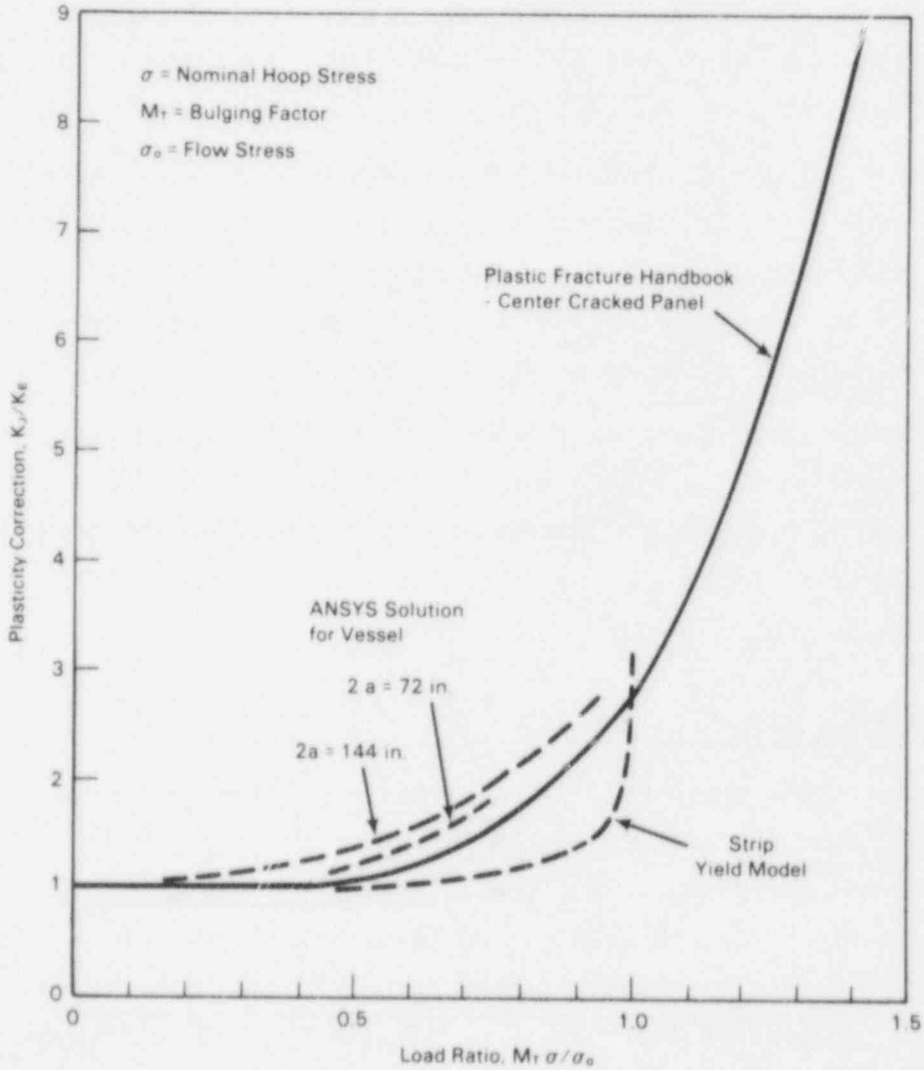

FIGURE G.2. Plasticity Correction Factor for Pressure Vessel with Axial Crack

The horizontal axis of Figure G.2 is labeled as the load ratio and is the nominal hoop stress taken as a ratio of the material flow stress. The effect of bulging for the cylindrical geometry is represented by multiplying the nominal stress by the M_T factor. For the stress-strain curve of Figure G.1, the flow stress was taken as the average of the engineering yield and ultimate strengths (525 MPa = 76.1 ksi).

The finite element solutions are believed to give the most reliable estimate of the effects of plasticity. However, these numerical results did not extend to values of load ratio greater than one. Also, finite element solutions are difficult and costly to compute, and, thus, are not readily generated for a range of vessel dimensions, crack lengths, and stress-strain curves. Thus, it was desirable to use these results to support the use of a more simplified method of calculation.

The simple strip yield model tends to underestimate the values of stress intensity factor until the load ratio becomes very nearly one. Then the model predicts an infinite value of stress intensity factor. This prediction is unrealistic in the light of the finite element analyses that show rapidly increasing but finite values of K_J for load ratios even greater than one.

The curve of the estimation scheme (EPRI/GE Plastic Fracture Handbook) agrees quite well with the finite element results over the range of load for which vessel solutions were calculated. At greater values of load ratio, the estimation scheme provided a means to extrapolate the trend of the finite element solutions.

SELECTED METHOD OF STRESS INTENSITY FACTOR CALCULATION

The failure mode analyses of this report were based on the curve calculated by the estimation scheme (solid curve of Figure G.2). It was assumed that this particular curve could be applied for the range of relevant vessel dimensions, crack dimensions, and stress-strain curves. The approach was to first calculate an elastic stress intensity factor and then to use Figure G.2 to correct for the effects of plasticity. The differences in yield strength, vessel dimensions, and crack size were factored in through the normalizing constants M_T and σ_0.

More exact methods of accounting for plasticity effects could have been used in the failure mode analyses. However, the selected method was believed to be a reasonable approximation that allowed a first-order correction to be made for plasticity effects. Other methods would have introduced prohibitive computational requirements for the repeated calculations of the Monte Carlo analysis.

CRACK OPENING AREA

Crack opening areas were calculated in the failure mode evaluations so that leak rates and depressurization effects could be treated. The crack opening areas for axial cracks were first calculated by using Equation (G.2) for elastic behavior. The elastic opening was then increased by the use of the plastic correction factor from Figure G.2. In the plastic analysis, the calculated opening area may depend on which crack tip is considered, because the flow stress can differ at the two ends of the crack due to different levels of neutron fluence and different materials (plate or weld metal) at each end of the crack. Two opening areas were calculated using the flow stress at each tip in turn. The resulting opening areas were then averaged.

The simulation model also recorded the growth of the maximum plastic opening area for the crack during the transient. This maximum area was used for a given time step, if it exceeded the plastic opening calculated for the current pressure and crack length. In this way, the effect of a large opening due to high pressures early in the transient was taken into account.

Figure G.3 provided the basis for using the plastic correction factor of Figure G.2, which was originally developed to calculate stress intensity factors. In this case, the factor of Figure G.2 is used in the calculation of the effects of plasticity on crack opening area. Figure G.3 shows numerical results from the same elastic-plastic finite element solutions that were used to generate the K_J curves of Figure G.2. The crack opening area is seen to be

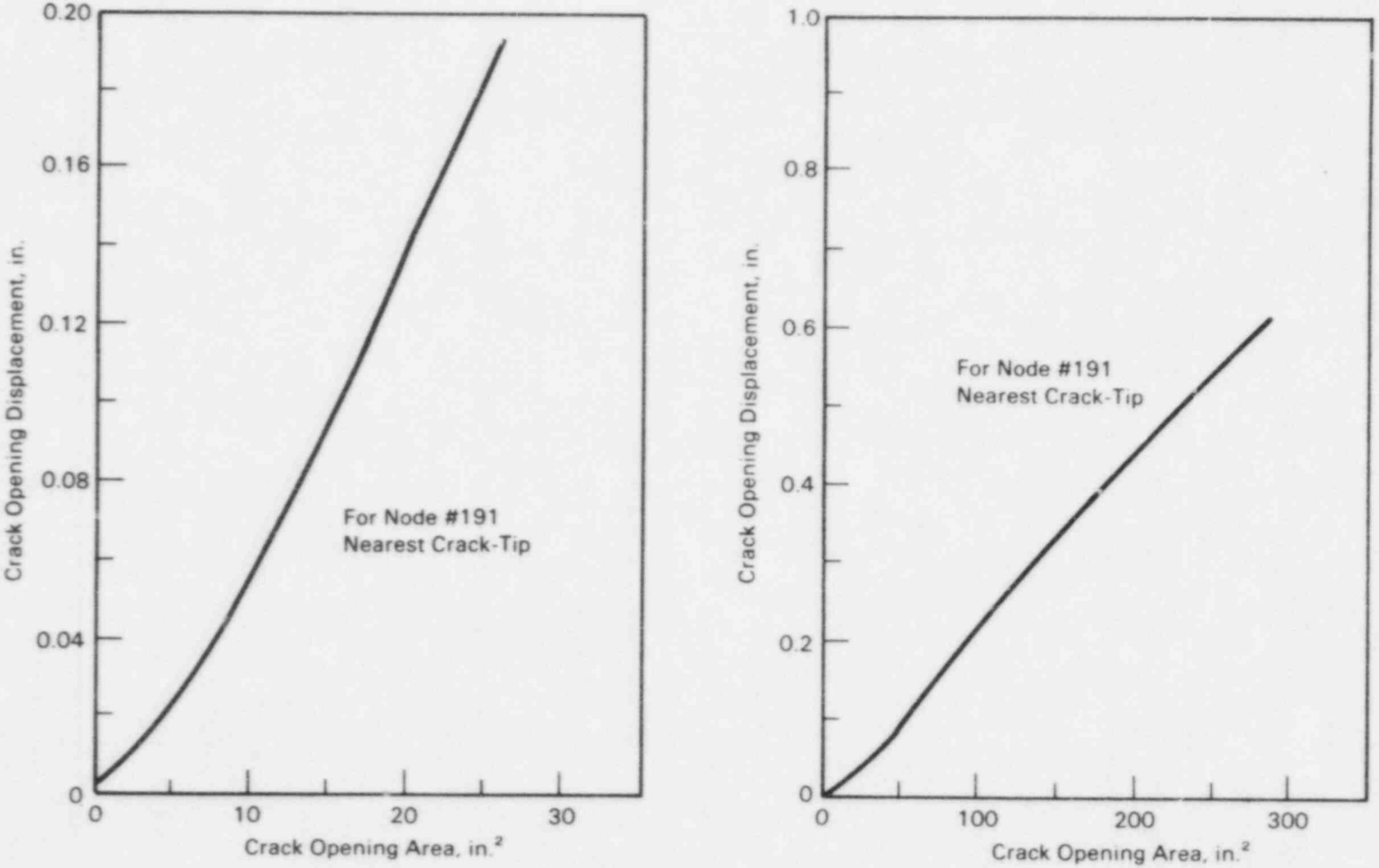

a. 72-Inch-Long Crack

b. 144-Inch-Long Crack

FIGURE G.3. Correlation of Crack Opening Areas and Crack Opening Displacements nearly proportional to the calculated crack opening displacement as measured at the node nearest to the crack tip. In particular, Figure G.3 shows that this approximation holds for crack lengths of both 72 and 144 in. and for a range of pressures extending from the elastic range into the plastic range. Because the crack tip displacement is directly related to stress intensity factor, it may be concluded that the opening area is also approximately proportional to the stress intensity factor.

CHANGE IN VESSEL VOLUME

As an axial crack opens from the action internal pressure, there is a bulging deformation in the vessel near the crack. This bulging deformation increases the volume of the vessel. For long cracks and high pressures, the change in volume can result in substantial reductions of the internal fluid pressure for PTS conditions for which the coolant water is highly subcooled. Results of the fracture mechanics calculations were applied to predict the change in vessel volume as a function of crack length and internal pressure.

A simple closed-form solution was first developed to relate the change in vessel volume to calculated crack opening areas. This simple relationship was then shown to be in relatively good agreement with the opening areas and the volume changes that had been calculated using elastic-plastic finite element analyses.

The assumed shape of the deformed vessel cross section is indicated in Figure G.4. The shape was taken to be the same as that for a split ring opened by concentrated radial loads at the location of the split. A solution for the radial deflection of the ring was derived by application of the governing equations for bending of a curved beam. The equation obtained was

$$W = (W_{max}/\pi)[(\pi - \theta)\cos\theta + \sin\theta]. \qquad (G.5)$$

A plot of this deflected shape is shown in Figure G.4.

The shaded area of Figure G.4 is a measure of the increase in volume of the vessel. This shaded area (ΔA) can be calculated by integration as follows:

$$\Delta A = 2R \int_0^\pi w d\theta$$

$$= (2R\, W_{max}/\pi) \int_0^\pi [(\pi - \theta) \cos \theta + \sin \theta]\, d\theta \qquad (G.6)$$

$$\Delta A = 8R\, W_{max}/\pi$$

R = vessel inner radius.

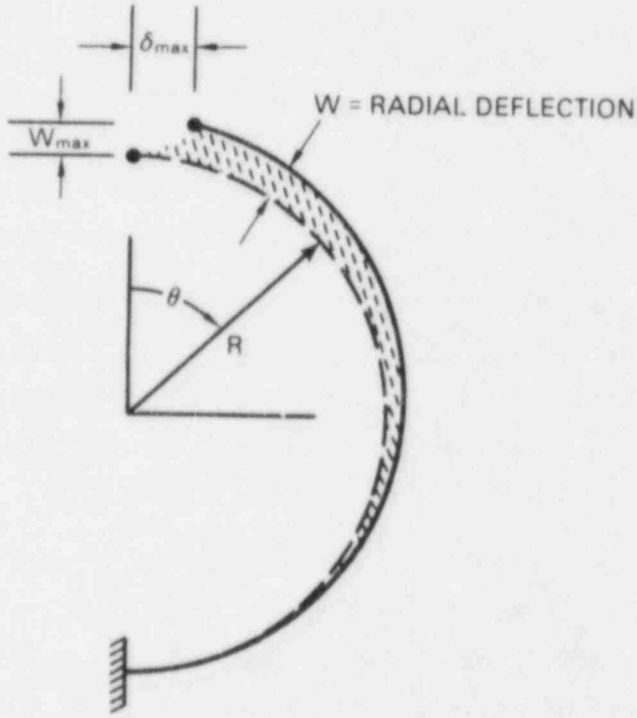

FIGURE G.4. Crack Opening Mode

The increase in vessel volume is obtained by integrating this change in cross-sectional area over the cracked length of the vessel. This is equivalent to use of a weighted average value of W_{max} over the length of the crack. For an assumed elliptical crack opening, this gives

$$W_{average} = \pi\ \delta_{max}/4 \tag{G.7}$$

$$\Delta A_{average} = (\pi/4)\ (8R\ \delta_{max}/\pi) = 2R\ \delta_{max} \tag{G.8}$$

so that

$$\Delta V = 2\ \delta_{max}\ R\ell \tag{G.9}$$

ΔV = change in vessel volume.

It is also convenient to relate the crack opening area to the change in vessel volume. This gives the simple relationship for crack opening area:

$$\text{Crack opening area} = \left(\frac{\pi}{4}\right)\left(\frac{\Delta V}{R}\right) \tag{G.10}$$

Figure G.5 shows a plot of results from detailed elastic-plastic finite element analyses. In this case, the crack length was 72 in. and the vessel inner radius was 90 in. The ratio between volume change and crack opening area is predicted to be 115 by the approximate solution of Equation (G.10). Figure G.5 shows calculated ratios that range from 98 to 110, with the higher ratios corresponding to higher pressures. On the basis of such comparisons, the simplified equation was judged to be sufficiently accurate for the failure mode simulations.

REFERENCES

DeSalvo, G. J., and J. A. Swanson. 1983. ANSYS Engineering Analysis System Users Manual. Swanson Analysis Systems, Inc., Houston, Pennsylvania.

Irwin, G. R., J. M. Krafft, P. C. Paris, and A. A. Wells. 1967. Basic Aspects of Crack Growth and Fracture. NRL Report 6598, Naval Research Laboratory, Washington, D.C.

Kumar, V., M. D. German, and C. F. Shih. 1981. An Engineering Approach for Elastic-Plastic Fracture Analysis. NP-1931, Electric Power Research Institute, Palo Alto, California.

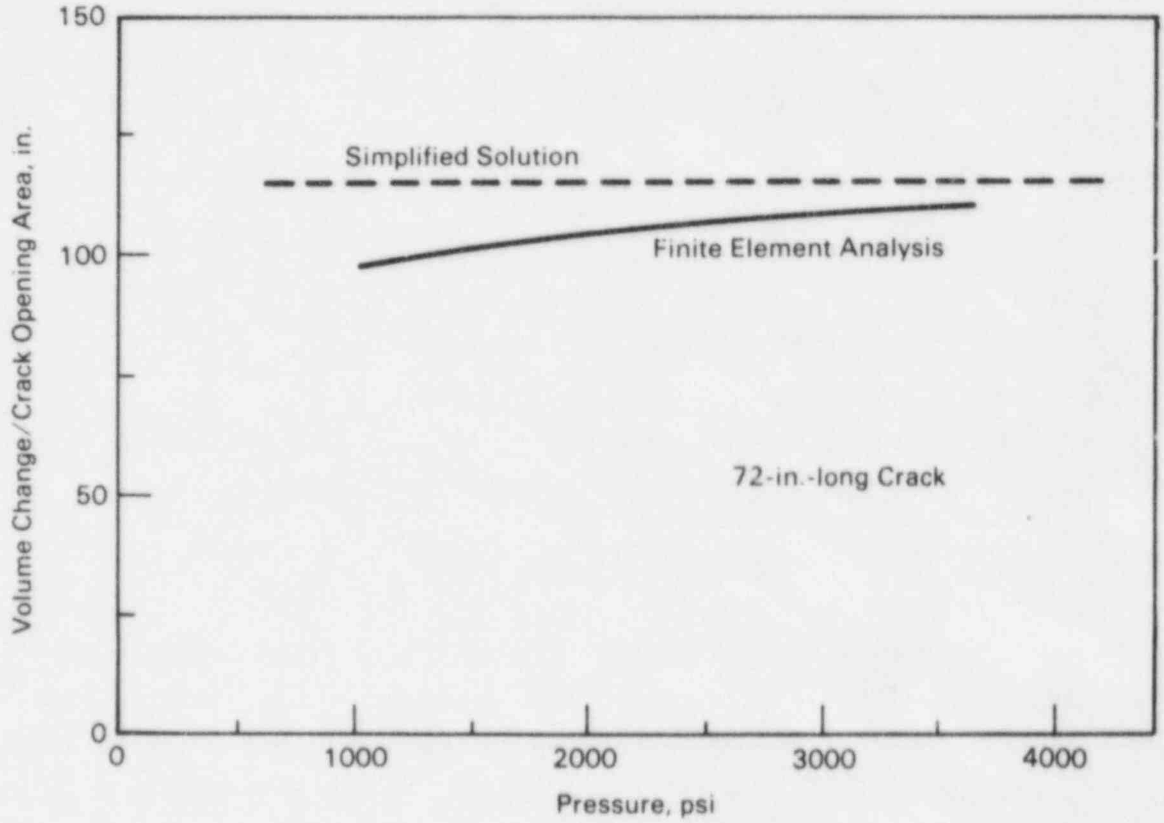

FIGURE G.5. Correlation of Vessel Volume Change and Crack Opening Area

Mayfield, M. E., T. P. Forte, E. C. Rodabaugh, B. N. Leis, and R. J. Eiber. 1980. Cold Leg Integrity Evaluation, NUREG/CR-1319, U.S. Nuclear Regulatory Commission, Washington, D.C.

Rooke, D. P., and D. J. Cartwright. 1976. Compendium of Stress Intensity Factors. Her Majesty's Stationery Office, London, United Kingdom.

Whitman, G. D., and R. H. Bryan. 1982. Heavy-Section Steel Technology Program Quarterly Progress Report for January-March 1982, NUREG/CR-2751 Volume 1, U.S. Nuclear Regulatory Commission, Washington, D.C.

APPENDIX H

DYNAMIC CRACK OPENING BEHAVIOR

APPENDIX H

DYNAMIC CRACK OPENING BEHAVIOR

This appendix describes calculations that predict the dynamic opening response of axial cracks in reactor pressure vessels. Trends from these finite element solutions were used to guide and support assumptions in the simplified analyses of vessel failure modes.

INTRODUCTION

Occurrence of a through-wall axial crack in a cylindrical pressure vessel will result in a complex fluid-structural dynamic response. Previous studies have investigated this phenomenon as it relates to crack propagation behavior (Caldis, Owen, and Taylor 1976; Maxey et al. 1972, pp. 70-81; Baum 1981). These studies have dealt mainly with very long cracks, as in gas pipelines, where deformations are large and the fluid pressure is treated only as a function of axial location. Another class of problem involves the sudden occurrence of a relatively short (one diameter or less) axial crack where deformations are small and the fluid pressure transient involves complex pressure distributions during the crack opening event. A suddenly occurring 2-dia-long axial crack in a pressurized pipe was studied by Ayres (1975). For this case, however, the displacements were large and the transient pressures were treated as spatially uniform.

The effort described in this appendix was to develop a basis for a simplified analysis method that can be used in probabilistic (Monte Carlo) calculations. This analysis investigates the fluid-structural response of a cylindrical pressure vessel to a suddenly occurring through-wall crack. Crack opening displacements were found to be small for the conditions of interest, supporting the application of linear elastic modeling techniques. For the initial crack opening event modeled, elapsed times are also small (1 to 6 milliseconds) and depressurization due to escaping fluid can be reasonably neglected. Decompression of the fluid occurs largely as a result of vessel volume changes, and is localized to the immediate vicinity of the moving vessel wall during short time intervals (0.5 to 2.0 milliseconds). To investigate this phenomenon, several different structural models were applied using the general purpose finite element code ANSYS (DeSalvo and Swanson 1983).

STRUCTURAL MODELING (NO FLUID)

Initially, a three-dimensional (3D) finite element model (Figure H.1) was used to predict dynamic crack opening displacements. Typical pressurized water reactor vessel dimensions were used. The inside radius is 90 in. and the wall thickness is 9 in. This model had no fluid elements, and bounding assumptions were made about vessel depressurization. Using an initial pressure of 500 psi, constant pressure and instantaneous depressurization load cases were simulated in transient dynamic analyses.

Two planes of symmetry are included in the model. One is located at the crack midspan and is perpendicular to the cylinder axis. The other is along the length of the crack and contains the cylinder axis. The third boundary of the model is a plane perpendicular to the cylinder axis located far enough away from the crack tip so that neglected bending effects are not significant. Imposed loads included both an internal surface pressure and the appropriate axial stress load that would occur in a pressurized cylinder. Sudden opening of a crack was simulated by removal of displacement constraints along the plane of the crack.

Results from the bounding load cases applied to this model provided estimates of upper and lower limits for crack opening response. To obtain a more realistic load history, pressurized fluid elements are required. However, incorporating fluid elements in the 3D model for transient analyses was estimated as too costly. Therefore, results from the 3D model were used as a basis for development of a two-dimensional (2D) model that includes fluid elements.

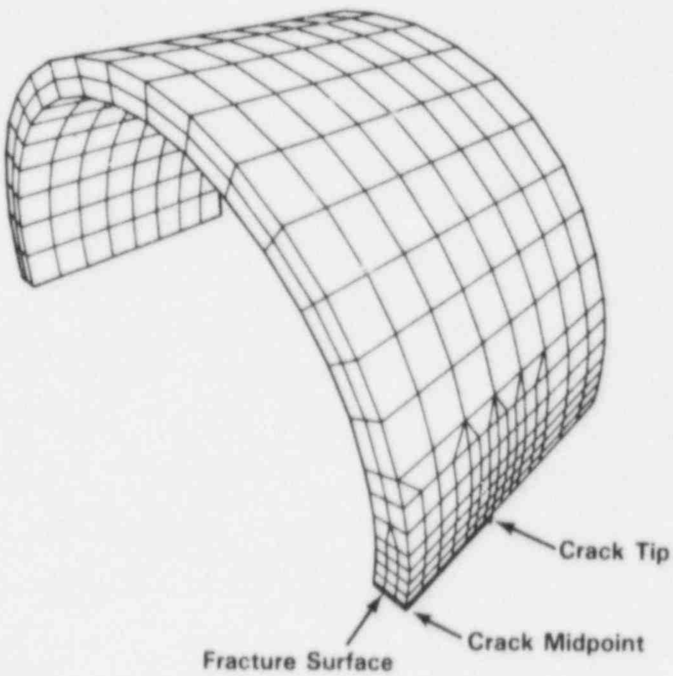

FIGURE H.1. Finite Element Mesh for the 3D Structural Analysis

FLUID STRUCTURAL MODEL

A series of predicted crack opening profiles from the 3D transient analyses is illustrated in Figure H.2. These elliptical opening profiles are typical of all the 3D simulations. These results indicate that, for a known crack length, the opening profile can be reasonably estimated from the midspan displacement. Therefore, a 2D model, designed to predict midspan displacements, can be expected to give good approximations to crack opening behavior.

For calibration with 3D results, the 2D model of Figure H.3 initially contained no fluid elements and was effectively a split ring. The split ring has been previously used by Emery et al. (1981) to model the opening of very long axial cracks in pipes. To properly model shorter cracks, the split ring model required additional stiffening. This stiffening, in the form of radially and tangentially oriented truss elements, simulated the bending and shear forces associated with the bulging around shorter cracks. The truss elements, shown in the inset of Figure H.3, were attached to each of the mid-thickness nodes of the split ring model. The stiffnesses of the truss ele-

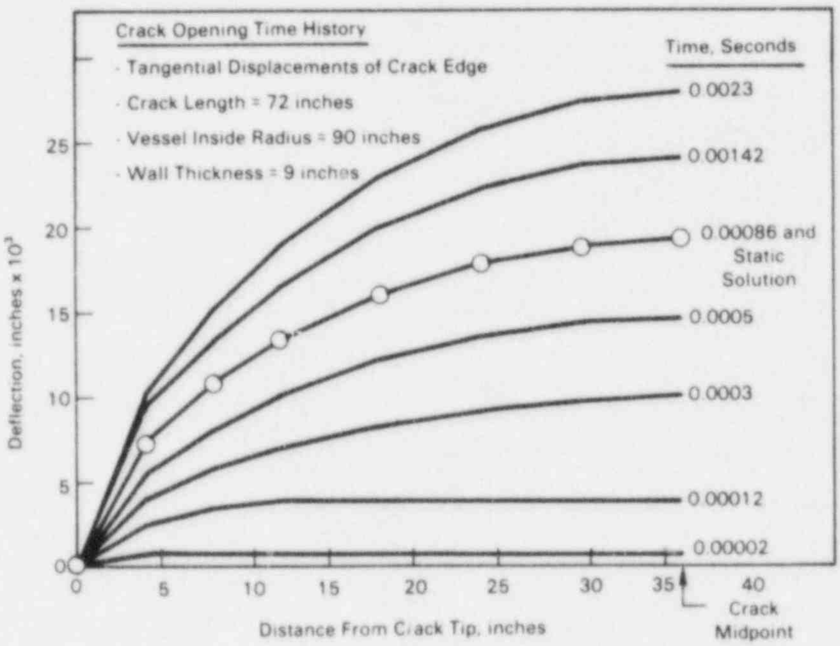

FIGURE H.2. Crack Profiles Predicted by the 3D Model

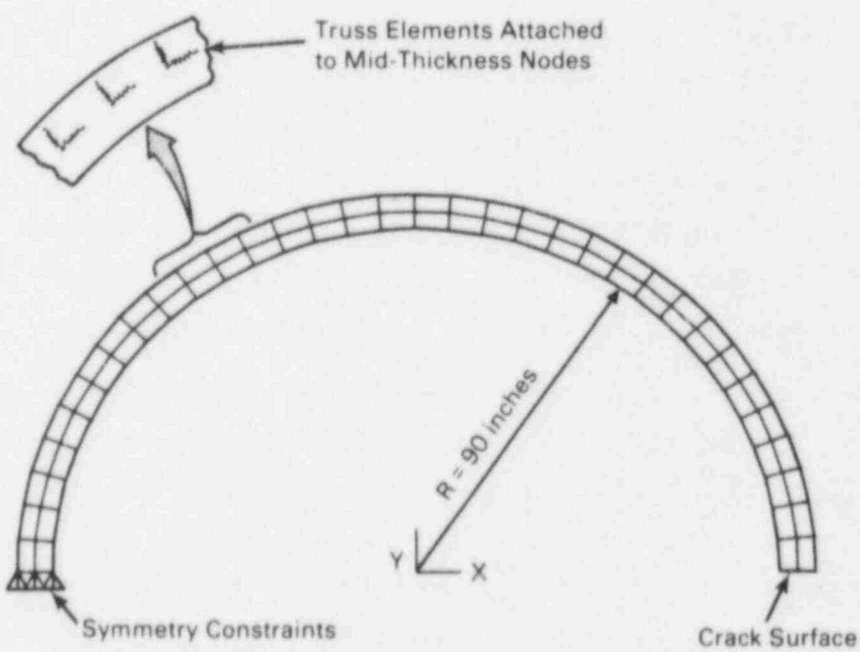

FIGURE H.3. Finite Element Model of the Split Ring ments were adjusted by a trial and error approach so that radial and tangential displacements for a static analysis would closely match those for the 3D model. Stiffnesses were matched for 72-in. and 144-in. crack lengths. The 2D model was also used to simulate the sudden opening of a crack by the removal of displacement constraints.

A comparison, between predictions of the two models, for dynamic simulation results for constant pressure and for instantaneous depressurization load cases is shown in Figures H.4 and H.5. The curves show radial and tangential displacement histories for a point at crack midspan of a 72-in. crack. The comparison shows that the rates of crack opening and maximum opening displacements are nearly the same. This indicates that the 2D model gives a good

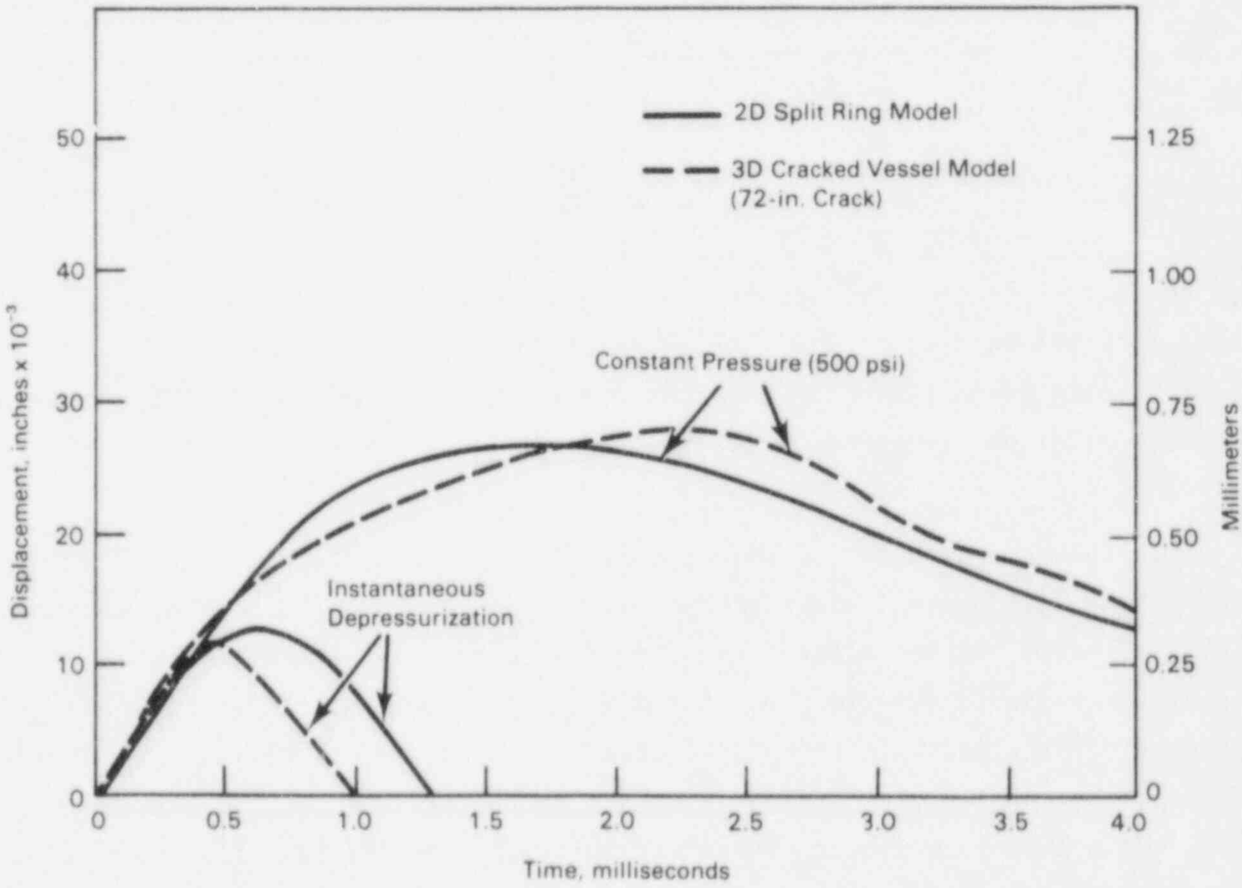

FIGURE H.4. Comparison Between 2D and 3D Models of Tangential Crack Opening Displacement

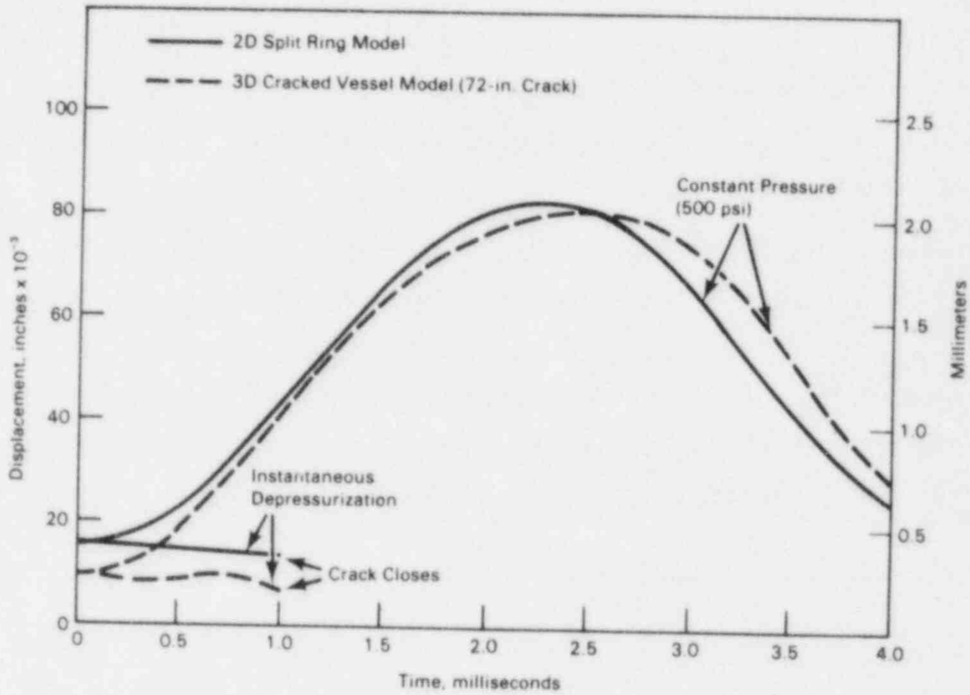

FIGURE H.5. Comparison Between 2D and 3D Models of Radial Crack Opening Displacements

approximation of the displacements of the 3D model at crack mid-length. Note that both models predict substantial crack opening displacements, even for the extreme case of instantaneous depressurization. The opening for instantaneous depressurization is caused by the release of strain energy from the vessel itself.

As the next step in the development of the model, the interior of the 2D model was filled with solid elements having material properties that simulated those of water. A low elastic modulus of 1800 psi was used with a high Poisson's ratio (0.499) to yield a realistic bulk modulus of 3×10^5 psi. The geometry of the model is shown in Figure H.6. Fluid pressure was simulated by a thermal expansion of the fluid elements combined with model boundary constraints and a plane strain element formulation. An initial pressure of 500 psi was used for comparative purposes in all analyses. Figure H.6 shows that a small semicircular void was left in the center of the model. This "hole", which is effectively a small semicircular rigid boundary, expedited the model

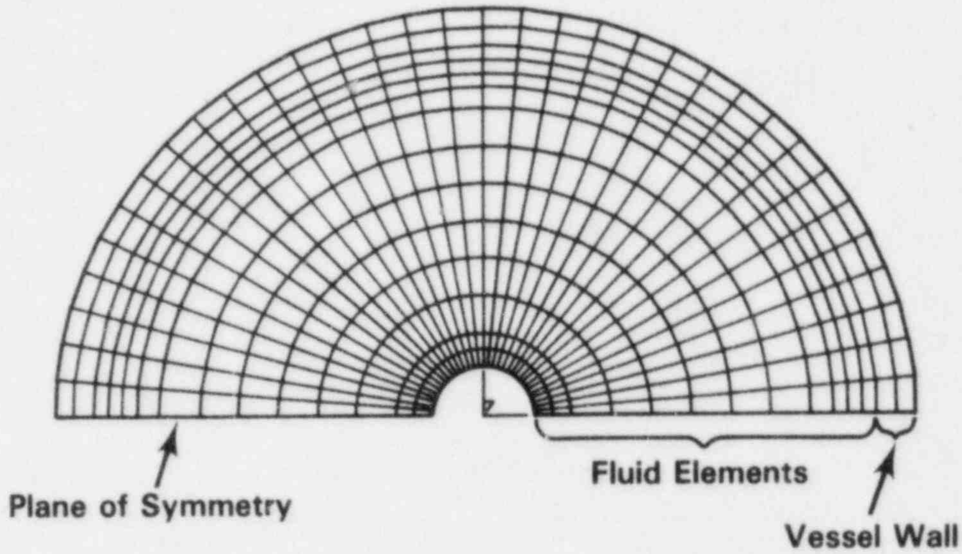

FIGURE H.6. Finite Element Mesh of the 2D FS Model

development by avoiding the tedious input of mesh transitions necessary to fill the space with elements. The effect on simulation results was found to be negligible.

FLUID ELEMENT BEHAVIOR

A series of stress contour plots, shown in Figures H.7 through H.10, shows the decompression behavior of the fluid. The contour lines indicate lines of constant pressure. Shear stresses were effectively zero, verifying the desired fluid type of behavior. Also, the calculated propagation speed of pressure waves in the modeled fluid agreed with handbook values for pressure wave speeds in water. Each of the contour plots represents an instant in time during the transient. Figure H.7 shows the initial localized depressurization of fluid in the immediate vicinity of the opening crack. Figures H.8 through H.10 show further depressurization and the development of complex pressure distributions at later times in the transient.

The contour plots indicate significant local decompression from the initial 500-psi pressure near the moving wall at the opening crack. This results in smaller pressures exerted on the vessel during crack opening than

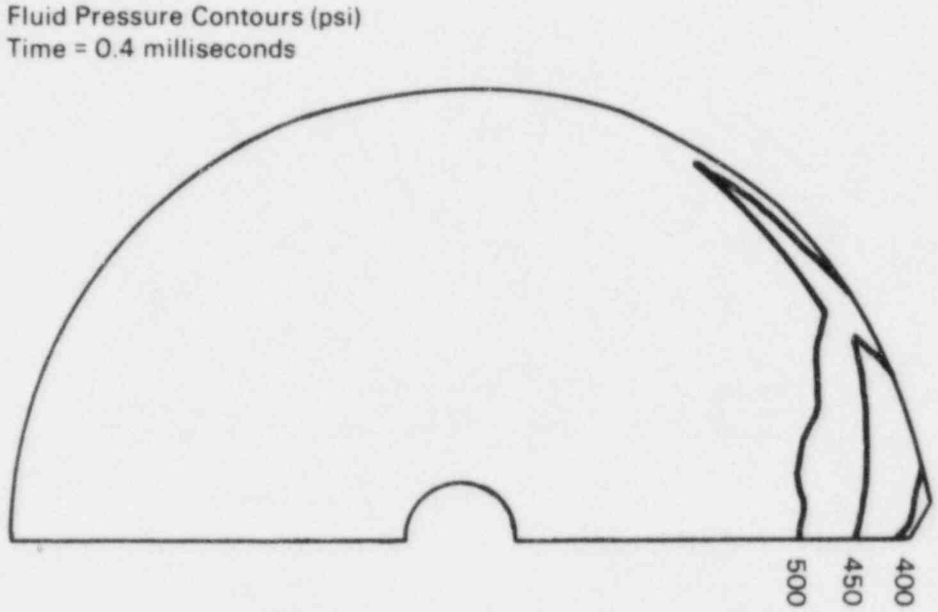

FIGURE H.7. Fluid Pressure Distribution at 0.4 Milliseconds

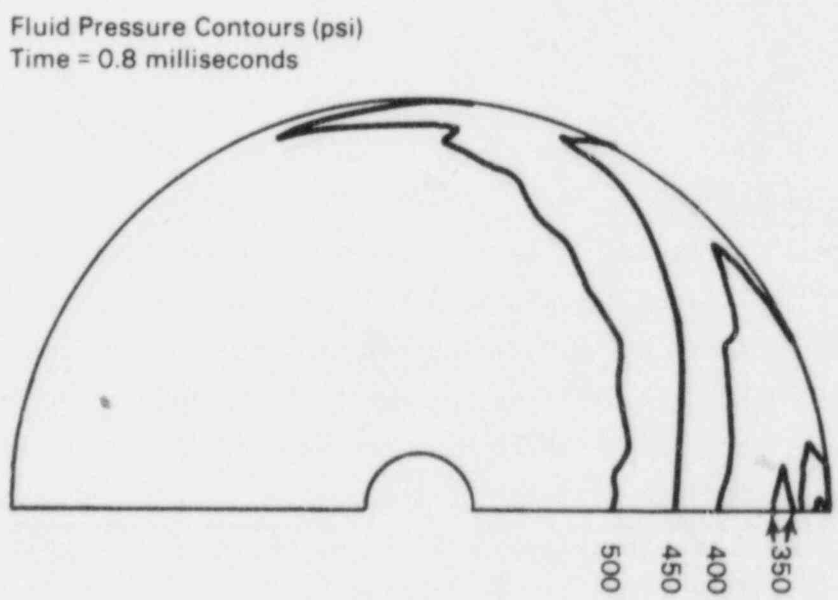

FIGURE H.8. Fluid Pressure Distribution at 0.8 Milliseconds

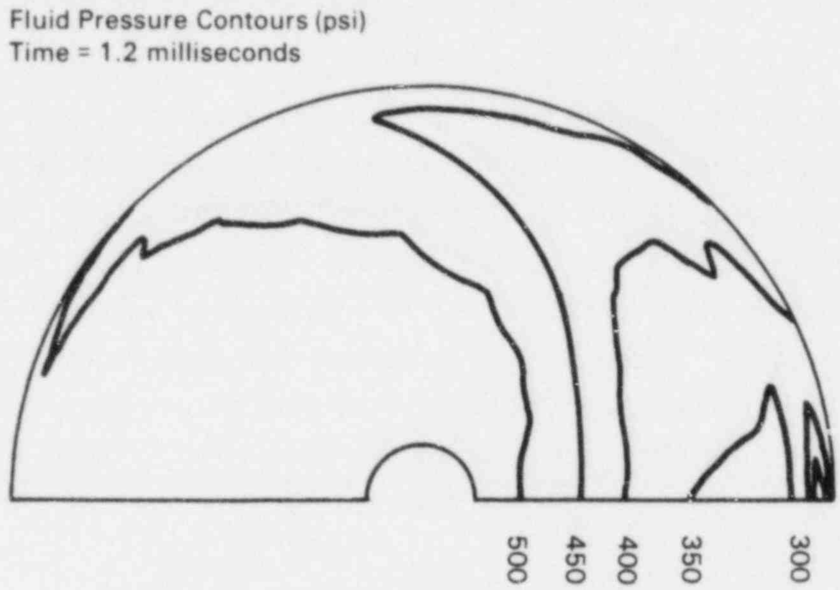

FIGURE H.9. Fluid Pressure Distribution at 1.2 Milliseconds

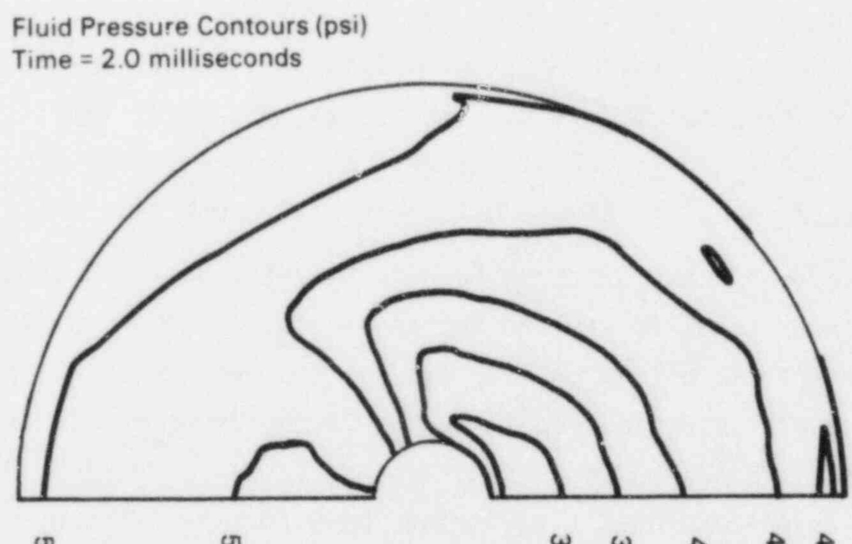

FIGURE H.10. Fluid Pressure Distribution at 2.0 Milliseconds would be predicted by a pressure calculation based on a uniform volume change. This effect will, in turn, cause crack opening displacements to be reduced.

It was noted that pressure contours near the vessel wall are not smooth and appear inconsistent. The contours are generated via nodal stresses, which are estimated by extrapolation of stresses from element integration points (DeSalvo and Swanson 1983). Element centroidal stresses were found to disagree with the pressure contours near the wall (see Figure H.7) in that they indicate a uniform decrease in pressure as the wall is approached. Therefore, it is believed that the calculated results are more accurate than what might be concluded from studying the contour lines. The nodal stresses used to generate the contours are believed to be inaccurate at the material interface (water/steel).

FLUID STRUCTURAL MODEL WITH CORE BARREL

A typical feature of nuclear reactor pressure vessels is the presence of cylindrical components (such as the core barrel) concentric to the main vessel. To investigate the effects of a 5-in.-thick cylinder on fluid depressurization and crack opening displacements, the model was modified to include the presence of the additional structure. This was accomplished by giving the ring of elements, shown in Figure H.11, material properties of steel.

The pressure contour plots in Figures H.12 through H.15 show that the internal cylinder tends to isolate the inner fluid region from the decompressive effects of the opening crack. The result is an effectively smaller volume of compressed liquid to absorb the decompressive effect of the bulging vessel. This produces a reduction in pressure local to the vessel wall and, therefore, reduces the driving force for the crack opening event.

COMPARISON OF PREDICTED RESPONSES

For comparison, displacement results from the 2D fluid-structural model and the 3D model are plotted together in Figures H.16 through H.19. Figures H.16 and H.17 show tangential and radial displacements for a 72-in. crack, while Figures H.18 and H.19 are for a 144-in. crack. Also shown in each of

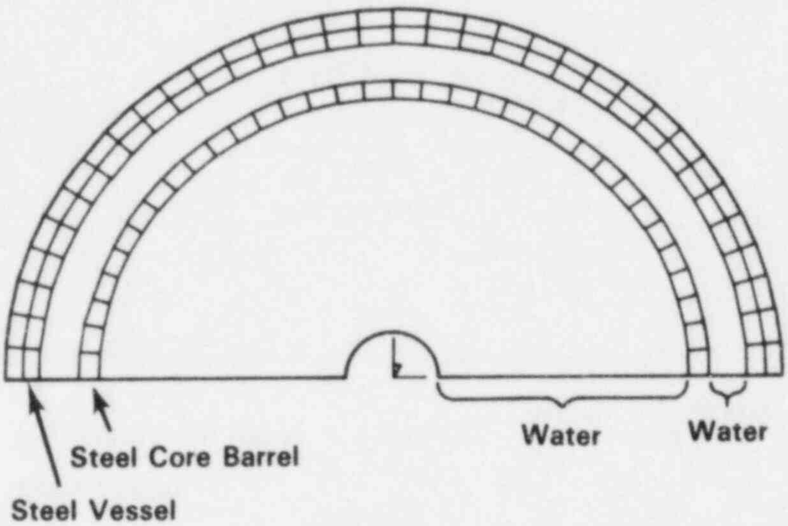

FIGURE H.11. Finite Element Model with Core Barrel Included

Fluid Pressure Contours (With Core Barrel) (psi)
Time = 0.4 milliseconds

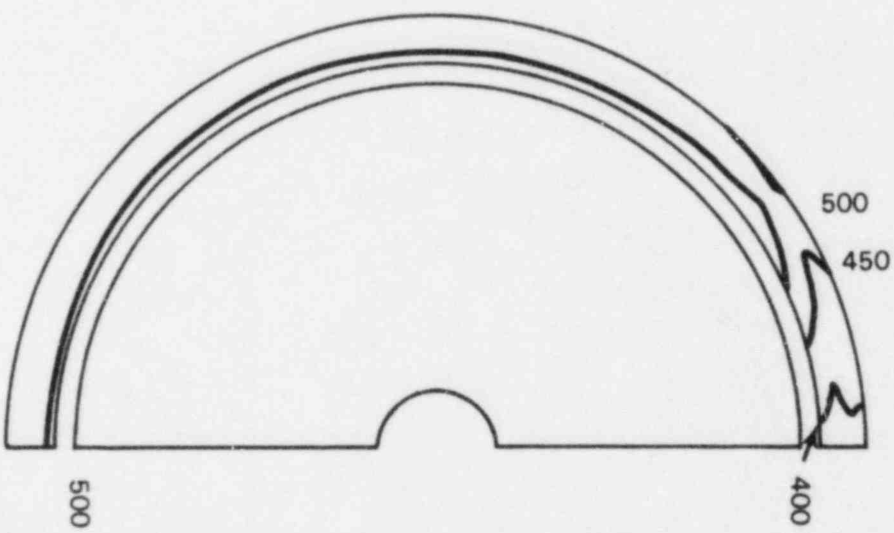

FIGURE H.12. Fluid Pressure Distribution at 0.4 Milliseconds (with Core Barrel)

Fluid Pressure Contours (With Core Barrel) (psi)
Time = 0.8 milliseconds

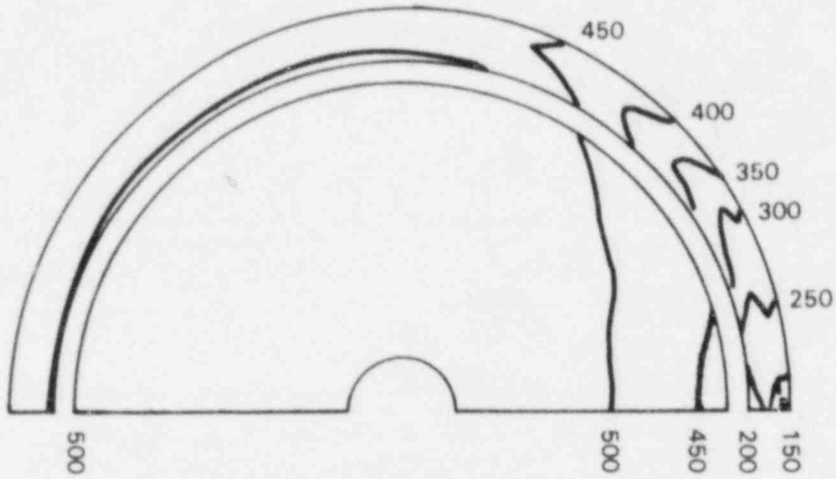

FIGURE H.13. Fluid Pressure Distribution at 0.8 Milliseconds (with Core Barrel)

Fluid Pressure Contours (With Core Barrel) (psi)
Time = 1.2 milliseconds

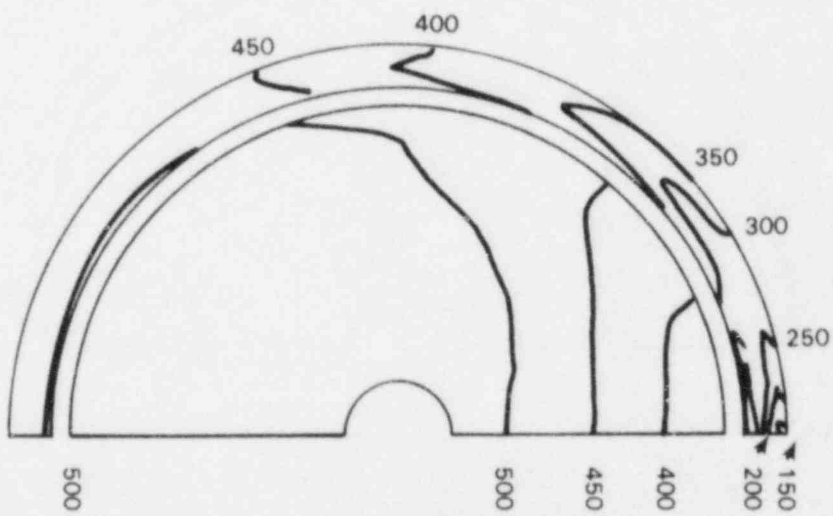

FIGURE H.14. Fluid Pressure Distribution at 1.2 Milliseconds (with Core Barrel)

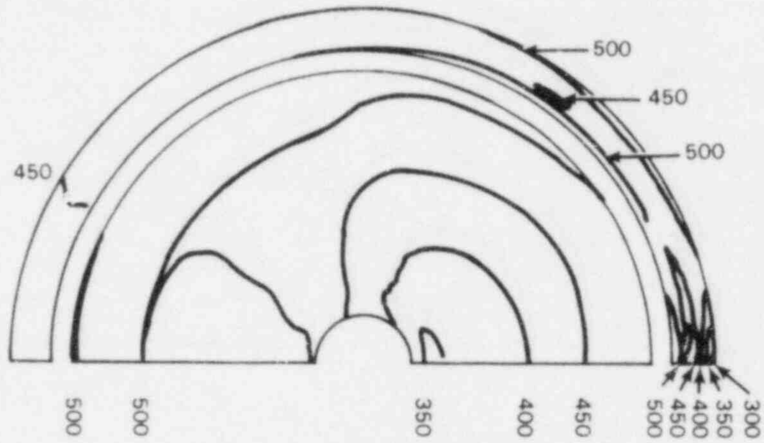

FIGURE H.15. Fluid Pressure Distribution at 2.0 Milliseconds (with Core Barrel)

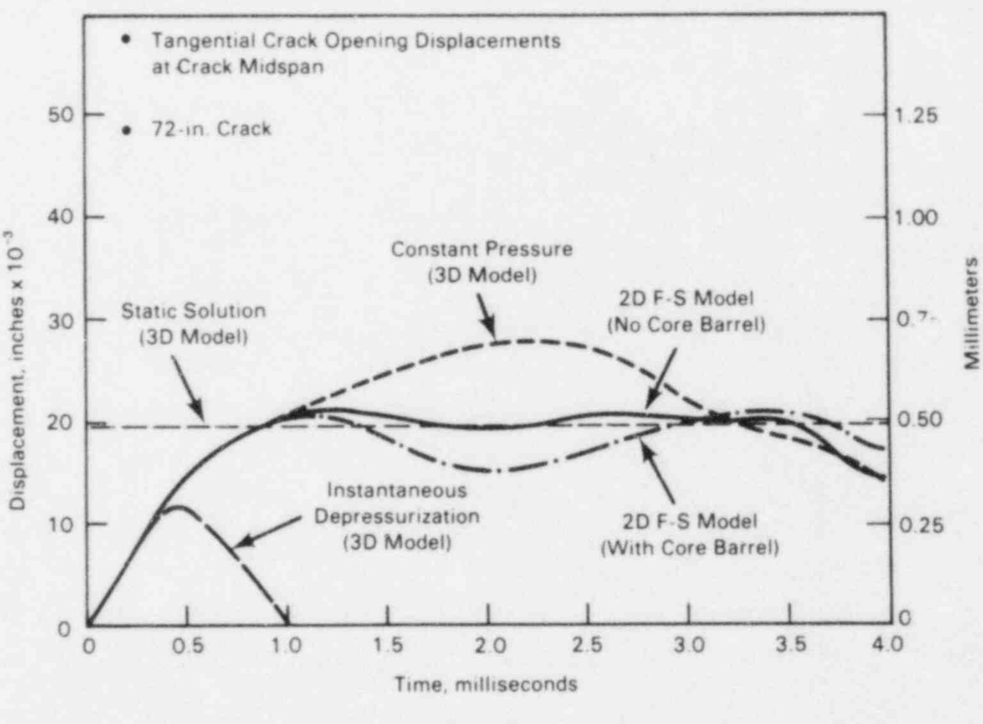

FIGURE H.16. Dynamic Crack Opening Results

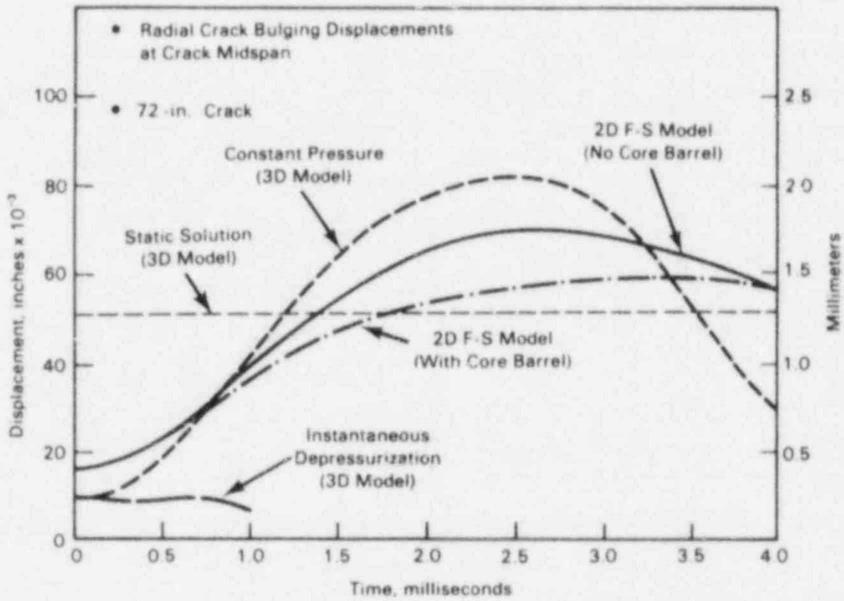

FIGURE H.17. Dynamic Crack Opening Results

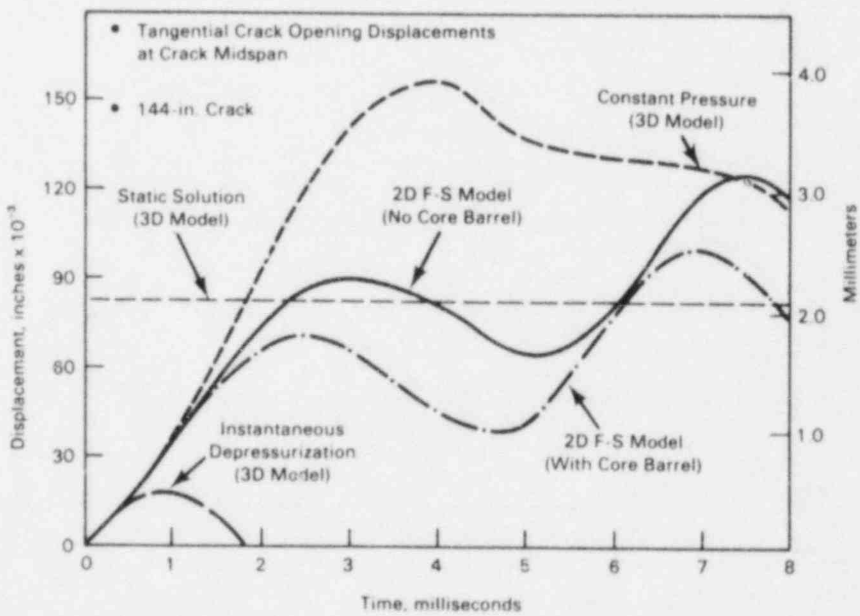

FIGURE H.18. Dynamic Crack Opening Results

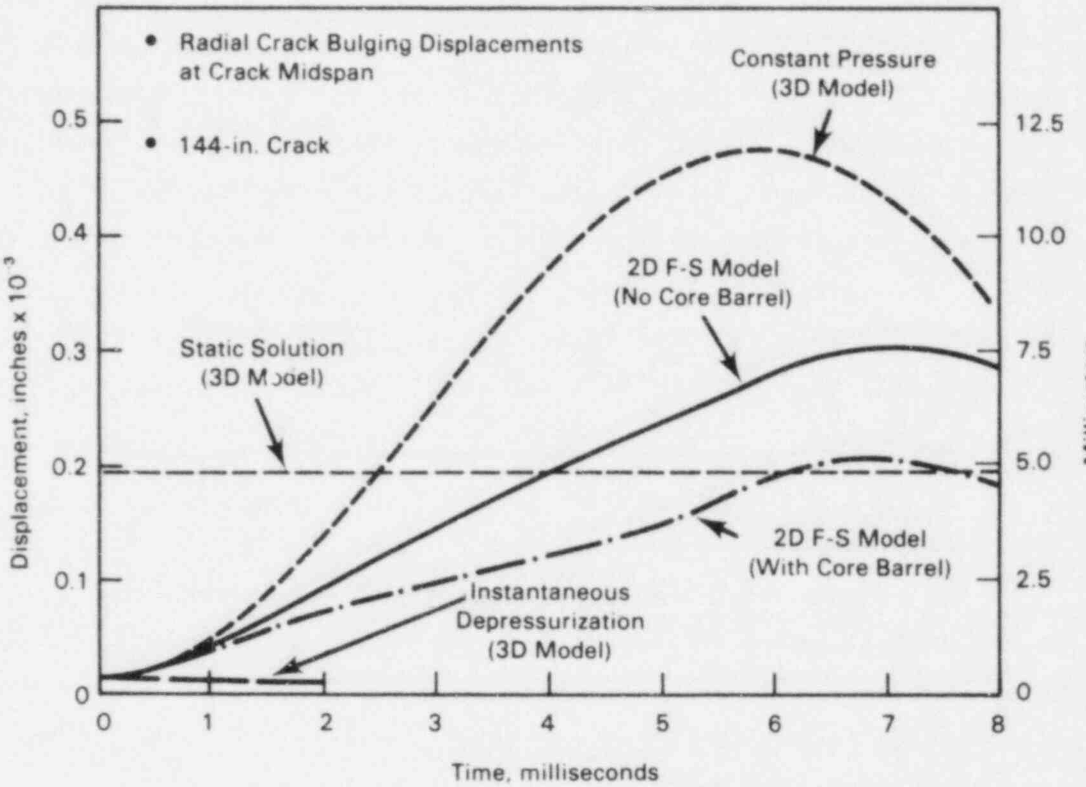

FIGURE H.19. Dynamic Crack Opening Results

the figures is the static crack opening displacement predicted by the 3D model for the initial pressure.

As expected, the 2D fluid-structural model predicts results intermediate to the bounding cases simulated by the 3D model. The depressurization of the fluid results in reduced maximum crack opening displacements. The core barrel, which enhances local fluid depressurization, causes additional reductions in crack opening displacements. These attenuated peak displacements are very close to the static displacements predicted by the 3D model for the initial pressure.

The 144-in. crack is predicted to have longer crack opening times and peak displacements that are nearly an order of magnitude larger than for the shorter 72-in. crack. This provides an indication of the sensitivity of crack opening response to crack length.

In summary, finite element models were developed that estimate the fluid-structural response of a pressurized cylinder to the sudden occurrence of an axial crack. It has been shown that a stiffened split ring model can be used to approximate dynamic crack opening behavior. From results obtained, it appears that the maximum crack opening displacements may be estimated from a static solution for the initial pressure. In effect, the dynamic amplification effect from sudden crack opening is offset by the reduction in pressure associated with fluid structural interactions. These conclusions apply for a relatively short crack in a fluid-filled vessel where crack opening displacements are small.

APPLICATION TO FAILURE MODE ANALYSIS

The detailed finite element results were applied to develop a simplified calculation method for the failure mode evaluations. In particular, the results of this appendix were used to address the effects of dynamic response on applied stress intensity factor for through-wall axial cracks. The results also allowed estimates of crack opening times to be made.

Stress Intensity Factor Solutions

The crack opening displacements from dynamic analyses were used to estimate crack tip stress intensity factors. In linear elastic fracture mechanics, it is shown that stress intensity factors are proportional to crack opening displacements. Published solutions for static loading (Rooke and Cartwright 1976) were used to calibrate the finite element models so that calculated displacements could be applied directly to estimate stress intensity factors by use of simple multipliers.

Figure H.20 shows trends of the estimates of stress intensity factors. The dependence of the stress intensity factor on the vessel depressurization history can be observed. Stress intensity factors in Figure H.20 are normalized in the customary manner with respect to the factor $\sigma\sqrt{\pi a}$, where σ is the hoop stress in the uncracked vessel and a is the half crack length. The static solution is based on published handbook results for axially cracked cylinders under constant pressure (Rooke and Cartwright 1976).

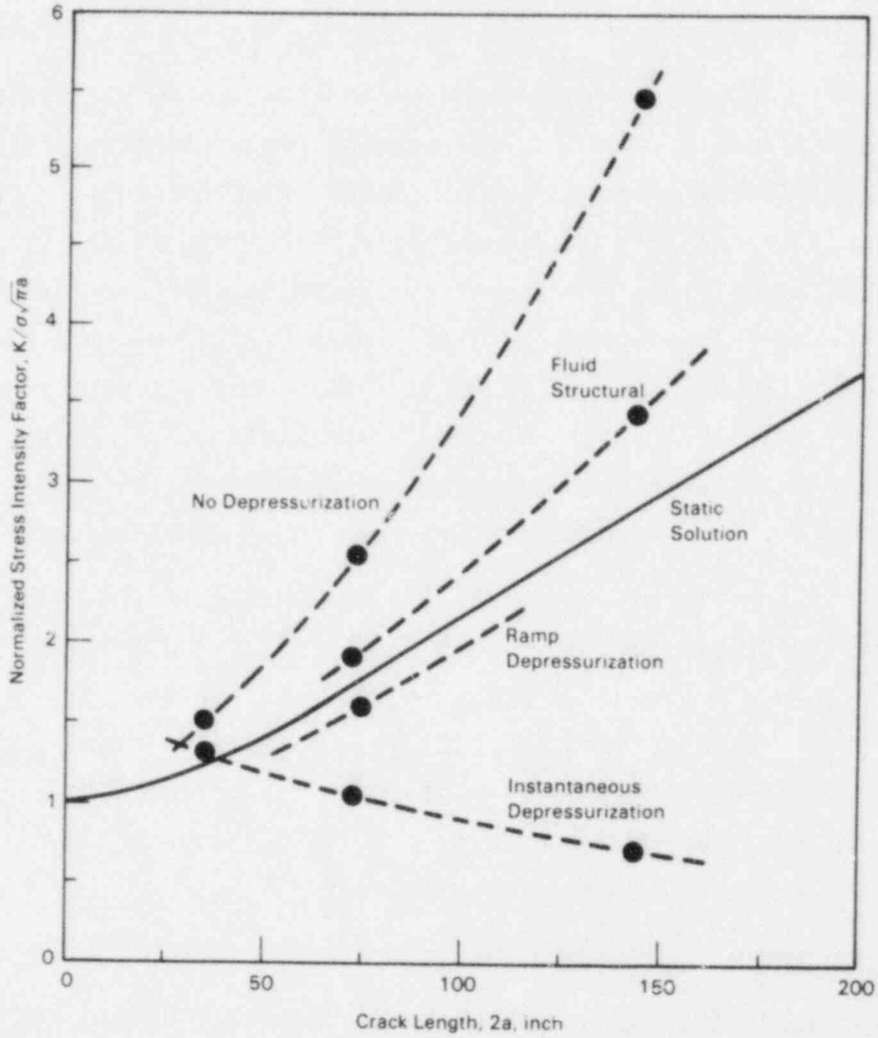

FIGURE H.20. Effects of Structural Dynamics and Depressurization on Stress Intensity Factor Due to Opening of Axial Crack in Vessel

One significant trend of the dynamic solutions is the significant opening of the crack for the bounding case of instantaneous depressurization. Therefore, a significant crack driving force will be present even for the most extreme assumption regarding depressurization. The stress intensity factor solutions of Figure H.20 shows a normalized factor of about 1.0 for instantaneous depressurization. This factor does not increase with crack length as do the factors for the static and sustained pressure solutions. In this regard, the factor of 1.0 for instantaneous depressurization is equivalent to neglecting the bulging factor that is commonly used to correct flat plate solutions for the effects of cylindrical geometry.

In Figure H.20, the dynamic solution for ramp depressurization to zero pressure over the period of the crack opening event gives a stress intensity factor that is roughly equal to the static solution for constant pressure. On the other hand, the dynamic stress intensity factors that neglect depressurization consistently exceed the static solutions for constant pressure. The curve labeled "fluid-structural" in Figure H.20 is perhaps the best basis for estimating stress intensity factors. This curve was plotted from Figures H.16 and H.18 using the results of the 2D model with core barrel. The greater of the two indicated displacement peaks was used to estimate the stress intensity factors, and, hence, the curve may be somewhat conservative.

In all of the failure model evaluations documented in this report, it was assumed that the static solution could be used to calculate dynamic stress intensity factors. The initial pressure was used for the static analysis with no consideration of reductions in pressure due to fluid structural interaction. This procedure greatly simplified the calculations. Figure H.20 indicates that this approximation gives relatively good estimates of the actual dynamic value of stress intensity factor.

Crack Opening Time

The depressurization that may occur during crack opening is estimated as part of the calculations of the failure mode evaluations. However, these results are provided only for information as a guide for identifying situations for which the simplifying assumptions are inappropriate.

The estimated time for the crack to open is used as an input parameter tc calculations for the loss of fluid through the opening crack. This loss reduces the volume of fluid in the vessel and, hence, reduces the pressure within the vessel.

Early in this research project, estimates of crack opening time were based on application of a beam model, which gave the prediction

$$\text{time} = \frac{\pi(2a)^2}{2\lambda^2}\left[\frac{12\ \rho/g}{Et^2}\right]^{\frac{1}{2}} \qquad (H.1)$$

where $2a$ = crack length

λ = 4.73

ρ/g = density of steel

E = elastic modulus

t = wall thickness.

Equation (H.1) predicts that the opening time is a function of the crack length squared and inversely proportional to the wall thickness of the vessel.

The results of the dynamic finite element solutions were plotted in Figure H.21. Evidently, the analysis of the cylindrical geometry of the vessel predicts a linear function of opening time versus crack length, as

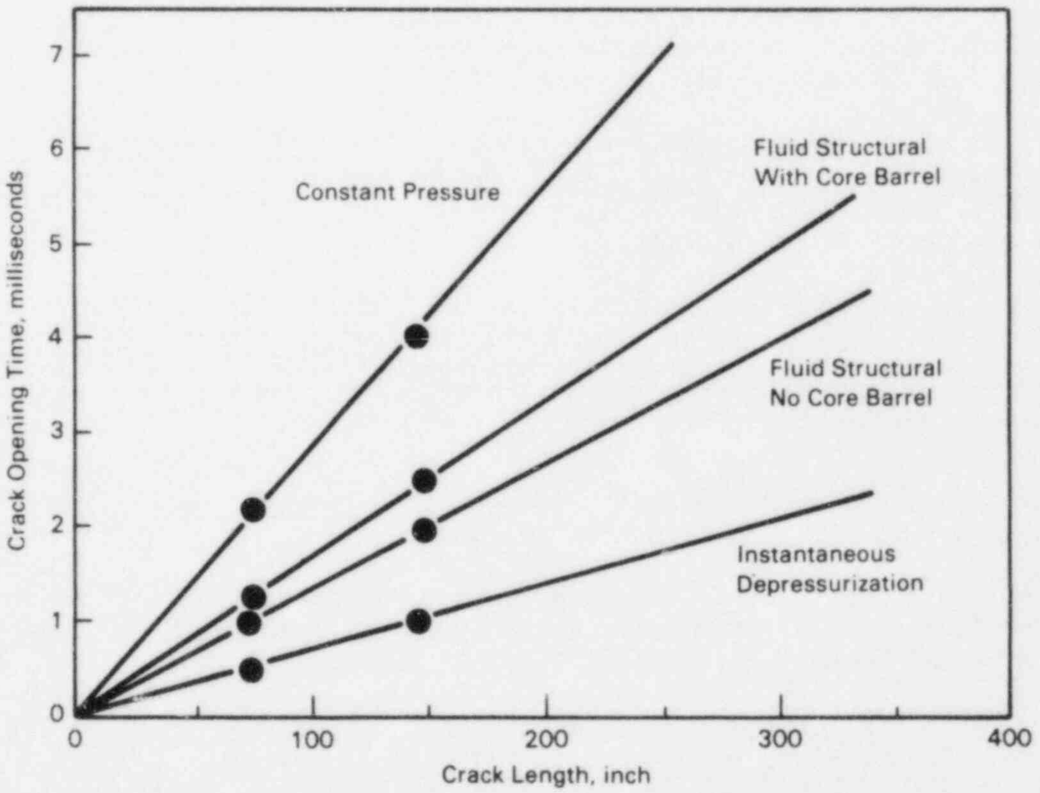

FIGURE H.21. Opening Times for Axial Cracks in Reactor Vessels opposed to the quadratic behavior of the beam approximation. The curve of Figure H.21 for the fluid structural model with core barrel was the basis for the predictive equation

$$\text{time} = 0.0012\ (\frac{2a}{t}) \qquad (H.2)$$

where t = wall thickness, in.

$2a$ = crack length, in.

time = time for crack to open, sec.

Equation (H.2) was used in the failure mode evaluations. It is applicable to steel vessels with the dimensions and crack lengths of interest to pressurized thermal shock analyses.

REFERENCES

Ayres, D. J. 1975. "Elastic-Plastic Dynamic Analysis of Opening Area of an Axial Crack in a Pipe Under Pressure." Paper L-7/6 presented at the 3rd International Conference on Structural Mechanics in Reactor Technology, September 1975, London, United Kingdom.

Baum, M. R. 1981. The Relationship Between Breach Development and the Depressurization Transient During Axial Rupture of a Gas-Pressurized Steel Pipe. RD/B/5025N81, Berkeley Nuclear Laboratories., Central Electricity Generating Board, United Kingdom.

Caldis, E. S., Owen, D. R. J., and Taylor, C. 1983. "Transient Dynamic Crack Propagation in Gas Pressurized Pipelines." In Transactions of the 7th International Conference on Structural Mechanics in Reactor Technology, Vol. B Thermal and Fluid/Structure Dynamics Analysis, Chicago, Illinois, August 22-26, 1983.

DeSalvo, G. J., and J. A. Swanson. 1983. ANSYS User's Manual. Swanson Analysis Systems, Inc., Houston, Pennsylvania.

Emery, A. F., M. Perl, A. S. Kobayashi, and W. J. Love. 1981. "The Use of the Split Ring in Modeling Ductile Axial Crack Extension in Pipe." Journal of Pressure Vessel Technology. 103:151-154.

Maxey, W. A., J. F. Kiefner, R. J. Eiber, and A. R. Duffy. Ductile Fracture Initiation, Propagation, and Arrest in Cylindrical Vessels." ASTM STP 514, American Society for Testing and Materials, Philadelphia, Pennsylvania.

Rooke, D. P., and D. J. Cartwright. 1976. Compendium of Stress Intensity Factors. Her Majesty's Stationery Office, London, United Kingdom.

APPENDIX I

<u>LEAK RATE CALCULATIONS</u>

APPENDIX I

LEAK RATE CALCULATIONS

Accurate prediction of leakage flow through the through-wall cracks at the vessel beltline region is important in estimating the vessel depressurization and subsequent crack behavior. This appendix will document the equations used to predict the flow of subcooled water through an open crack.

Battelle Columbus Laboratory has developed a detailed analytical model to predict the choked flow through cracks (Mayfield et al. 1980). The model is basically applicable to the case where the flow changes to the two-phase regime before it reaches the exit. This model is valid for the case where the upstream liquid is close to saturation, such as in the case of primary piping cracks at the operating conditions of a LWR (for PWRs, p = 2250 psia, T = 550°F) and when the crack length (L) to the hydraulic diameter (D_h) ratio is large ($L/D_h >> 12$). For the case of PTS, when the downcomer liquid is significantly subcooled, the pressure drop through the crack is not sufficient to cause the liquid to flash before it exits the vessel. A typical case would be p = 2000 psia, T = 300°F. The pressure has to drop from 2000 psia to 67 psia before liquid flashes. An approximate calculation showed that, for the case of a 72-in.-long crack ($L/D \cong 57$), ΔP due to friction is about 200 psi and ΔP due to area change is about 300 psi. The exit pressure is therefore about 1500 psi, and the liquid is still significantly subcooled. For the larger crack sizes, the L/D_h ratio is even smaller, and the exit liquid would be more subcooled. Therefore, for the current PTS analysis, the two-phase model is judged to be inadequate. The subcooled choke model should be used.

SUBCOOLED CHOKE FLOW

In the subcooled choke flow, water stays in liquid phase until it reaches the exit where the pressure drops to the saturation pressure (corresponding to fluid temperature in vessel). The Bernoulli equation is applicable:

$$v_c = [v_o^2 + 2g_c\ (P_o - P_{sat})/\rho]^{\frac{1}{2}} \tag{I.1}$$

where v_o is the upstream (vessel) velocity and P_o is upstream pressure minus the frictional pressure drop. P_{sat} is the saturation pressure, and ρ is the average liquid density along the crack. In this case the upstream density may be used for ρ. The parameter g_c is a conversion factor (= 32.2 lbm-ft/lbf-sec^2).

For PTS calculations, $v_o = 0$, and Equation (I.1) becomes

$$v_c = [2g_c\ (P_o - P_{sat})/\rho]^{\frac{1}{2}} \tag{I.2}$$

The choked mass flux is then

$$G_c = C_D\ \rho\ v_c = C_D\ [2g_c\rho(P_o - P_{sat})]^{\frac{1}{2}} \tag{I.3}$$

If ρ is in units of lbm/ft^3 and p is in units of lbf/ft^2, then G_c is in units of lbm/sec-ft^2.

The discharge coefficient C_D is included to account for the contraction effect. For a circular opening, its value is 0.61. For an elongated crack opening, C_D should be larger than 0.61. Therefore, this value would yield slightly conservative results (i.e., slower depressurization).

To calculate P_o, the frictional pressure drop needs to be estimated using the equation

$$\Delta P_f = \frac{1}{2}\ f\ (\frac{L}{D_h})\ \frac{G_c^{\ 2}}{g_c\rho_\ell} \tag{I.4}$$

where $f = [2\ \ell n\ \frac{D_h}{2\delta} + 1.74]^{-2}$ is the friction factor.

The parameter δ is the height of protrusion of the roughness grain from the mean surface. Abdollahian and Chexal (1983) suggested a value of 5.1 x 10^{-3} mm (2.0 x 10^{-4} in.) for δ. The calculated values of f for different cracks are given in Table I.1.

TABLE I.1. Calculated Flow Rates Through Cracks of Various Lengths (Pressure = 2000 psia and Temperature = 300°F)

	Crack Length, in.			
	72	96	120	144
Hydraulic diameter (D_h), in.	0.14	1.04	4.16	14
L/D_h	57	7.69	1.92	0.57
Friction factor (f)	0.006	0.003	0.002	0.001
Break mass flux (G_c), lbm/sec-ft^2	15189	16060	16129	16129
Crack opening area, in.^{2}	5	50	250	1000
Break flow rate, lbm/sec	527	5576	28000	112000

If we ignore the pressure drop due to crack turning, then

$$P_o = P_{DC} - \Delta P_f \tag{I.5}$$

where P_{DC} is the vessel downcomer pressure.

Equations (I.3), (I.4), and (I.5) are solved iteratively to obtain the choked mass flux G_c.

NUMERICAL RESULTS

Using typical boundary conditions for PTS transients P_{DC} = 2000 psia, T = 300°F, we have

$$P_{sat} = 67 \text{ psia}$$
$$\rho_\ell = 39 \text{ lbm/ft}^3$$

The calculated choke flow rates are given in Table I.1. As can be seen, as the crack opening becomes large ($L/D \leq 1$), the flow rate is linearly proportional to the opening area. This is because the effect of frictional pressure drop across the crack is not important for large crack openings.

TRANSIT TIME FOR SONIC WAVE

During the first few milliseconds when the crack starts to go through the wall, the break flow starts from zero until it reaches the choked value. Within this period, the decompression and compression waves will travel back and forth inside the vessel at the sonic speed. As discussed before, because the water will remain in a liquid phase through the crack in a typical PTS transient, the sonic velocity used in Appendix H, i.e., 4700 ft/sec, is correct. Therefore, the traveling time of the waves is also correct.

REFERENCES

Abdollahian, D., and B. Chexal, 1983. Calculation of Leak Rates Through Cracks in Pipes and Tubes. NP-3395, Electric Power Research Institute, Palo Alto, California.

Mayfield, M. E., T. P. Forte, E. C. Rodabaugh, B. N. Leis, and R. J. Eiber. 1980. Cold Leg Integrity Evaluation. NUREG/CR-1319, U.S. Nuclear Regulatory Commission, Washington, D.C.

APPENDIX J

FRAGMENTATION MISSILE EVALUATION

APPENDIX J

FRAGMENTATION MISSILE EVALUATION

This appendix presents the evaluations of missiles that may be accelerated in the horizontal direction as the result of fragmentation of a vessel during a fracture event. Although there is a vast amount of information in the literature on blast and fragmentation phenomena, there is no methodology available to predict precise fragment sizes and velocities for use in predictions of hazards and damage from pressure vessel accidents. This appendix first provides a brief survey of available information on fragmentation and missiles as a guide to literature on these topics. The second part of this appendix interprets data from a selected collection of vessel failures, and concludes that fragments are quite possible for vessels that fracture under conditions of pressurized thermal shock. The final sections of this appendix present methods and example calculations that predict missile velocities and penetration depths for concrete impact.

LITERATURE SURVEY

A number of systematic literature surveys have been performed over the years on the general issue of hazards associated with pressure vessels. No attempt was made in this study to perform a comprehensive survey, because such background information is readily available in Moore (1967), Gawaltney (1968), Baker (1984a), Brown (1985), Pittman (1972, 1976), and Proctor (1967). In addition, the literature contains numerous references to specific incidents involving industrial accidents of vessels that fractured either in service or during preservice hydrotests. For example, see Banks (1973) and Weck (1966). Further, a vast body of information from the field of military ordnance and ballistics is relevant to the current concern with missile hazards in nuclear power plants.

A computerized literature search provided about 300 listings. Those papers and reports of most interest were obtained and used as a basis for determining the possibility of fragmentation during vessel fracture. The next section summarizes an interpretation of the data from a carefully selected collection of vessel burst incidents. These incidents involved both accidents and bursts that occurred under well controlled experimental conditions.

PRESENTATION OF EXPERIMENTAL DATA

After preliminary evaluation of available documents, seven reference sources were judged to be suitable and adequate to identify trends in fracture behavior. These references provided descriptions of some two dozen fracture cases for examination. Of principal interest was evidence of crack curving and branching, because these behaviors produce fragments. Other information also was compiled from the selected reports, to identify any common factors among those vessels that fragmented and as against those vessels that did not fragment. Table J.1 provides a list of the fracture conditions. The selected references are summarized below.

- Weck (1966) - Submerged defects in the weld-metal doubtless triggered the fracture. The base metal would have arrested a dynamic crack of no less than 13 in. to have prevented vessel failure. The weld-metal yield strength was approximately 100 ksi; the base-metal yield strength was about half that, or about 50 ksi. The local stresses were probably >50 ksi at the 5/8-in. diameter internal flaw. Hence, the crack driving force was about $0.6S\sqrt{\pi a} > 30$ ksi $\sqrt{in.}$ The K_{Id} of the weld was 30 ksi $\sqrt{in.}$ (for CVN ≅ 10). After the initial failure, the crack can be assumed to have propagated into a vessel stress of $pr/t = 5000(34)/5.75 = 29.6$ ksi. Driving conditions for a crack about 13 in. long were then $K \cong 29.6\sqrt{\pi(6.5)} = 134$ ksi $\sqrt{in.}$ Estimating the base-metal toughness from CVN correlations, the dynamic arrest toughness K_{Id} was less than 100 ksi $\sqrt{in.}$ Under these conditions, fracture is judged to be "certain". The vessel had an R/t of about 6. The resulting fragments were two or more times bigger than $\sqrt{Rt}$.
- Banks (1973) - A tank failed from an initial "thumbnail" defect that was about 4.5 in. long and 0.5 in. deep. The crack was in the heat-affected

TABLE J.1. Failure Conditions and Fracture Types for a Selection of Tests and Service Failures

				Failure Conditions				
Event Date	Reference	Dia./Thk/ Length, in.	Temp.	CVN @ Temp., ft-lb	Pressure, psi	Medium	Initial Crack Dimension, in.	Fracture Type
1970	Banks (1973)	106/1.1/≈500	54°F	≈9	420	Water	4-1/2 long x ≈ 0.5 deep	Branching fragment (one)
1965	Weck (1966)	67/5.8/≈600	50°F	≈10 W; ≥40P W = weld; P = plate	5000	Water	Internal crack ≈5/8 diameter in weld	Branching fragments (four)
196x	Adachi (1969)	6/2.5/open	Unknown	Unknown	Unknown (gun)	Gas	Unknown	Fragments (multiple)
1961	Bates and Greenberg (1966)	≈18/≈1.2/≈150	Near 70°F	Various	2650 to 3900	Air	20 long x ≈ 1-1/8 deep	Three of three tests fragmented, blowing out one piece
1961	Bates and Greenberg (1966)	≈18/≈1.2/≈150	Various	Various	4200 to 15,200	Water	None, 10, 20 x various	Two of three tests fragmented, one piece each
1954	Pellini (1976)	≈75/3.0/≈100	Unknown	Unknown	Unknown	Water	Unknown	Fragment (one piece)
1943	Shank (1954)	66/0.45/400?	<32°F		None	Impact	None	Fragments (five pieces)
1943	Shank (1954)	460/0.66/sphere	<10°F	Unknown	≈50	H_2	Unknown	Fragments (twenty plus)

zone of the fillet weld securing a manhole flange. Two fracture toughness tests at the failure temperature produced elastic limit results of 35.1 and 43.2 ksi $\sqrt{in.}$, while the maximum loads had values of 58.3 and 64.2 ksi $\sqrt{in.}$ The calculated conditions were 64.5 ksi $\sqrt{in.}$ The vessel R/t was about 48. The resulting fragment length was about $\sqrt{Rt}$, while the fragment width was approximately a third of this dimension.

- Adachi (1969) - This example of a gas-driven fracture was selected only to show fragment size trends. From approximate scaling of the photograph on page 304, the vessel dimensions were a wall thickness of about 2.5 in. and a diameter of about 6.0 in. This gives an R/t of about 1.2. The smaller fragment appears to be a little longer than $\sqrt{Rt}$ and about half $\sqrt{Rt}$ in width.

- Bates and Greenberg (1966) - Sixteen full-size pressure vessels were given various heat treatments and then pressurized to failure. Fourteen were intentionally defected. Three of the vessels were burst with air pressure, and the remaining 13 vessels were burst with hydraulic pressure. Slots of various lengths and depths were machined into the vessel walls to promote failure. It is assumed that the final rupture began as tearing of the ligament, leading to a dynamic cracking state at the ends of the slots. To arrest the crack at this point, the required material toughness can be approximated as $K_c = [(pr/t)/\sqrt{\pi(slot/2)}]$ and compared with the estimate of dynamic toughness (from a CVN correlation). Air-burst vessels produced one long fragment, which was somewhat wider than $\sqrt{Rt}$. Two of the water-burst vessels produced one triangular fragment each, with a dimension of about $\sqrt{Rt}$ on each side. One vessel, with an unintentional defect, burst under a water pressure at 15,200 psi and produced multiple branching, and almost produced fragments. The R/t ratio varied from about 6 to 8 for the series of 16 tests.

- Pellini (1976) - Pellini's figure on page 243 shows fragmentation that developed by a crack curving back on itself, in much the same manner as the crack discussed by Weck (1966). In this case, the manhole was included in the fragment.

- Shank (1954) - An empty steam drum was being shipped by rail during the winter. In an accident, the drum was impacted by a train coupling. Five fragments were knocked out of the wall of the steam drum; three were relatively small and two were larger. Two of the small fragments were a little less than $\sqrt{Rt}$ in width and three times that in length. The other small fragment was triangular, with a dimension of a little more than $\sqrt{Rt}$ on a side.
- Shank (1954) - A hydrogen storage tank failure (illustrated in Shank's Figure 8) produced more than 20 fragments. The smaller fragments were estimated to be a bit more than $\sqrt{Rt}$ in minor dimension. The R/t of 350 is not relevant to reactor pressure vessels, but the fragment sizes nevertheless appear to follow the $\sqrt{Rt}$ trend.

DISCUSSION OF EXPERIMENTAL DATA

The relevant data from the cited sources consists of 17 fracture events where the ratio (R/t) is in the neighborhood of 7: 16 from Bates and Greenberg (1966) and one from Weck (1966). These are tabulated in Table J.2, and include an assumed correlation between Charpy V-notch properties at failure temperature (CVN) and dynamic toughness, K_{Id}. The listed crack is dimensioned as the intentional slot (or unintentional flaw), plus an end correction of about one thickness. It is the crack dimension that would have been sustained if the material were "just tough enough"; a conceptual, not practical argument.

In all the cases reported by Bates and Greenberg (1966), a ligament, between the slot or flaw and the inner wall, broke fast enough that the vessel didn't immediately depressurize. Such a fracture process is assumed to have caused a dynamic state on full-thickness material at the slot/flaw termini. The length of that crack is tabulated as "crk". K_{cd} is the "driven" intensity for "crk" under the hoop stress, pr/t, where p is the maximum recorded pressure. "Lnth" is the approximate uniform section length; end fittings terminated the overall dimensions.

FIGURE J.2. Analysis of Experimental Data for Conditions Relevant to Fragmentation Behavior

Fracture Number	CVN, ft-lb	K_{Id}, ksi $\sqrt{in.}$	Press., ksi	Rad, in.	Thkns, in.	Mod., 10^6 psi	Crk, in.	r/t	pr/t, ksi	K_{cd}, ksi $\sqrt{in.}$	Lnth, in.	Water/Air	Branching/Fragments
1	30	54.0	15.2	9.77	1.2	29.8	4.5	8.14	124.0	329.0	150	Water	Branching
2	25	49.5	7.4	9.76	1.3	29.8	11.5	7.51	55.6	236.0	150	Water	None
3	55	79.0	8.5	9.76	1.4	29.8	21.5	6.97	59.3	344.0	150	Water	None
4	35	59.6	9.7	9.75	1.45	29.8	21.5	6.72	65.2	379.0	150	Water	None
5	25	49.5	8.4	9.76	1.3	29.8	21.5	7.51	63.1	366.0	150	Water	None
6	17	41.1	8.9	9.76	1.5	30.2	11.5	6.51	57.9	246.0	150	Water	None
7	37	61.5	2.65	9.75	1.5	29.9	21.5	6.5	17.2	100.0	150	Air	Fragments
8	16	40.2	6.9	9.76	1.5	30.1	11.5	6.51	44.9	191.0	150	Water	None
9	30	54.0	8.4	9.76	1.3	30.1	11.5	7.51	63.1	268.0	150	Water	None
10	73	96.0	8.2	9.76	1.25	29.8	11.5	7.81	64.0	272.0	150	Water	None
11	34	58.7	9.0	9.76	1.45	30.1	21.5	6.73	60.6	352.0	150	Water	None
12	28	52.4	9.5	9.76	1.55	30.1	11.5	6.3	59.8	254.0	150	Water	None
13	49	73.0	3.5	9.75	1.5	29.9	21.5	6.5	22.8	132.0	150	Air	Fragments
14	33	57.6	3.9	9.75	1.5	30.0	21.5	6.5	25.4	147.0	150	Air	Fragments
15	20	44.5	6.2	9.76	1.1	30.1	11.5	8.87	55.5	234.0	150	Water	Fragments
16	25	49.5	4.2	9.75	1.5	29.9	3.0	6.5	27.3	59.3	150	Water	Fragments
17	40	64.1	5.0	34.0	5.75	30.0	13.0	5.91	29.6	134.0	600	Water	Fragments

Fracture 15 in Table J.2 is shown with a wall of 1.1 in.; however, the minimum wall, as noted in the text, was 0.958 in. Its fracture condition can be seen as Flask 23A, which was hydrostatically burst, and fragmented as shown in Bates and Greenberg (1966). It was also the only flask tested in the "normalized" condition. For whatever reason, this flask did not "group" with the others that fragmented.

The data interpretation was assisted by considering the difference between the "driving" conditions as measured by K_{cd} and the resisting toughness as indicated by CVN transformed into a K_{Id} representation. The results suggested that fragmentation can occur under hydraulic as well as gas pressures. In the examples listed in Table J.2 (neglecting No. 15), the "breakthrough" driving forces were only somewhat larger than the resisting capacity of the material. That is, $K_{cd}/K_{Id} < 3$. The vessels that fragmented were not "brittle" in the CVN sense because all had CVN values above 25 ft-lb at the failure temperature. Clearly, in all six cases, the ligament fracture and continuing crack growth moved fast enough that depressurization did not soon occur.

With respect to reactor vessels, the slots of the cited tests could be interpreted to represent a failed vertical weld. The running crack then came up against the next course (which would be base material, due to the staggered welds). If the circumferential welds were relatively as tough (as in the tests), then penetration into the base material might occur. Otherwise, the circumferential weld (or HAZ) would be expected to fail, with some other consequences. However, nothing is indicated from this evaluation of test data that would make the fragmentation picture different.

Study of these and other references suggests that, when base material is suitably tough, a running crack will be slowed enough to soon arrest or depressurize the vessel, or both. This argument was not pursued or developed here.

Another aspect of interpretation needs mention; that is the absolute pressure involved. In the examples listed in this report, failure pressures were very high. The three air-burst cases were at about 3000 psi; most others were at two to three times that pressure. During an experiment when the only recorded data about failure is the maximum pressure, more detailed information can be desired. Did the failing ligament (Bates and Greenberg 1966) allow some depressurization? That is, what was the actual elastic hoop stress when the running crack reached the slot termini?

In short, it does not seem prudent to attempt extracting too much more out of the data other than an indication of fragment sizes. In this regard, all the varied references seemed to point to a conclusion that fragments with dimensions on the order of $\sqrt{Rt}$ will result from sudden fractures, even for cases without pressurization.

OTHER EVALUATIONS OF ARREST BEHAVIOR

Battelle-Columbus Laboratory (BCL) has also reviewed data from pipe and vessel fracture tests as part of a recent project for NRC (Wilkowski et al. 1984) with similar conclusions. This information is summarized in Figure J.1.

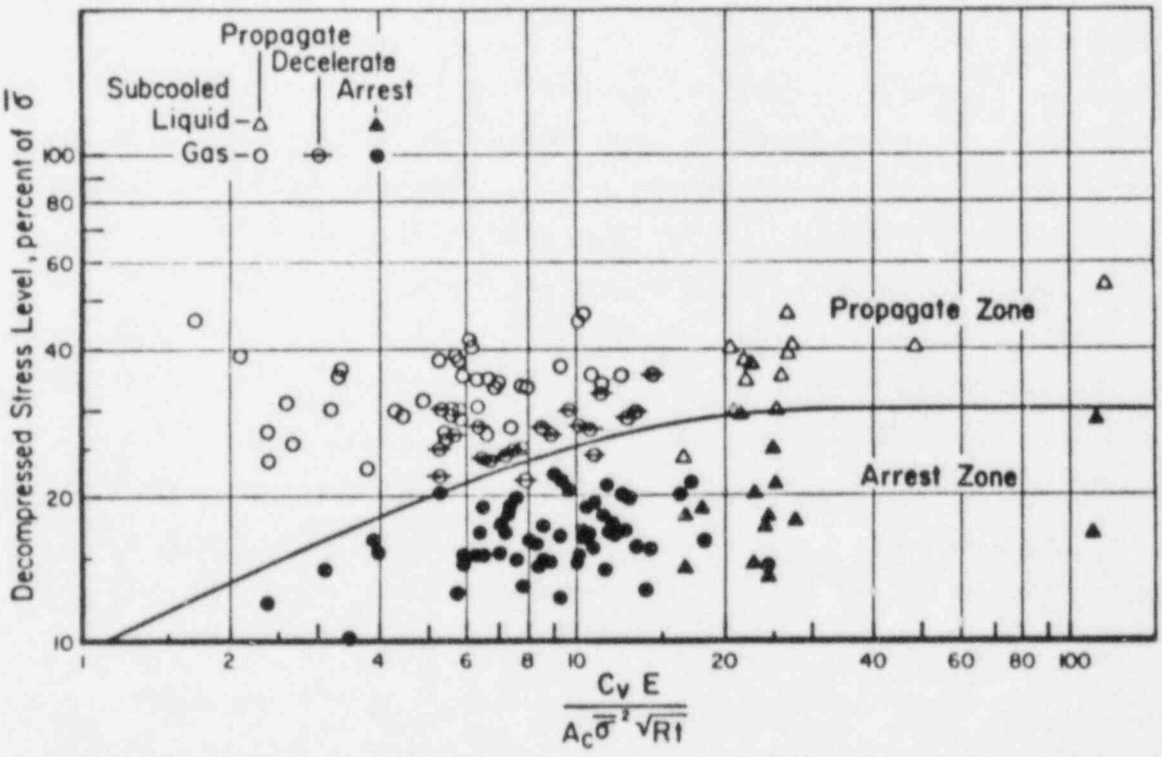

FIGURE J.1. Determination of the Arrest Stress Level

In Figure J.1, an empirically based curve separates an arrest zone from a propagate zone, which are defined as follows:

- propagate zone - The axial crack continues to propagate without any limit on the final crack length. In effect, the crack grows down the length of the vessel or pipe at a greater velocity than the depressurization wave.
- arrest zone - The axial crack arrests after limited crack growth because the crack grows at a slower velocity than the axial movement of the depressurization wave. The BCL model is based primarily on pipeline tests and does not predict the extent of axial crack growth prior to an arrest event. Thus, for PTS analysis, the model does not give an estimate of the final size of the opening in the vessel although it does indicate the conditions that will produce a very large opening.

The following definitions apply to the parameters in Figure J.1:

- C_v = Charpy impact energy, ft-lb
- A_c = cross-sectional area of Charpy specimen
- E = elastic modulus
- $\bar{\sigma}$ = flow stress of vessel material
- R = mean radius of vessel
- t = wall thickness of vessel.

The decompressed stress level is the hoop stress in the wall of the uncracked vessel for the depressurized state. For a gas this is the same as the initial pressure, while for a subcooled liquid this is the saturation pressure at the temperature of the test.

Figures J.2 and J.3 show the arrest/propagate boundary in a format more closely related to terms of PTS evaluations. Typical vessel parameters were used for radius, wall thickness, modulus, and flow stress. The depressurized stress was based on the saturation curve shown as an insert of Figure J.2. The following observations can be made:

- Crack arrest will occur for the governing coolant temperatures associated with through-wall cracking in a PTS event.
- Crack arrest is only mildly dependent on the impact energy in the CVN energy range of 50 to 200 ft-lb of relevance to reactor vessels. These

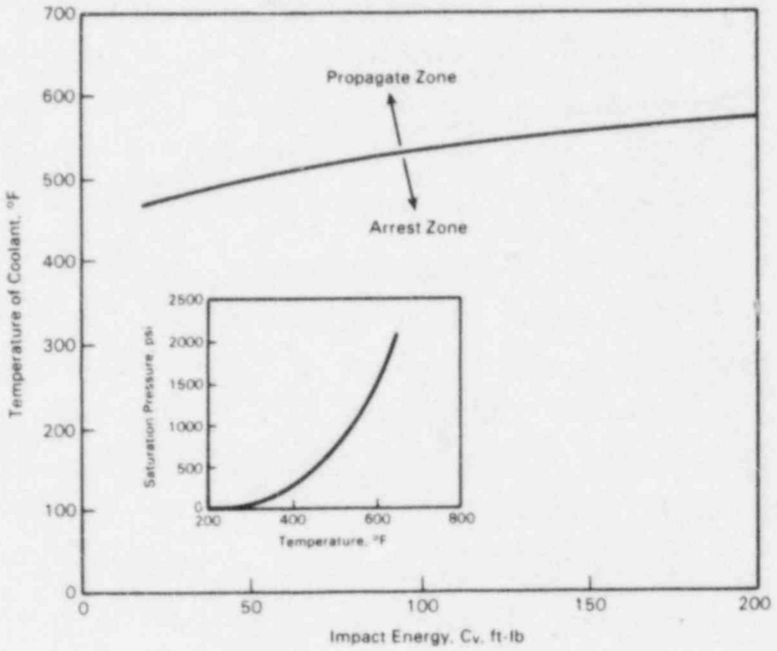

FIGURE J.2. Arrest and Propagate Zones for PTS Conditions

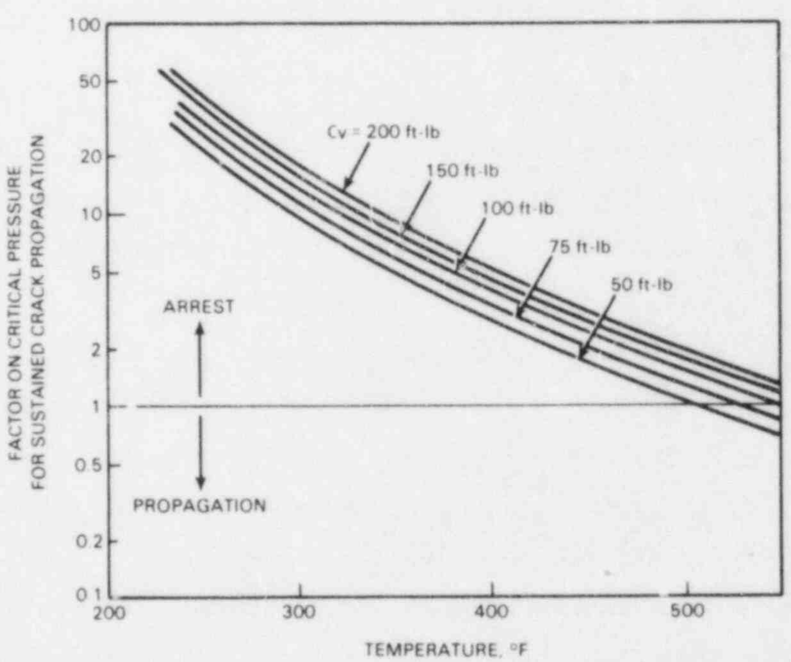

FIGURE J.3. Margin in Pressure for PTS Conditions Relative to Pressure to Sustain Crack Propagation arrest predictions, however, do assume that the material is at upper shelf temperatures and, thus, do not apply to the lower shelf or transition temperature range.

- A substantial margin exists between the pressure required to sustain unstable or unlimited crack growth and the saturation pressures relevant to PTS fracture events. It appears that cracks in vessels will have a tendency to arrest, once they grow into material at upper shelf temperatures. Nevertheless, the ductile tearing resistance of the vessel material and the depressurization rates may be insufficient to bring about complete arrest until the axial crack has extended a substantial fraction of the vessel length.

CONCLUSIONS OF FRAGMENTATION EVALUATIONS

Considering all the described reference information, it is concluded that fragments can be generated from fast-running fractures caused by either gas or liquid pressurizations. Fragments tend to have one dimension approximately equal to the parameter $\sqrt{Rt}$; the other dimension(s) may be anything larger than a few wall thicknesses.

Trends in the data were sought in an unsuccessful attempt to establish a clear-cut criterion that could be used to predict the conditions for which fragments will be formed. Lacking such a criterion, it was considered prudent to assume the formation of fragments for all PTS vessel fractures involving cracks that did not arrest at the ends of the axial weld with the initial through-wall crack. The evaluation then continued by estimating the velocities of the fragments and by predicting the ability of these fragments to penetrate the concrete adjacent to the reactor vessel.

FRAGMENT VELOCITIES

The velocities of fragments must be estimated to permit evaluations of the potential damage from missile impact. A review of the literature on this topic indicated that the available methods and equations did not apply to the conditions of vessel fracture during PTS events. The conditions addressed in the literature were high energy situations in which the energy is provided by compressed gases, saturated liquids, explosives, detonations, etc. In contrast, the kinetic energy to fragments produced in PTS events is provided by subcooled water.

Fragment velocities have often been estimated by assuming that a fixed fraction of the available energy contained within the vessel becomes kinetic energy of the resulting missiles. This is the basis of the often cited Gurney equation and its modifications (Moore 1967; Gurney 1943). A similar approach is taken here to estimate fragment velocities by consideration of the energy available from decompression of subcooled water. This neglects the additional energy provided by the thrust associated with the saturated water following decompression. The results for the upper head missile evaluation of Appendix K indicates that this contribution is relatively small and can be neglected in light of other conservatisms in the velocity estimates.

In the energy balance approach, all of the energy available from decompression of the water is assumed to be converted into kinetic energy. This kinetic energy is associated with the fragment and a volume of water that is ejected along with the fragment as the decompression occurs. The ejected water is assumed to have the same velocity as the fragment, and the ejected volume is taken equal to the increase in water volume associated with decompression of the water within the vessel to ambient pressure.

The calculations used to generate the predicted velocities of Figure 5.3 in Section 5 of this report were based on the following typical parameters for a PTS scenario:

- radius of vessel = 7 ft
- length of vessel = 25 ft
- volume of vessel = 3800 ft^3
- bulk modulus of water = 300,000 psi
- energy available from decompression of water = 3.6×10^6 ft-lb
- volume of water ejected with fragment missile = 25 ft^3.

The calculational method is conservative (the predicted fragment velocities are too great) in the sense that it is assumed that only one missile is produced in each vessel fracture, whereas the kinetic energy will often be partitioned among several missiles. On the other hand, the calculation will tend to be somewhat unconservative because:

- The energy from fluid in other portions of the primary coolant system may contribute to the fragment velocity.
- Energy will be supplied by the saturated liquid after the initial decompression.
- Energy may be supplied by decompression of steam voids in the upper part of the vessel.

An additional consideration that applies to the velocities for relatively small missiles is that the fragment velocity should not exceed the calculated velocity for a jet of water escaping through an opening in the vessel wall. Equation (I.2) of Appendix I predicts a jet velocity of 410 ft/sec for the assumed coolant conditions. This velocity is shown as an upper bound on the predictions of Figure 5.3 for fragments with weights less than about 250 lb.

Another check on the velocity calculation is provided by the limiting case of a very large fragment of 185,000 lb. Such a fragment(s) would correspond to the symmetrical acceleration of the 12-ft-long beltline portion of the vessel treated as a single fragment in the energy balance approach. The calculated velocity of the fragment(s) is about 35 ft/sec as indicated by Figure 5.3. This can be compared with the velocity predicted for the upper head in the detailed calculations of Appendix K. Figure K.11 indicates a velocity of about 29 ft/sec for the 585,000-lb upper head. Adjusting this velocity upward (on the basis of equivalent kinetic energy) to account for the differences in weights (185,000 versus 585,000 lb) gives a velocity of about 50 ft/sec for the upper head calculation.

The upper head velocity is somewhat higher than the 35 ft/sec velocity of the fragment estimate, but is sufficiently close to provide a rough check on the accuracy of the method. It should also be noted that the prediction of fragment velocity would actually be conservative for this example of a large scale fragmentation. In practice, the method would treat the fragmentation of the 185,000-lb vessel beltline as producing many smaller fragments. Hence, the velocity for each of these smaller fragments would be read from Figure 5.3 as much greater than 35 ft/sec.

CONCRETE PENETRATION

The final step in the missile evaluation, following estimates of the sizes and velocities of the missiles, is to evaluate the potential damage caused by impact of the missiles with other components of the reactor system. The trajectory of horizontal missiles will first result in impact with the concrete shielding that is adjacent to the vessel in the arrangement of PWR reactors. If the missile is arrested by the shield, as the current calculations indicate, then no further calculations of missile damage are required.

Two approaches can be used to predict the penetration of concrete by missiles. Specialized finite element and finite difference computer codes are capable of predicting the deformation and fracture processes associated with impact and penetration (Zukas et al. 1982). These calculations are difficult, costly, and time-consuming. The alternative and recommended approach is to apply empirical equations that have been developed by the military for ballistic calculations. These equations have generally been developed on the basis of missile sizes, shapes, and velocities that differ significantly from the parameters for potential vessel missiles. Nevertheless, the use of these equations should be acceptable unless small margins against penetration dictate more precise evaluation methods.

Published reviews (Moore 1967; Gawaltney 1968; Baker 1984b) are good sources of equations to predict concrete penetration. The supporting data and method of derivation of these empirical equations are not usually available due to the classified nature of the original military ballistics studies. For the demonstration calculations of the current study, the BRL formula (Gawaltney 1960) for reinforced concrete was selected as follows

$$P = 7.8 \frac{W}{D^2} D^{1/5} \left(\frac{V}{1000}\right)^{4/3} \tag{J.1}$$

where D = diameter of missile (in.)

P = thickness of concrete slab that will be perforated (in.)

W = weight of missile (lb)

V = striking velocity (ft/sec).

While other equations should also give acceptable predictions, this equation was selected for several reasons. The equation was developed for reinforced concrete and does not require detailed consideration to describe the properties of either the concrete or reinforcement. In addition, the equation explicitly includes the effect of the thickness, and does not require consideration of back surface effects. In comparison with other equations, this formula appears to give conservative predictions of the resistance of concrete to penetration for the relatively slow missiles of interest to vessel failure. In this range of velocities, the empirical equations lack supporting data from the high velocities of military tests, and conservatism is a desired feature of the predictive equations when used in an extrapolation mode.

When the penetration depth becomes greater than two-thirds of the concrete thickness, spalling (expulsion of material from the opposite side of the impacted barrier) may occur. Unless there is a steel plate on this surface, the potential damage from secondary missiles should be addressed. However, the exploratory calculations of this report indicate that penetration depths will generally be insufficient to produce spalling.

Calculations were performed for a range of potential missile sizes and impact velocities. As a point of reference, a concrete thickness of 5 ft was assumed as typical for the concrete shielding barrier adjacent to the vessel. In the calculations it was assumed that the missiles impacted at worst-case orientations (minimum frontal area) that would produce a maximum penetration depth.

In one set of calculations, the missile size was varied and the impact velocities were the bounding values as estimated above as a function of missile weight. The objective was to determine whether large missiles or small missiles will have the greater potential to penetrate concrete barriers. Large missiles will have greater mass, and this greater mass will favor penetration. On the other hand, the smaller missiles will have greater velocities and smaller frontal areas, and both of these factors will favor penetration. The calculations indicated the relative trade-offs between the governing parameters.

Three representative fragments were selected for evaluation as follows:

- A 250-lb fragment was selected because this is the most massive fragment that is predicted to attain the bounding velocity of 410 ft/sec for the assumed fluid condition of the PTS event.

- A 24 x 24 x 8.5-in.-thick fragment of the vessel wall was chosen. This fragment weighed 1380 lb and had an estimated impact velocity of 254 ft/sec. The significance of this fragment is that it has the approximate dimensions of the $\sqrt{Rt}$ trend noted in the above evaluation of empirical data on fragmented vessels. Of further significance is that fragments much greater than 24 x 24 in. will be too large to rotate into a worst-case (edge-on) orientation within the confined space between the reactor vessel and the concrete barrier.

- The final fragment had the assumed dimensions of 72 x 72 x 8.5 in.-thick, and was selected solely for determining the trend for much larger but lower-velocity fragments. A fragment of this size would approach the size of an entire plate of the beltline region of the vessel. Impact was assumed to be edge-on, even though the size of the fragment would probably not allow it to rotate to this orientation within the limited space between the vessel and the concrete barrier.

Table J.3 gives the results of calculations for the maximum thickness of a reinforced concrete barrier that each of the three missile can penetrate. The impact orientations are indicated by the frontal areas, which, for purposes of the calculations, were converted into circular impact areas with a

TABLE J.3. Predicted Penetration Depths for Representative Missiles Produced by Fragmentation of a Vessel

Missile Dimensions, in.	Missile Weight, lb	Impact Velocity, ft/sec	Frontal Area, in.	Equivalent Impact Diameter, in.	Predicted Perforation Thickness, in.
8 x 8 x 13.8	250	410	8 x 8	9.03	11.3
24 x 24 x 8.5	1,380	254	24 x 8.5	16.0	11.8
72 x 72 x 8.5	12,470	136	72 x 8.5	27.9	17.8

diameter giving the same area of impact. This approximation was required to apply Equation (J.1), which actually predicts penetration for end-on impact of long cylindrical rods.

The results shown in Table J.3 indicate that the perforation thickness is relatively independent of the size of the missile. The effect of increasing missile weight is offset by the lower impact velocity and increased area of impact for the larger missiles. Disregarding the 12,470-lb missile as unrealistic, the predicted perforation depths are about 12 in. or 1 ft for the range of realistic missile sizes. A typical barrier thickness of about 5 ft is about five times greater than the minimum thickness required to arrest the expected vessel fragments.

A second set of calculations focused on the 24 x 24 x 8.5-in. fragment, which was viewed as a worst case. The perforation thickness was then calculated as a function of impact velocity; the results are shown in Figure 5.4 of this report. The predicted impact velocity to perforate the 5-ft thickness of the assumed typical barrier is nearly 1000 ft/sec. This far exceeds the expected velocity of 254 ft/sec. It also greatly exceeds the bound on impact velocity for small fragments (the 410-ft/sec limit imposed by consideration of the jet velocity for escaping fluid for the pressure and temperature conditions of interest).

A final step in the evaluation of concrete penetration was a review of the results of tests performed at Sandia National Laboratory for the Electric Power Research Institute (Woodfin 1983). In these tests, fragments of a steam turbine disc were accelerated with a rocket sled into a 4.5-ft-thick reinforced concrete slab. The missile weights and impact velocities were about the same as those estimated in this report for vessel fragments. Although these tests did not give sufficient data to derive predictive equations [like Equation (J.1)], the data provided a basis against which to check the conservatism of the empirical equation used in this study. Such a check was desirable because it was believed that the supporting data for Equation (J.1) covered only smaller but higher velocity missiles than those of interest to reactor vessel fragmentation.

Table J.4 summarizes the results of the impact tests documented in Woodfin (1983). The concrete thickness was about the same as assumed in this study, but the missile weights and impact velocities were somewhat greater. The extent of steel reinforcement in the test slab was intended to be typical of that for the wall of a concrete containment building for a PWR plant. As such, the level of reinforcement may be greater than for the concrete structure that surrounds a typical reactor vessel.

The test results are consistent with the current predictions because all the missiles penetrated less than half of the thickness of the concrete target. The second test listed in Table J.4 comes closest to approximating the estimated impact conditions for the worst-case vessel fragment (3250 lb versus 1380 lb and velocity of 300 ft/sec versus 254 ft/sec). The penetration depth is about the same as the perforation thickness for the vessel fragment, even though the calculated kinetic energy of the impacting fragment is about

TABLE J.4. Results of Impact Tests of Turbine Fragment Missiles Impacted with 4.5-Ft-Thick Reinforced Concrete Slab

Missile Weight, lb	Impact Velocity, ft/sec	Impact Orientation	Penetration Depth, in.
3250	295	Sharp	17
3250	300	Blunt	13
3250	428	Sharp	24
4540	377	Sharp	26

three times greater for the turbine missile test. This indicates that the current use of Equation (J.1) should give conservative estimates for penetration evaluations.

REFERENCES

Adachi, J. 1969. "Fracture Design Practices for Ordnance Structures." In Fracture, Vol. V, Chapter 5, pp. 285-381, Academic Press, New York, New York.

Baker, W. E. 1984a. "Blast and Fragments from Bursting Pressure Vessels." In Impact, Fragmentation and Blast (Vessels, Pipes, Tubes, Equipment), PVP-Vol. 82, American Society of Mechanical Engineers, New York, New York.

Baker, W. E. 1984b. "Impact Effects of Industrial Missiles." In Impact, Fragmentation and Blast (Vessels, Pipes, Tubes, Equipment), PVP-Vol. 82, American Society of Mechanical Engineers, New York, New York.

Banks, B. 1973. "Pressure Vessel Failure During Hydrotest." Welding and Metal Fabrication. January 1973, pp. 4-12.

Bates, R. C., and H. D. Greenberg. 1966. "A Study of the Fracture Resistance of Steel Pressure Vessels by Means of Charpy, Drop Weight, and Full Size Burst Tests." In Application of Fracture Toughness Parameters to Structural Metals, ed. H. D. Greenburg, pp. 91-145, Met. Soc. Conf. #31, Gordon and Breach, New York, New York.

Brown, S. J. 1985. "Energy Release Protection for Pressurized Systems. Part I. Review of Studies into Blast and Fragmentation." Applied Mechanics Review. 38(12):1625-1651.

Gawaltney, R. C. 1968. Missile Generation and Protection in Light-Water-Cooled Power Reactor Plants. ORNL-NSIC-22, Oak Ridge National Laboratory, Oak Ridge, Tennessee.

Gurney, R. W. 1943. Initial Velocities of Fragments from Bombs, Shells, and Grenades. BRL Report 405, U.S. Army Ballistics Research Laboratory, Aberdeen Proving Grounds, Maryland.

Moore, C. V. 1967. "The Design of Barricades for Hazardous Pressure Systems." Nuclear Engineering and Design. 5:81-97.

Pellini, W. S. 1976. Principles of Structural Integrity Technology. Office of Naval Research, Arlington, Virginia.

Pittman, J. F. 1972. Blast and Fragment Hazards from Bursting High Pressure Tanks. NOLTR 72-102, Naval Ordnance Laboratory, Silver Spring, Maryland.

Pittman, J. F. 1976. Blast and Fragments from Superpressure Vessel Rupture. NSWC/WOL/TR 75-87, Naval Surface Weapons Center, White Oak, Silver Spring, Maryland.

Proctor, J. F. 1967. "Adequacy of Explosion-Response Data in Estimating Reactor-Vessel Damage." Nuclear Safety. 8(6):565-572.

Shank, M. E. 1954. "A Critical Survey of Brittle Failure in Carbon Steel Structures Other than Ships." In Symposium on Effect of Temperature on the Brittle Behavior of Metals with Particular Reference to Low Temperatures, pp. 45-110, ASTM STP 158, American Society of Testing and Materials, Philadelphia, Pennsylvania.

Weck, R. 1966. Brittle Fracture of a Thick Walled Pressure Vessel. British Welding Research Association Report, Abington, United Kingdom.

Wilkowski, G. M., M. F. Kanninen, C. W. Marshall, J. Pan, C. Popelar, D. Broek, J. Ahmad, and R. Gilbert. 1984. "Summary of NRC Phase I Degraded Piping Program - Instability Analyses and Review of Experimental Programs to Evaluate J/T Instability Predictions." In Circumferential Cracks in Pressure Vessels and Piping - Vol. II, PVP- Vol. 95, American Society of Mechanical Engineers, New York, New York.

Woodfin, R. L. 1983. Full-Scale Turbine Missile Concrete Impact Tests." EPRI NP-2745, Electric Power Research Institute, Palo Alto, California.

Zukas, J. A., T. Nicholas, H. F. Swift, L. B. Greszczuk, and D. R. Curran. 1982. Impact Dynamics. John Wiley and Sons, New York, New York.

APPENDIX K

UPPER HEAD MISSILE GENERATION STUDY

APPENDIX K

UPPER HEAD MISSILE GENERATION STUDY

This appendix describes analyses that were carried out to investigate the response of a reactor vessel following a complete circumferential fracture occurring under PTS conditions. Predictions were made for the vertical motion of the resulting fragments under the combined effects of fluid thrust and attached piping restraint. The model developed for the analysis is a simplified approach to the problem based on assumptions of an instantaneous rupture and an isentropically expanding fluid.

The work presented in this appendix considers two support conditions. In the (fixed) bottom supported Oconee-1 reactor vessel model, only a single fragment, the upper vessel section, is subject to motion. The lower vessel section, being fixed, remains stationary. The other model considers a reactor vessel supported from the top (see Figure K.1). The lower portion of the vessel is suspended at some fixed height above ground and is subject to downward acceleration in the event of a complete circumferential break.

The objective of the top support model was to develop the methodology for missile generation analysis for top supported vessels such as those at the Calvert Cliffs and H. B. Robinson plants. However, the sample calculations were performed using vessel parameters of the Oconee-1 reactor. Predictions include values for maximum upward velocity and displacement for the upper vessel fragment and downward impact velocities for both the upper and lower vessel fragments.

PROBLEM DESCRIPTIONS

Figure K.2 describes the basic problem under analysis. Table K.1 defines the nomenclature used in the analysis. Rupture is assumed to occur instantaneously at time $t = 0$. This causes the vessel to separate into two fragments,

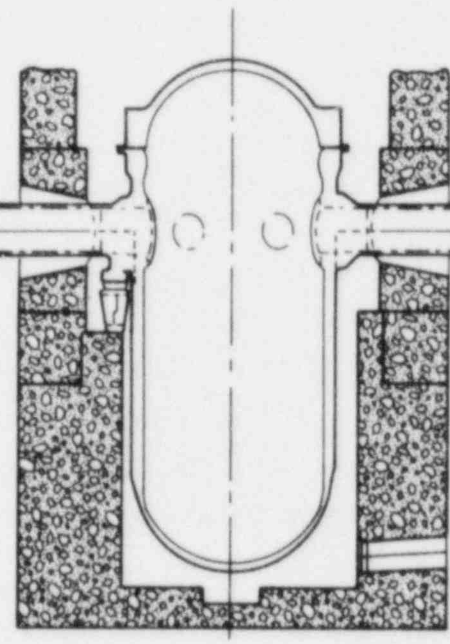

FIGURE K.1. Top Supported Vessel

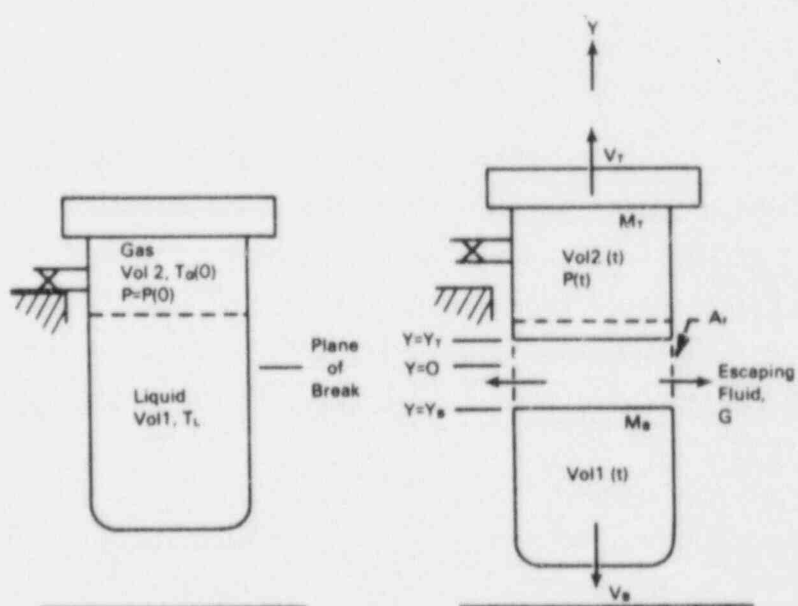

a. Prior to Rupture

b. After Rupture

FIGURE K.2. Model of Ruptured Vessel

TABLE K.1. Nomenclature

A_f = flow area (crack area)

A_p = projected area of vessel

C = pressure coefficient for Burnell equation

d = shell diameter

F = net upward force

F_k = load due to attached piping

g = gravity

G = mass flux

h = crack opening width dimension

h_s = enthalpy of steam

$\dot{m}$ = mass flow rate

m = mass of contained fluid

M = total mass of vessel fragment

n = step number

P = pressure

P_{SAT} = saturation pressure

sv = specific volume of contained fluid

V = vessel velocity

vol = volume

y = vertical displacement

t = time

ρ = fluid density

Subscripts

1 = liquid

2 = steam

B = bottom vessel fragment

T = top vessel fragment

an upper and a lower component, each defined with a total mass, M_T and M_B, respectively. The break is assumed to occur near the midpoint of the vessel.

The thrust exerted by the expanding fluid accelerates the two fragments in opposite directions. Displacement occurs along the y-axis, and the resulting area allows fluid to escape. The momentum of the escaping fluid is perpendicular to the direction of motion and therefore does not contribute to the acting thrust. Effects of flow resistance through internal structure are neglected. Fluid remaining in the lower fragment is assumed to move with the fragment, although its mass is not considered as part of the total mass M_B.

The presence of gas in the upper plenum provides a more severe condition than that of a vessel filled completely with subcooled liquid. Therefore, a steam void is incorporated into the model and is assumed to occupy the entire region above the fuel core. It is assumed that no mass or energy is transferred between the gas and liquid during the initial stage of depressurization. However, instantaneous flashing of the liquid is assumed to occur when the system pressure reaches the saturation pressure of the liquid. Beyond this point, the pressure of the steam is kept constant by this process.

ANALYSIS

The equation of motion and initial conditions for the two vessel fragments are:

$$M_T \frac{d^2 y_T}{dt^2} = F_T; \; y_T(0) = 0, \; \frac{dy_T}{dt}(0) = 0 \qquad (K.1)$$

$$M_B \frac{d^2 y_B}{dt^2} = F_B; \; y_B(0) = 0, \; \frac{dy_B}{dt}(0) = 0 \qquad (K.2)$$

where F_T and F_B are defined as the net upward forces acting on the top and bottom fragments, respectively. The individual force components are depicted in Figure K.3, and the resulting forces are determined as follows:

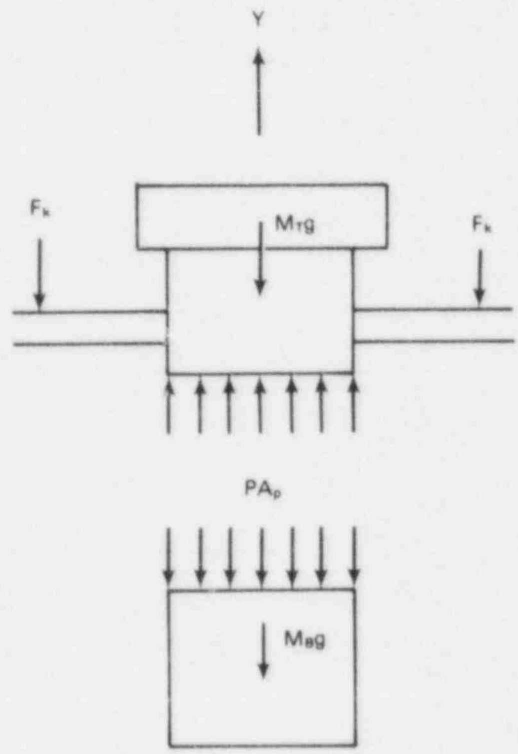

FIGURE K.3. Free-Body Diagram of Vessel Fragments

$$F_T = PA_p - F_K - M_{Tg} \qquad (K.3)$$

$$F_B = -PA_p - M_{Bg} \qquad (K.4)$$

The additional force on the upper fragment, F_K, represents a restraining force due to attached piping on the upper head assembly.

Load-deflection characteristics of the piping are given by Figure K.4. This curve was predicted by finite element analyses using the characteristics of Oconee-1 primary coolant piping. A conservative (lower bound) prediction of piping stiffness assumed that the piping was fixed only at the reactor vessel and steam generator. Intermediate supports, including those at the coolant pumps, were neglected. Following 6 in. of free motion, the piping was assumed to contact concrete structure at the vessel inlet nozzles. Loads associated with crushing or flattening of the large-diameter piping at the impact locations were estimated using data from Alzheimer et al. (1984).

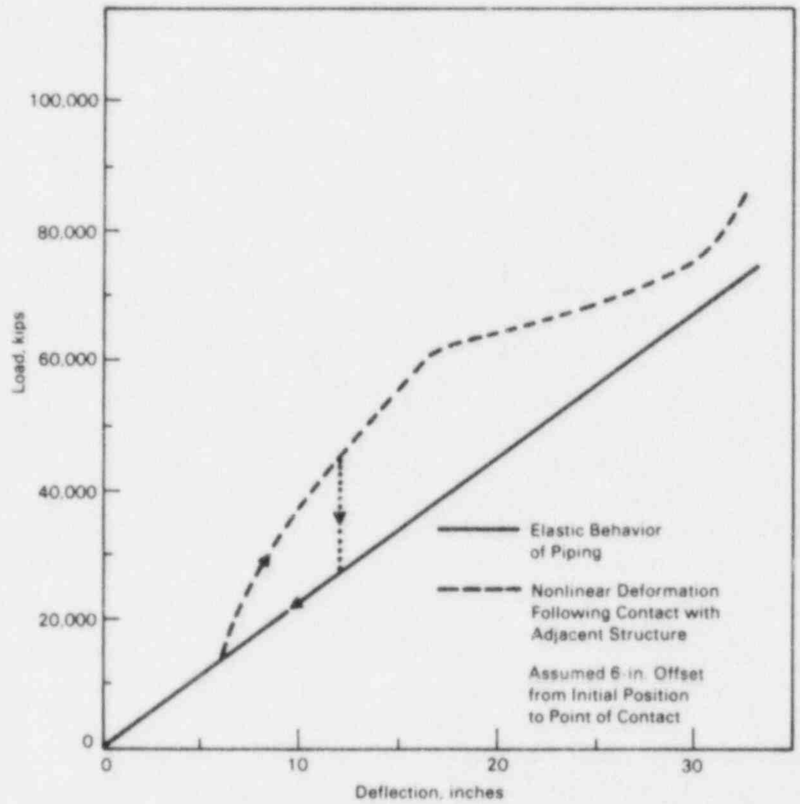

FIGURE K.4. Combined Stiffness of 28- and 36-Inch Pipes

The pressure force exerted on the fragments is defined by the change in state of the confined fluid during the process. The gas of volume 2 (see Figure K.2) is assumed to undergo an isentropic expansion, while the liquid of volume 1 is defined with a constant specific volume. The specific volume of the gas can be determined by:

$$SV_2 = \frac{vol2}{m_2} \tag{K.5}$$

where vol2 is accumulated by the differential volume dvol2:

$$dvol2 = dvol1 + Ap\ dy_T - dy_B \tag{K.6}$$

With the specific volume and entropy known, the corresponding state of the gas can be determined. The pressure of the gas then defines the system pressure. All property values are determined from appropriate steam tables.

The mass balance equations for each of the fluids are:

$$\frac{dm_1}{dt} = \dot{m}_1 \tag{K.7}$$

$$\frac{dm_2}{dt} = \dot{m}_2 \tag{K.8}$$

where $\dot{m}_1$ and $\dot{m}_2$ are the rates of discharge of the liquid and gas, respectively. The fluid flow rates are evaluated from the computed mass flux G and flow area A_f:

$$\dot{m} = G\, A_f \tag{K.9}$$

$$A_f = h\pi d \tag{K.10}$$

The time-dependent variable h is that portion of the crack opening that could effectively allow the particular fluid to escape.

The mass flux of the liquid is determined using the Burnell critical-flow equation (Tong and Weisman 1970),

$$G = \sqrt{2g_c\rho_\ell[P - (1-C)P_{sat}]}, \tag{K.11}$$

which was developed to predict the flow of flashing water through an orifice. The pressure coefficient C is a function of the saturation pressure P_{sat} and is assumed a constant value of 0.25 for the present case. The mass flux of the steam is determined using the break mass flow characteristics of Figure K.5, which gives mass flux as a function of stagnation enthalpy and pressure.

The analysis is carried out using the forward difference method and the following set of equations:

$$F_{Tn} = P_{n-1}\, A_p - F_k - M_T g \tag{K.12}$$

$$F_{Bn} = -P_{n-1}\, Ap - M_B g \tag{K.13}$$

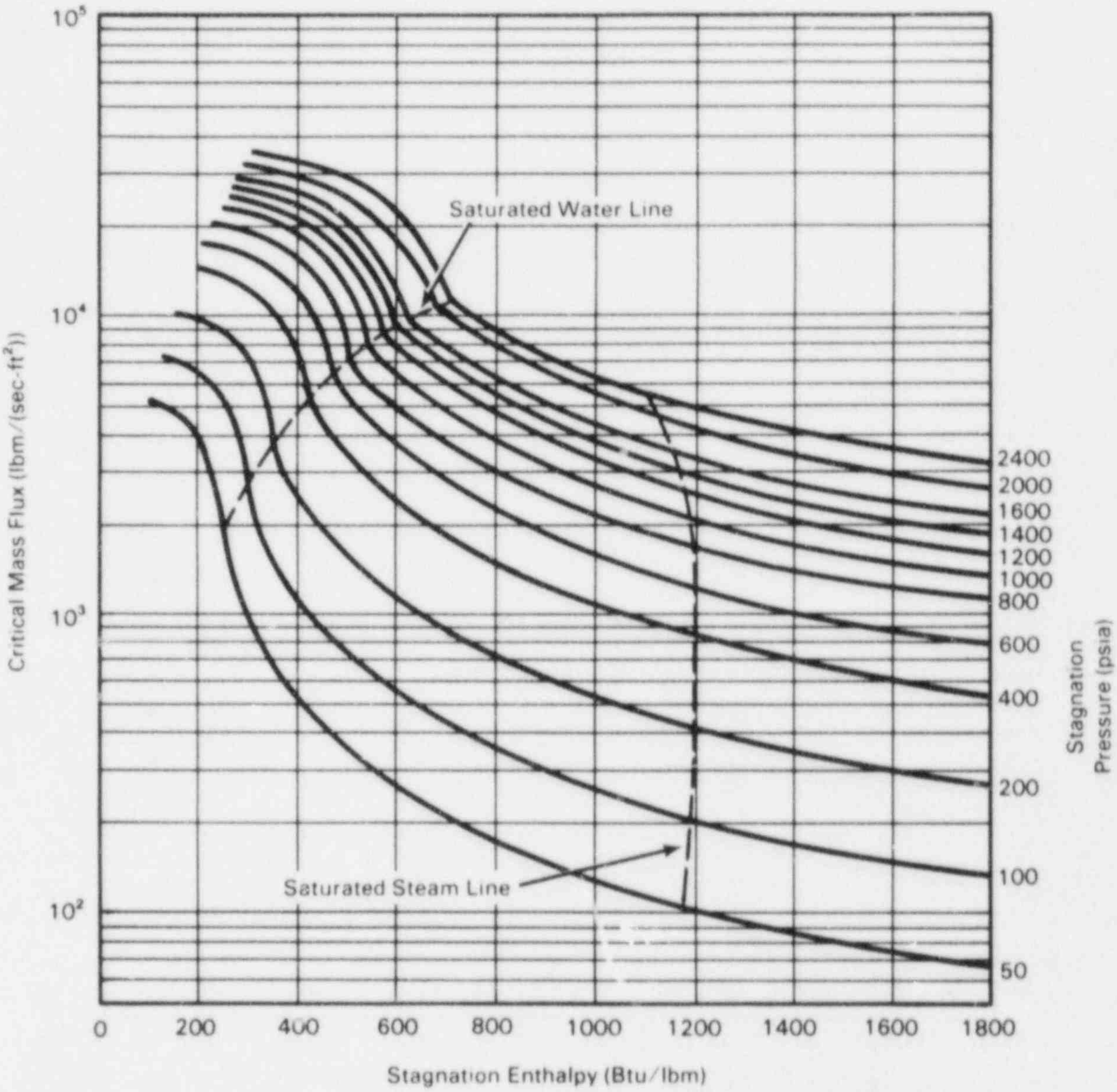

FIGURE K.5. Nomograph--Critical Mass Flux Versus Stagnation and Enthalpy

Source: Moore and Rettig (1973)

$$V_{in} = V_{in-1} + \frac{F_{in}}{M_T} \Delta t \qquad (K.14)$$

$$Y_{in} = Y_{in-1} + \Delta Y_{in} \qquad (K.15)$$

$$\Delta Y_{in} = [\frac{V_{in} + V_{in-1}}{2}] \Delta t \qquad (K.16)$$

(where i is taken for each fragment)

$$G_{1n} = \sqrt{2g_c\rho_1[P_{n-1} - (1-C)\ P_{SAT}]} \qquad (K.17)$$

$$G_{2n} = f\ (P_{n-1}, h_{s,n-1}) \qquad (K.18)$$

(see Figure K.5)

$$\dot{m} = G_n A_{f\ n} \qquad (K.19)$$

$$A_f = h\pi d,\ h = f(y, y_L, Y_B) \qquad (K.20)$$

$$m_n = m_{n-1} - \dot{m}_n \Delta t \qquad (K.21)$$

$$\Delta vol1 = \dot{m}_1 \Delta t / \rho_1 \qquad (K.22)$$

$$\Delta vol2 = \Delta vol1 + Ap|\Delta y_T - \Delta y_B| \qquad (K.23)$$

$$vol2_n = vol2_{n-1} + \Delta vol2 \qquad (K.24)$$

for which n is the corresponding time step and Δt is the time-step size chosen for the computations. The calculations are continued until the upper vessel fragment returns to its original position.

The analysis and equations for the case of the bottom supported vessel are essentially a special case of the above equations for the top supported condition.

Solutions of the above equations were performed numerically. A special purpose computer code was written to expedite the calculations.

RESULTS FOR BOTTOM SUPPORT

Two limiting cases were chosen for analysis and are described in Figure K.6. In Case 1, the upper head is detached from the core support assembly and the weight of the fuel and core support are not included in the total weight of the upper head assembly. In Case 2, the core support assembly, together with the core, remains attached to the upper head, thereby significantly increasing the weight of the missile. It is expected that Case 1 will present conservative results, giving rise to a greater maximum velocity and upward motion. However, it is of interest to determine the conditions of the upper head with an attached fuel assembly because this can lead to potentially more serious consequences in core damage.

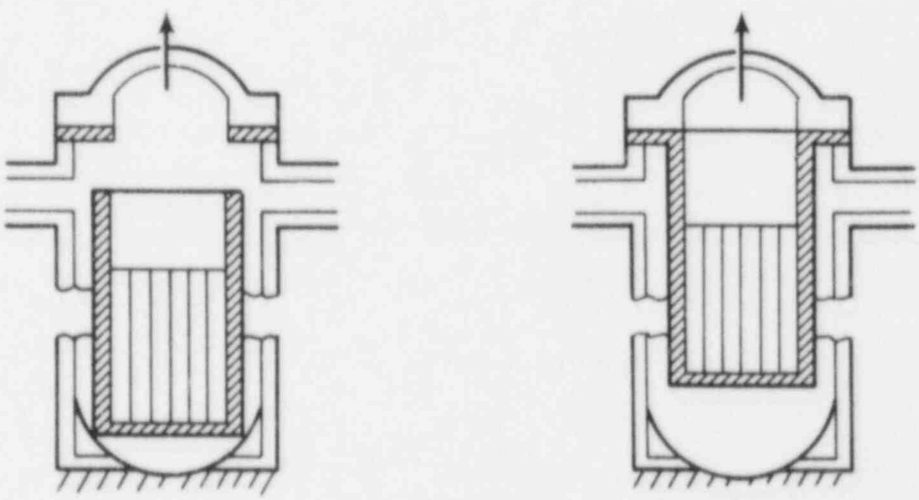

$M_T = M_{\substack{upper \\ vessel}}$

a. Case 1

$M_T = M_{\substack{upper \\ vessel}} + M_{\substack{core \\ support}} + M_{\substack{fuel \\ assembly}}$

b. Case 2

FIGURE K.6. Considered Upper Head Assembly Configurations

For both cases, the initial conditions of the vessel were defined with superheated steam at 1000 psia and 620°F and compressed liquid at 400°F. These conditions were selected as a worst-case bounding scenario that would give maximum thrust on the vessel and still be within the parameters of a pressurized thermal shock event. The specific vessel under consideration is that of the Oconee reactor. Design data used in the analysis are given in Table K.2. The clearance between the primary loop piping and the penetrators in the adjacent walls was assumed to be 6 in. This corresponds to the given piping load characteristics with a 6-in. offset. The calculations were carried out using a time step of 0.0001 sec. The duration of the event in each case remained under 160 ms.

Figure K.7 shows the evaluated pressure characteristics of the confined fluid. Figures K.8 and K.9 show the relative magnitudes of each of the forces acting on the upper assembly. The resulting net thrust force characteristics are given in Figure K.10. Following the initial loading due to the instantaneous rupture, the thrust on the upper head remains positive until the resistance from the attached piping begins to dominate over the pressure force. The net force then becomes increasingly negative until the maximum height is reached when the velocity is zero. At this point the missile begins its descent back to its original position. The discontinuity in the force is due

TABLE K.2. Oconee Reactor Vessel Data

Total coolant volume, ft^3	4,058
Shell ID, in.	171
Weight, lb:	
Vessel (dry)	646,000
Closure head	158,000
Studs, nuts and washers	39,500
Control rod drive	65,000
Fuel assembly	274,350
Core support assembly	335,000
Estimated weight of upper head assembly:	
Without core and core support	585,500
With core and core support	1,194,850

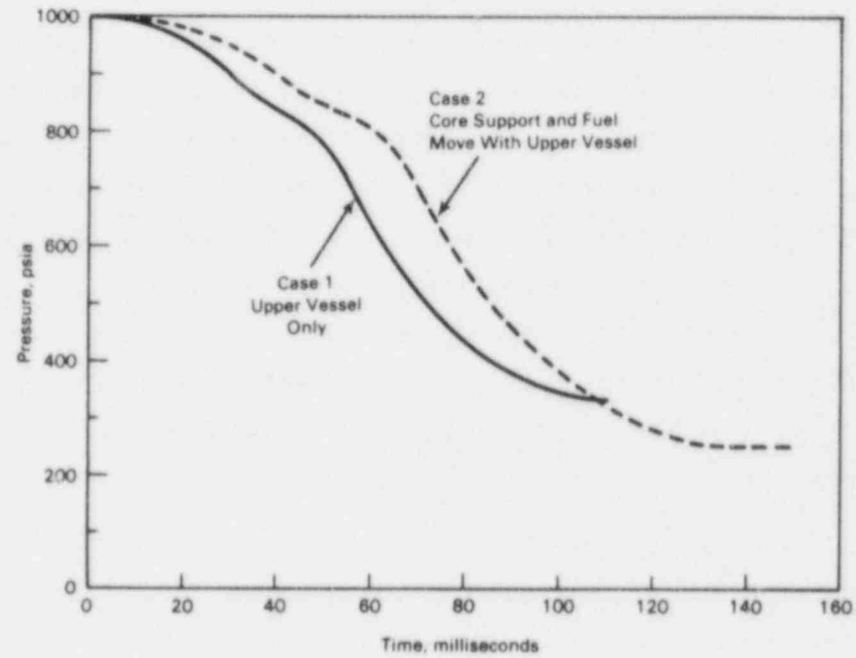

FIGURE K.7. Pressure Characteristics for Bottom Support Condition

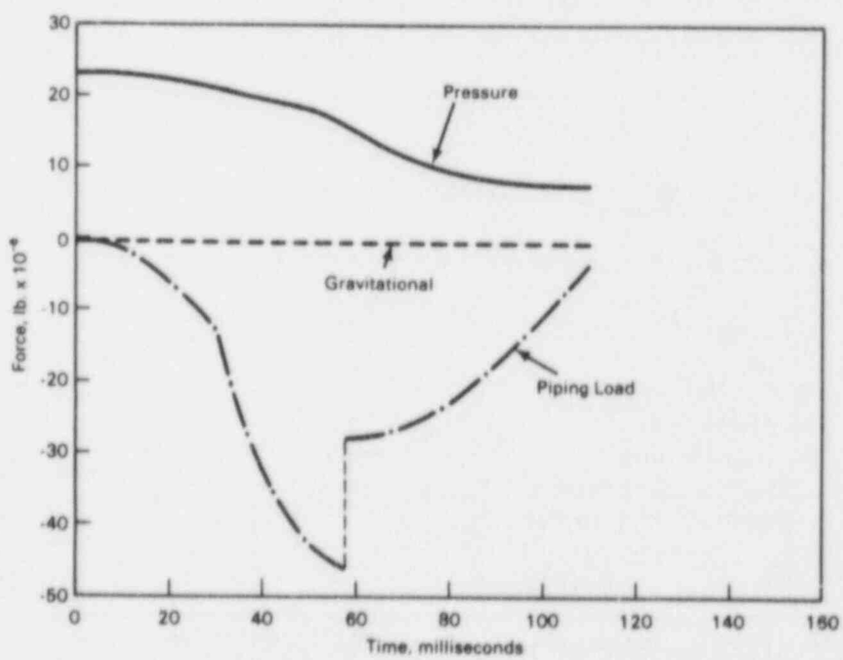

FIGURE K.8. Force Components for Case 1 with Bottom Support

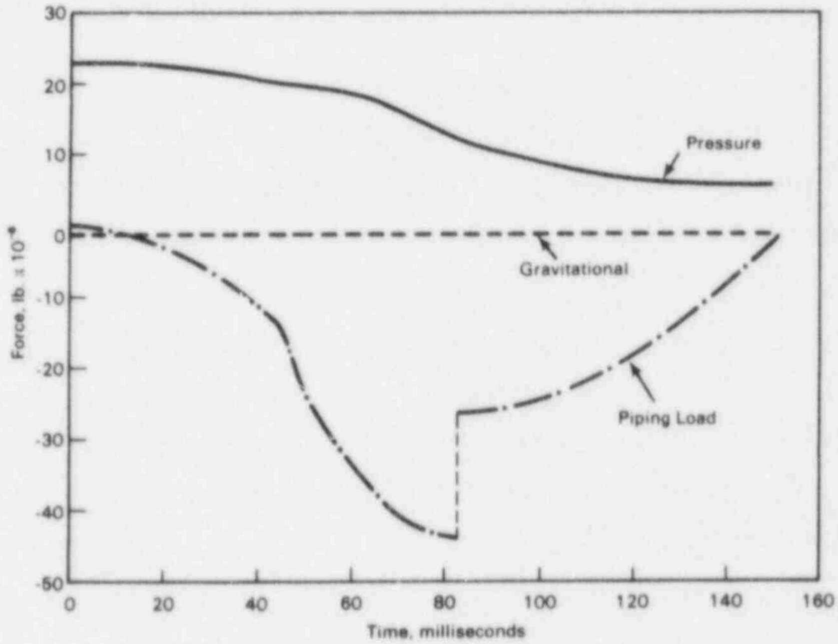

FIGURE K.9. Force Components for Case 2 with Bottom Support

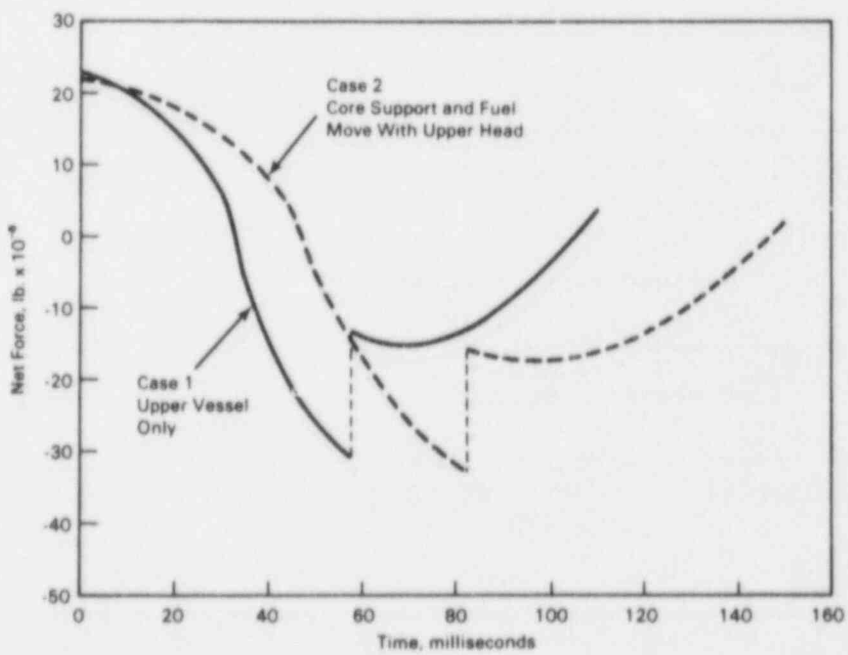

FIGURE K.10. Thrust Force Characteristics for Bottom Support Condition to the assumed change in loading characteristics of the piping (see Figure K.4).

Figures K.11 and K.12 show the velocity and displacement characteristics. Peak velocities for both upward and downward motion are greater for Case 1. However, the total displacement achieved in Case 1 is only 3% greater than that of Case 2. A summary of the final results is given in Table K.3.

As shown by the results, the effect of the attached piping is quite significant, both on upward and downward travel. Beyond an upward deflection of about 6 in., the piping characteristics clearly dominate. The total upward displacement is restricted to about 1 ft by the piping load. Furthermore, the piping load contributes to the momentum for downward motion and thus increases the velocity on the return impact.

The presence of gas in the upper plenum is also a significant factor in the analysis. Although the bottom support calculations did not allow for any liquid to flash into steam, the assumption appears to be satisfactory in this case as the fluid pressure remains well elevated during the lift portion of the event (Figure K.7).

TABLE K.3. Summary of Upper Head Missile Generation Study for Bottom Support Condition

(Initial conditions: P = 1000 psia, T_g = 620°F, T_L = 400°F)

Case	Defined Mass of Upper Assembly, (lb)	Upward Motion V_{MAX} ft/s	Upward Motion Y_{MAX} ft	Return Impact, ft/s
1	Upper vessel = 585,500	28.8	1.04	25.7
2	Upper vessel + Core support + Fuel assembly = 1,194,850	19.5	1.00	20.8

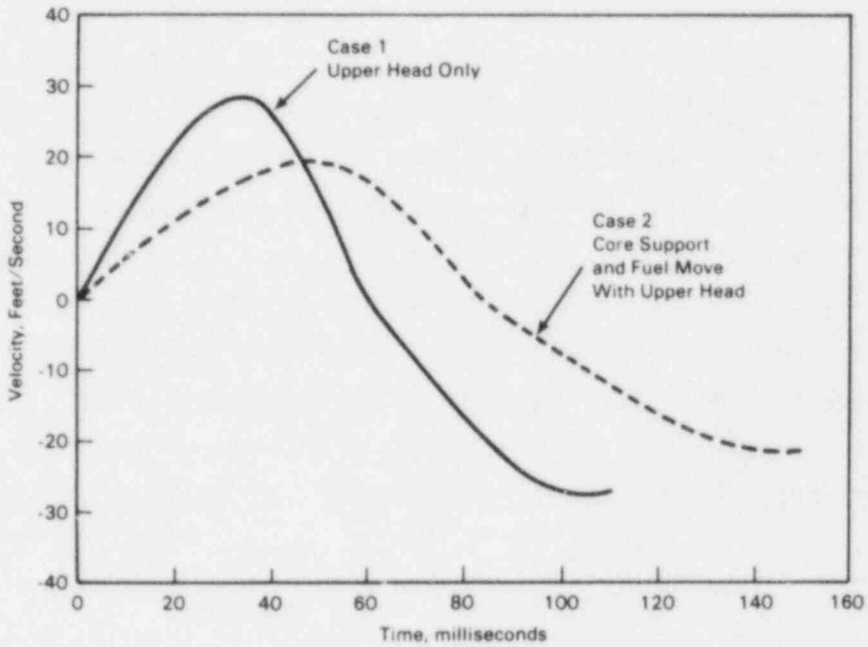

FIGURE K.11. Velocity Characteristics for Bottom Support Condition

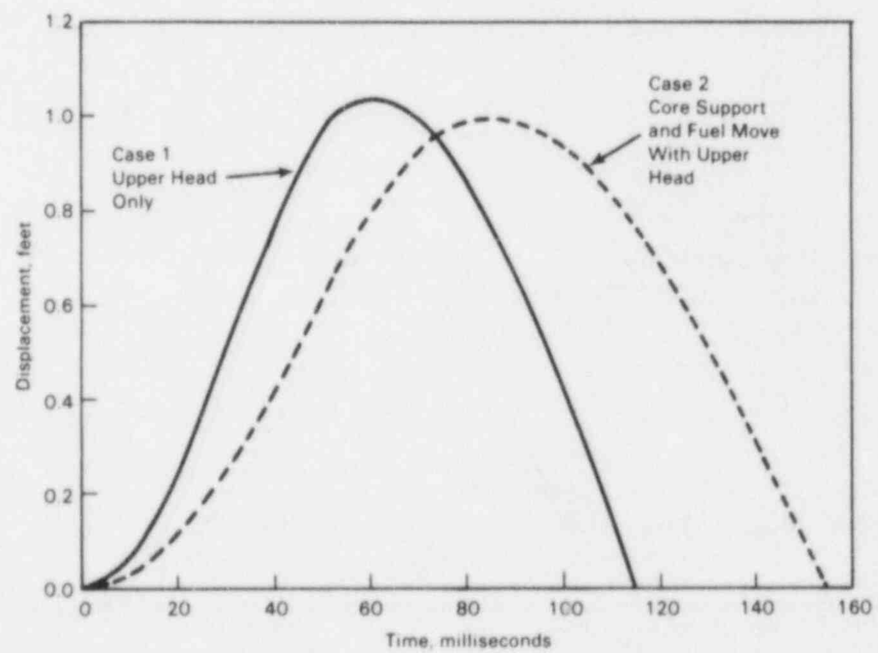

FIGURE K.12. Displacement Characteristics for Bottom Support Condition

RESULTS FOR TOP SUPPORT

Two limiting cases were chosen for analysis of the top support condition. These are described in Figure K.13. In Case 1, the core and core support are detached from the upper head assembly, and the associated weights are included in the total weight of the lower vessel fragment. In Case 2, the core support assembly, together with the core, remains attached to the upper head, thereby significantly increasing the weight of the upper vessel fragment. It is expected that Case 1 will present conservative results, giving rise to a greater maximum velocity and displacement for the upper vessel. However, it is of interest to determine the conditions of the upper head with an attached fuel assembly, because this can lead to potentially more serious consequences in core damage.

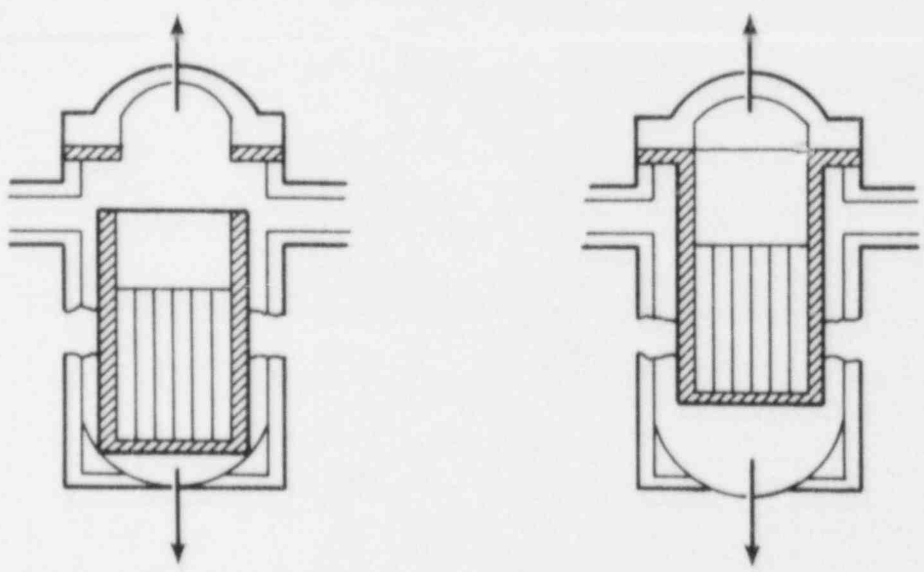

$M_T = M_{\text{upper vessel}}$

$M_B = M_{\text{lower vessel}} + M_{\text{core support}} + M_{\text{core}}$

a. Case 1

$M_T = M_{\text{upper vessel}} + M_{\text{core support}} + M_{\text{core}}$

$M_B = M_{\text{lower vessel}}$

b. Case 2

FIGURE K.13. Description of Considered Vessel Fragments

For both cases, the initial conditions of the vessel were defined as for the bottom support analyses, with superheated steam at 1000 psia and 620°F and compressed liquid at 400°F. Vessel data for the Oconee-1 reactor were again used in the analysis and are given in Table K.2. The parameters of the Oconee-1 vessel were roughly the same as those for the top supported Calvert Cliffs-1 and H. B. Robinson-2 vessels. Vessel parameters were not changed in the analyses, to allow direct comparison of vessel response for the two support conditions. The clearance between the primary loop piping and the penetrators in the adjacent wall structure was assumed to be 6 in. This corresponds to the given piping load-deflection characteristics with a 6-in. offset. The calculations were carried out to a maximum displacement for the lower vessel of 3 ft. A time step of 0.1 ms was used. The duration of the event in each case remained under 160 ms.

Figure K.14 shows the computed pressure characteristics of the confined fluid. Figures K.15 through K.18 show the relative magnitudes of each of the forces acting on the upper and lower vessel fragments. The resulting net thrust force characteristics are given in Figures K.19 and K.20. Following the initial loading due to the instantaneous rupture, the thrust on the upper head remains positive until the resistance from the attached piping begins to dominate over the pressure force. The net force then becomes increasingly negative until the maximum height is reached when the velocity is zero. At this point the upper vessel fragment begins its descent back to its original position. The discontinuity in the force is due to the assumed change in loading characteristics of the piping (see Figure K.4). Figures K.21 through K.24 show velocity and displacement characteristics. Peak velocities of both upward and downward motion of the upper vessel fragment are greater for Case 1. The total upward displacement achieved in Case 1 is about 30% greater than that of Case 2. Impact velocity of the lower vessel fragment is greater in Case 2. Table K.4 gives a summary of the results for a lower vessel displacement of 2 ft. Similar results for other ground clearances can be obtained from Figures K.21 through K.24 by reading values corresponding to the appropriate lower vessel displacement.

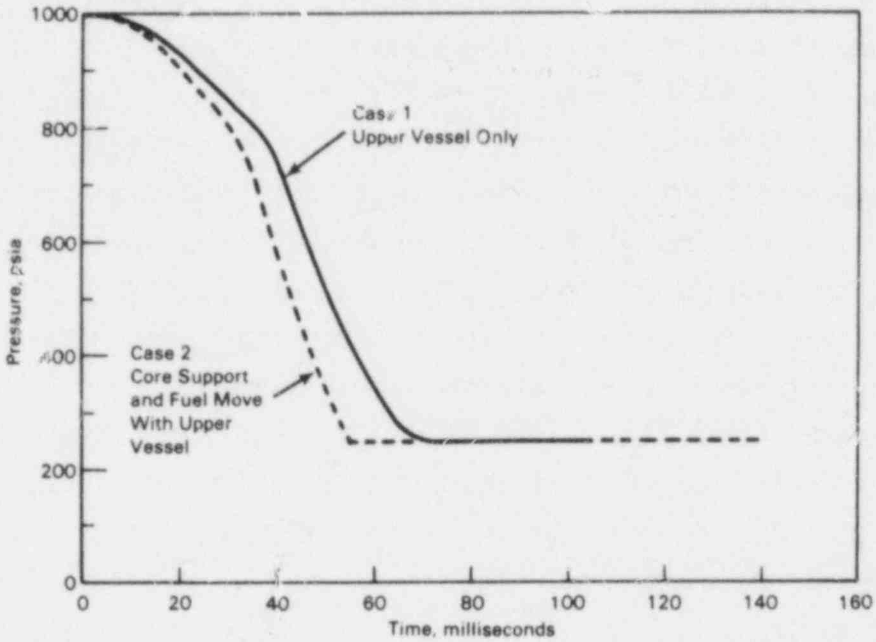

FIGURE K.14. Pressure Characteristics for Top Support Condition

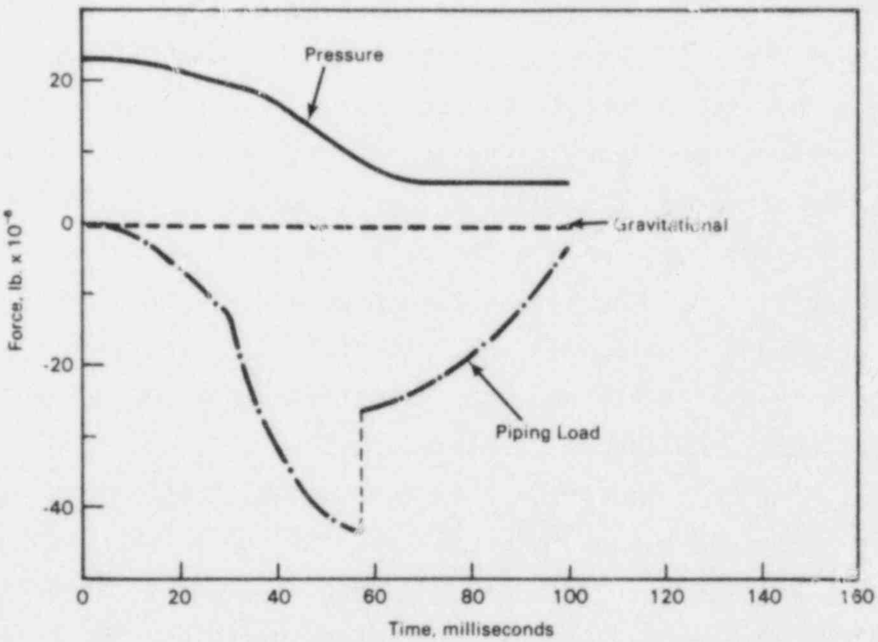

FIGURE K.15. Upper Head Force Components for Case 1 with Top Support

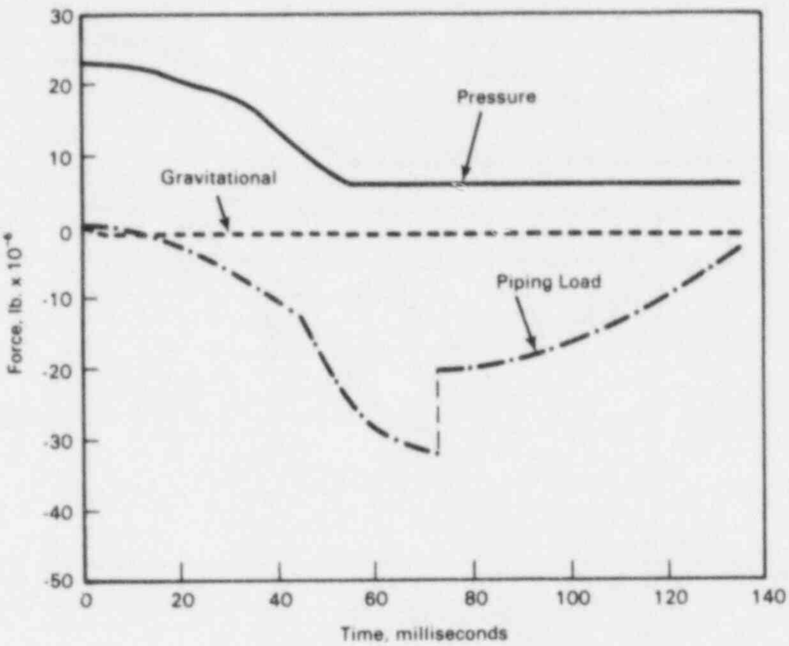

FIGURE K.16. Upper Head Force Components for Case 2 with Top Support

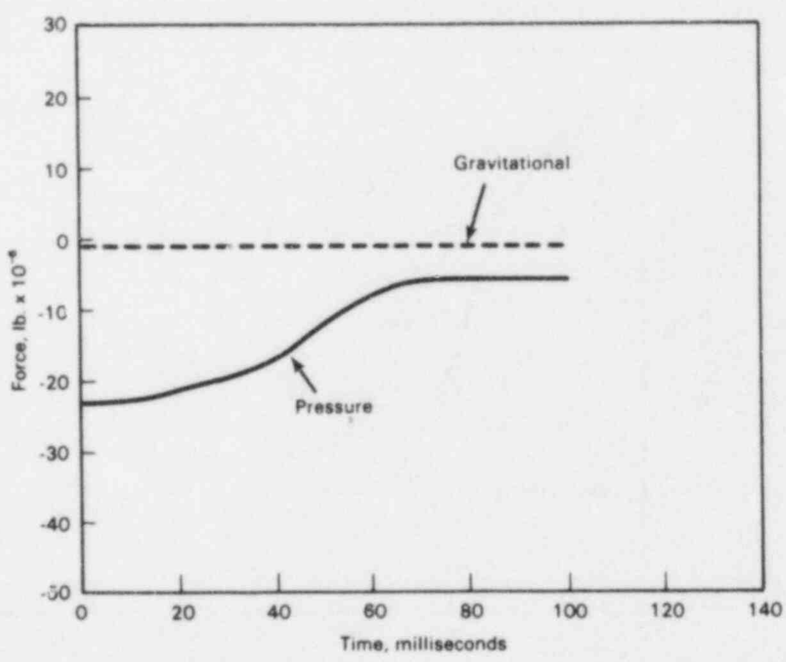

FIGURE K.17. Lower Vessel Force Components for Case 1 with Top Support

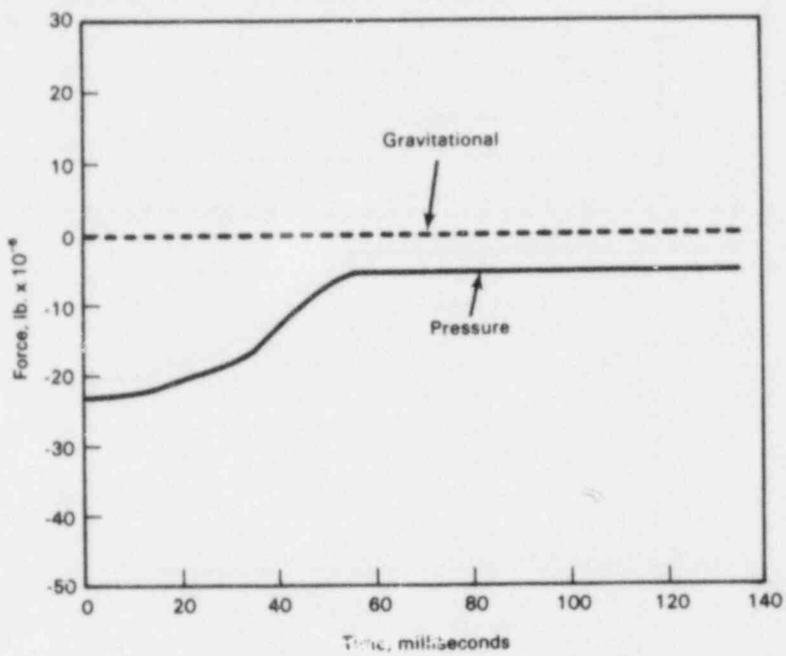

FIGURE K.18. Lower Vessel Force Components for Case 2 with Top Support

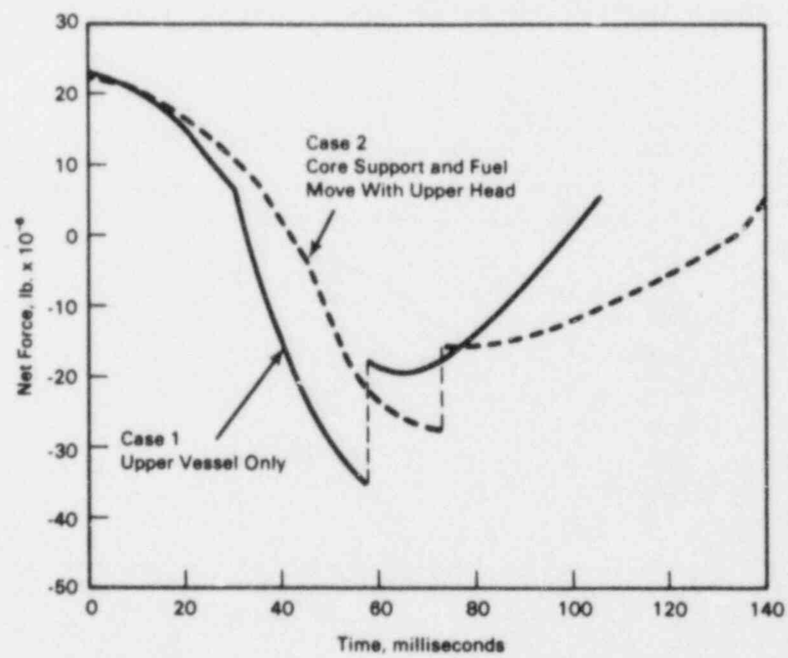

FIGURE K.19. Thrust Force Characteristics of Upper Head Assembly for Top Support Conditions

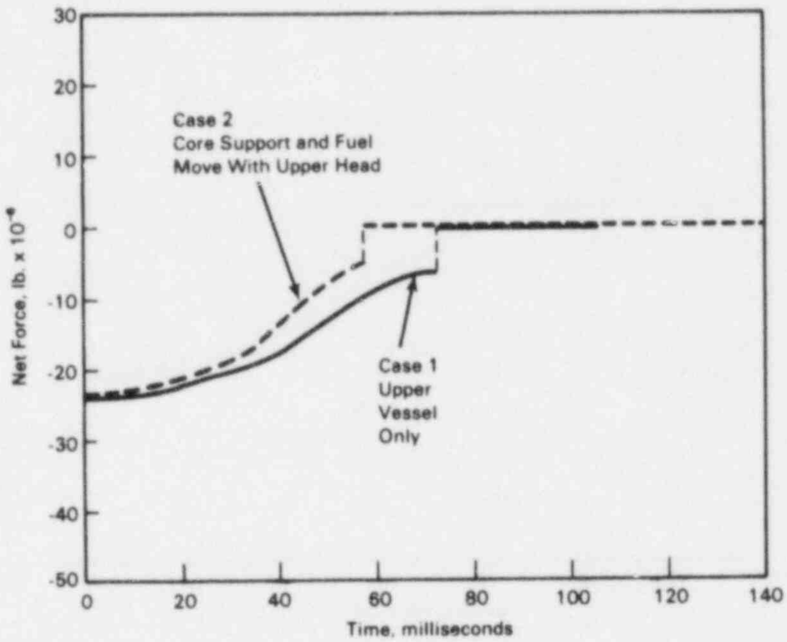

FIGURE K.20. Thrust Force Characteristics of Lower Vessel for Top Support Conditions

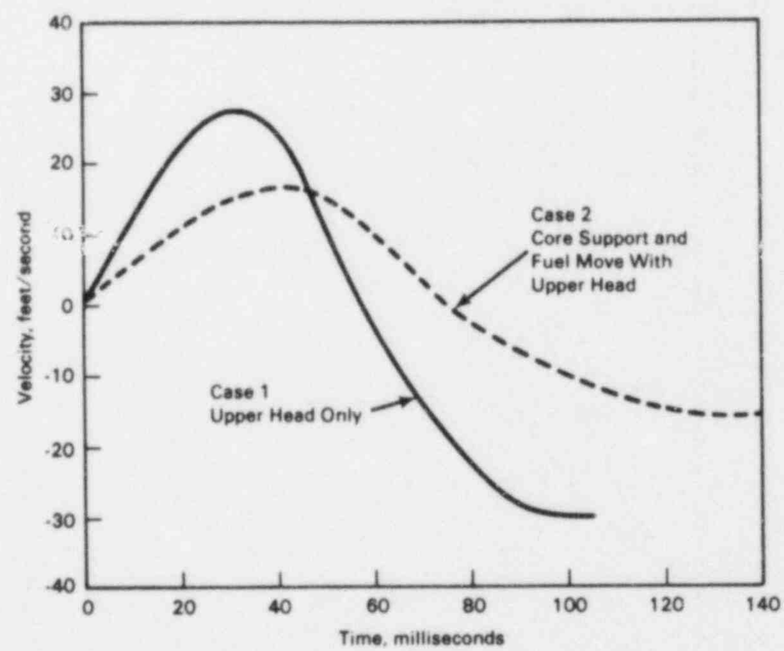

FIGURE K.21. Velocity Characteristics of Upper Head Assembly for Top Support Condition

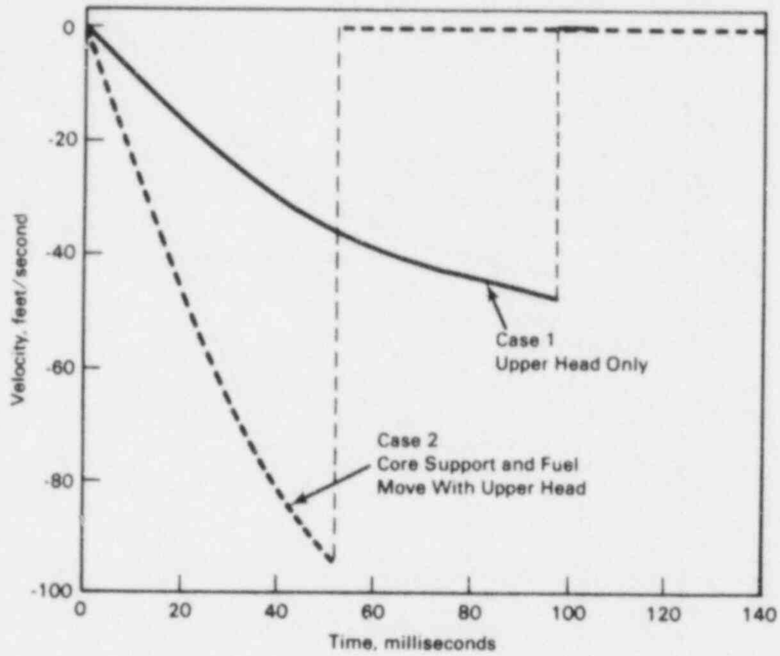

FIGURE K.22. Velocity Characteristics of Lower Vessel for Top Support Condition

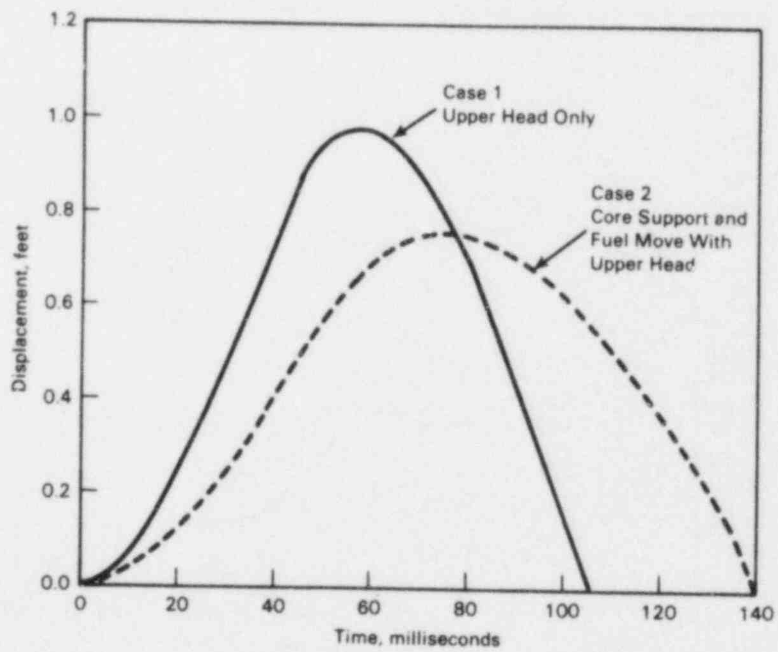

FIGURE K.23. Displacement Characteristics of Upper Head Assembly for Top Support Condition

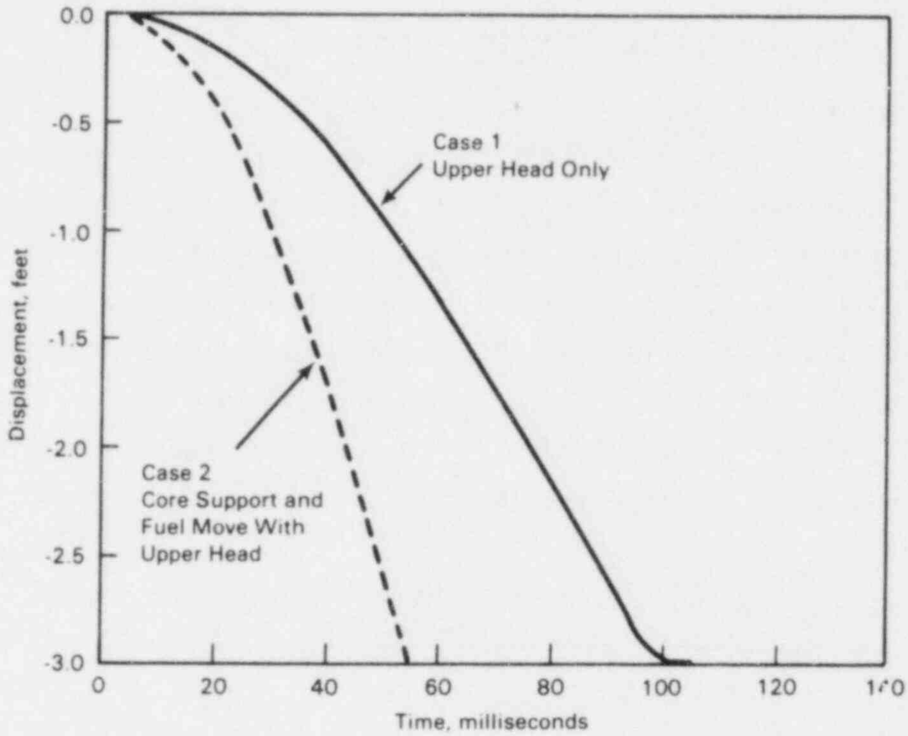

FIGURE K.24. Displacement Characteristics of Lower Vessel for Top Support Condition

As shown by the results, the effect of the attached piping on the upper vessel is quite significant, both on upward and downward travel. Beyond an upward deflection of about 6 in., the piping characteristics clearly dominate. The total upward displacement of the fragment is restricted to a maximum value of 1 ft by the piping load. However, the piping load actually contributes to the momentum for downward motion and thus increases the velocity on the return impact.

The simplifying assumption of instantaneous flashing should be conservative for both upward motion of the upper vessel fragment and the downward motion of the lower vessel fragment. The lower pressure that would actually occur would cause a slightly greater impact velocity for the upper vessel fragment. The significance of this factor, however, should be relatively small in comparison to that of the attached piping.

COMPARISON OF TOP AND BOTTOM SUPPORTED RESULTS

As stated before, the vessel data and initial conditions used in the analysis of the top supported condition are consistent with those of the bottom supported condition. The main difference in the models is in the support arrangement. This gives rise to a lower vessel fragment for the top support condition, which is subject to motion when the break occurs. In comparing results (see Table K.4), the maximum height attained by the upper vessel fragment is about 6% less in Case 1 and 24% less in Case 2 than those determined by the fixed bottom model. The downward impact velocities are greater in Case 1 by 17% and less in Case 2 by 27%.

TABLE K.4. Summary of Missile Generation Study for Top Support Condition

Initial Conditions:

$P = 1000$ psia

$T_{steam} = 620°F$

$T_{liquid} = 400°F$

Total lower vessel displacement = 2 ft

Case	Component	Upward Motion V_{MAX}, ft/s	Upward Motion Y_{MAX}, ft	Downward Impact, ft/s
1	Upper vessel (M_T = 585,500 lb)	28.0	0.98	29.2
	Lower vessel + Core support + Fuel assembly (M_B = 932,350 lb)	----	----	43.3
2	Upper vessel + Core support + Fuel assembly (M_T = 1,194,850 lb)	16.4	0.76	15.1
	Lower vessel (M_B = 323,000 lb)	----	----	85.4

The effect of lower vessel motion is more significant in Case 2, where a much greater rate of depressurization is observed. In this case the fuel assembly remains with the upper head, thus leaving the lower vessel fragment with a smaller mass. Consequently, a higher acceleration is achieved, which causes a greater rate of volume expansion. As shown by the results, the main portion of system depressurization occurs prior to the time at which peak displacement is achieved. In Case 1, depressurization is still occurring at peak displacement, and the effect of lower vessel motion is of less significance.

DISCUSSION AND CONCLUSIONS

The analyses predict that the upper head missile will arrest after about 1 ft of vertical motion. This conclusion applies for both top and bottom support of the reactor vessel.

The assumed conditions for the fluid thrust forces are believed to be conservative. At the time of maximum probability of through-wall cracking during a PTS event, the fluid temperatures are likely to be much lower than those assumed in the current calculation. Also, the assumed presence of a large steam void in the upper part of the vessel is conservative. The effect of fluid in the primary coolant loop, but outside the vessel, was not considered in the evaluations. The thrust from this fluid will be more sustained than that provided by the fluid in the vessel itself. However, the additional thrust will be small compared to that from the rapid expansion of the fluid in the vessel.

The large-diameter coolant piping will be deformed about 6 in. diametrically. This will entail significant plastic deformation of the relatively ductile piping materials. The only consequence of this deformation that needs to be addressed is the complete severance of all the primary coolant pipes. Only complete severance would permit the upper head to become a missile that could leave the vessel cavity. Although cracking of the piping at the points of impact with the concrete structure cannot be precluded, complete pipe

APPENDIX L

PRESSURE DROP ACROSS CORE

APPENDIX L

PRESSURE DROP ACROSS CORE

Estimates of the dynamic pressure loading on a reactor core structure following severe vessel ruptures are presented. The results are applicable to considerations of core structural integrity during PTS events.

The rupture considered is characterized by an instantaneous failure of an entire circumferential weld resulting from PTS. Under these conditions, the magnitudes of the pressure drop across the core may be substantial. This investigation was carried out as part of an effort to assess vessel and core integrity during such an event.

Values for core pressure drop were determined from the results of two separate studies. The first set of results was obtained from the study given in Appendix K. Pressure drop values were calculated based on the predicted relative velocities between the core channels and coolant as presented in Appendix K. The other set of pressure drop values was based on a study performed at Los Alamos National Laboratory (LANL) where the TRAC-PF1 code was used to calculate the vessel blowdown transients upon rupture. In both cases, assumptions were made to provide maximum fluid thrust conditions in the vessel. Loop components other than the vessel were not included in either of the analyses.

A range of initial fluid conditions is covered by the two sets of calculations and includes both saturated and subcooled cases. The first study (PNL study) used one set of initial conditions and gave results for both a top-supported and bottom-supported (e.g., Oconee-1) vessel. The LANL calculations included four transients, each run with different initial conditions using a single vessel model. A basic description of the analysis and modeling assumptions used in each of the studies is given in the next two sections. Final results and discussion are presented in the subsequent section.

FRAGMENT DYNAMIC RESPONSE APPROACH (PNL)

In the event of a complete circumferential fracture, the resulting vessel fragments are subject to acceleration by the thrust of the expanding fluid. The analysis of Appendix K predicts the dynamic response of the vessel fragments and, in particular, the upper fragment, which consists of the upper head assembly and core structure. The model developed for the analysis basically includes the reactor vessel, the support configuration, and the restraint from attached piping. As mentioned before, effects due to fluid from other components of the primary coolant system were not considered.

The behavior of the lower vessel fragment depends upon the support feature. If the vessel is bottom-supported such as the Oconee-1 reactor vessel, then it remains stationary. If the vessel is top supported such as those at Calvert Cliffs and H. B. Robinson plants, then the lower fragment will drop from its suspended height above ground. The support configuration is important in the core pressure drop calculation because it will affect the relative velocity between the core and coolant. The effect of the attached piping on the upper head is to restrict the vertical motion of the upper vessel fragment.

The model used in the analysis for the top-supported vessel is shown in Figure L.1. The initial vessel conditions are the same as those in Appendix K. They consist of subcooled coolant at 400°F in the core and superheated steam at 620°F and 1000 psia filling the upper head and upper plenum region. The presence of the steam void was chosen to provide maximum fluid thrust conditions for the given system pressure. Rupture of the vessel is assumed to occur instantaneously. Displacement of the vessel fragments(s) occurs in the vertical direction, and the resulting crack opening allows fluid to escape. The liquid coolant residing in the lower vessel fragment remains with the vessel and is assumed incompressible. The steam void is assumed to undergo an isentropic expansion. With these conditions, the equation of motion for the vessel fragments was solved. Velocity and displacement characteristics were obtained for the moving fragments. Figure L.2 shows the predicted system depressurization for the two cases.

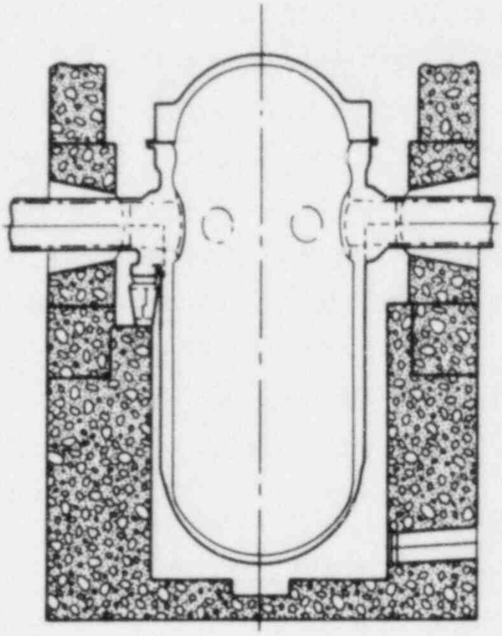

FIGURE L.1. PNL Vessel Rupture Model

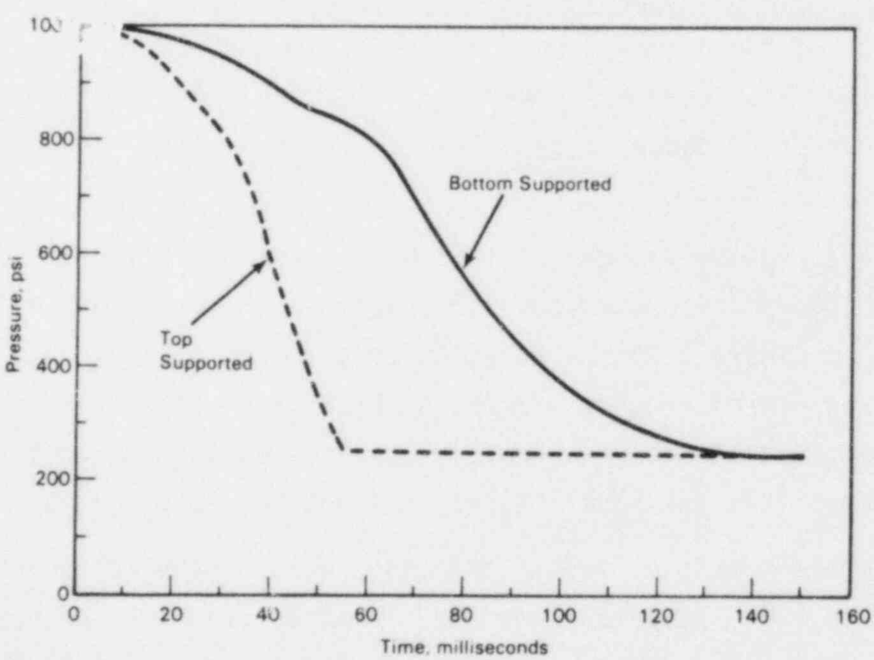

FIGURE L.2. PNL Vessel Rupture Model Depressurization Characteristics

Values for core pressure drop were determined using the predicted relative motion between the vessel and coolant as described in Appendix K. The problem was handled in a quasi steady-state manner using one-dimensional flow analysis. The computed fragment velocities were used to define the relative velocities between the core channel and coolant. Predicted fragment displacements were used to define the separate flow lengths for the liquid and steam. A geometry of a single subchannel surrounded by four fuel pins was selected for the analysis. Pressure losses due to surface friction, elevation, and grid spacers and end fittings were included. Additional calculations were made to check for the possibility of choked flow. For both subcooled and saturated fluid conditions, the critical mass flux was not exceeded. Therefore, no limitation due to flow choking needs to be considered.

TRAC-PF1 BLOWDOWN APPROACH (LANL)

Calculations of the hydrodynamic blowdown transient following a complete circumferential vessel fracture were performed at LANL using the TRAC-PF1 code (Lime 1983). The model used in the analysis consisted of the vessel (Westinghouse Zion-1) and the surrounding containment area. The hot- and cold-leg piping and other loop components were not included. One-dimensional flow modeling was used. A description of the TRAC-PF1 model is given in Figure L.3.

The vessel rupture was characterized by eliminating the bottom vessel shell from the model; i.e., no solid boundary exists between the lower plenum cell (node 8 of Figure L.3) and adjacent containment cell (node 9). This incorporates an effective circumferential break and allows the coolant to escape from the vessel and into the surrounding containment area. The analysis assumes that the lower vessel fragment has no effect on the process.

Four different initial fluid conditions were chosen for analysis and are listed in Table L.1. Computed blowdown characteristics of the upper-head, upper-plenum, and core regions are given in Figure L.4. As shown by these curves, depressurization occurred rapidly for subcooled conditions, on the

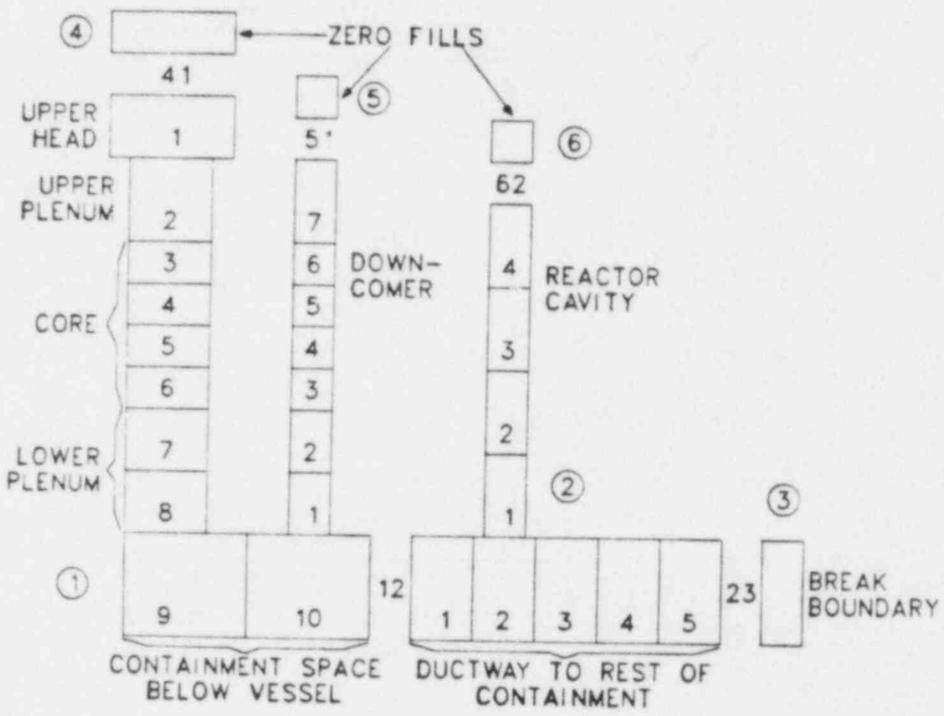

FIGURE L.3. LANL Vessel Rupture Model

TABLE L.1. LANL Vessel Rupture Model - Initial Vessel Conditions

Case	Temperature	Pressure	Description
1	394°K (250°F)	15.9 MPa (2300 psia)	Vessel subcooled throughout and completely filled. Degree of subcooling = 226°K (407°F), P_{sat} = 0.205 MPa (30 psia).
2	422°K (300°F)	15.9 MPa (2300 psia)	Vessel subcooled throughout and completely filled. Degree of subcooling = 198°K (356°F), P_{sat} = 0.463 MPa (67 psia).
3	450°K (350°F)	15.9 MPa (2300 psia)	Vessel subcooled throughout and completely filled. Degree of subcooling = 170°K (307°F), P_{sat} = 0.935 MPa (136 psia).
4	558°K (545°F)	6.9 MPa (1000 psia)	Core and lower plenum saturated, downcomer subcooled at 288.7°K (60°F), and upper head and upper plenum voided.

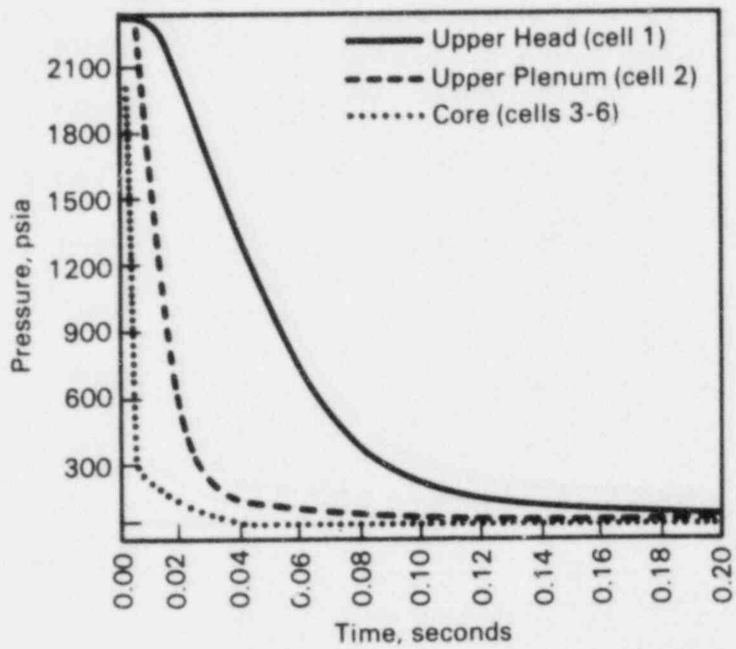

a. Case 1 - 2300 psia, 250°F

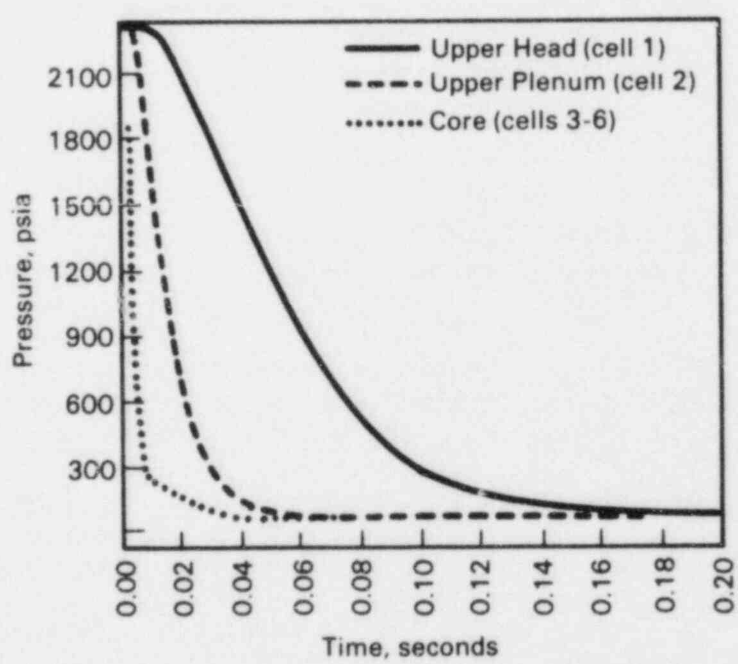

b. Case 2 - 2300 psia, 300°F

FIGURE L.4. TRAC-PF1 Results: Upper Head, Upper Plenum, and Core Pressures

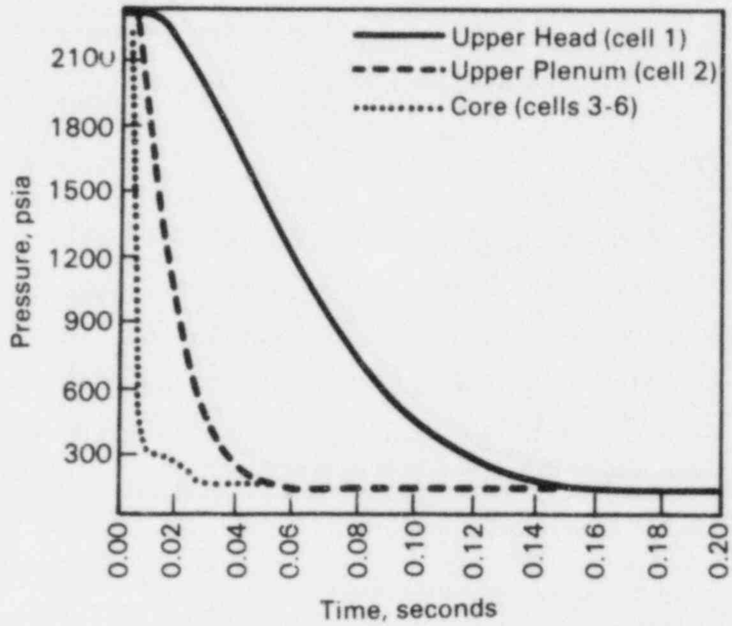

c. Case 3 - 2300 psia, 350°F

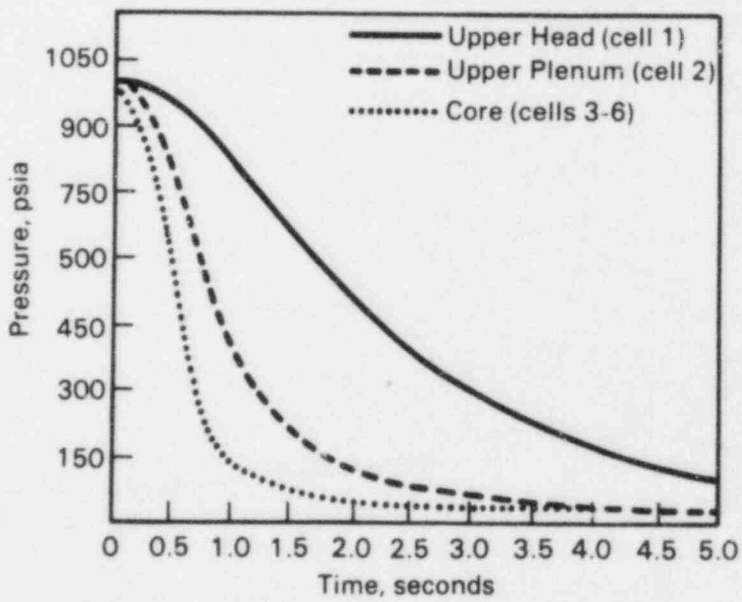

d. Case 4 - 1000 psia, 545°F

FIGURE L.4. (Contd)

order of 100 ms. For the saturated case, the rate of depressurization was much slower, on the order of seconds. This was due to the occurrence of flashing. Core pressure drop results are given in the next section.

RESULTS AND DISCUSSIONS

Core pressure drop based on vessel fragment velocities obtained from the PNL study are shown in Figure L.5. Numerical values are listed in Table L.2. Values were computed for the duration of the simulation, which, in both cases was about 150 ms, at which time the upper vessel returns to its original position. The pressure drop is defined with respect to the top of the core. Negative values thus represent downward motion of the upper fragment as evidenced by the relative velocity values.

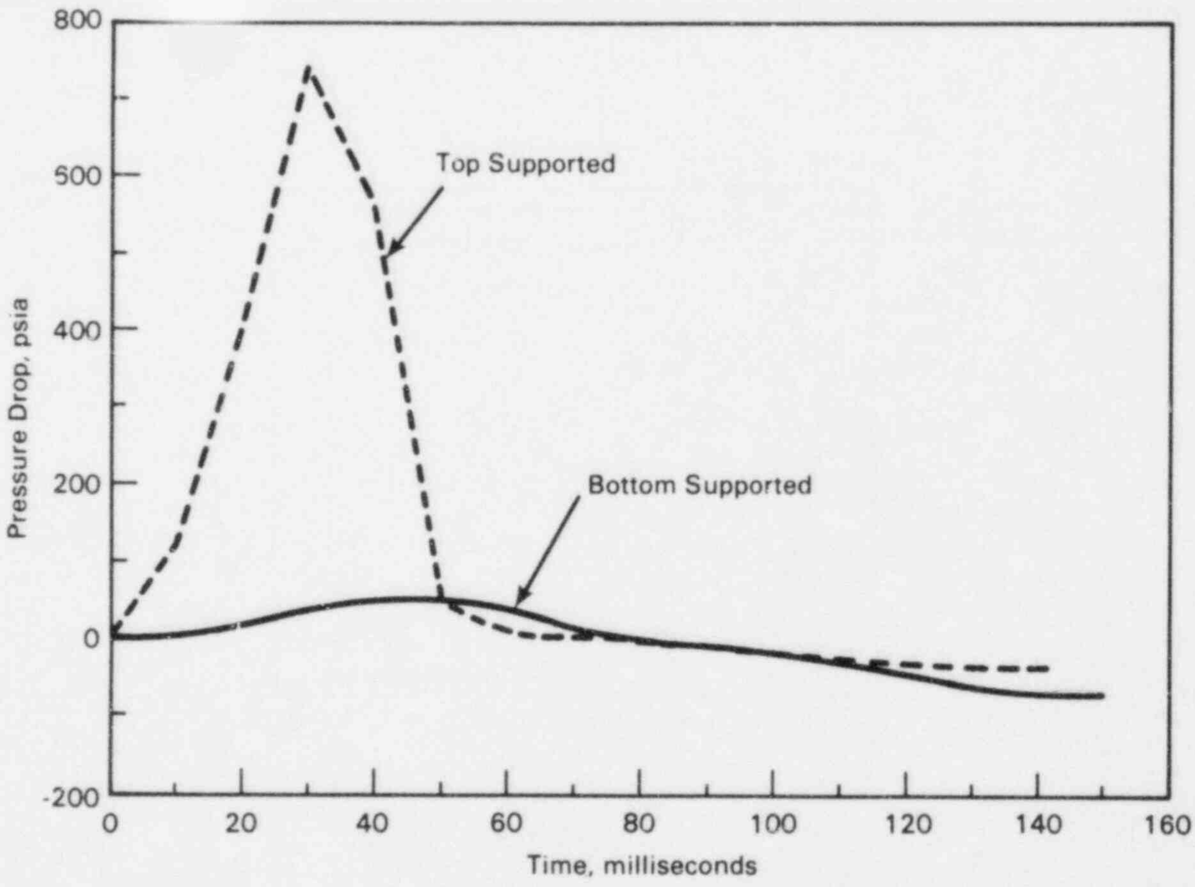

FIGURE L.5. PNL Vessel Rupture Model Pressure Drop Characteristics

TABLE L.2. Core Pressure Drop Values Based on (PNL) Fragment Velocity Results

Time, ms	Bottom-Supported Vessel V_r, ft/s	Bottom-Supported Vessel ΔP, psia	Top-Supported Vessel V_r, ft/s	Top-Supported Vessel ΔP, psia
0.0	0.0	0.0	0.0	0.0
10.0	5.8	2.1	28.8	118.9
20.0	11.1	17.0	55.9	401.4
40.0	18.5	49.2	97.9	564.0
50.0	19.2	52.4	15.3	47.8
60.0	16.2	36.6	10.2	11.4
70.0	10.4	13.9	3.2	-1.7
80.0	2.5	-2.8	-2.4	-4.5
90.0	-3.2	-6.1	-6.5	-10.0
100.0	-7.8	-14.7	-10.1	-18.3
110.0	-12.3	-28.7	-13.0	-27.4
120.0	-16.2	-45.5	-14.9	-34.8
130.0	-19.2	-61.4	-15.8	-38.9
140.0	-21.0	-72.2	-15.6	-38.3
150.0	-21.2	-74.6		

(a) V_r = relative velocity between core channel and coolant

Results are presented for both top-supported and bottom-supported vessels. As previously stated, a circumferential break causes both upper and lower vessel fragments to move in the top-supported configuration. It was assumed that the liquid coolant moves along with the lower fragment while the core remains attached to the upper head assembly (upper fragment). The relative velocities between the core channel and coolant are therefore much greater for the top-supported vessel and result in higher pressure drops. The maximum computed value is 737 psia for an initial system pressure of 1000 psia, and occurs at 30 ms.

Core pressure drop characteristics obtained from LANL TRAC-PF1 predictions are given in Figures L.6 through L.8 and in Table L.3. Results corresponding to the initial conditions of Case 1 in (Table L.1) were not included, because this represented the least severe case. The core pressure drop is defined by the difference in pressure between the upper plenum and the upper cell of the lower plenum (node 2 and node 7, respectively). The maximum value for subcooled conditions at 2300 psia is about 2222 psia, occurring at 4 ms (Case 2). The maximum value for the saturated case with an initial pressure of 1000 psia is 727 psia, occurring at 400 ms.

Results given in this report cover a range of possible initial conditions for the described vessel failure mode. It is important to realize, however, the differences in approach each of the studies have taken. The two sets of results are not necessarily comparable, because each was obtained from a distinctly different model. The PNL model considered rupture to occur at a weld located midway on the vessel. Core pressure drop was determined by the relative velocities between core channel and coolant imposed by the acceleration of the vessel fragments. In addition to the fluid thrust forces, the dynamic response of the fragments included the effects of the attached piping restraint and gravity. Coolant was allowed to escape from the vessel by one-dimensional flow in the lateral direction. The coolant residing in the core channels was considered to be stationary. Actual flow acceleration was therefore not present in this model.

In the TRAC-PF1 model, rupture was simulated by eliminating the vessel bottom. In this case, the core pressure drop is a result of the flow of escaping coolant through the core channels, and free acceleration of fluid is allowed to occur. Effects due to the presence of the lower vessel (lower fragment) were neglected. Free acceleration from the system pressure to a back pressure (containment pressure) is not expected to occur in reality, because the crack opening and, thus, the flow, is most likely to be restricted as envisioned in the PNL study.

In conclusion, LANL results are believed to be extremely conservative when compared with PNL results. It is recommended that, in a plant-specific

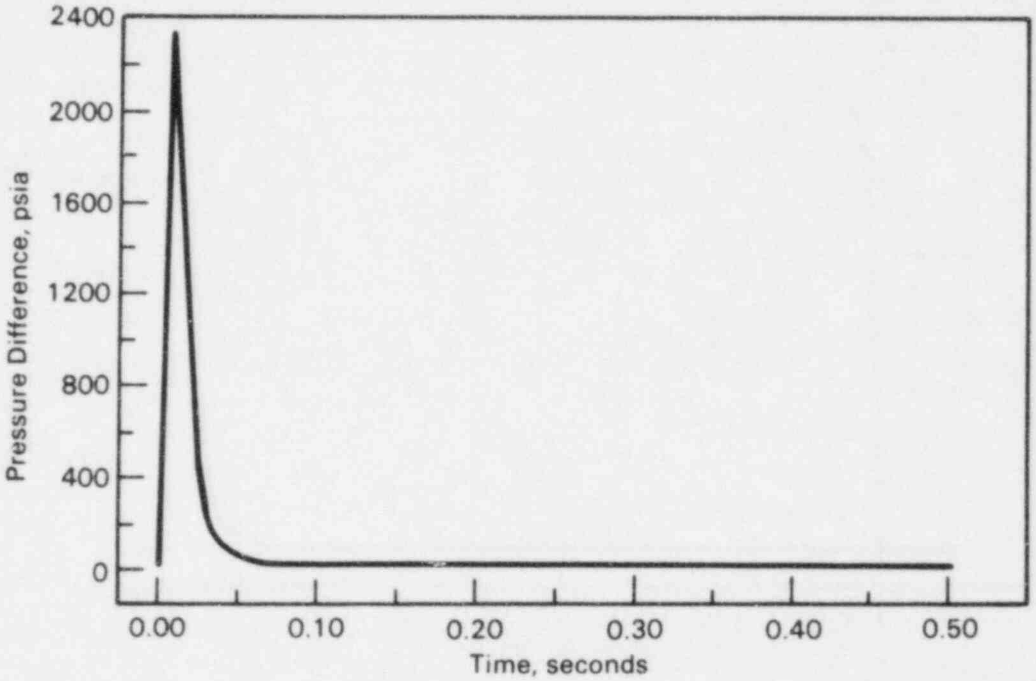

FIGURE L.6. TRAC-PF1 Vessel Rupture Model Pressure Drop Characteristics - Case 2

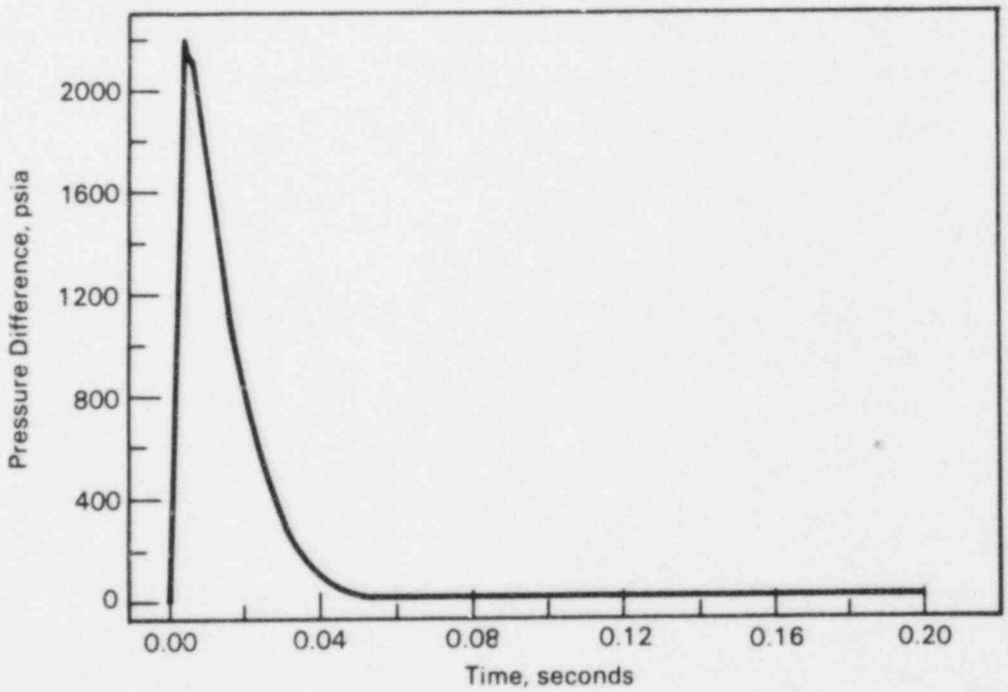

FIGURE L.7. TRAC-PF1 Vessel Rupture Model Pressure Drop Characteristics - Case 3

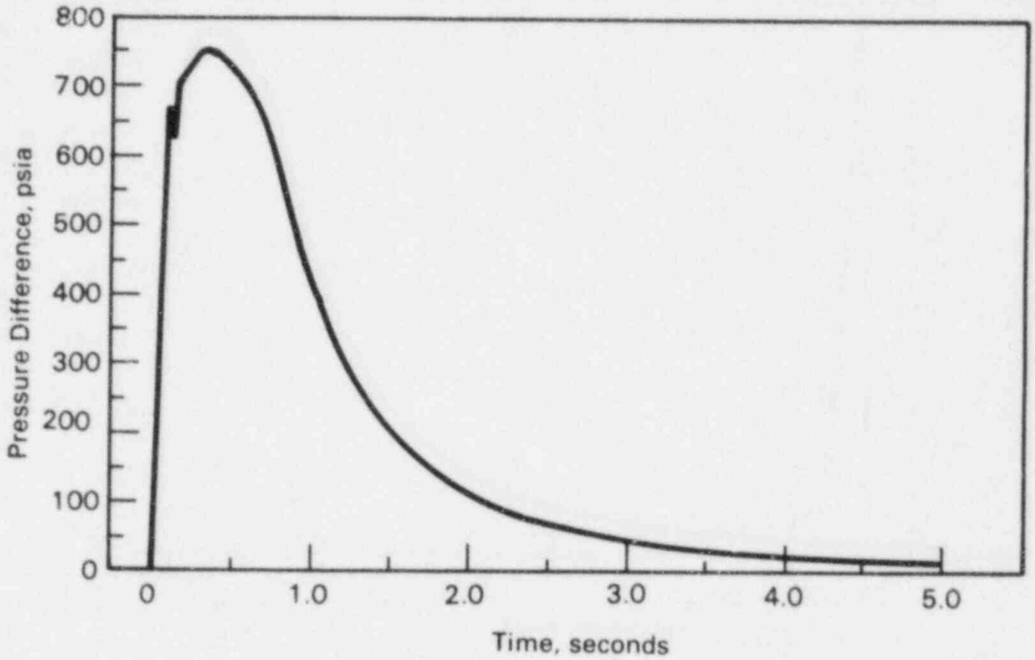

FIGURE L.8. TRAC-PF1 Vessel Rupture Model Pressure Drop Characteristics - Case 4

analysis, the primary loop components (namely the steam generators, pressurizer, and hot and cold legs) be included in the modeling, to obtain a better estimate of the system pressure through the transient.

REFERENCE

Lime, J. F. 1983. Hydrodynamic Blowdown Calculations of a Severe Vessel Rupture Using the TRAC-PF1 Code. LA-UR-83-358, Los Alamos National Laboratory, Los Alamos, New Mexico.

TABLE L.3. Core Pressure Drop Values Based on (LANL) TRAC-PF1 Blowdown Calculations

Time, ms	ΔP, psia Case 2 300°F 2300 psia	Case 3 350°F 2300 psia	Case 4 545°F 1000 psia
0.0	0.0	0.0	0.0
2.0	1824.7	1447.6	
4.0	2222.5	2166.1	
6.0	2065.2	2055.6	
8.0	1795.8	1841.2	
10.0	1540.0	1579.6	
12.0	1304.9	1413.4	
14.0	1097.6	1224.4	
16.0	920.9	1057.4	
18.0	765.4	907.4	
20.0	630.3	772.4	34.5
30.0	216.1	291.1	
40.0	81.4	95.7	301.8
50.0	40.0	31.0	
60.0	22.7	10.3	669.3
70.0			
80.0	7.9	8.2	661.2
90.0	4.4	9.1	
100.0	2.7	9.6	616.8
200.0	6.0	22.9	725.2
400.0	727.1		
600.0			657.8
800.0			526.1
1000.0			390.1
1200.0			288.8
1400.0			219.1
1600.0			168.4
1800.0			132.4
2000.0			106.6
2200.0			87.6
2400.0			73.1

DISTRIBUTION

No. of
Copies

OFFSITE

U.S. Nuclear Regulatory Commission
Division of Technical Information
and Document Control
7920 Norfolk Avenue
Bethesda, MD 20014

D. G. Ball
Oak Ridge National Laboratory
P.O. Box Y
Oak Ridge, TN 37830

R. D. Cheverton
Oak Ridge National Laboratory
P.O. Box Y
Oak Ridge, TN 37830

G. R. Irwin
Department of Mechanical Engineering
University of Maryland
College Park, MD 20742

C. E. Johnson
U.S. Nuclear Regulatory Commission
Division of Risk Analysis
Office of Nuclear Regulatory
Research
Washington, DC 20555

R. E. Johnson
U.S. Nuclear Regulatory Commission
Generic Issues Branch
Mail Stop 268 Phillips Bldg.
Washington, DC 20555

R. W. Klecker
U.S. Nuclear Regulatory Commission
Division of Engineering
Technology/RES
Materials Engineering Branch
Washington, DC 20555

No. of
Copies

P. N. Randall
U.S. Nuclear Regulatory
Commission
Division of Risk Analysis
Office of Nuclear Regulatory
Research
Washington, DC 20555

M. Vagins
Division of Engineering
Technology
Office of Nuclear Regulatory
Research
U.S. Nuclear Regulatory
Commission
Washington, DC 20555

R. Woods
Division of Safety Tech-
nology
Nuclear Reactor Regulation
U.S. Nuclear Regulatory
Commission
Washington, DC 20555

No. of
Copies

38 Pacific Northwest Laboratory

W. E. Anderson
M. C. C. Bampton
S. H. Bian
S. H. Bush
D. B. Cearlock
E. L. Courtright
M. R. Garnich
D. K. Kreid
K. K. Nomura
L. T. Pedersen (2)
G. J. Posakony
J. T. A. Roberts
E. P. Simonen
F. A. Simonen (15)
R. A. Stokes
D. S. Trent
Publishing Coordination (2)
Technical Information (5)

NRC FORM 335 (2-84) NRCM 1102, 3201, 3202 — U.S. NUCLEAR REGULATORY COMMISSION

BIBLIOGRAPHIC DATA SHEET

SEE INSTRUCTIONS ON THE REVERSE

1. REPORT NUMBER (Assigned by TIDC, add Vol. No., if any)
NUREG/CR-4483
PNL-5727

2. TITLE AND SUBTITLE
Reactor Pressure Vessel Failure Probability Following Through-Wall Cracks Due to Pressurized Thermal Shock Events

3. LEAVE BLANK

4. DATE REPORT COMPLETED
MONTH: March — YEAR: 1986

5. AUTHOR(S)
F.A. Simonen, M.R. Garnich, E.P. Simonen, S.H. Bian, K.K. Nomura, W.E. Anderson, L.T. Pedersen

6. DATE REPORT ISSUED
MONTH: April — YEAR: 1986

7. PERFORMING ORGANIZATION NAME AND MAILING ADDRESS (Include Zip Code)
Pacific Northwest Laboratory
P.O. Box 999
Richland, Washington 99352

8. PROJECT/TASK/WORK UNIT NUMBER

9. FIN OR GRANT NUMBER
B2510

10. SPONSORING ORGANIZATION NAME AND MAILING ADDRESS (Include Zip Code)
Division of Safety Review and Oversight
Office of Nuclear Reactor Regulation
U.S. Nuclear Regulatory Commission
Washington, D.C.

11a. TYPE OF REPORT
Technical

b. PERIOD COVERED (Inclusive dates)

12. SUPPLEMENTARY NOTES

13. ABSTRACT (200 words or less)
A fracture mechanics model was developed at the Pacific Northwest Laboratory (PNL) to predict the behavior of a reactor pressure vessel following a through-wall crack that occurs during a pressurized thermal shock (PTS) event. This study contributed to a U.S. Nuclear Regulatory Commission (NRC) program to study PTS risk. The model predicts the arrest, reinitiation, and direction of crack growth for a postulated through-wall crack and thereby predicts the mode of vessel failure. A Monte-Carlo type of computer code was written to predict the probabilities of the alternative failure modes with the fracture mechanics properties of the various welds and plates of a vessel as random variables. Plant-specific calculations for the Oconee-1, Calvert Cliffs-1, and H. B. Robinson-2 reactor pressure vessels for the conditions of postulated transients predicted that 50% or more of the through-wall axial cracks will turn to follow a circumferential weld. This predicted failure mode results in a potential vertically-directed missile consisting of the upper head assembly. Missile arrest calculations predict that such vertical missiles, as well as all potential horizontally directed fragmentation type missiles, will be confined to the vessel enclosure cavity. The PNL failure mode model is recommended for use in future evaluations of other plants, to determine the failure modes that are most probable for postulated PTS events.

14. DOCUMENT ANALYSIS – a. KEYWORDS/DESCRIPTORS
Pressurized water reactor
Pressurized thermal shock

b. IDENTIFIERS/OPEN-ENDED TERMS

15. AVAILABILITY STATEMENT
Unlimited

16. SECURITY CLASSIFICATION
(This page) Unclassified
(This report) Unclassified

17. NUMBER OF PAGES

18. PRICE

UNITED STATES
NUCLEAR REGULATORY COMMISSION
WASHINGTON, D.C. 20555

OFFICIAL BUSINESS
PENALTY FOR PRIVATE USE, $300

SPECIAL FOURTH-CLASS RATE
POSTAGE & FEES PAID
USNRC
WASH. D.C.
PERMIT No. G-67

120555078877 1 1AN1RM11S
US NRC
ADM-DIV OF TIDC
POLICY & PUB MGT BR-PDR NUREG
W-501
WASHINGTON DC 20555